

REPORT DOCUMENTATION PAGE			Form Approved OMB No. 0704-0188	
Public reporting burden for this collection of information is estimated to average 1 hour per response, including the time for reviewing instructions, searching existing data sources, gathering and maintaining the data needed, and completing and reviewing the collection of information. Send comments regarding this burden estimate or any other aspect of this collection of information, including suggestions for reducing this burden, to Washington Headquarters Services, Directorate for Information Operations and Reports, 1215 Jefferson Davis Highway, Suite 1204, Arlington, VA 22202-4302, and to the Office of Management and Budget, Paperwork Reduction Project (0704-0188), Washington, DC 20503.				
1. AGENCY USE ONLY (Leave blank)		2. REPORT DATE December 15, 2003	3. REPORT TYPE AND DATES COVERED Technical 08/01/01 to 12/15/03	
4. TITLE AND SUBTITLE Some Features of Tip Gap Flow Fields of a Linear Compressor Cascade			5. FUNDING NUMBERS N00014-99-1-0302	
6. AUTHORS Qing Tian and Roger L. Simpson				
7. PERFORMING ORGANIZATION NAME(S) AND ADDRESS(ES) Department of Aerospace and Ocean Engineering Virginia Polytechnic Institute and State University Blacksburg, Virginia 24061-0203			8. PERFORMING ORGANIZATION REPORT NUMBER VPI-AOE-286	
9. SPONSORING/MONITORING AGENCY NAME(S) AND ADDRESS(ES) Office of Naval Research, 800 N. Quincy Street Arlington, Virginia 22217			10. SPONSORING/MONITORING AGENCY REPORT NUMBER	
11. SUPPLEMENTARY NOTES				
12a. DISTRIBUTION/AVAILABILITY STATEMENT Unlimited			12b. DISTRIBUTION CODE	
<p>13. ABSTRACT (Maximum 200 words) This report presents results from an experimental study of three-dimensional turbulent tip gap flows in the linear cascade wind tunnel for two different tip gap clearances ($t/c=1.65\%$ and 3.3%). Three experimental techniques are used to measure the tip gap velocity field and static pressure field on the end-wall: a three-orthogonal-velocity-component fiber-optic laser Doppler anemometer (3D-LDA) system, surface oil flow visualization, and a scani-valve pressure measurement system. The end-wall skin friction velocity is calculated from near-wall LDA data and pressure gradient data using the near-wall momentum equation.</p> <p>The statistics of Reynolds stresses and triple products in the two-dimensional turbulent boundary layer and three-dimensional turbulent boundary layer were examined using a velocity fluctuation octant analysis. The octant analysis for the two-dimensional turbulent boundary layer reveals that ejections and sweeps are the dominant coherent motions. The octant analysis for the three-dimensional turbulent boundary layer in the tip gap shows that the dominant octant events are partially different from those in the two-dimensional turbulent boundary layer, but ejections and sweeps are still the dominant coherent motions. For the three-dimensional turbulent boundary layer in the moving wall flow, the near-wall shear flow reinforces the sweep motion to the moving wall and weakens the out-ward ejection motion in the shear flow dominant region. Between the passage flow and the shear flow is the interaction region of the high speed streaks and the low speed streaks. This is the first time that the coherent structure of the three-dimensional turbulent boundary in the linear cascade tip gap has been studied.</p>				
14. SUBJECT TERMS Three-dimensional Flow, Turbulent Boundary Layers, compressor flows, tip gap flows			15. NUMBER OF PAGES 208	
			16. PRICE CODE	
17. SECURITY CLASSIFICATION OF REPORT UNCLASSIFIED	18. SECURITY CLASSIFICATION OF THIS PAGE UNCLASSIFIED	19. SECURITY CLASSIFICATION OF ABSTRACT UNCLASSIFIED	20. LIMITATION OF ABSTRACT UNLIMITED	

ABSTRACT

Some Features of Tip Gap Flow Fields of a Linear Compressor Cascade

QING TIAN

This thesis presents some results from an experimental study of three-dimensional turbulent tip gap flows in the linear cascade wind tunnel, for two different tip gap clearances ($t/c=1.65\%$ and 3.3%). The experiments focus on near-wall flow field measurements for the stationary wall and moving wall, and static pressure measurement on the low end-wall for the stationary wall case. The representative flows were pressure driven, three-dimensional turbulent boundary layers in the linear cascade tunnel for the stationary wall case, and the combination of the pressure driven and shear driven flow for the moving wall case.

Several experimental techniques are used in the studies: a three-orthogonal-velocity-component fiber-optic laser Doppler anemometer (3D-LDA) system, surface oil flow visualization, and a scanivalve system for static pressure measurement through pressure ports on the end-wall. From the details of the oil flow visualization pattern on the end-wall, some features of the passage flow, cross flow, and the tip leakage vortex in this cascade flow were captured. Oil flow visualization on the blade surface reveals the reattachment of the tip leakage vortex on the blade surface. The static pressure results on the lower end-wall and mid-span of the blade show huge pressure drop on the lower end-wall from the pressure side to the suction side of the blade and from mid-span to the lower end wall. The end-wall skin friction velocity is calculated from near-wall LDA data and pressure gradient data using the near-wall momentum equation.

The statistics of Reynolds stresses and triple products in two-dimensional turbulent boundary layer and three-dimensional turbulent boundary layer was examined using a velocity fluctuation octant analysis in three different coordinates

20040123 026

(the wall collateral coordinates, the mid tip gap coordinates, and the local mean flow angle coordinates). The velocity fluctuation octant analysis for the two-dimensional turbulent boundary layer reveals that ejections of the low speed streaks outward from the wall and the sweeps of high speed streaks inward toward the wall are the dominant coherent motions. The octant analysis for the three-dimensional turbulent boundary layer in the tip gap shows that the dominant octant events are partially different from those in the two-dimensional turbulent boundary layer, but ejection and sweep motions are still the dominant coherent motions. For the three-dimensional turbulent boundary layer in the moving wall flow, the near-wall shear flow reinforces the sweep motion to the moving wall and weakens the out-ward ejection motion in the shear flow dominant region. Between the passage flow and the shear flow, is the interaction region of the high speed streaks and the low speed streaks. This is the first time that the coherent structure of the three-dimensional turbulent boundary in the linear cascade tip gap has been studied.

ACKNOWLEDGEMENTS

I wish to give my thanks to some of the people who made this thesis possible:

My advisor, Dr. Roger Simpson, who gave much guidance and assistance throughout the whole project; My committee members, Dr. William Devenport, who was my first course professor at Virginia Tech and Dr. Karen Thole, who gave insight to this work; My other professors at Virginia Tech, who give me the academic foundation to do this work; My undergraduate advisor, Dr. Nan Jiang at Tianjin University in China, who taught me the basic research skill necessary for my future work;

My current co-workers without whom I never would have finish this thesis. Specifically I would like to thank my partner Genglin Tang for teaching me the technique of LDA; My colleagues in our research group: Gwibo Byun, Todd Lowe, Jacob George, Shereef Sadek, Kevin Pisterman, Devin Stewart, Jeremy Bennington who gave insight for this work; The shop technicians: Steve Edwards, Bruce Stanger, Mike; My friends: Ruolong Ma, Lei Xie, and Michael Nakles.

The Office of Naval Research for the funding of the project is thanked, for their support under grant N00014-99-1-0302.

Finally, I would like to express my deepest appreciation to my wife, Yishan Liang, parents, sister, and sister in law who showed me the endless support and love.

Table of Contents

ABSTRACT	i
ACKNOWLEDGEMENTS	iii
Table of Contents	iv
List of Tables	vi
List of Figures	vii
NOMENCLATURE	xiii
1. INTRODUCTION	1
1.1 PERSPECTIVE OF THE PREVIOUS STUDY	1
1.2 OBJECTIVE OF THE PRESENT STUDY	4
1.3 ORGANIZATION OF THIS THESIS	6
2. APPARATUS AND INSTRUMENTS	7
2.1 WIND TUNNEL	7
2.1.1 Test Section	8
2.1.2 Moving Belt System	10
2.1.3 Plastic Tent	11
2.1.4 Cooling System	12
2.2 OIL FLOW VISUALIZATION	12
2.3 PRESSURE MEASUREMENT	13
2.3.1 Pressure Plate	13
2.3.2 Pressure Transducer	14
2.3.3 Scanivalve System	15
2.3.4 Open Jet Tunnel	16
2.3.5 Issues in the pressure measurement	16
2.4 LASER DOPPLER VELOCIMETER (LDV) SYSTEM	18
2.4.1 Optical table, and fiber optic probe	19
2.4.2 Signal processing electronics	20
2.4.3 SEEDING SYSTEM	24

2.5 DATA QUALITY	24
3. RESULTS AND DISCUSSION	33
3.1 OIL FLOW VISUALIZATION	33
3.1.1 Flow Visualization on the end-wall	33
3.1.2 Flow Visualization on the blade surface	35
3.1.3 The Oil Flow Direction and Wall Shear Stress Direction Measurement ..	36
3.1.4 Flow Structure in the Linear Cascade Tunnel	40
3.2 STATIC PRESSURE MEASUREMENTS	43
3.2.1 Static Pressure Coefficient C_p on the End-wall	44
3.2.2 Pressure Gradient and Quadric surface fit	47
3.2.3 Correction to the Separation line location	49
3.2.4 K pressure coefficient calculation	50
3.3 THE NEAR-WALL VELOCITY PROFILE FOR THE TIP GAP FLOW WITH PRESSURE GRADIENT	52
3.4 COMPARING WITH WALL SHEAR STRESS CHARACTERISTICS IN OIL FLOW	55
4. OCTANT ANALYSIS	79
4.1 OBJECTIVE OF OCTANT ANALYSIS	79
4.2 OVERVIEW OF COHERENT STRUCTURES AND MODELS FOR TURBULENT BOUNDARY LAYERS	80
4.3 OCTANT DEFINITIONS	86
4.4 MEAN FLOW ANGLES	89
4.5 THE COORDINATE SYSTEMS	91
4.6 MEAN VELOCITY FIELD	94
4.7 CONDITIONAL AVERAGING	96
4.8 RESULTS AND DISCUSSION	99
4.9 OCTANT ANALYSIS CONCLUSIONS	115
5. CONCLUSIONS	161
6. REFERENCE	165
Appendix A	170
Appendix B	182
Vita	195

List of Tables

Table 2.1 Parameters of the cascade blades	26
Table 3.1 Location of separation line relative to the blade surface.....	57
Table 3.2 The interpolated pressure data for 3.3% tip gap ratio in the bed coordinates	58
Table 3.3 Friction Velocity Comparision with and without Gressure Gradient $t/c=1.65\%$	60
Table 3.4 Friction Velocity Comparision with and without Gressure Gradient $t/c=3.3\%$	62
Table 4.1 Octant definition	123
Table 4.2 The sign of each octant in individual flow quantities	123
Table 4.3 The relationship between the different coordinate systems in the different tip gaps	123
Table a 7.1 Pressure Gradients Results for both Two Tip Gaps.....	180

List of Figures

Figure 2.1	Top view of fan and diffuser in the cascade tunnel	27
Figure 2.2	Side view of fan and diffuser in the cascade tunnel.....	27
Figure 2.3	Test section of the linear cascade tunnel.....	28
Figure 2.4	Side view of the test section of the linear cascade tunnel	28
Figure 2.5	Moving belt system in the linear cascade tunnel	29
Figure 2.6	Pressure plot is put under the blade	29
Figure 2.7	The dimension of the pressure plate and the relative positions of the pressure tap	30
Figure 2.8	Detail drawing of the pressure taps and plate surface	30
Figure 2.9	Bulgy and concave surface on the pressure plate.....	31
Figure 2.10	Block sketches of the optic table and laser beams paths	31
Figure 2.11	Fringe model: superposition of two laser beams.	32
Figure 2.12	Comparison with DNS data and cascade tunnel data	32
Figure 3.1	Oil flow visualization on the end-wall in the bed coordinates (Muthanna, 2002, $t/c=1.65\%$)	64
Figure 3.2	Oil flow visualization on the end-wall in the bed coordinates ($t/c=3.3\%$)	64
Figure 3.3	Mean velocity flow field in the tip gap and tip leakage vortex ($t/c=1.65\%$) in the separation coordinates.....	65
Figure 3.4	Mean velocity flow field in the tip gap and tip leakage vortex ($t/c=3.3\%$) in the separation coordinates.....	65
Figure 3.5	Oil flow visualization on the blade surface	66
Figure 3.6	Oil flow streaks in the wall shear stress direction measurement using digitized oil flow pictures	66
Figure 3.7	The comparison between the average sublayer flow angles and the wall shear stress angles relative to the x-axis in the bed coordinates $t/c=1.65\%$	67

Figure 3.8 The comparison between the average sublayer flow angles and the wall shear stress angles relative to the x-axis in the bed coordinates $t/c = 3.3\%$	67
Figure 3.9 Wall shear stress direction $t/c = 1.65\%$ (measured from the digitized oil flow pictures)	68
Figure 3.10 Wall shear stress direction $t/c = 3.3\%$ (measured from the digitized oil flow pictures)	68
Figure 3.11 Wall shear stress angles relative to the x-axis in the bed coordinates changing along pitchwise $t/c = 1.65\%$ (measured from the digitized oil flow pictures)	69
Figure 3.12 Wall shear stress angles relative to the x-axis in the bed coordinates changing along pitchwise $t/c = 3.3\%$ (measured from the digitized oil flow pictures)	69
Figure 3.13 Flow structure in the Linear Cascade Tunnel based on the oil flow visualization	70
and mean LDV velocity data	70
Figure 3.14 A schematic of ADAS (automated data acquisition system)	70
Figure 3.15 A picture of ADAS (automated data acquisition system)	71
Figure 3.16 Pressure plate with pressure taps	71
Figure 3.17 Pressure plate underneath the blades	72
Figure 3.18 Contours of static pressure coefficient measured on the end-wall $t/c = 3.3\%$	72
Figure 3.19 Contours of static pressure coefficient measured on the end-wall $t/c = 1.65\%$	73
Figure 3.20 Contours of static pressure on the end-wall $t/c = 1.65\%$ (from Sangmook Shin)	73
Figure 3.21 Static pressure comparison on the end-wall and on the mid span of the blade $t/c = 3.3\%$ at blade contour locations	74
Figure 3.22 Static pressure comparison on the end-wall and on the mid span of the blade $t/c = 1.65\%$ at blade contour locations	74
Figure 3.23 Pressure gradient C_{pz} plot at $z/P_w = -1.05$ $t/c = 3.3\%$ in the bed coordinates	75
Figure 3.24 Pressure gradient C_{px} plot at $z/P_w = -1.05$ $t/c = 3.3\%$ in the bed coordinates	75

Figure 3.25 Pressure gradient C_{pz} plot at $x/P_w=0.21$ $t/c=3.3\%$ in the bed coordinates	76
Figure 3.26 Pressure gradient C_{px} plot at $x/P_w=0.21$ $t/c=3.3\%$ in the bed coordinates	76
Figure 3.27 Skin friction velocity (in Table 4) comparison with and without pressure gradient $t/c=1.65\%$	77
Figure 3.28 Skin friction velocities (in Table 5) comparison with and without pressure gradient $t/c=3.3\%$	77
Figure 3.29 Measurement positions in the bed coordinate system $t/c=1.65\%$...	78
Figure 4.1 Octant names	124
Figure 4.2 Conceptual drawing of eddies in each octant	124
Figure 4.3 Flow Angle in the Bed Coordinates.....	125
Figure 4.4 Flow Angle in the Bed Coordinates FA: Flow Angles	126
Figure 4.5 Flow Angle in the Bed Coordinates FA: Flow Angles	127
Figure 4.6 Flow Angle in the Bed Coordinates FA: Flow Angles	128
Figure 4.7 Mean U at $X/C_a=0.42$ cross section in the chord coordinate (Tang 2004)	129
Figure 4.8 Mean V at $X/C_a=0.42$ cross section in the chord coordinate (Tang 2004)	129
Figure 4.9 Mean W at $X/C_a=0.42$ cross section in the chord coordinate (Tang 2004)	130
Figure 4.10 Mean flow angles at $X/C_a=0.42$ cross section in the chord coordinate (Tang 2004)	130
Figure 4.11 TKE results at $X/C_a=0.42$ cross section in the chord coordinate (Tang 2004).....	131
Figure 4.12 Moving wall flow mean velocities, in bed coordinate system (Kuhl 2001)	131
Figure 4.13 Moving Wall Flow Angle (Kuhl 2001)	131
Figure 4.14 The population variation in the condition sampling	132
Figure 4.15 The population variation in the condition sampling	133
Figure 4.16 The Reynolds stress uv variation in the condition sampling.....	134
Figure 4.17 The Reynolds stress uv variation in the condition sampling.....	135
Figure 4.18 Octant contributions to Reynolds stress, wall collateral coordinates	136

Figure 4.19 Octant contributions to Reynolds stress uu (U_{ref} is the free-stream velocity, local mean flow angle coordinates)	137
Figure 4.20 Octant contributions to Reynolds stress vv (U_{ref} is the free-stream velocity, local mean flow angle coordinates)	138
Figure 4.21 Octant contributions to Reynolds stress ww (U_{ref} is the free-stream velocity, local mean flow angle coordinates)	139
Figure 4.22 Octant contributions to Reynolds stress uv (U_{ref} is the free-stream velocity, local mean flow angle coordinates)	140
Figure 4.23 Octant contributions to Reynolds stress uw (U_{ref} is the free-stream velocity, local mean flow angle coordinates)	141
Figure 4.24 Octant contributions to Reynolds stress vw (U_{ref} is the free-stream velocity, local mean flow angle coordinates)	142
Figure 4.25 Octant contributions to uuv (U_{ref} is the free-stream velocity, local mean flow angle coordinates)	143
Figure 4.26 Octant contributions to uuw (U_{ref} is the free-stream velocity, local mean flow angle coordinates)	144
Figure 4.27 Octant contributions to vvw (U_{ref} is the free-stream velocity, local mean flow angle coordinates)	145
Figure 4.28 Octant contributions to uvv (U_{ref} is the free-stream velocity, local mean flow angle coordinates)	146
Figure 4.29 Octant contributions to uww (U_{ref} is the free-stream velocity, local mean flow angle coordinates)	147
Figure 4.30 Octant contributions to vww (U_{ref} is the free-stream velocity, local mean flow angle coordinates)	148
Figure 4.31 Octant contributions to uvw (U_{ref} is the free-stream velocity, local mean flow angle coordinates)	149
Figure 4.32 Octant contributions to uuu (U_{ref} is the free-stream velocity, local mean flow angle coordinates)	150
Figure 4.33 Octant contributions to vvv (U_{ref} is the free-stream velocity, local mean flow angle coordinates)	151
Figure 4.34 Octant contributions to www (U_{ref} is the free-stream velocity, local mean flow angle coordinates)	152
Figure 4.35 Octant contributions to Reynolds stress, local mean flow coordinates	153

Figure 4.36 Octant contributions to triple product, local mean flow coordinates	154
Figure 4.37 Octant contributions to triple product, local mean flow coordinates	155
Figure 4.38 Dominant Octant Events in the 2D TBL.....	156
Figure 4.39 Dominant Octant Events in the 3D TBL.....	156
Figure 4.40 Dominant Octant Events in the moving wall flow	157
Figure 4.41 Out side sublayer near-wall sweep-ejection motion for 2D TBL...	158
Figure 4.42 The near wall sweep-ejection motion for 3D TBL in the blade tip gap	159
Figure 4.43 The near wall seep-ejection motion for 3D TBL above Moving Wall	160
Figure a.1 The dimension of the pressure plate and the relative positions of the pressure tap	171
Figure b.1 Octant contributions to Reynolds stress uu (U_{ref} is the free-stream velocity, wall collateral coordinates)	183
Figure b.2 Octant contributions to Reynolds stress uu (U_{ref} is the free-stream velocity, mid tip gap coordinates).....	184
Figure b.3 Octant contributions to Reynolds stress vv (U_{ref} is the free-stream velocity, wall collateral coordinates)	185
Figure b.4 Octant contributions to Reynolds stress vv (U_{ref} U_{ref} is the free-stream velocity, mid tip gap coordinates).....	186
Figure b.5 Octant contributions to Reynolds stress ww (U_{ref} is the free-stream velocity, wall collateral coordinates)	187
Figure b.6 Octant contributions to Reynolds stress ww (U_{ref} is the free-stream velocity, mid tip gap coordinates).....	188
Figure b.7 Octant contributions to Reynolds stress uv (U_{ref} is the free-stream velocity, wall collateral coordinates)	189
Figure b.8 Octant contributions to Reynolds stress uv (U_{ref} is the free-stream velocity, mid tip gap coordinates).....	190
Figure b.9 Octant contributions to Reynolds stress uw (U_{ref} is the free-stream velocity, wall collateral gap coordinates).....	191
Figure b.10 Octant contributions to Reynolds stress uw (U_{ref} is the free-stream velocity, mid tip gap coordinates).....	192

Figure b.11	Octant contributions to Reynolds stress \overline{vw} (U_{ref} is the free-stream velocity, wall collateral gap coordinates)	193
Figure b.12	Octant contributions to Reynolds stress \overline{vw} (U_{ref} is the free-stream velocity, mid tip gap coordinates).....	194

NOMENCLATURE

2DTBL	Two-Dimensional Turbulent Boundary Layers
3DTBL	Three-Dimensional Turbulent Boundary Layers
B	Points found just between the camberline and the pressure side of the blade
C	Points found on the camberline of the blade
C_a	Axial Chord length: 13.868 cm
Chord length	25.4 cm
C_p	Coefficient of pressure
D	Diameter of the measurement volume
DNS	Direct Numerical Simulation
FA	Flow angle: $\arctan(W/U)$
FGA	Flow gradient angle: $\arctan(dW/dy/dU/dy)$
H	Threshold in the conditional average
LDV	Laser Doppler Velocimeter
n	Number of points in ensemble
N	total number of valid samples
P	Points found on the pressure side of the blade
pitchwise	the direction aligned with the z direction in the bed coordinate and also with the two rollers in the moving wall case
P_w	Passage width: 23.851 cm
$P_{ref, static}$	the static pressures of the undisturbed free stream
$P_{ref, total}$	the stagnation pressures of the undisturbed free stream
$P_{local, static}$	the static pressure on the end-wall
QSV	Quasi-Streamwise Vortex
R^2	the correlation coefficient of the curve fit
Re_θ	Momentum thickness Reynolds number: $U_e \theta / \nu$

Re_t	Reynolds number based on the tip gap thickness: $U_e t / \nu$
S	Points found on the suction side of the blade
SSA	Shear stress angle: $\arctan(-\overline{v'w'}/-\overline{u'v'})$
Spanwise	the direction aligned with the y direction in the bed coordinate
t	Tip gap thickness
TBL	Turbulent Boundary Layer
t/c	tip gap to chord ratio
u, v, w	Instantaneous velocities (x, y, and z axes)
u', v', w'	Velocity fluctuations (x, y, and z axes)
U, V, W	Mean velocities
U	Points found on the upstream of the pressure side of the blade
U_e	Free-stream Velocity, always in the upstream direction
u_i, v_i, w_i	instantaneous velocity of the ith valid sample
$\overline{u'^2}, \overline{v'^2}, \overline{w'^2}$	Reynolds normal stresses
$\overline{u'v'}, \overline{u'w'}, \overline{v'w'}$	Reynolds shear stresses
$\overline{(u'^2)^+}, \overline{(v'^2)^+}, \overline{(w'^2)^+}$	Reynolds normal stresses normalized by wall-shear-stress
$\overline{(u'v')^+}, \overline{(u'w')^+}, \overline{(v'w')^+}$	Reynolds shear stresses normalized by wall-shear-stress
$\overline{u'u'v'}, \overline{u'u'w'}, \overline{v'v'w'},$ $\overline{u'v'v'}, \overline{u'w'w'}, \overline{v'w'w'},$ $\overline{u'v'w'}, \overline{u'u'u'}, \overline{v'v'v'},$ $\overline{w'w'w'}$	triple products
$u_{\tau} = \sqrt{\frac{\tau_w}{\rho}}$	Wall-shear-stress velocity
V_{belt}	Velocity of the Belt
x, y, z	Tunnel coordinate system for cascade tunnel
y^+	Distance from the wall normalized by the wall-shear stress.
Δy	The wall position refinement
β_i	Weighted population percentage in octant i.

1. INTRODUCTION

1.1 PERSPECTIVE OF THE PREVIOUS STUDY

The primary goal of the study of the basic component of the complex flow through a linear cascade wind tunnel is to get greater insight into the complex flow through turbomachinery. Through experimental study, accurate computational models can be developed and the benefits of such models include much more reliable and quicker analysis of the configuration, and also the better initial designs of rotors. Since much of the noise in turbomachinery is created by the turbulence field, it is necessary to have a complete description of the turbulence field in the turbomachinery.

Research on the three-dimensional flow in axial turbomachinery with a tip gap can be traced back to the 1920s as reviewed by Prasad (1977). The tip leakage flow and its rolling up into a vortex have been clearly demonstrated and described by Lakshminarayana (1970). In the early 1980s, most of the investigations on axial compressor flow fields were concerned with rotor wake characteristics and with the interaction region of the casing wall boundary layer, the wake and the tip leakage flow. Experimental studies with the special emphasis on the leakage flow development near and in the tip clearance region have been conducted by Bindon (1985 a, b) and Moore and Tilton (1988) for a linear cascade.

Kang and Hirsch (1993, 1994) presented the experimental results from a study of the three-dimensional flow in a seven-blade (NACA 65-1810) linear compressor

Chapter 1

cascade tunnel with stationary end-wall for tip clearance levels of 1.0, 2.0 and 3.3 percent of chord. This paper presents more information on the secondary flow and vorticity within and behind a linear compressor cascade. The no-clearance case is compared with these results. A 5-hole probe was used to measure pressure field. The static pressures on the blade surfaces and end-wall were also recorded by using static pressure tubes. Surface flow visualization focused on Paint-trace visualization on the end-wall and ink-trace visualization focused on the blade tip surface for those three tip gaps. In all tip gap cases, a multiple tip vortex structure (tip leakage vortex, tip separation vortex, secondary vortex and passage vortex) was found. The secondary vortex was formed on the suction side due to the separation vortex under the blade tip. The separation vortex was formed while the separate flow rolled up from the pressure side edge. The generation of the tip leakage vortex makes the passage vortex move closer to the end-wall and to the suction side of the blade. The tip leakage vortex has high total pressure loss and low static pressure value.

Based on above experiment data, Kang and Hirsch also presented numerical simulation results of the three-dimensional tip gap flow. To get further insight into the complex three-dimensional flow phenomena, a three-dimensional Navier-stokes solver, with the algebraic turbulence model of Baldwin-Lomax or the Two-equation K-Epsilon turbulence model for closure, has applied to compressor cascade under the experimental condition. Flow structure, static and total pressures, velocity profiles, secondary flows and vorticity are compared with the experiment data for stationary case. The code predicts well the flow structure observed in experiments and shows the details of the tip leakage flow and the leading edge horseshoe vortex in the 1.65% chord ratio tip gap case.

Chapter 1

S. Shin (2001) at Virginia Tech did the numerical simulation for the tip leakage flow with stationary wall in the linear cascade tunnel whose tip gap is equal to 1.65% chord ration. A three-dimensional unstructured incompressible RANS code has been developed using artificial compressibility and Spalart-Allmaras eddy viscosity model. This code is applied to a linear cascade that has eight GE rotor B section blades with 1.65% tip clearance to chord ratio and a high stagger angle of 56.9° , in the same experimental condition done by Kuhl *et al* (2000) using LDA, focussing on the near-wall flow measurement and Muthanna (1998) studing the flow field downstream of the cascade for same tip gap with hot wire probe measurement at Virginia Tech. The overall multi-vortex structure of the tip clearance flow is well predicted. Loss of loading due to tip leakage flow and reloading due to tip leakage vortex are presented. The Spalart-Allmaras turbulence model is adequate for this type of flow field except at locations where the tip leakage vortex of one blade interacts with the wake of a following blade.

At Virginia Tech, three component velocity and turbulence measurements are conducted by using four sensors hot wire probe. Muthanna (1998) studied the flow field downstream of the cascade for a tip gap of 0.83%, 1.65%, and 3.3% chord and made cross sectional measurements of downstream tip leakage vortex flow. These measurements revealed the structure of a tip leakage vortex and its trajectory downstream of the cascade. Wang (2000) made measurements in cross sections downstream of the cascade at tip gaps of 0.83%, 1.65% and 3.3% chord, at stations 1.51, 2.74 and 3.75 axial chords downstream of the leading edge of the blade row, with and without wall motion. His results shows that wall motion influences the leakage vortex by flattening and shearing the turbulence and mean velocity distributions of the vortex but does not alter the basic mechanisms that govern the

Chapter 1

development of its mean flow and turbulence structure. Muthanna (2002) made further studies to examine the flow's behavior both in the presence and absence of grid-generated free-stream turbulence. Extensive measurements on the stationary wall case for a tip gap of 1.65% chord were made at 0.8, 0.23 axial chords upstream and 0, 0.27, 0.48, 0.77, 0.98, and 1.26 axial chords downstream of the leading edge of the blade row. Significant effects on the flow field due to the grid generated turbulence were revealed. Ma (2003) investigated the inflow to the cascade, the mean blade loading at the middle span, and the periodic and aperiodic behavior, as well as pressure fluctuation in the downstream tip leakage flow, with and without vortical inflow disturbance, as a function of tip gap and streamwise location.

1.2 OBJECTIVE OF THE PRESENT STUDY

While above discussion mainly concentrated on the compressor cascades and rotors, the most recent study using 3D LDV to investigate the turbulent nature of tip leakage vortices has been performed by Kuhl *et al* (2001) in the linear cascade tunnel in the Virginia Tech. There are four kinds of flow examined. The first flow is the idealization of the wake from stator blades using two half-delta wing vortex generators. The second flow is the idealization of flow through a stationary set of linear cascade compressor blades. The third flow is the idealization of flow through a moving set of linear cascade compressor blades. The fourth flow is the same as the third flow with idealized wakes from upstream stator blades.

The results of those experiments showed that the major driving force of the flow under the blade in the tip gap is the pressure difference across the blade. The pressure force causes the end-wall friction velocity to increase in the downstream direction and

Chapter 1

also from the pressure side to the suction side. This flow is a three-dimensional high turbulence flow, through the Reynolds shear stress distribution. The effective viscosity is not isotropic, from the judgment of flow angle, shear stress angle, flow gradient angle. The previous studies produced a less complete view of the turbulence flow field. It was limited to one tip gap and insufficient profiles were obtained to capture the flow structure and characteristics. Measurements are needed at more locations under the blade, with different tip gaps near the tip leakage vortex.

The present investigation utilizes several experimental techniques in a study of the tip gap flow field of a compressor cascade with stationary wall for two different tip gaps ($t/c=1.65\%$, $t/c=3.3\%$). The objective of the LDV measurements is to obtain a detailed description of the mean and turbulent tip gap flow field with tip leakage and separation vortex for the non-moving wall. The objectives of the surface oil flow visualization are to get the approximate position of the tip leakage vortex, in order to specify the measurement locations for LDV measurement and also to study the mean flow features. The objectives of the static surface pressure measurement on the end-wall are to determine the pressure gradient in the flow field around the tip gap and this pressure gradient information is useful in examining the surface vorticity flux, checking whether the flow is relaminarized or not due to the huge acceleration in the blade tip gap, and comparing skin friction velocity calculation with and without pressure gradient. The moving wall study is used to simulate some of the rotational effects that would be presented in a compressor rotor. The statistics of the Reynolds stress and triple products for the LDV velocity data is investigated by using velocity fluctuation octant analysis to examine the near-wall coherent structure for the 2DTBL and 3DTBL of the tip gap flow. This study also can help the numerical investigation of the same configuration. With the results obtained on this experiment, a detailed

Chapter 1

description of the turbulence field will be obtained to advance the understanding and calculation of such flows.

1.3 ORGANIZATION OF THIS THESIS

This thesis is comprised of six large chapters: chapter 1, chapter 2, chapter 3, chapter 4, chapter 5, and chapter 6. Every chapter has its own focus. Figures can be found at the end of each chapter.

Chapter 2 discusses the experiment apparatus in this turbulence flow measurement, including oil flow visualization, LDV measurement, pressure measurement, and a brief description of the setup of Cascade. Chapter 3 is about flow visualization results on the end-wall and on the blade surface, includes how to digitize the oil flow and use AutoCAD to measure the oil flow angle, discusses the flow structure, and also investigates the static pressure measurement results on the end-wall for two tip gaps, skin friction calculation with and without pressure gradient. Chapter 4 presents the statistic results of Reynolds stresses and triple products from the octant analysis to LDV data. Chapter 5 includes the conclusion and results of previous four chapters. Chapter 6 is about the reference papers used in this thesis.

2. APPARATUS AND INSTRUMENTS

2.1 WIND TUNNEL

Experimental measurements were conducted at low speed linear cascade wind tunnel in the department of aerospace and ocean engineering at Virginia Tech. Details of the aerodynamic design of the cascade tunnel are given in table 2.1. The blades were instrumented with pressure taps on the surfaces in the mid-span of the blades (#4 and #5). The blades were cantilevered on the tunnel beam, so they could be moved relative to the end-wall to vary the tip gap clearance by adjusting the fixture on the beam or add some fixed washer between the beam and the tunnel frame. The periodicity of the cascade flow was checked and compared by measuring the static and stagnation pressure in the upstream, downstream and freestream along the pitchwisewise (pitchwise is the direction aligned with the z direction in the bed coordinate and also with the two rollers in the moving wall case). By comparing the pressure distribution measured at mid-span with those in the previous measurements by Muthanna (1998, 2002), Wang (2000), and Ma (2003), the tunnel calibration was confirmed and matched with previous experimental condition. For more detail about the tunnel calibration, see Tang (2004).

Chapter 2

This wind tunnel is an open type and powered by a 15 hp motor with a fan. Air from the fan, as shown in figure 2.1 and 2.2 is supplied to a test section after first passing through a diffuser, a series of flow conditioning screens, a section of honeycomb to remove the mean swirl of the flow, another series of flow conditioning screens and a contraction and then into the test section as shown in figure 2.3, Muthanna (1998).

The flow is tripped by a square bar mounted on the lower suction slot as shown in figure 2.3 and 2.4. There are two three-quarter inch high suction slots on the upper and lower end-wall at 7.48 inch in front of the cascades and with these slots, the inlet flow boundary layer is removed (see figure 2.4). The nominal running conditions are the speed of 25m/s and temperature of $25\text{ }^{\circ}\text{C} \pm 1\text{ }^{\circ}\text{C}$.

A simultaneous three-orthogonal velocity component fiber optic laser Doppler anemometer (LDA) is designed to measure the three-dimensional turbulent flow with tip leakage vortex through the tip gap with and without moving wall. A scanivalve system was used to measure static pressure on the blade surface and on the end-wall. Hot-wire probe measurements were also performed in the wake region with the same facility by Muthanna (1998, 2002), Wang (2000), and Ma (2003).

2.1.1 TEST SECTION

The test section consists of eight cantilevered GE rotor B section blades, plywood bed, optical glass inserts, Teflon sheet, and plexiglass roof, Muthanna (1998). The entrance of the test section is a rectangular cross section of 65 inches \times 10 inches.

Chapter 2

In order to remove boundary layers from the inlet flow, suction slots are put on the upper and lower end-wall at the entrance of the test section.

The drawing of this linear cascade is shown in figure 2.3. By the calculations performed by Moore et al (1996) and the limitation of the space available to build the cascade tunnel, eight GE rotor B section blades with seven passages configuration were chosen. The blades have a chord of 10 inches and an effective span about 10 inches. The blades spacing is 9.39 inches. The blades (#4 and #5) were instrumented with pressure taps on surfaces at several positions in the mid-span of the blades (#4 and #5). These pressure taps were used in the calibration process described by Tang (2004). Eight blades were cantilevered on the tunnel beam, so they could be moved relative to the end-wall to vary the clearance gap at the tip by adjusting the fixture on the beam or add some fixed washer between the beam and the tunnel frame. Here, three different tip gap flows were tested. The first flow is 1.65% tip gap to chord ratio with stationary wall, the second flow is 3.3% tip gap to chord ratio with stationary wall and the third flow is 3.3% tip gap to chord ratio with moving wall. The plywood bed is mounted underneath the cascade of compressor blades and supported by the steel tunnel frame. This plywood bed has a dimension of $31.50inch \times 126.00inch \times 0.75inch$. In order to reduce the friction and avoid the melting of the Teflon belt in moving wall study, the Teflon sheet is specially coated on the top of the plywood bed, by using epoxy glue. A plexiglass insert is mounted underneath blades #4, 5, and 6. The Plexiglass insert has an optical glass insert underneath blade #5 in figure 2.3. The optic glass insert has an eight inches diameter. Inserts with different optical glass insert positions make LDV measurement under the blade for multiple different positions possible. There are three optical glass positions used in LDA measurement.

2.1.2 MOVING BELT SYSTEM

Figure 2.5 shows the position of the drive roller and free rollers relative to the tunnel and the Mylar belt (0.01 inch thick Dupont Mylar D) is looped around these two parallel cylindrical rollers, approximately 165 inches apart at either end of the plywood bed, Wang (2000). The Mylar belt is fused together at the belt joint as shown in figure 2.5. Drive roller is driven by the motor, fixed on the concrete floor. The motor speed is adjusted by a variable speed controller. Since drive roller is connected to the motor with timing belt, the speed of driving roller changes with the motor speed. The free roller is controlled with screws mounted on either end of the drum in order to control the axial position of the belt. By adjusting these screws, the difference of tension axially across the belt makes the belt back and forth across the rollers. While starting and stopping the belt, much adjustment to these screws is required to prevent it from slipping along the rollers. In order to keep the belt speeds at the required belt speed (21m/s), very fine adjustment is needed to control the belt position. The level of control is dependent on the particular belt. The amplitude of the vibration was measured by imaging the tip gap of the one of the center blades in the method described by Wang *et al.* (2000). The belt speed stability was better than 0.24% r.m.s, Ma (2003).

A belt leading edge cover prevents the tunnel air from getting under the belt and lifting it up. The belt leading edge cover is taped on the suction slot and overlaps the moving Mylar belt. The belt leading edge cover Mylar is the same material as the belt in figure 2.4.

Chapter 2

The friction between the moving Mylar and the stationary Teflon bed scratch the Mylar bed in the direction of movement of the belt and produce many tiny white particles. When the scratches form directly over the laser optic glass inserter and these white particles accumulate on the glass surface, laser beams are easy to be blocked and no data can be taken. To prevent scratches from forming in this area, 16 tapes are attached longitudinally along the bed surface and one tap which extends the entire length of the belt and lifts the area next to it just enough to prevent scratches from forming is attached the underside of the belt next to the measurement volume Those tapes are 8.3 mils thick 3M 5453 PTFE Glass Cloth tape. The tape is high temperature tape that resists melting caused from the friction between the tape and the moving Mylar .

2.1.3 PLASTIC TENT

Since this linear compressor cascade tunnel is an open tunnel and LDV measurement need to trace particles in order to measure particles velocity carried by the flow in the tunnel, a semitransparent plastic tent is need to cover the whole wind tunnel including the fun and the test section, Kuhl (2001). A steal frame was built in order to support this plastic containment. The joint of the plastic tent and the concrete floor sealed by using gray duck tap, and also weights are added on the bottom of the tent. The tent is semitransparent in order to review the test section.

Once this plastic tent is built, the effect, which this plastic containment has on the flow field in the tunnel need to be considered. From the mean velocity measurement with and without this plastic containment, the difference is neglectable.

Chapter 2

This test proves the plastic containment has little defect on the local flow field in the tunnel. For more detail of this test, please check Dave Kuhl's thesis (2001).

2.1.4 COOLING SYSTEM

Since the wind tunnel is closed in the plastic tent, the air temperature increases while the fan is working. To keep the air in the tent at a constant temperature about 25°C, air conditioner must be put near the inlet of the tunnel fan. By considering the room space of the plastic containment and work efficient of the fan, the proper air conditioner with right power is chosen. Air conditioner blows cool air into the tent and exhausts warm air into the surrounding room.

2.2 OIL FLOW VISUALIZATION

Surface oil flow visualizations for two different tip gaps ($t/c=1.65\%$ and 3.3%) were done on the lower end-wall of the blade, in the blade passage to investigate tip gap flow and tip leakage vortex and also on the blade suction surface to observe the secondary vortex due to the tip separation vortex.

In order to do oil flow visualization on the end-wall, a black adhesive paper (18.7 inch \times 10.83 inch) was put under the tip gap on the tunnel floor. A mixture of 15 ml. titanium dioxide, 40 ml. kerosene and 1ml. of oleic acid was painted on this black adhesive paper. In order to avoid the static effects coming from the brush and the plastic paper, aluminum foil was put under and above the plastic paper at the corner and grounded. The tunnel was run for about 5 minutes until all the kerosene evaporated, and then a fixative was used to preserve the traces. Oil flow visualization on the blade surface has the same procedure as the end-wall flow visualization. Since

Chapter 2

the blade surface is normal to the horizontal tunnel bed, the gravitational effect is very big, and most gravitational effect comes from kerosene. Thus mixture rate (15 ml. titanium dioxide, 25 ml. kerosene and 1ml. of oleic acid) is different to those on the end-wall case.

Oil flow visualization is a simple and efficient way to find the average flow characteristics, and oil flow results are reliable in those regions with less gravitational effect and boundary separation. Movement of the oil mixture driven by the flow and the formation of the oil flow patterns could be clearly revealed and recorded. Various details (wall stress flow angle and separation line) on these flow visualizations can be digitized by a scanner.

2.3 PRESSURE MEASUREMENT

Pressure measurement described in this thesis was done in the linear cascade wind tunnel comprising eight blades at Virginia Tech. The spatial periodicity of the flow was checked and compared by measuring the static and stagnation pressure in the upstream, downstream of test section and free stream along the pitchwise of the blade (pitchwise is the direction aligned with the z direction in the bed coordinate and also with the two rollers in the moving wall case). For more detail about the tunnel calibration, see Tang (2004). Static pressure measurement on the end-wall was done with a pressure plate, one pressure transducer and scanivalve system.

2.3.1 PRESSURE PLATE

Chapter 2

This plexiglass pressure plate was made in the AOE workshop with 8 inches diameter and 426 pressure taps in the plate. It is located under blade 5 (figure 2.6) to measure the static pressure on the end-wall in the linear cascade tunnel at Virginia Tech.

The detail dimension of the pressure plate and relative positions of the pressure taps are as shown in figure 2.7. These pressure taps on the plate surface are connected to copper tubes using epoxy glue, which are connected to one end of the plastic pressure tubes. The other ends of the pressure tubes are connected to ten scani valve connectors, each with 48 ports. The diameter of those pressure taps on the plate surface must be small enough (about 0.02 inches) without affecting the local flow field. In order to avoid local static pressure errors, the plate surface must be smooth and without burrs or too concave edge (see figures 2.8 and 2.9), around the pressure taps. For the burr case, the measured local static pressure will be lower, and for the concave case, it will be too higher, as compared with the real static pressure (see figure 2.9). This pressure plate insert was put where optical glass insert (eight-inch diameter) is located in the plexiglas insert under the blade 5. In order to make measurement under the entire blade, two same size plexiglas inserts with two different positions of the pressure plate inserters are needed.

2.3.2 PRESSURE TRANSDUCER

In order to avoid different offset voltages and drift from different pressure transducers, only one pressure transducer was used. From previous experimental experience, two pressure transducers made the final pressure data unreliable. But in

Chapter 2

order to get the pressure coefficient, the reference pressure and measurement pressure need to be measured at the same time. Here, the measurement pressure is the difference of local static pressure on the pressure plate and static pressure in the free-stream and the reference pressure is the difference of stagnation pressure and static pressure in the free-stream. Every scanivalve connector has 48 ports and 5 of them were connected to a multi-pressure connector, sequentially to measure the reference pressure after every 10 ports. Before making measurements, the pressure transducer was calibrated by using an inclined fluid manometer. The measurement range of the pressure transducer should be in $-2.5-2.5$ in H_2O . The pressure transducer used in the experiment is a Setra 239. Since the input pressure is proportional to the output voltage, the slope between the pressure and voltage needs to be calculated. Again different transducers have different offset voltage and drift, which explains why two different pressure transducers make the experiment less reliable.

2.3.3 SCANIVALVE SYSTEM

The scanning valve pressure measurement system, CTLR2P/S2-S6 by Scanivalve Corp., was used to take the pressure measurement. It has a 48 ports scanning device that is controlled by a solenoid motor run by a 286 IBM PC. Each port is connected to the pressure transducer in a predetermined programmable sequence and the computer reads the output of the pressure transducer, calculates measurement pressure, reference pressure and coefficients (C_p) and stores it in a file with the specific port number. It was designed to use two Setra 239 pressure transducers, one for measuring pressure for each port and the other one as a reference

Chapter 2

transducer for the tunnel dynamic pressure. But the drifting and different offset voltages coming from different transducers may make C_p calculation unreliable. Thus only one pressure transducer was used. A data acquisition board (DT 2801) was used for analog to digital conversion.

2.3.4 OPEN JET TUNNEL

Before the pressure measurements in the cascade tunnel, in order to find any leakage and blockage of the pressure tubes, pressure measurements were done in the open jet tunnel at aerospace engineering department at Virginia Tech. The pressure plate was placed in the insert and mounted in the test section normal to the flow direction. Thus the flow dynamic pressure was measured. Since this pressure plate was put in the center of the test section, the dynamic pressure distribution on the pressure plate should be even. Where the pressure tubes with a pressure value beyond 5% difference were considered as where leakage or blockage happened. New pressure tubes replace the used ones and the connecting parts between pressure the plate and copper tubes were checked. After the leakage and blockage check, pressure measurements were done in the cascade tunnel.

2.3.5 ISSUES IN THE PRESSURE MEASUREMENT

Measurement positions of the pressure ports

During the pressure measurement, it is impossible to measure all the measurement positions one by one. It is necessary to find an efficient and reliable way to measure the measurement position of the pressure ports. As in figure 2.7, it shows

Chapter 2

relative position of the pressure ports in the plate coordinate system and the blue line is parallel to the x-axis in the plate coordinate system. In the real measurement, in order to cover as much measurement area as possible, the pressure plate needs to be rotated four times and every time, needs to be rotated 45 degree. It is very difficult to measure the rotation angle precisely, thus there exists some uncertainty in the rotation angle measurement. The uncertainty introduced by the rotation is discussed in the Appendix A.1. In the measurement, the initial direction of the blue line should match with the x-axis in the bed coordinate system. Once the position of the pressure plate center in the bed coordinate system is known, pressure tap positions on the pressure plate in the bed coordinate system can be obtained through the coordinate transform. In the data processing, the small adjustment to these angles is needed to make the pressure contour plot smooth. The uncertainty for the rotation angles is less than 0.25 degree.

Offset voltages coming from different pressure transducers

The input pressure difference across the transducer is proportional to the output voltage. The zero pressure offset voltage and drift change with temperatures in the pressure measurement, and differs with pressure transducer. In order to avoid the different offset voltages coming from the different pressure transducers, only one pressure transducer can be used.

During the pressure measurement, except for the connector in use, all of the scanivalve connectors need to be sealed using taps. Experience proves that without seal, the measured local static pressure on the plate will be changed.

2.4 LASER DOPPLER VELOCIMETER (LDV) SYSTEM

The LDV provides coincident instantaneous velocity data at a single point in the flow field. By using a traverse system, which is fixed with LDV head, laser light source (the measuring volume) can move point by point and it is possible to perform an area analysis for the flow field. The technique is non-invasive to the local flow field since laser light is the measuring tool. With proper experimental design, LDV can reach difficult measurement locations with the experiment requirement without disturbing the flow field.

In the present study, a unique, three-velocity-component, fiber-optic LDV probe was used in the experimental measurements, which was described in detail by Chesnakas and Simpson (1994). It was designed specifically to measure the complete coincident instantaneous velocity vector and full Reynolds-stress tensor from the viscous sublayer to the edge of the boundary layer of the tip gap flow and tip leakage vortex on the end-wall of the cascade tunnel. The five laser beams cross with each other at one point (measurement volume). One pair of the blue beams and two pairs of the green beams measure the instantaneous velocity of the particle in three directions. These three directions form the optical coordinates. This measurement volume has a diameter nearly of $55\mu\text{m}$. Very precise near-wall measurements can be obtained by this system. The fringe spacing for each pair of the laser beams is about $5\mu\text{m}$. This system consists of three parts: (1) the optical table and the fiber optic probe; (2) the signal processing electronics and (3) the seeding system, which are discussed below.

2.4.1 OPTICAL TABLE, AND FIBER OPTIC PROBE

The LDV probe is a two-color, three-component, fiber-optic design. Lights for the probe come from the blue and green beams of an argon-ion laser and scattered light is collected in off-axis backscatter. A schematic block diagram of this LDV system is shown in figure 2.10. The laser beam is launched from the laser and into prism beam splitter. The beam is reflected by the inner surface of the prism beam splitter, and the green and blue beams with different reflect in angles are separated. Two mirrors are used to change the green beam path, before it passes through a bragg cell. In order to keep the beam polarization direction fixed, one polarization rotators is put in front of that bragg cell. After passing through the polarization rotator, the green beam will be polarized along two mutual vertical directions (horizontal and vertical). By rotating the polarization rotator, the power of each component for the green beams can be adjusted and balanced, without changing the settings of the laser. After the bragg cell, the green beams are shifted by different frequencies, 0MHz, +50MHz, and -27 MHz. Two mirrors are also used to change blue beam path, before it passes through a bragg cell. No polarization rotators are used for blue beam. After the bragg cell, the blue beams are shifted by different frequencies, 0MHz and +40MHz. Now these five beams are launched into fiber couplers, transported by single polarization fibers and launched out of the LDV probe.

When two laser beams cross at their waist, a set of equally spaced fringes (light and dark bands) that are parallel to the bisector of the beams (figure 2.11) is created. The Bragg cells provide frequency shifting to the laser beams and cause the fringes to move in order to avoid the directional ambiguity of signals. Without frequency

Chapter 2

shifting, the direction of the velocity of the particle carried by the flow through the fringes is ambiguous

In this three-velocity-component LDV system, there are three pairs of intersected beams to measure the flow velocity projected in three orthogonal directions. Once the particle passes through the measurement volume, three signals from the velocity components normal to the fringes are produced. In order to distinguish different signals, a different frequency shift for each pair of intersected beams is chosen. For this system used in present study, two blue beams are shifted by 0MHz and +40MHz, and the three green beams are shifted by 0MHz, +50MHz, and -27MHz.

The five laser beams are then launched into the optical probe by passing through the laser to fiber couplers and the polarization-preserving fibers. The measurement volume is right at the focus of the receiving lens. The off-axis backscatter light passing through the optical glass window will be collected by the receiving lens, and launched into the photo detector (PM tube) unit by receiving fiber. Then the optical signals are transformed into the electrical signals (voltages) and carried to the electrical system.

2.4.2 SIGNAL PROCESSING ELECTRONICS

Before the signals get into Macrodyne, the frequency processor, those voltage signals have to be amplified after passing through the amplifiers, and through the filter to be cleaned. Since the signal from the green beams PM tube is blending signals of three green beams, the signals is split into two after the splitter. All of these

Chapter 2

components (amplifier, filter and splitter) are ensembled in one circuits board. After amplification, signal cleaning and split, electronic signals, which contain the frequency information coming from the PM tubes, will be processed by Macrodyne (FDP 3100). There are three Macrodynes, referred as MAC1, 2, and 3. The signals from the blue beams are channeled to MAC2, the signals from green (0, +50) to MAC3, the signals from green (0,-27) to MAC1. The Macrodynes take the difference of the signals from the PM tube and the signals from the RF generator as inputs and output. Under current Bragg cell settings and to avoid signal crosstalk and ambiguity, the bandwidth of the frequency processor cannot be set larger than 0-5MHz. In the case of a highly turbulent flow, the bandwidth of the processor needs to be enlarged in order to get bigger velocity range and the differences between three Bragg cell settings need to be enlarged as well. In present measurement, the measurements were made with the validation percentage in the range of 98% to 100%, which resulted in minimuml noisy data. One block of 30000 samples was taken for each measurement point. (Only 15000 samples were taken when the data rate was lower than 50 samples/s).

A computer (IBM 386/33C PC) along with a Dostek (1400A Laser Velocimeter Interface with TCEM daughterboard option) is used to collect and store the data from the macrodynes. Since the LDV system as any other electronic measurement system, a certain amount of the noise always exists. The method used to remove noise from the data was that used by Ölçmen and Simpson (1995). A parabola was fitted to each side of the logarithm of the velocity component histogram ordinate in the range between 1% and 80% of the peak histogram value. The data lying outside of the intersection of the parabolas with the ordinate value were discarded; if one of the

Chapter 2

velocity components was deemed unusable, all three were discarded. The clean velocity information for all three components of the velocity was transformed into tunnel coordinates and saved. Two more parabola fits were fit to each side of the logarithm of the histogram this time to the transformed data, and the noise was moved.

Final time series data files have 5 columns, first column is events, second column is u , instanous velocity component on the x direction in the tunnel coordinate system, third column is v , instanous velocity component on the y direction in the tunnel coordinate system, forth column is w , instanous velocity component on the w direction in the tunnel coordinate system, and fifth column is the arriving time. Regularly every profile has 30000 samples. Mean velocity and Reynolds shear stress, normal stress, and triple product can be calculated using following formulars.

Mean velocity:

$$U = \frac{\sum_{i=1}^N u_i}{N} \quad (1)$$

Reynolds normal stress:

$$\overline{u'^2} = \frac{\sum_{i=1}^N (u_i - U)^2}{N} \quad (2)$$

Reynolds shear stress:

$$\overline{u'v'} = \frac{\sum_{i=1}^N (u_i - U)(v_i - V)}{N} \quad (3)$$

Triple product:

$$\overline{u'^3} = \frac{\sum_{i=1}^N (u_i - U)^3}{N} \quad (4)$$

Chapter 2

$$\overline{u'v'^2} = \frac{\sum_{i=1}^N (u_i - U)(v_i - V)^2}{N} \quad (5)$$

where

N - total number of valid samples;

u_i, v_i - instantaneous velocity of the i th valid sample.

Kuhl and Simpson (2000) showed that the only significant velocity bias for this LDV system is the velocity gradient bias. Since measurement volume isn't a single point, but a volume with space. The particles passing through the measurement volume may have different velocities due to their different positions within the measurement volume. While a flow with a high velocity gradient (such as in boundary layer) is measured, velocity gradient broadening happens. Durst (1992) suggested that the measured normal stresses are greater than the true normal stresses by the amount of $\left(C \partial U / \partial y\right)^2$ due to velocity gradient broadening, namely:

$$\overline{u'^2}_m = \overline{u'^2}_t + AD^2 \left(\partial^2 U / \partial y^2 \right)$$

where

A is a constant of $1/24$

D - diameter of the measurement volume;

$\partial U / \partial y$ - mean velocity gradient at the measurement point.

In present study, D is equal to $55\mu\text{m}$ obtained by Chesnakas and Simpson (1994). They proved that in such a small measurement volume, those parts of values coming from velocity gradient broadening were much less than the uncertainties of measured normal stresses, thus negligible. Ölçmen *et al* (1998) investigated the

Chapter 2

instrument broadening effects on the measured frequency by the Macrodyne FDP3100, and proved that these broadening effects were negligible. For more detail of the discussion of the post-processing techniques, please see the dissertation of Tang (2004).

2.4.3 SEEDING SYSTEM

In LDV, particles moving with the flow serve as the signal source by scattering laser light. The geometric and physical parameters of the particles influence the quality of the signals coming from the photodetector in the LDV system. It is desirable to seed the flow to obtain adequate data rates and good signal quality. This seeding system was described by Ölçmen and Simpson (1995). An aerosol generator designed by Echols and Young (1963) was used to seed the flow. The fluid used in the generator is dioctyl phthalate (DOP) with a measured mean particle size of about $1\mu\text{m}$. The smoke is injected into the flow just upstream of the exit of the contraction and the blunt leading edge of the test section floor.

2.5 DATA QUALITY

Before the tests of the experiment, the data quality must be assessed. The data quality is assessed by plotting the upstream profiles in the inflow against a comparable Ölçmen's two-dimensional flow in the boundary tunnel with the free stream speed of 27 m/s at the Aerospace and Ocean Engineering Department of Virginia Tech. The second check is the comparison with DNS. Figure 2.12 shows the comparison between profiles UD at $X/C_a = -0.33$ for $t/c = 1.65\%$, Ölçmen's 2D

Chapter 2

profile and the DNS results of Spalart (1988) over a flat plate at two different Re 's number. The boundary thickness in the inflow based on profiles UD is about 0.67 inch ($\delta^+ \approx 1000$), and Re_θ is about 1730. In figures 2.12 a, b, c and d, the difference of square root of the peak values in the shear stress $-\overline{(u'v')^+}$ between the experiment profile UD and the DNS data $Re_\theta=1410$ should be less than five percent. The differences in the shear stress $-\overline{(u'v')^+}$ between the DNS and the experimental data, is caused by the differences in Re_θ . There is one other source, which could cause differences between the DNS data and the experimental data and that is uncertainties in skin friction velocity. The uncertainty for the skin friction velocity calculation is less than 3%. It is clear that most of these differences are quite small but may still have some effects on the normalized Reynolds stresses.

The DNS data with the $Re_\theta=1410$ shows consistency with the experiment data (UD) in $\overline{(u'^2)^+}$, $\overline{(v'^2)^+}$ plots and their peak values are almost same. As discussed in AGARD (1996), the differences in Re_θ can affect the peak values in figure 2.12, and it is stated that the peak values of $\overline{(u'^2)^+}$, $\overline{(v'^2)^+}$, and $\overline{(w'^2)^+}$ have a dependence on the Reynolds number. The reported square root of the peak value of $\overline{(u'^2)^+}$ is about 2.75 from $Re_\theta=1000$ to 2000 in AGARD (1996). Our data shows square root of the peak $\overline{(u'^2)^+}$ of 2.7 at $Re_\theta=1730$. The DNS data shows the same value of the square root of the peak $\overline{(u'^2)^+}$ at $Re_\theta=1410$. Thus within the experiment uncertainties, two-dimensional experimental data is very close to the DNS data.

Table 2.1 Parameters of the cascade blades

Blade section	GE rotor B section
Blade number	8
Chord length	25.4 cm
Inflow angle	65.1°
Stagger angle	56.9°
Pitch	0.929 of the chord
Span	1.0 of the chord
Axial Chord length	13.868 cm
Passage width	23.6 cm
Renolds numner based on the chord	4.03×10^5
Tip gap height	0.0165 of chord and 0.033 of chord

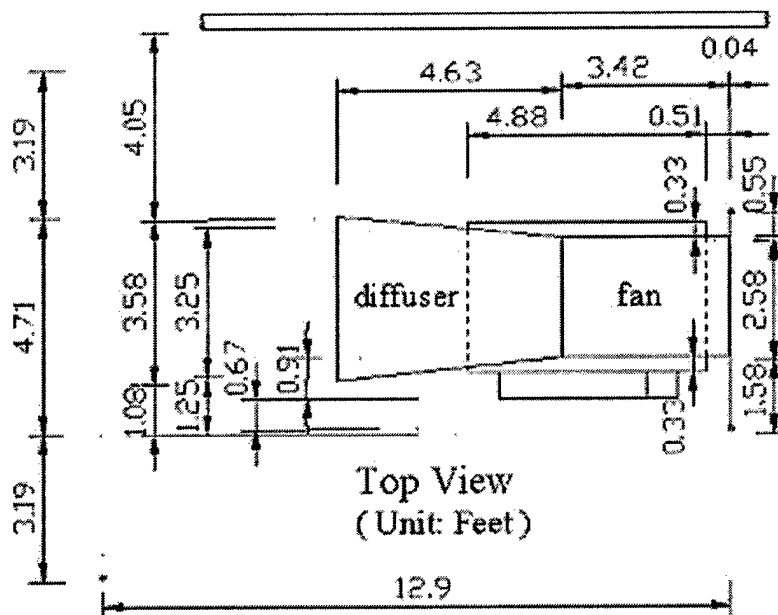


Figure 2.1 Top view of fan and diffuser in the cascade tunnel

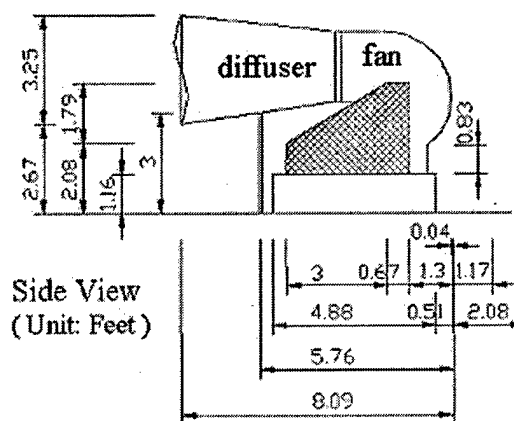


Figure 2.2 Side view of fan and diffuser in the cascade tunnel

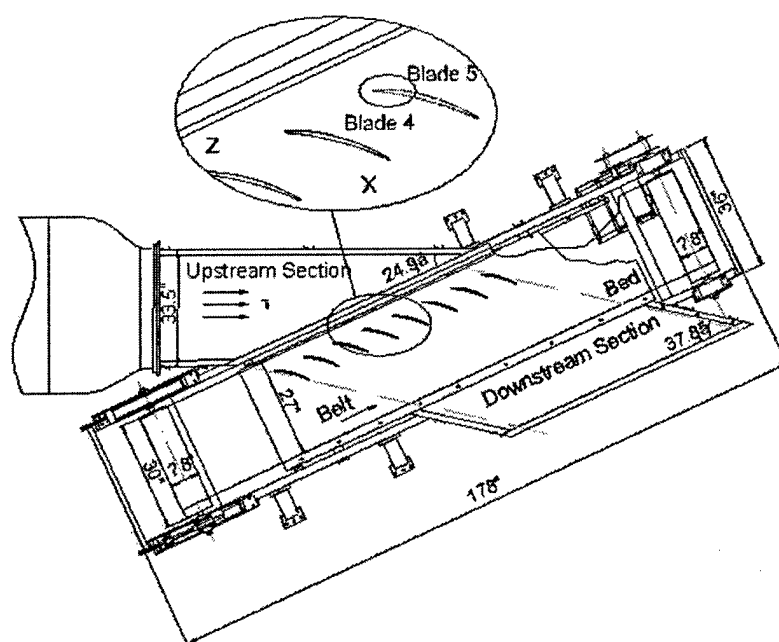


Figure 2.3 Test section of the linear cascade tunnel

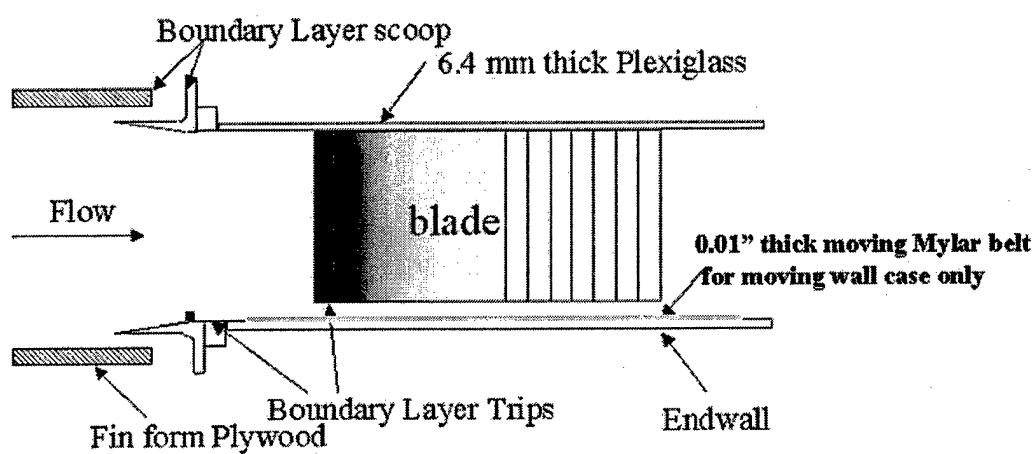


Figure 2.4 Side view of the test section of the linear cascade tunnel

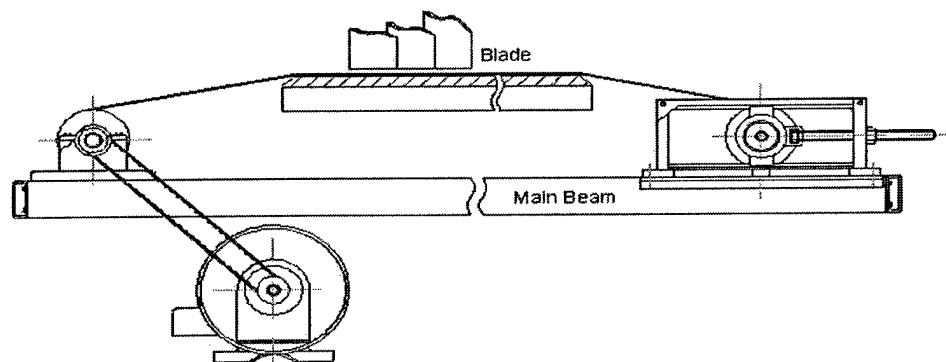


Figure 2.5 Moving belt system in the linear cascade tunnel

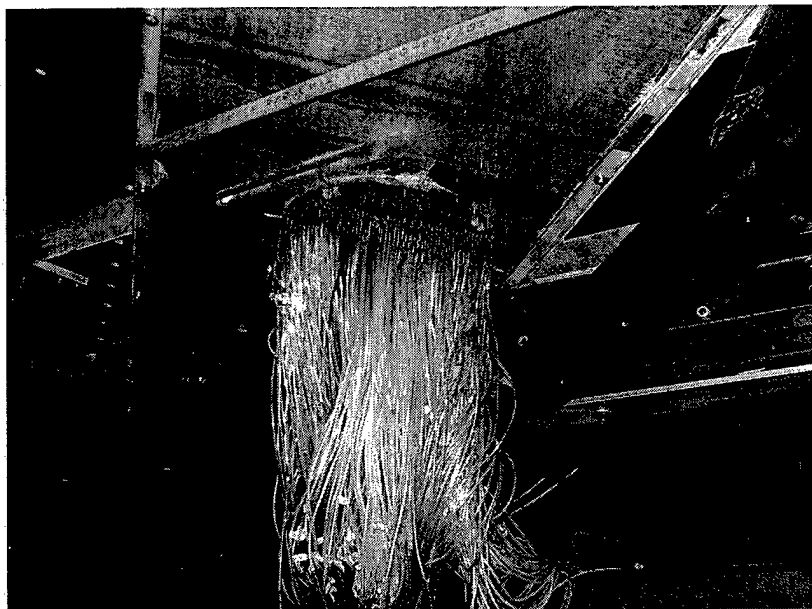


Figure 2.6 Pressure plot is put under the blade

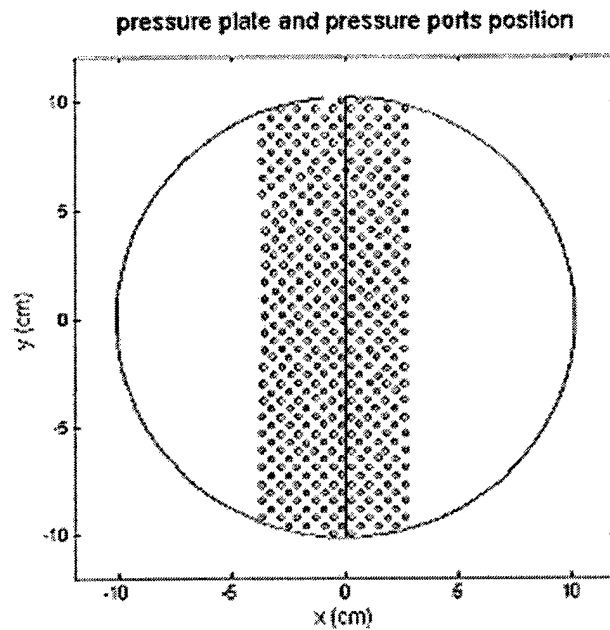


Figure 2.7 The dimension of the pressure plate and the relative positions of the pressure tap

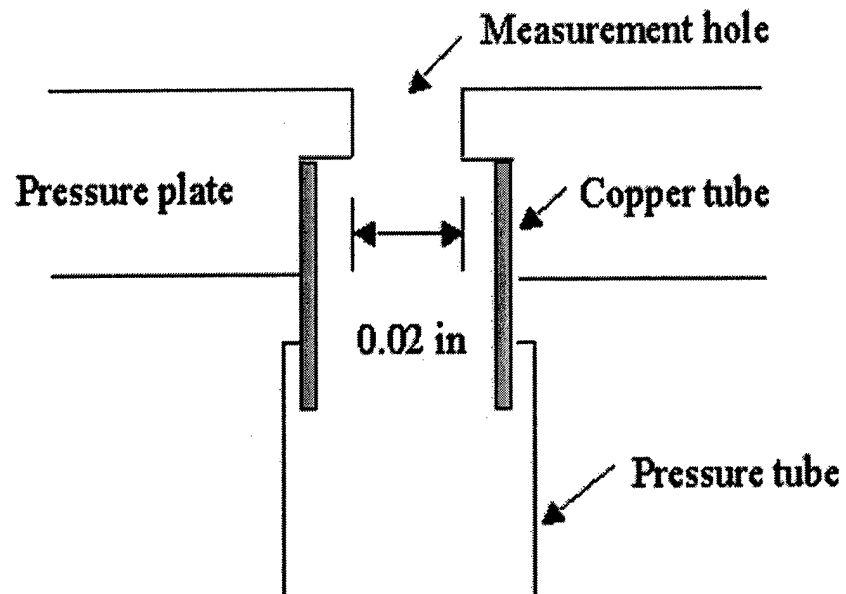


Figure 2.8 Detail drawing of the pressure taps and plate surface

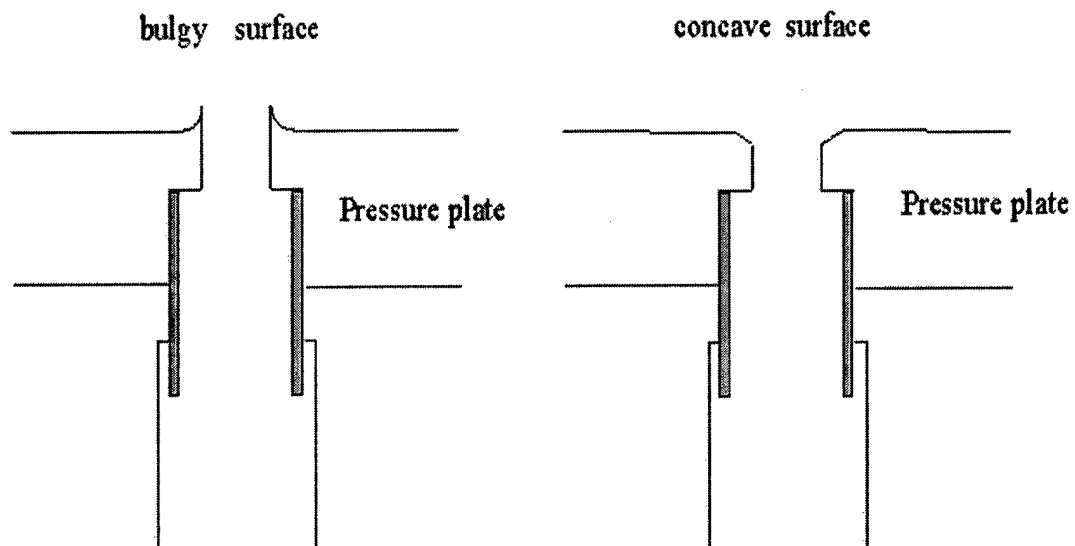


Figure 2.9 Bulgy and concave surface on the pressure plate

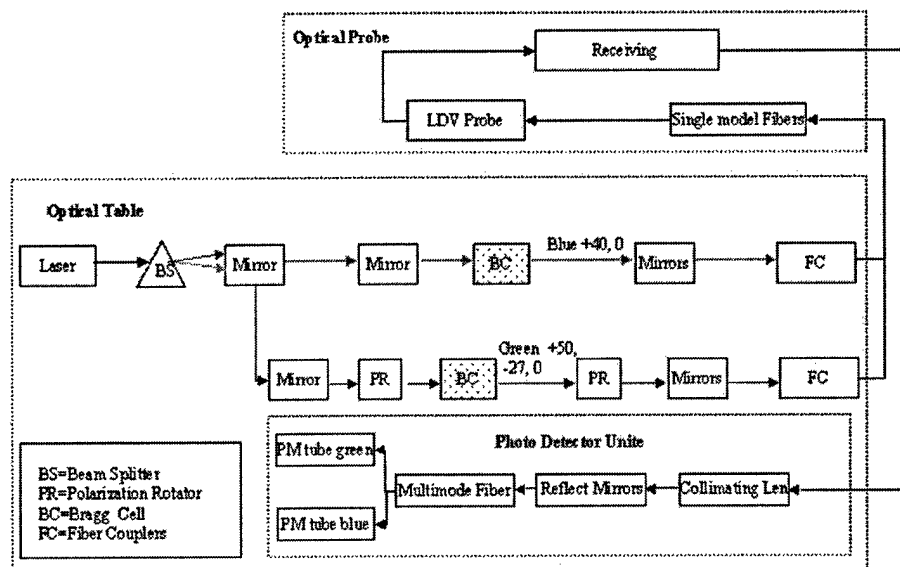


Figure 2.10 Block sketches of the optic table and laser beams paths

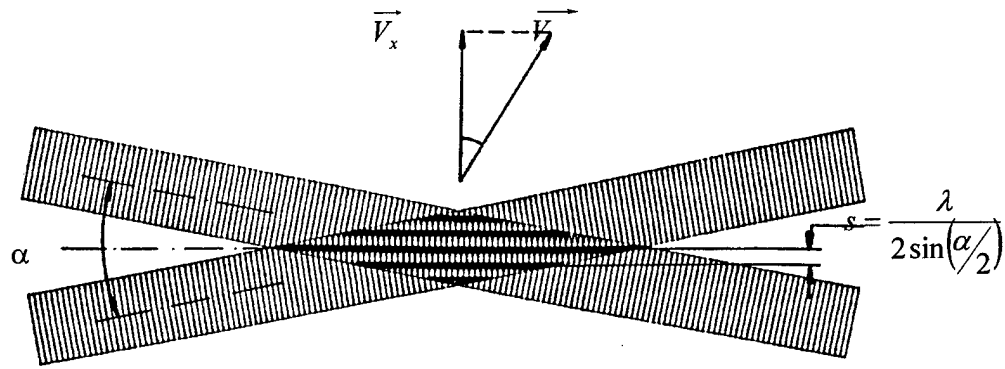
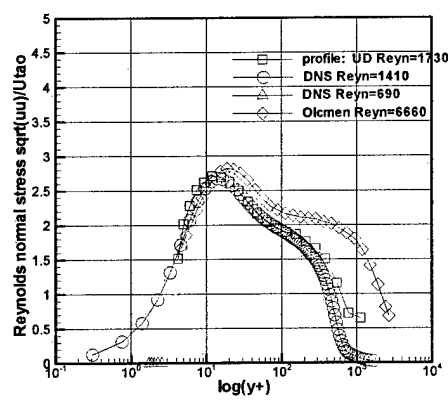
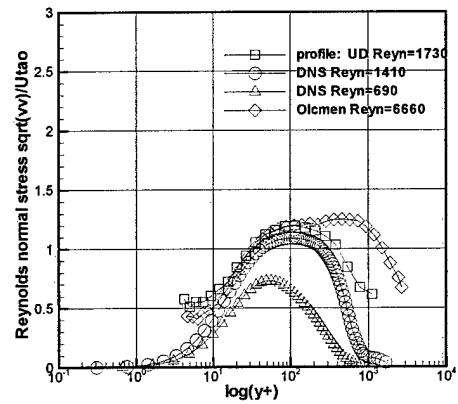


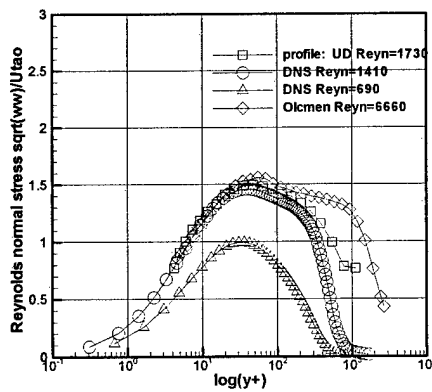
Figure 2.11 Fringe model: superposition of two laser beams.



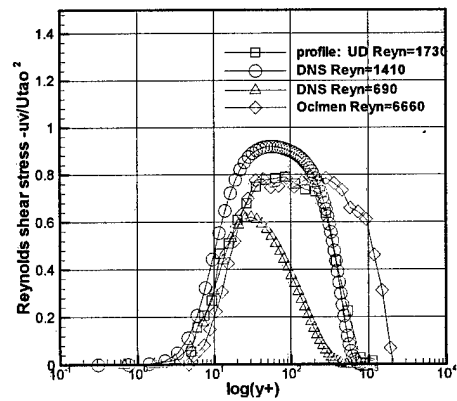
[a]



[b]



[c]



[d]

Figure 2.12 Comparison with DNS data and cascade tunnel data

3. RESULTS AND DISCUSSION

3.1 OIL FLOW VISUALIZATION

3.1.1 FLOW VISUALIZATION ON THE END-WALL

Surface oil flow visualizations for two different tip gaps ($t/c=1.65\%$ and 3.3%) were done on the lower end-wall with tip gap clearance. The running conditions are at the speed of 25m/s and temperature of $25\text{C}^{\circ} \pm 1\text{C}^{\circ}$. A black adhesive plastic sheet ($18.7\text{ inch} \times 10.8\text{ inch} \times 0.008\text{ inch}$) was mounted under the tip gap on the tunnel floor. A mixture of proportion of 15 ml. titanium dioxide, 40 ml. kerosene and 1ml. of oleic acid was painted on this black adhesive plastic sheet. In order to avoid possible static electricity effects coming from the oil brush and the plastic, aluminum foil was put under and above the plastic at the edge and grounded. The tunnel was run for about 5 minutes until all the kerosene evaporated, and then a fixative was sprayed to the surface to preserve the traces. This black plastic sheet was removed, and various details of this surface oil flow pattern were digitized by a scanner, and presented in figure 3.1 and figure 3.2. The movement of the oil mixture driven by the flow and the formation of the oil flow patterns could be clearly revealed and recorded. Figure 3.1 shows the flow pattern under the blade 5 for $t/c=1.65\%$ on the end-wall from

Chapter 3

Muthanna (2002). Figure 3.2 shows a close up of flow pattern of the lower end-wall in the passage between blades 3 and 4 for $t/c=3.3\%$ case.

From the details of flow pattern on the oil flow visualization, there are two different kinds of flows in this cascade inner flow. One is the flow in the passage between the blades, and the other one is the cross flow under the tip gap, mainly driven by the pressure difference between the pressure and suction sides of the blade. These two different flows meet together on the suction side of blade and roll up, forming the tip leakage vortex. Assuming that the dark regions in the flow visualization that sweep away the oilflow mixture correspond to regions of high shear flow, we observe that three dark regions from the detail of the flow visualization in each figure.

One dark region is underneath the blade, especially in the middle part of blade, as shown in the figures 3.1 and 3.2. In this region, the flow is mostly driven by the pressure difference between the two blade sides. This high shear flow is responsible for removing the white titanium dioxide paint and leaving the dark streaks, as a result of this pressure driven tip-gap flow. These streaks correspond to the near-wall shear stress direction, which are almost perpendicular to the blade chord. This observation matches with what has been observed in studies of the mean flow direction from the near-wall LDV velocity data. Figure 3.1 and figure 3.2 are indicative of very strong shear flow under the tip gap.

A second dark region is next to the tip leakage vortex region, as shown in the figures 3.1 and 3.2. As mentioned above, after the cross flow goes through the tip gap, it impinges into the passage flow, rolls up and forms the tip leakage vortex. This region is where the vortex lifts flow off of the wall. The width of the dark region

around the separation line is probably due to the low frequency unsteadiness of the tip leakage vortex.

Another interesting feature in the figures 3.1 and 3.2 is the dark region in upstream of the tip leakage vortex. It also implies that there is flow structure that has high shear flow. Previous studies (Muthanna, 2002) have all suggested that there might be a passage vortex present, engulfed by the tip leakage vortex.

3.1.2 FLOW VISUALIZATION ON THE BLADE SURFACE

The oil flow visualization on the blade surface used the same experimental procedure as the end-wall flow visualization. Since the blade surface is normal to the horizontal tunnel bed, there exists a gravitational effect, which is greater with a less viscous oil mixture. The mixture rate (15 ml. titanium dioxide, 25 ml. kerosene and 1ml. of oleic acid) is more viscous from that used in the end-wall case. Oil flow visualization on the blade surface was done for both tip gaps with and without a moving wall. For the moving wall case, the moving belt moves at 21 m/s along the pitchwise. The black adhesive plastic sheet was put on the blade surface along the blade tip edge. Since it is impossible to do end-wall oil flow visualization for the moving wall case, the blade surface visualization becomes important to discover the flow field difference between the moving wall and non-moving wall.

Oil flow visualization on the blade surface in the figure 3.5 reveals the reattachment of the tip leakage vortex on the blade surface. From the figure 3.5, a reattachment line exists in both two moving wall cases and non-moving wall cases for both tip gaps. For the 3.3% tip gap to chord ratio, the reattachment lines with and

Chapter 3

without moving wall have the same shape (the same slope) and different initial position. For the moving wall case with a 3.3% tip gap, the reattachment moves toward the leading edge of the blade. It gives us more ideas about the behaviour of the tip leakage vortex in the moving wall case, and shows that the origin of the tip leakage vortex moves upstream, as compared with the non-moving wall case. For 1.65% tip gap case, the same features can be observed.

3.1.3 THE OIL FLOW DIRECTION AND WALL SHEAR STRESS DIRECTION MEASUREMENT

As mentioned above, those streaks in the oil flow pictures correspond to the oil flow direction, which can be measured and compared with the average wall shear stress direction in the viscous sublayer from the LDV measurements. Various details of this flow in the oil flow visualization are digitized by a high resolution scanner. With these digitized oil pictures, AutoCAD, an engineering design software, was used to measure the oil flow direction in the oil flow pictures. Figure 3.6 shows how the oil flow directions are measured. Each circle center in the figure corresponds to a position where the oil flow directions are measured. In order to measure the oil flow direction, we need to draw a line passing through the circle center and tangent to the streaks. The angle between this line and x-axis in the bed coordinates is the measured the oil flow angle from the oil flow picture. The oil flow angles shown in the following figures are defined as angles between the streaks and the x-axis in the bed coordinate system, choosing the counter clockwise as the positive direction. In order to get the best line, which is tangent to the streaks, the streaks need to be magnified as

Chapter 3

much as possible and the tangent line is drawn. The uncertainty for the angle of tangent line should be less than one degree (Appendix A.3).

While the air blows over the oil surface and carries the oil with it, the streaky deposit of the titanium powder remains to mark the local oil flow direction of the flow at the oil sheet surface. The gravitational and pressure gradient effects may cause the invalidity of the oil and streaks do not be necessary to be aligned with the local flow direction at the surface. In the cascade tunnel, tremendous pressure gradient exists under the blades and on the suction side of the blade. The Relationship between the local oil flow direction and the wall shear stress direction need to be visited. The motion of a thin oil sheet on a surface under a turbulent boundary layer in low speed and high speed tunnels is reviewed by Squires in 1962. The following equations (Squires 1962) governing the motion of a thin oil sheet under a turbulent boundary are given as equations (3.1) and (3.2)

$$U = \frac{1}{\mu} \left[\frac{\partial P}{\partial x} \left(\frac{y^2}{2} - hy \right) + \tau_x y \right] \quad (3.1)$$

$$W = \frac{1}{\mu} \left[\frac{\partial P}{\partial z} \left(\frac{y^2}{2} - hy \right) + \tau_z y \right] \quad (3.2)$$

Where τ_x and τ_z are the x and z components of the mean skin friction in the turbulent boundary in the bed coordinates, which can be calculated by using the least square fit to the viscous sublayer velocity data from the LDV measurements. U, W is the mean velocity components of the oil velocity with corresponding forms from the streamlines in the oil flow images. μ is the viscosity of the oil. $\frac{\partial P}{\partial x}$ and $\frac{\partial P}{\partial z}$ are the

Chapter 3

static pressure gradient on the end-wall. h is the oil thickness. During the visualization process, oil thickness changes from the initial thickness to the one closing to zero and the intersurface between the oil and air is what we are interested in. Let y equal to the oil thickness, and the governing equation becomes

$$U = \frac{1}{\mu} \left[-\frac{h^2}{2} \frac{\partial P}{\partial x} + \tau_x h \right] \quad (3.3)$$

$$W = \frac{1}{\mu} \left[-\frac{h^2}{2} \frac{\partial P}{\partial z} + \tau_z h \right] \quad (3.4)$$

As $h \rightarrow 0$, $-\frac{h^2}{2} \frac{\partial P}{\partial x}$ and $-\frac{h^2}{2} \frac{\partial P}{\partial z}$ approach to zero much faster than $\tau_x h$ and $\tau_z h$, and these two terms $(-\frac{h^2}{2} \frac{\partial P}{\partial x}$ and $-\frac{h^2}{2} \frac{\partial P}{\partial z})$ are negligible, equation 3.3 and 3.4

become

$$U = \frac{1}{\mu} (\tau_x h) \quad h \rightarrow 0 \quad (3.5)$$

$$W = \frac{1}{\mu} (\tau_z h) \quad h \rightarrow 0 \quad (3.6)$$

Considering $\tau_x = \tau \cos(\theta_1)$ and $\tau_z = \tau \sin(\theta_1)$,

$$\tan(\theta_2) = \tan(\theta_1) \quad (3.7)$$

Where θ_2 is the oil flow direction and θ_1 is the wall shear stress direction

It means that as the oil thickness becomes thinner and thinner, the oil flow direction is more aligned with the wall shear stress direction. Here, wall shear stress direction is defined as the average flow angles from the LDV measurements in the viscous sublayer, which are related to the x-axis in the bed coordinates and obeyed the right hand rule. In the real oil flow visualization experiment, the initial oil thickness is depended on how the oil is painted on the oil sheet, which changes with the oil

Chapter 3

mixture and different brushes. During the process of the visualization, the oil thickness become thinner as the air blows the oil away, and also the oil thickness changes along streamwise from the upstream to the downstream and along the downstream, more oil is accumulated. While close the separation line of the tip leakage vortex, more oil is accumulated there and oil thickness is much higher than other places, $-\frac{h^2}{2} \frac{\partial P}{\partial x}$ and $-\frac{h^2}{2} \frac{\partial P}{\partial z}$ are no longer negligible, the difference between the oil flow direction and the wall shear stress direction is huge, as the scatter points off the 45 degree line shown in the figures 3.7 and 3.8.

Figures 3.7 and 3.8 show that the oil flow angles match well with near wall shear stress angles from the LDV velocity data, except those regions close to the tip leakage vortex separation line. The oil follows the boundary layer surface streamline except near separation where it tends to form an envelope upstream of the true separation envelope. The distance by which separation is apparently altered depends on the oil thickness, but it is independent of the oil viscosity (Squires, 1962). The root mean square of these flow angles difference except those close to the separation line is $\pm 1.65^\circ$ and the uncertainty of the flow angles in the LDV measurement is approximately ± 0.5 degree, (Kuhl, 2001), the angle uncertainty from the oil flow measurement is about $\pm 1^\circ$ (Appendix A.3). It gives us more confidence in these wall shear stress angles from the oil flow measurement, and it is also a simple way to measure wall shear stress angles of those positions where we are interested but do not have LDV data. Thus it can be concluded that oil flow direction is aligned with the wall shear stress direction, as the oil thickness is close to zero. The low frequency unsteadiness of the tip leakage vortex may partially contribute to the difference

Chapter 3

between the oil flow direction and wall shear stress direction while close to the separation line.

For every tip tap, there were more than 1000 oil flow angles measured. These positions covered the region between blades and under locations blades, including where LDV measurements are available or not. Figures 3.9 and 3.10 show the measurement positions and the oil flow direction of the oil flow. The passage flow and tip gap cross flow are as clearly shown in these two figures. Figures 3.11 and 3.12 show how oil flow angle changes along the pitchwise of the blades (pitchwise is the direction aligned with the z direction in the bed coordinate and also with the two rollers in the moving wall case) across the passage and from pressure side to the suction side. In figures 3.11 and 3.12, in the upstream regions of the passage, the oil flow angles change a little even under the blade and almost are constant in the passages because the passage flow is much stronger than the tip gap cross flow. While going downstream, the cross flow becomes progressively stronger, the tip leakage vortex forms and has bigger effects on the flow direction, and the oil flow angles change much along the pitchwise, especially near the tip leakage vortex and blade tip, as shown in figures 3.11 and 3.12.

3.1.4 FLOW STRUCTURE IN THE LINEAR CASCADE TUNNEL

From the oil flow visualization on the end-wall (figure 3.1 and figure 3.2), and on the blade surface (figure 3.5), the tip leakage vortex, the passage vortex and reattachment of tip leakage vortex can be found, which are consistent with the observation from the oil flow visualization by Muthanna (2002). From the LDV

Chapter 3

measurements (figures 3.3 and 3.4), the tip leakage vortex and the blade tip separation vortex on the blade tip surface are captured. Figure 3.13 generalizes a multiple tip vortex structure based on the oil flow visualization and LDV measurement. Tip gap flow is strongly accelerated in to the tip gap. This can be seen clearly from high shear stress dark region in the oil flow visualization on the end-wall (figures 3.1 and 3.2) and also the LDV measurement (figures 3.3 and 3.4). The crossing point of the blade surface and the dividing stream surface between the fluid, which is swept into the gap and that which is driven across the passage changes with the tip gap thickness. In the oil flow visualization figures, the tip gap cross flow is seen to leave the tip region approximately at $X/C_a = 0.14$ for $t/c = 1.65\%$, but for $t/c = 3.3\%$, $X/C_a = 0.38$.

Cascade blades generally have a sharp corner at the entrance to the gap. Therefore, a separation vortex forms at the corner. Since there is no flow visualization on the blade tip, this feature can only be found in the LDV measurements in figure 3.3 and figure 3.4. Kang & Hirsch (1996) have reported separation vortices on the blade tips of the compressor blades in their cascade measurement and also presented that there are quite high shear stresses on the blade tip in the region next to the separation vortex. This high shear stress is accompanied by correspondingly high levels of convective heat transfer. This may help explain the "burn out" which sometimes occur in the region on the actual turbine blades.

As described in previous discussion (3.1.1), there are two basic flows in this cascade inner flow; one is the passage flow along the passage between the blades, the other one is the cross flow under the tip gap, mainly driven by the pressure difference between the blades. These two different flows meet together on the suction side of blade and roll up, forming the tip leakage vortex. As shown in the oil flow picture, the tip leakage flow pushes the passage vortex away from the suction surface. There is

Chapter 3

strong interaction between the tip leakage vortex and the passage vortex, resulting in the engulfment of the passage vortex. This interaction leads to considerable mixing as well as turbulence production, which ultimately results in loss production. So far, we can see similar structural features of these two different tip gap flows for a stationary wall: a passage flow, a tip gap cross flow, a region of high wall shear stress under the blade tips, and the separation line associated with the tip leakage vortex. The qualitative nature of these two high shear stress regions is similar to some extent. The periodicity of the cascade flow is visible as shown in the figure 3.2, and the cross flow is at an angle of approximately 90 degrees to the chord line of the blade, through the tip gap region for both inflow cases.

Differences exist between these two tip gap flows. In the oil flow visualization, the crossing points of the blade surface and separation line are approximately at $X/C_a = 0.14$ for the $t/c = 1.65\%$ case, but for the $t/c = 3.3\%$ case, at $X/C_a = 0.38$. It means that by increasing tip gap, the cross flow effect takes greater distance to develop and the separation line and tip leakage vortex move toward downstream. In the table 3.1, Z is the distance between the separation line and the suction side of blade surface along the pitchwise, and at the same cross section, the separation line of the 1.65% case is much farther away from the blade than that in the 3.3% case at the same cross section. It also implies the tip leakage vortex and tip leakage separation happen further upstream for the $t/c = 1.65\%$ case. Since increasing the leakage of the blade, the cross flow endures a longer distance from pressure side to the suction side and will lose more kinetic energy. Relatively, the cross flow becomes weaker and passage flow becomes relatively stronger. The passage flow will push the tip leakage vortex toward downstream.

3.2 STATIC PRESSURE MEASUREMENTS

The static pressure measurements on the end-wall were done using an automated data acquisition system (ADAS) with a pressure tap plate with 426 pressure ports, one pressure transducer and a scanivalve system. A schematic of the ADAS is illustrated in figures 3.14 and 3.15. The pressure taps are connected through tygon tubing to a scanivalve connector. The scanivalve connector is a rotary multiple-port switch that permits multiple pressure inputs to be connected to a common output. The output of the scanivalve system is directed to a pressure transducer (Setra 239) that converts a pressure difference into a voltage. The pressure transducer has one of the ports connected at all times to $p_{ref, static}$, the static reference pressure in the free stream. The other ports are connected to the scanivalve, which measures static pressure at various locations on the pressure plate. The voltage from the pressure transducer is transmitted to the computer where the voltage signal is digitized using an Analog/Digital (A/D) board and stored.

Since there are 426 pressure taps on the pressure plate in the present experiment, pressure taps were connected through tygon tubing to 10 scanivalve connectors. Every scanivalve connector has 48 pressure ports. The input connections to the scanning valve are as follows:

- Ports 0, 11, 21, 31, and 41 are connected to the $P_{ref, total}$ tube by using a multi-connector to measure the stagnation pressure in the free stream.
- Ports except those above are connected to the corresponding pressure taps located on the pressure plate.

Chapter 3

- One of the ports of the pressure transducer is connected at all times to P_{ref} , static, the static reference pressure in the free stream.

The pressure transducer was calibrated, using a manometer to relate the output voltage by the transducer to actual pressure readings. The calibration equation, valid for the entire range of measured pressures, is of the form $h = aV + b$ where h is the reading of the manometer (in inches of manometer liquid), V is the voltage produced by the pressure transducer, a and b are coefficients obtained through linear regression applied to the calibration points. The measurement range of the pressure transducer is ± 2.5 inch water. Parameter a is equal to 5, and parameter b is much more dependent on the offset voltages, which is not a constant and drops with time. After turning on the pressure transducer, 30 minutes were need to be waited to reduce the offset voltage.

3.2.1 STATIC PRESSURE COEFFICIENT C_p ON THE END-WALL

For $t/c = 1.65\%$ and 3.3% cases, mean static pressure distributions on the surface of the pressure plate on the end-wall under the blade 5 (figure 3.16) were measured with a series of pressure taps. The 426 taps were arranged in a rectangular mesh with the smallest spacing about 5mm between adjacent taps on the plastic plate. Measurements were taken using 10 connectors and each of them has 48 ports and connects via a scanivalve to a single transducer. In order to measure the entire region under the blade, the pressure plate was placed in two optic inserts which have two different optic glass insert locations and for every location, the pressure data were taken at four orientations. The experiments were made under the same condition as

Chapter 3

we take the LDV data, namely $U_{ref}=(25\pm0.4)$ m/s , $T=(25\pm1)$ C°, and $Re_\theta \approx 1700$.

The static pressure coefficient C_p is calculated as:

$$C_p = \frac{P_{local,static} - P_{ref,static}}{P_{ref,total} - P_{ref,static}} = \frac{P_{local,static} - P_{ref,static}}{\frac{1}{2} \rho U_{ref}^2} \quad (3.8)$$

Where $P_{ref, static}$ and $P_{ref, total}$ are the static and stagnation pressures of the undisturbed free stream, measured by a pitot-static tube mounted upstream of the front section of the tunnel before the flow turning. $P_{local, static}$ is the static pressure on the end-wall.

Note that because the single pressure transducer has a linear pressure to voltage relationship, the drift of the pressure transducer cancels in the C_p calculation. The static pressure on the end-wall was measured with the tip clearance set to 1.65% and 3.3% of chord. Contours (figure 3.18 and figure 3.19) of the static pressure measured on the end-wall are shown the final pressure distribution covering the suction side and pressure side of the blade. It is obvious that there is a huge pressure gradient between the pressure side and the suction side. The static pressure increases from the upstream to the downstream. From the pressure side and to the suction side, the static pressure decreases and then increases. The distributions are remarkably similar for both tip gaps.

Pressures calculated with the Navier-Stokes code using K-epsilon model from S.Shin (2001) are shown in figure 3.20 for the 1.65% chord tip clearance case with stationary wall. Comparing calculation results with the experiment results, both results show a tremendous pressure gradient between the pressure side and the suction side. The static pressure increases from the upstream to the downstream. From the

Chapter 3

pressure side and to the suction side, the static pressure decreases and then increases. Even though the coordinates are different, these two contour plots from the experiment and calculation looks similar and the position of the troughs in pressure contour plots are almost consistent with each other. With flow visualization of flow on the end-wall for both 1.65% and 3.3% of tip clearance to chord ratio oil, the trajectory of the tip leakage vortex coincides with a trough in pressure contour plots measured on the end-wall. The CFD calculation has a similar trough. The origin of the trough is close to the lowest pressure contour on the end-wall, which is located close to the blade tip. The pressure trough is identical with the separation line of the tip leakage vortex, and it means that the origin of tip leakage vortex is associated with the position of the local lowest pressure on the end-wall. The local minimum pressure location is at the origin of the tip leakage vortex. The position of minimum pressure on the end-wall moves to downstream of the leading edge as the tip clearance is increased, so the tip leakage vortex also moves toward downstream.

Static pressure data along the edge of the blade tip on the end-wall was extracted from the original static pressure data on the end-wall, using quadric surface fitting to the original static pressure data and compared with static pressure data in the mid-span of the blade. In figure 3.21, with the 3.3% clearance, the minimum pressure is located at about 40% of axial chord length from the leading edge on the suction side of the blade; This location matches with the initial location of the separation line from the oil flow visualization measurement (for $t/c=3.3\%$, $X/C_a=0.38$). As shown in the figures 3.18 and 3.19, the position with the local minimum static pressure is approximately at the beginning of the tip leakage vortex.

Chapter 3

As in previous discussion (3.1.4), the tip gap flow accelerates in the tip gap region and pressure lost does work and increase the kinetic energy. Although the position of the minimum pressure changes with the different tip gaps, the difference between the highest pressure and the lowest pressure for these two cases is about 0.75 for the C_p and essentially the same. The bulk of the gap flow appears to experience very similar driving pressure differences for a wide range of clearances.

3.2.2 PRESSURE GRADIENT AND QUADRIC SURFACE FIT

The pressure gradient $\vec{\nabla}(C_p)$ described in Cartesian coordinates is as following:

$$\vec{\nabla}(C_p) = \frac{\partial(C_p)}{\partial(x)} \vec{i} + \frac{\partial(C_p)}{\partial(y)} \vec{j} + \frac{\partial(C_p)}{\partial(z)} \vec{k}. \quad (3.9)$$

However, the pressure data are only available on the pressure plate surface. Thus, the pressure gradient which can be obtained is the pressure gradient along the surface

$$\vec{\nabla}(C_p)|_{surf} = \frac{\partial(C_p)}{\partial(x)} \vec{i} + \frac{\partial(C_p)}{\partial(z)} \vec{k}. \quad (3.10)$$

The static pressure on the end-wall is a function of the x and z in the bed coordinates. Since positions of the original pressure data are irregular, the pressure information where the LDV data is available is still unknown. In the later discussion of the skin friction velocity calculation, a pressure gradient is required at LDV location in order to do a curve fit with the viscous sublayer ($y^+ < 9$) velocity data to

Chapter 3

calculate the skin friction velocity. The original pressure data need to be interpolated in order to get the pressure and pressure gradients at the desired locations. Here a quadric surface equation was fit to the local static pressure data $C_p = f(x, z)$ on the end-wall in order to interpolate the pressure data, ie,

$$C_p = a_1x^2 + a_2z^2 + a_3zx + a_4x + a_5z + a_6 \quad (3.11)$$

By using the least square quadric surface fit to the original static pressure data, pressure gradient data can be extracted. The derivation of the least square quadric surface fit can be found in the Appendix A.4. The benefit of the quadric surface fit is that the local pressure information can be obtained, based on the pressure data in the vicinity of the specified position, and the interpolated pressure result and pressure gradient are more local and closer to the real pressure.

One issue about the quadric surface fit is how many data points are going to be used in the least square fit. Since there are 6 unknowns in the quadric surface equation, at least 6 data points need to be used. Also more data points included, the less local pressure information can be included. For the $t/c=3.3\%$ tip gap case, 2 cases are tested, one is 10 data points, the other is 20 data points. The results from 10 data points are much more reliable and local than the one in 20 data points as shown in the table 3.2, because in 10 points fit, the average radius of these surface fit regions is 0.8 cm and average correlation coefficient is about 0.98, but for 20 points fit, the average radius is 1.2 cm and average correlation coefficient is about 0.96. Since 10 points fit has higher correlation coefficient and small radius (the distance between the interpolation point and the farthest data point used in the interpolation), the 10 data points least square quadric surface fit is used in the interpolation of the pressure data. Figures 3.23 to 3.26 show that pressure gradients plots at the planes $x/P_w=0.21$ and $z/P_w=-1.05$ (P_w is

Chapter 3

the passage width), and the pressure gradient changes continuously, and there are two peak value, which is corresponding to the appearance of pressure valley in the pressure contour.

In figures 3.9 and 3.10, the oil flow direction in the near-wall region shows that the flow in this region is almost normal to the axial chord line, but approximately opposite to the pressure gradient direction. With this comparison, the pressure gradient in the tip gap flow is a favorable pressure gradient, and away from the suction side, an adverse pressure gradient appears. Since the main gap flow was nearly parallel to these lines normal to the axial chord line, the resulting pressure differences are essentially those driving the flow into the gap, up to the tip leakage vortex.

3.2.3 CORRECTION TO THE SEPARATION LINE

LOCATION

As discussed in the section 3.1.3, although wall shear stress angles measured from the oil flow picture match very well with the average flow angles in the viscous sublayer from LDV data at the most locations, wall shear stress angles near the tip leakage vortex separation showed huge differences from the LDV results. Also the oil flow experiment is a time-averaged process. Oil mixture may have some affect to the local flow field, especially near the separation line, because more oil is accumulated while closer to the separation line and oil becomes thicker. Thus the separation line position from the oil flow needs to be corrected. Assuming that the corrected line is parallel to the oil flow separation line and passes through the local minimum skin

Chapter 3

friction, the separation line can be corrected. Figures 3.18 and 3.19 show that for the $t/c=3.3\%$ and 1.65% , separation lines with correction, match with the troughs in the pressure contours, because the low pressure trough is generated by the tip leakage vortex. Due to the limited number of profiles near the tip leakage vortex, there is still some uncertainty existing in these corrected separation lines and based on the distribution of profiles in the vicinity of the separation line, the uncertainty for the separation line in the 3.3% tip gap is less than 0.35 cm and 0.25 cm for the 1.65% tip gap.

3.2.4 K PRESSURE COEFFICIENT CALCULATION

Most of the pressure gradient in the tip gap is a favorable pressure gradient.

$k = \frac{\nu}{U_e^2} \frac{dU_e}{ds}$ coefficients represent the strength of the pressure gradient. For

$k < 5 \times 10^{-7}$, there is a mild pressure gradient, for $k > 5 \times 10^{-7}$, there is a strong pressure gradient. For a mean two-dimensional flow with $k > 3 \times 10^{-6}$, turbulent flow can become laminarescent again after some downstream distance, and the flow becomes free-stream, entrainment ceases, and there is no more semi-log layer mean velocity profile, intermittent, laminar and turbulent. (Simpson, 1979)

$$k = \frac{\nu}{U_e^2} \frac{dU_e}{ds} \quad (3.5)$$

Considering Bernoulli's equation, ignoring body force along streamline and using the definition of pressure coefficient,

Chapter 3

$$\frac{U_e^2}{2} + \frac{P}{\rho} = \text{constant} \quad \text{along streamline} \quad (3.6)$$

$$C_p = \frac{P_{\text{local,static}} - P_{\text{ref,static}}}{P_{\text{ref,total}} - P_{\text{ref,static}}} = \frac{P_{\text{local,static}} - P_{\text{ref,static}}}{\frac{1}{2} \rho U_\infty^2} \quad (3.7)$$

The final formula using to calculate k , which is represented by the pressure coefficient and U_e is

$$k = \frac{-\nu U_\infty^2}{2U_e^3} \frac{dC_p}{ds} \quad (3.8)$$

where ν is the kinematic viscosity, C_p is pressure coefficient, U_e is the outer layer velocity, U_∞ is the free-stream velocity, and $\frac{dC_p}{ds}$ is the component of the pressure gradient on the streamline. Since it's hard to define U_e in the tip gap flow, we assume that U_∞ and U_e are almost same, equation (3.8) becomes

$$k = \frac{-\nu}{2U_\infty} \frac{dC_p}{ds} \quad (3.9)$$

Tables 3.3 and 3.4 show the k values for every position where the LDV data were taken. From the tables 3.3 and 3.4, both of the tip gaps, most of the k values are greater than $k > 3 \times 10^{-6}$. Turbulent flow in the tip gap becomes uncorrelated by the strong acceleration as shown by Tang (2004).

3.3 THE NEAR-WALL VELOCITY PROFILE FOR THE TIP GAP FLOW WITH PRESSURE GRADIENT

In the two-dimensional turbulence boundary near a wall, the turbulent eddies are strongly influenced by the presence of the wall. In the wall flow, viscosity plays no small role. Viscosity is strongly responsible for flow instabilities near the wall that grow and develop into vortices that in turn produce the Reynolds shearing stresses. These vortices appear to occur periodically with a well-defined lateral spacing transversely across the wall.

For mean three-dimensional turbulent flow, there is no law of the wall, but in order to normalize the velocity, a characteristic velocity scale, such as the skin friction velocity, is needed (Simpson 1996). The pressure gradient can appreciably change the near-wall mean velocity profile. As a result, the wall drag as well as the entire flow structure can be strongly influenced, good reason for closely examining the wall flow structure.

Throughout the near-wall region certain terms of the governing momentum equations can be discarded as being negligibly small compared to those remaining. For sufficiently small values of y , all derivatives with respect to x are negligible; at $y=0$ all derivatives with respect to x and z are exactly zero. Since the wall is impermeable, $v=0$ at $y=0$, and the continuity equation requires that $v=0$ as long as

$\frac{\partial u}{\partial x} = \frac{\partial w}{\partial z} = 0$. Thus the momentum equation in the direction of the wall shear stress

reduces to

$$-\frac{1}{\rho} \frac{\partial P}{\partial s} + \frac{\partial}{\partial y} \left(-\overline{u'v'} + \nu \frac{\partial U}{\partial y} \right) = 0 \quad (3.10)$$

Chapter 3

Integration with respect to y , where produces $\frac{\partial P}{\partial s}$ is the component of the surface pressure gradient in the wall shearing stress direction:

$$-\overline{u'v'} + \nu \frac{\partial U}{\partial y} = \frac{\tau}{\rho} = \frac{\tau_w}{\rho} + \frac{y}{\rho} \frac{dP_\infty}{ds} \quad (3.11)$$

$$\frac{\partial u'}{\partial x} + \frac{\partial v'}{\partial y} + \frac{\partial w'}{\partial z} = 0 \quad (3.12)$$

Considering the above fluctuation continuity equation, just away from the wall, the u and w are proportional to y and mean v is proportion to y^2 . Thus $-\overline{u'v'}$ is proportional to y^3 ,

It is reasonable that we assume $-\overline{u'v'} = C_3 y^3$ in the viscous sublayer, substitute it into the momentum equation (3.9), and integrate with respect to y to produce

$$U = C_1 y + C_2 y^2 + C_4 y^4 \quad (3.13)$$

$$\text{Where } C_1 = \frac{\tau_w}{\mu}, C_2 = \frac{U_\infty^2}{4\nu} \frac{dC_p}{ds} \quad u_\tau = \sqrt{\frac{\tau_w}{\rho}}$$

Once the pressure gradient along the surface skin friction line is calculated, C_2 is known. In order to get C_1 and C_4 , a curve fit need to be done with the viscous sublayer ($y^+ < 9$) velocity data. Once C_1 is known, through the relationship between friction velocity and wall shear stress, the skin friction velocity, which is the characteristic velocity scale in the wall region can be obtained. Experience has shown that turbulent velocity fluctuations and the mean velocity in the wall region can be scaled on u_τ .

The inner layer of a mean three-dimensional flow should approximately follow equation (3.13). In the case of the viscous sublayer data ($y^+ < 9$), the mean velocity profiles were curve fit using a model equation ($Q = C_1 y + C_2 y^4$) without a pressure

Chapter 3

gradient term and the other equation ($Q = C_1 y + C_2 y^2 + C_4 y^4$) with a pressure gradient, where $Q = \sqrt{U^2 + W^2}$, U and W are mean velocities. While doing this curve fit, the following criteria need to be considered. For both sublayer model equations, there are three unknowns, namely, C_1 , C_2 , and wall position refinement (Δy). Thus the number data points used in the curve fit should be greater than four in the viscous sublayer ($y^+ < 9$). Due to the measurement volume and tranverse system, one cannot define exactly where is the wall surface ($y=0$). The uncertainty of the wall location is about $50 \mu m$ (which is the diameter of the measurement volume). In this wall refinement, Δy should fall within this ± 50 microns interval. This is also the acceptable tolerance. If wall position refinement (Δy) is greater than $50 \mu m$, it is indicative that there is some problem with the data or that the first point is much too far away from the wall, and these results become unreliable. The correlation coefficient of the curve fit is the quantity used to define how well the model equation fits to the experimental data. Equation (3.14) is the formula for calculating the correlation coefficient for the curve fit. Q_c is the value from the curve fit, and Q_e is the experimental data. An acceptable correlation coefficient R^2 is greater than 0.99. The uncertainties of the skin friction velocities are less than 5% as shown in Appendix A.6.

$$R^2 = \frac{\sum_D (Q_c(r) - \overline{Q_c(r)})(Q_e(r) - \overline{Q_e(r)})}{((\sum_D (Q_c(r) - \overline{Q_c(r)})^2)(\sum_D (Q_e(r) - \overline{Q_e(r)})^2))^{1/2}} \quad (3.14)$$

Where

$$\overline{Q_e(r)} = \frac{\sum_D Q_e(r)}{D} \quad \overline{Q_c(r)} = \frac{\sum_D Q_c(r)}{D}$$

Chapter 3

From friction velocity values in tables 3.3 and 3.4, the maximum difference in skin friction velocity with and without consideration of the pressure gradient term is more than 10 percent. Once the difference is greater than 5% in the friction velocity value, this will contribute to a big difference in the normalized velocity and Reynolds stress. Thus, friction velocity with pressure gradient must to be used in the velocity normalization. In figures 3.29 and 3.30, profiles e1, e2, and e3 for the 1.65% tip gap, x3 and x5 for the 3.3% tip gap are close to the tip leakage vortex separation line and from the friction velocity distribution (figures 3.27 and 3.28), these profiles are near local minima friction velocity values. This trend matches with the definition of a three-dimensional separation that near the separation line, the wall shear stress is the local minimum wall shear stress (Wetzel,1998).

3.4 COMPARING WITH WALL SHEAR STRESS CHARACTERISTICS IN OIL FLOW

The shear stress changes with the extent of the oil flow darkness pattern; much darker pattern means a higher shear stress. From the oil flow (figures 3.1 and 3.2), following features can be observed. For every cross section, from the pressure side to the suction side, the shear stress should increase and possibly after a maximum value, it will decrease. From the leading edge to the trailing edge, the shear stress increases, and then decreases. In figures 3.27 and 3.28, these two figures show how the skin friction velocity changes from the leading edge to the trailing edge and from the suction side to the pressure side from the LDV data. This friction velocity calculation shows the same trend as the observation from the oil flow.

Chapter 3

Figures 3.3 and 3.4 show mean velocity vector plots in the tip leakage vortex region from the LDV measurement in the separation coordinates. It is obvious that the tip-leakage vortex is one of the dominant features in the cascade flow. In the tip gap region, flow is accelerated due to the pressure difference of the two blade sides, and decelerated under tip leakage vortex due to the effect of the tip leakage vortex on the suction side of the blade. It means that skin friction values increase then decrease from the pressure side to the suction side of the blade, and the minimum skin friction value happens while it is close to the separation line. In the vicinity of separation, unlike the two-dimensional separation case, whose skin friction goes to zero, the skin friction has locally the lowest value, which helps us to find the real separation position to calibrate the separation line from the oil flow. This trend matches very well with the skin friction velocity calculated from the LDV data and the observation from the oil flow, as shown in the figures 3.27 and 3.28.

As previous assumption in the correction of the separation, it assumes that the separation line passes through the local minima skin friction point in the LDV measurement. From the friction velocity calculation with pressure gradient (in tables 3.3 and 3.4), for 1.65% tip gap, profile E2, which is in the tip leakage vortex region, has the local minima friction velocity which is at $Z/C_a = -1.45$ in the $x/C_a = 0.18$ cross plane in the bed coordinates as shown in figures 27 and 29, and the correction separation line should pass this point, but the position of the separation line from the oil flow at the same cross section is at $Z/C_a = -1.41$. For 3.3% tip gap, profile x5, which is in the tip leakage vortex region, has the local minima friction velocity which is at $Z/C_a = -2.04$ in the $X/C_a = 0.42$ cross plane in the bed coordinates as shown in figures 28 and 30, and the correction separation line should also pass through this point, and the position of the separation line from the oil flow at the same cross

Chapter 3

section is at $Z/C_a = -1.98$. Now we can say that the separation line of the oil flow is much closer to the blade than that which we get from the friction velocity calculation. Apparently the dominant force that act on the finite thickness oil flow material around the separation are from the upstream passage flow, which moves the oilflow separation line downstream of the actual line. This result shows that the oil near separation tends to form an upstream of the true separation envelope and distance by which separation is apparently altered depends on the oil thickness.

Table 3.1 Location of separation line relative to the blade surface

X / C_a	Z / C_a	
	$t/c = 3.3\%$	$t/c = 1.65\%$
2.280	0.480	2.143
2.627	1.105	2.463
2.905	1.650	2.707
3.217	2.070	2.920
3.530	2.553	3.221

Chapter 3

Table 3.2 The interpolated pressure data for 3.3% tip gap ratio in the bed coordinates

profile	t/c=3.3%		20 points		10 points		R ²		radius (cm)	
	Z/Ca	x/Ca	cpz(/cm)	cpx(/cm)	cpz(/cm)	cpx(/cm)	20 points	10 points	20 points	10 points
1D	-0.96	0.01	0.036	0.038	0.033	0.041	0.991	0.991	1.4	0.98
1B	-0.85	0.01	0.018	0.022	0.018	0.026	0.983	0.999	1.73	1.23
1U	-0.76	0.01	-0.001	0.017	-0.01	0.004	0.925	0.961	1.72	1.37
2S	-1.02	0.04	0.048	0.049	0.055	0.055	0.955	0.995	1.27	0.97
2C	-0.97	0.04	0.033	0.047	0.032	0.048	0.992	0.991	1.39	0.97
2P	-0.92	0.04	0.025	0.038	0.02	0.039	0.988	0.996	1.43	1.03
2U	-0.87	0.04	0.017	0.024	0.023	0.022	0.99	0.99	1.46	1.09
3S	-1.15	0.09	0.046	0.057	0.042	0.066	0.964	0.976	1.18	0.88
3C	-1.1	0.09	0.054	0.067	0.074	0.086	0.966	0.953	1.26	1
3B	-1.07	0.09	0.05	0.072	0.059	0.09	0.955	0.972	1.32	0.95
3P	-1.03	0.09	0.045	0.07	0.048	0.074	0.964	0.988	1.38	0.99
3U	-0.96	0.09	0.02	0.049	0.019	0.052	0.989	0.997	1.47	0.96
4S	-1.22	0.12	0.058	0.036	0.053	0.022	0.975	0.957	0.93	0.63
4C	-1.16	0.12	0.061	0.082	0.079	0.062	0.969	0.967	1.07	0.9
4B	-1.12	0.12	0.058	0.093	0.069	0.094	0.966	0.967	1.24	0.96
4P	-1.1	0.12	0.056	0.084	0.081	0.119	0.962	0.982	1.27	0.99
4U	-1.03	0.12	0.033	0.069	0.033	0.075	0.978	0.997	1.39	1
5S	-1.35	0.18	0.079	-0.009	0.06	-0.038	0.951	0.983	0.69	0.53
5C	-1.3	0.18	0.097	0.077	0.112	0.084	0.948	0.953	0.78	0.59
5B	-1.26	0.18	0.118	0.136	0.137	0.135	0.984	0.994	0.87	0.61
5P	-1.22	0.18	0.098	0.139	0.138	0.191	0.971	0.986	0.95	0.65

Chapter 3

5U	-1.15	0.18	0.063	0.111	0.057	0.153	0.978	0.981	1.05	0.78
E1	-1.4	0.18	0.017	-0.102	-0.005	-0.087	0.967	0.991	0.72	0.51
E2	-1.45	0.18	-0.018	-0.138	-0.029	-0.144	0.973	0.968	0.7	0.58
6S	-1.51	0.27	0.067	-0.066	0.052	-0.089	0.955	0.988	0.74	0.54
6C	-1.42	0.27	0.217	0.232	0.231	0.273	0.965	0.975	0.67	0.56
6B	-1.39	0.27	0.199	0.264	0.241	0.292	0.971	0.987	0.69	0.54
6P	-1.35	0.27	0.162	0.245	0.193	0.262	0.982	0.947	0.73	0.55
6U	-1.28	0.27	0.088	0.146	0.069	0.142	0.973	0.996	0.95	0.63
7S	-1.74	0.42	0.111	0.252	0.065	0.267	0.992	0.994	1.11	0.68
7C	-1.71	0.42	0.183	0.362	0.176	0.372	0.989	0.997	1.02	0.76
7B	-1.67	0.42	0.24	0.465	0.342	0.544	0.98	0.996	1.05	0.71
7P	-1.61	0.42	0.239	0.452	0.264	0.501	0.984	0.997	0.99	0.69
7U	-1.52	0.42	0.126	0.227	0.119	0.222	0.991	0.997	0.96	0.66
X1	-1.85	0.42	-0.035	0.037	-0.036	0.074	0.938	0.994	1.25	0.96
X4	-1.91	0.42	-0.056	-0.005	-0.061	-0.005	0.953	0.969	1.26	0.96
X2	-1.94	0.42	-0.06	-0.021	-0.056	-0.044	0.963	0.974	1.28	1.02
X3	-1.99	0.42	-0.066	-0.056	-0.056	-0.097	0.914	0.964	1.33	0.99
X5	-2.04	0.42	-0.068	-0.101	-0.101	-0.196	0.873	0.992	1.31	1
8S	-2.07	0.65	0.05	0.124	0.054	0.125	0.983	0.936	1.19	0.83
8C	-2.01	0.65	0.072	0.203	0.089	0.243	0.953	0.98	1.4	0.94
8B	-1.97	0.65	0.073	0.216	0.115	0.309	0.951	0.996	1.35	0.99
8P	-1.93	0.65	0.098	0.221	0.111	0.25	0.99	0.993	1.33	0.96
9S	-2.4	0.99	0.009	0.042	0.011	0.039	0.985	0.992	1.27	0.83
9C	-2.38	0.99	0.013	0.036	0.01	0.034	0.926	0.959	1.19	0.83
9B	-2.36	0.99	0.012	0.03	0.009	0.028	0.936	0.979	1.18	0.8
9P	-2.35	0.99	0.014	0.027	0.008	0.024	0.933	0.883	1.19	0.74

Chapter 3

Table 3.3 Friction Velocity Comparison with and without Gressure Gradient $t/c=1.65\%$

profile	t/c=1.65%		Yshift	Utao1 W/O		R^2	Yshift	Utao 2 with		R^2	C2	k
	Z/Ca	x/Ca		Pressure				Pressure				
1C	-0.74	0.01	17.86	0.83	0.985	0.985	23.7	0.8	0.99	2.22E+07	-8.67E-07	
1D	-0.93	0.01	9.1	0.96	1	1	3.6	1.03	1	-6.10E+07	2.38E-06	
1B	-0.85	0.01	35.9	1.11	0.999	0.999	34.5	1.13	0.999	-2.05E+07	7.98E-07	
1U	-0.76	0.01	-11.25	0.9	0.995	0.995	-13.4	0.92	0.996	1.66E+07	-6.45E-07	
2S	-1.02	0.04	19.5	1.06	0.999	0.999	16.6	1.12	0.998	-7.66E+07	2.98E-06	
2C	-0.97	0.04	20.97	1	0.997	0.997	13.8	1.1	0.998	-6.75E+07	2.63E-06	
2P	-0.92	0.04	-20.14	1.23	0.99	0.99	-21.2	1.27	1	-3.95E+07	1.54E-06	
2U	-0.87	0.04	0.24	0.9	0.996	0.996	-8.9	0.99	0.999	-4.10E+07	1.60E-06	
3S	-1.15	0.09	-1.34	1.25	0.995	0.995	-7.2	1.4	0.998	-1.46E+08	5.67E-06	
3C	-1.1	0.09	-9	1.16	0.997	0.997	-14.7	1.31	0.998	-1.82E+08	7.08E-06	
3B	-1.07	0.09	10.48	0.98	0.994	0.994	23.9	0.95	0.996	-1.47E+08	5.74E-06	
3P	-1.03	0.09	2	1.27	0.995	0.995	2	1.33	0.992	-1.30E+08	5.06E-06	
3U	-0.96	0.09	-4.38	1.23	0.99	0.99	-8.8	1.33	0.99	-4.43E+07	1.73E-06	
4S	-1.19	0.12	11.36	1.27	0.995	0.995	1.6	1.46	0.997	-1.55E+08	6.03E-06	
4C	-1.14	0.12	-3.2	1.36	0.999	0.999	-4.9	1.45	0.998	-2.69E+08	1.05E-05	
4B	-1.12	0.12	-4.01	1.18	0.996	0.996	-3.9	1.25	0.993	-2.75E+08	1.07E-05	
4P	-1.09	0.12	-3.5	1.51	0.99	0.99	-9.7	1.72	0.999	-2.08E+08	8.10E-06	
4U	-1.06	0.12	-2.78	1.15	0.997	0.997	-4.6	1.21	0.993	-1.44E+08	5.61E-06	
5S	-1.32	0.18	6.66	1.48	0.999	0.999	2.6	1.61	0.998	-2.56E+08	9.98E-06	
5C	-1.26	0.18	-7	1.26	0.995	0.995	-6.3	1.33	0.991	-3.49E+08	1.36E-05	
5B	-1.23	0.18	-20.25	1.84	0.994	0.994	-21.9	2.02	0.999	-4.44E+08	1.73E-05	

Chapter 3

5P	-1.2	0.18	-4.81	1.33	0.998	-6.6	1.43	0.997	-3.29E+08	1.28E-05
5U	-1.17	0.18	13.23	1	0.999	-1.9	1.3	0.986	-3.92E+08	1.53E-05
E1	-1.4	0.18	-29.56	0.95	0.997	-28.7	0.9	0.995	7.71E+07	-3.00E-06
E2	-1.45	0.18	16.48	0.82	0.994	7.8	0.88	0.989	6.86E+07	-2.67E-06
E3	-1.49	0.18	32.99	0.96	0.995	31	0.94	0.993	5.55E+07	-2.16E-06
6S	-1.51	0.27	8.22	1.49	0.995	2.4	1.67	0.995	-1.10E+08	4.28E-06
6C	-1.42	0.27	-5.88	1.52	0.999	-5.9	1.58	0.999	-3.88E+08	1.51E-05
6B	-1.39	0.27	-11.38	1.73	0.996	-10.5	1.76	0.992	-5.11E+08	1.99E-05
6P	-1.35	0.27	-5.52	1.67	0.995	-7.7	1.79	0.99	-4.43E+08	1.73E-05
6U	-1.32	0.27	34.24	1.54	0.972	15.7	1.88	0.984	-2.77E+08	1.08E-05
7S	-1.74	0.42	6.41	1.19	0.994	9.8	1.18	0.997	-1.05E+08	4.09E-06
7C	-1.67	0.42	-20.13	1.74	0.998	-22.4	1.94	0.999	-3.80E+08	1.48E-05
7B	-1.63	0.42	-27.13	2.36	0.997	-29.6	2.43	0.967	-5.21E+08	2.03E-05
7P	-1.6	0.42	-7.9	2.33	0.998	-13.3	2.75	0.994	-5.42E+08	2.11E-05
7U	-1.58	0.42	3.3	1.13	0.993	3.2	1.25	0.993	-3.81E+08	1.48E-05
8S	-2.03	0.65	17.49	0.98	0.996	4.9	1.17	0.998	-1.61E+08	6.25E-06
8C	-2	0.65	21	1.76	<4 points	7.9	2.08	0.997	-5.21E+08	2.03E-05
8P	-1.93	0.65	-3.76	1.67	0.995	-4.6	1.73	0.991	-2.19E+08	8.53E-06
8U	-1.84	0.65	6.36	1.07	0.994	17.3	0.96	0.999	-1.05E+07	4.10E-07
9S	-2.4	0.99	27.24	1.18	0.986	15.3	1.33	0.992	-1.74E+07	6.76E-07
9C	-2.38	0.99	43.24	1.2	0.98	21.8	1.41	0.981	-2.75E+07	1.07E-06
9B	-2.36	0.99	37.97	0.96	0.998	48.5	0.9	0.999	-2.23E+07	8.69E-07
9P	-2.35	0.99	21.49	1.04	0.993	12.1	1.14	0.996	-2.38E+07	9.29E-07
9U	-2.25	0.99	47	0.87	0.995	45.4	0.89	0.992	-1.86E+07	7.23E-07
UB	-0.91	-0.33	16.81	1.13	0.991	no pressure data				
UD	-0.96	-0.33	31	1.08	0.997					
UU	-0.85	-0.33	25	0.9	0.997					

Chapter 3

Table 3.4 Friction Velocity Comparison with and without Gressure Gradient $t/c=3.3\%$

profile	t/c=3.3%		Yshift	Utao1 W/O		R^2	Yshift	Utao2 with		R^2	C2	k
	Z/Ca	x/Ca		Pressure				Pressure				
1D	-0.96	0.01	-9.52	1.02		1	-12	1.06		1	-2.55E+07	9.95E-07
1B	-0.85	0.01	86	0.88		1	85	0.9		1	-9.78E+06	3.81E-07
1U	-0.76	0.01	26.47	0.88		0.992	17	0.95		0.997	9.27E+06	-3.61E-07
2S	-1.02	0.04	37	1		0.98	18.9	1.19		0.992	-4.85E+07	1.89E-06
2C	-0.97	0.04	5.31	1.15		0.996	0.7	1.23		0.999	-2.67E+07	1.04E-06
2P	-0.92	0.04	-20.77	1.06		0.99	-28.4	1.19		1	-1.61E+07	6.27E-07
2U	-0.87	0.04	7.3	0.91		0.99	-1	1		0.996	-1.43E+07	5.55E-07
3S	-1.15	0.09	79.44	1.02		0.996	56.1	1.18		0.999	-4.74E+07	1.85E-06
3C	-1.1	0.09	15	1.11		0.992	5	1.26		0.998	-7.93E+07	3.09E-06
3B	-1.07	0.09	-51.28	1.05		0.998	-49.3	1.01		0.998	-5.97E+07	2.32E-06
3P	-1.03	0.09	26.94	0.86		0.994	38.9	0.8		0.999	-4.95E+07	1.93E-06
3U	-0.96	0.09	47.99	0.79		0.999	55	0.77		1	-1.55E+07	6.05E-07
4S	-1.22	0.12	26.24	1.04		0.999	25.3	1.07		0.999	-4.96E+07	1.93E-06
4C	-1.16	0.12	40.23	1.25		0.995	40.5	1.28		0.996	-8.23E+07	3.20E-06
4B	-1.12	0.12	-25.14	1.05		0.994	-25.3	1.06		0.993	-3.55E+07	1.38E-06
4P	-1.1	0.12	21.88	0.94		0.997	16.1	1.03		0.998	-9.53E+07	3.71E-06
4U	-1.03	0.12	27.73	0.87		0.995	33.2	0.84		0.996	-3.81E+07	1.48E-06
5S	-1.35	0.18	15.47	1.31		1	18	1.29		1	-4.14E+07	1.61E-06
5C	-1.3	0.18	18.23	1.14		0.999	19.4	1.16		1	-1.20E+08	4.67E-06
5B	-1.26	0.18	20.23	1.4		0.997	17.4	1.48		0.999	-1.59E+08	6.20E-06
5P	-1.22	0.18	2	1.04		0.997	-6.2	1.21		1	-1.76E+08	6.86E-06
5U	-1.15	0.18	0.73	0.97		1	-0.6	1.02		1	-8.05E+07	3.13E-06

Chapter 3

E1	-1.4	0.18	19	1.07	0.99	9.1	1.18	0.998	5.69E+06	-2.21E-07
E2	-1.45	0.18	23	1.11	0.975	10.7	1.25	0.989	8.65E+06	-3.37E-07
6S	-1.51	0.27	14.47	1.4	0.993	7.1	1.57	0.995	9.13E+05	-3.56E-08
6C	-1.42	0.27	-2.5	1.16	0.993	5.5	1.66	0.994	-3.00E+08	1.17E-05
6B	-1.39	0.27	8.44	1.35	0.992	0.9	1.57	1	-3.20E+08	1.25E-05
6P	-1.35	0.27	30	1.1	0.996	25.8	1.24	0.998	-2.62E+08	1.02E-05
6U	-1.28	0.27	28.5	0.94	0.999	24.2	1.02	0.998	-1.09E+08	4.24E-06
7S	-1.74	0.42	2.5	1.66	0.998	1	1.74	0.998	-2.15E+08	8.37E-06
7C	-1.71	0.42	17.73	1.92	0.995	11.4	2.13	1	-3.47E+08	1.35E-05
7B	-1.67	0.42	-34.77	1.56	0.997	-53.4	1.91	0.994	-5.54E+08	2.16E-05
7P	-1.61	0.42	31.75	1.53	0.991	19.6	1.83	0.996	-4.71E+08	1.83E-05
7U	-1.52	0.42	85.47	1.08	0.992	55.6	1.35	0.997	-2.01E+08	7.81E-06
X1	-1.85	0.42	35	1.7	0.988	24.1	1.87	0.994	-3.38E+07	1.32E-06
X4	-1.91	0.42	-6.2	1.8	0.974	5.3	1.62	1	3.51E+07	-1.37E-06
X2	-1.94	0.42	24.5	1.51	0.983	15.8	1.63	0.98	6.13E+07	-2.39E-06
X3	-1.99	0.42	12.48	1.04	0.995	31.6	0.81	0.999	9.49E+07	-3.70E-06
X5	-2.04	0.42	8.86	0.77	0.989	9.5	0.66	0.995	1.43E+08	-5.59E-06
8S	-2.07	0.65	11.48	1.15	0.989	6.3	1.26	0.989	-1.02E+08	3.96E-06
8C	-2.01	0.65	-9.28	1.18	0.996	-7.8	1.22	0.999	-1.85E+08	7.22E-06
8B	-1.97	0.65	24.49	1.13	0.999	13.2	1.32	1	-2.36E+08	9.21E-06
8P	-1.93	0.65	8.99	0.96	0.999	3.3	1.09	0.998	-2.00E+08	7.80E-06
9S	-2.4	0.99	13.81	0.8	0.997	11.5	0.82	0.997	-1.05E+07	4.08E-07
9C	-2.38	0.99	5.6	0.93	0.987	7	0.9	0.997	-6.31E+06	2.46E-07
9B	-2.36	0.99	29.61	0.7	0.981	53.1	0.59	0.99	-2.53E+06	9.87E-08
9P	-2.35	0.99	47	0.87	0.995	15.7	0.92	0.995	-2.08E+06	8.10E-08
UU	-0.85	-0.33	16.48	1.06	0.998	no pressure data				
UD	-0.96	-0.33	20.23	0.95	0.998					

Chapter 3

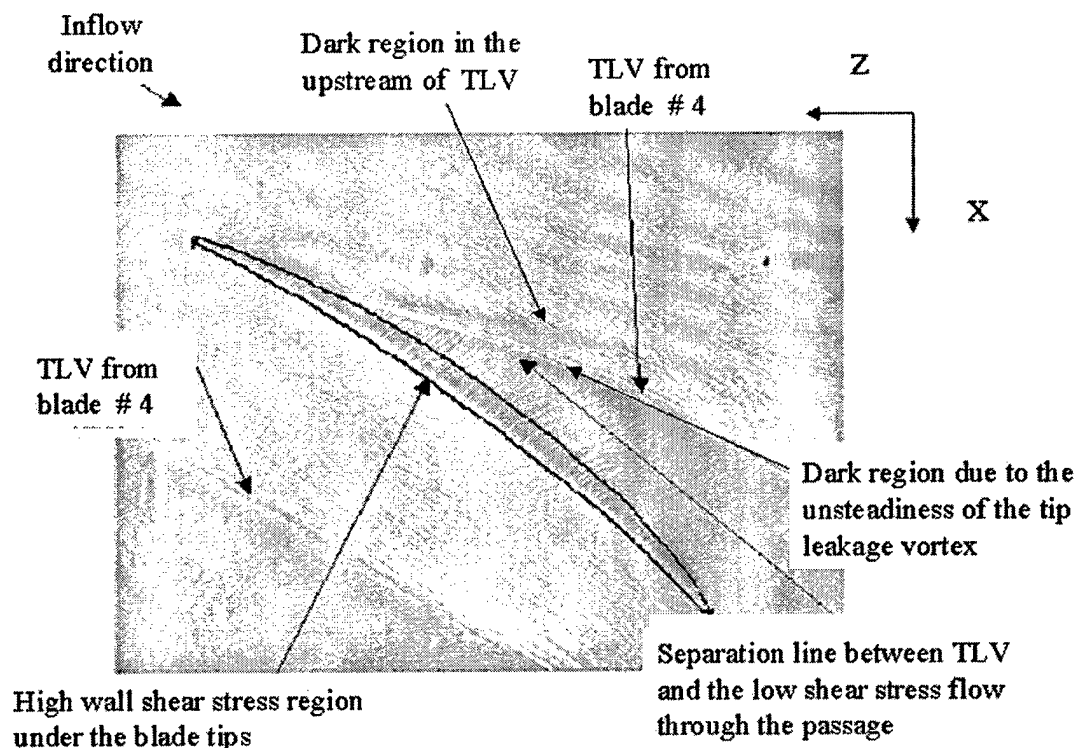


Figure 3.1 Oil flow visualization on the end-wall in the bed coordinates (Muthanna, 2002, $t/c=1.65\%$)

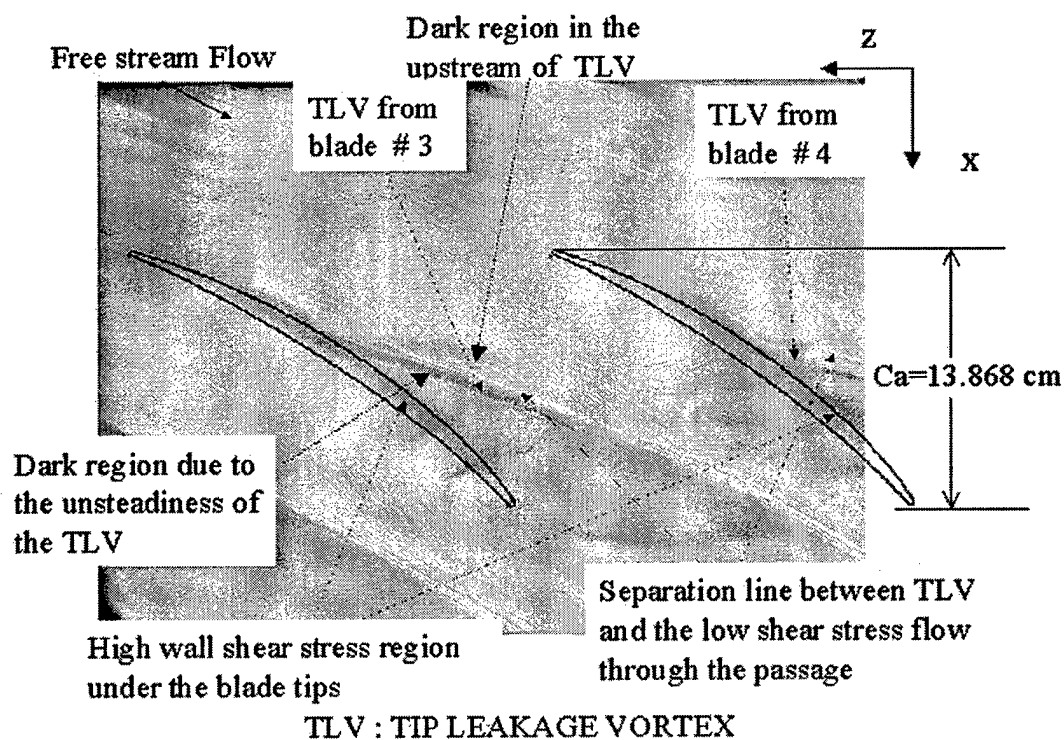


Figure 3.2 Oil flow visualization on the end-wall in the bed coordinates ($t/c=3.3\%$)

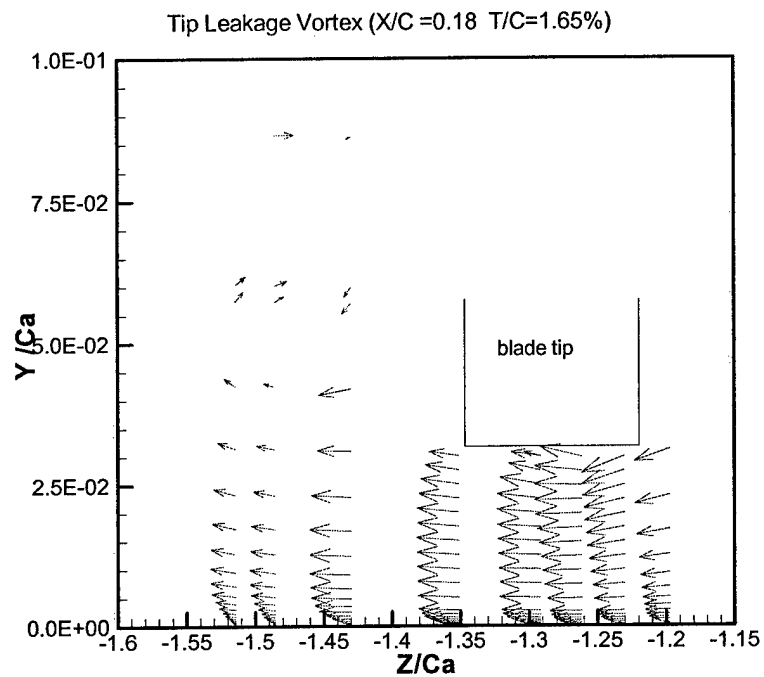


Figure 3.3 Mean velocity flow field in the tip gap and tip leakage vortex ($t/c = 1.65\%$) in the separation coordinates

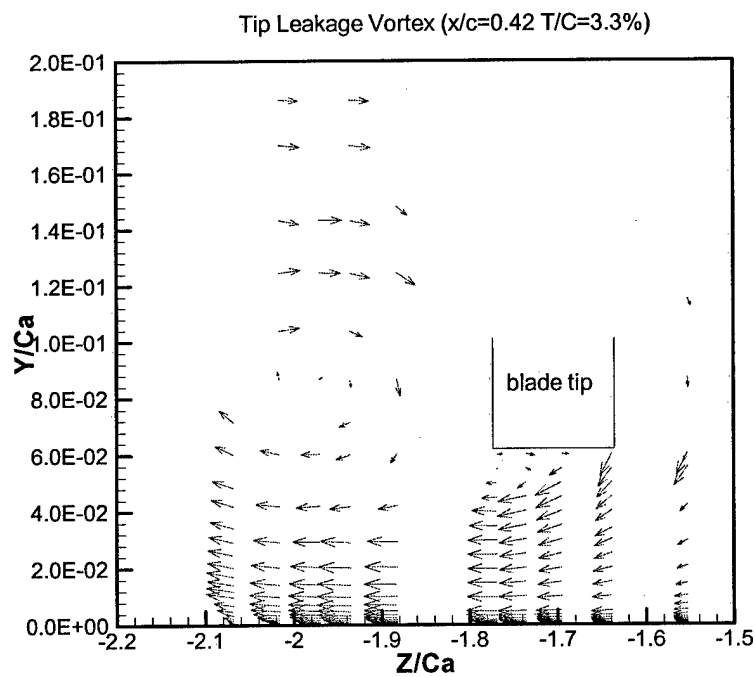
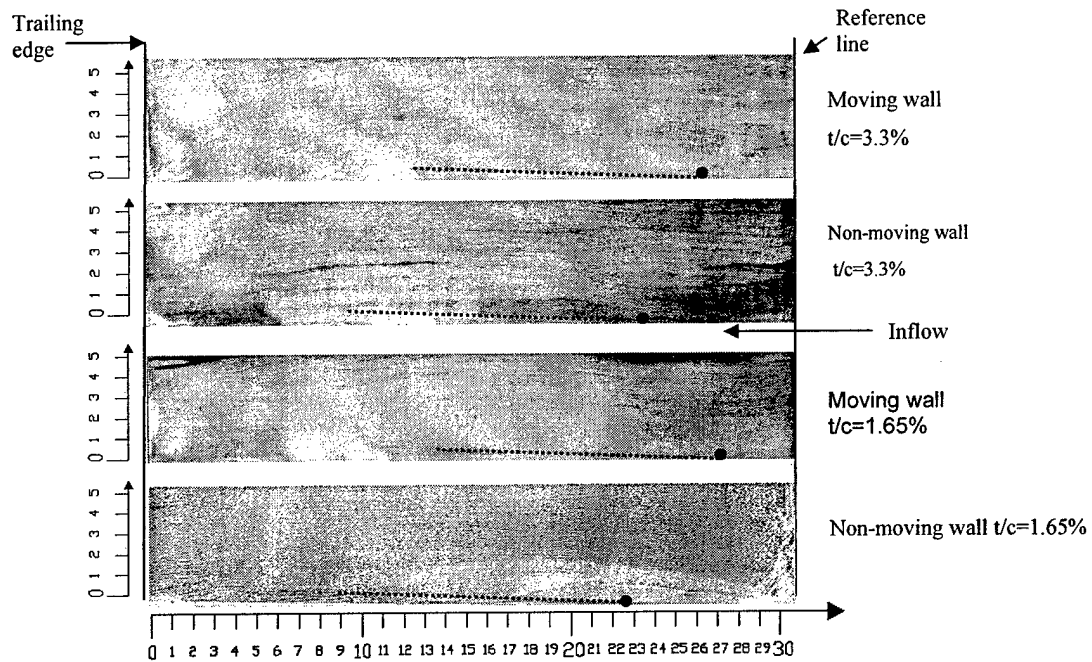


Figure 3.4 Mean velocity flow field in the tip gap and tip leakage vortex ($t/c = 3.3\%$) in the separation coordinates

Chapter 3



● represents the initial position of the reattachment on the blade surface

Figure 3.5 Oil flow visualization on the blade surface

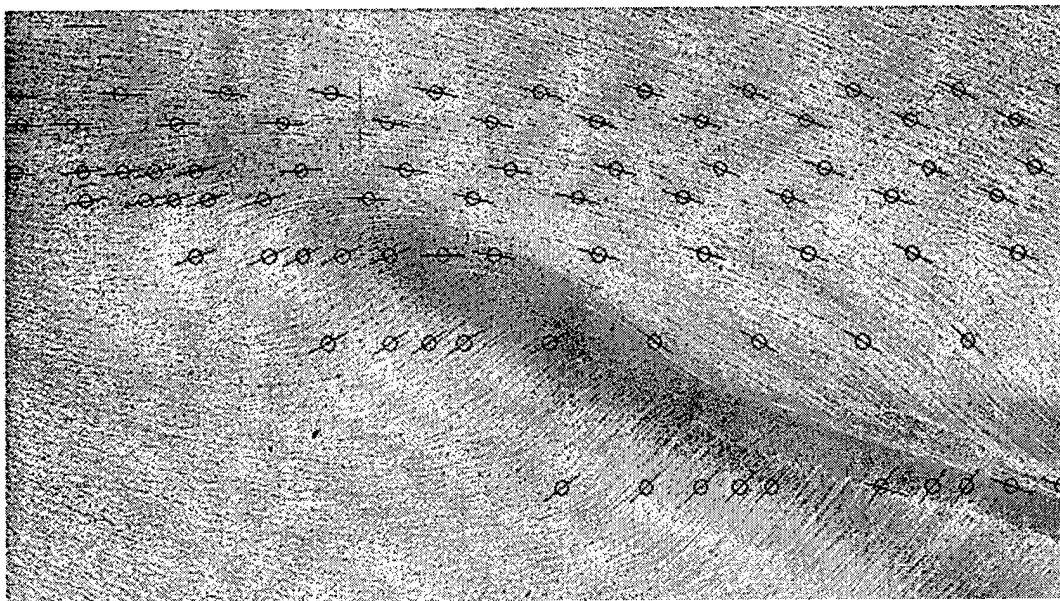


Figure 3.6 Oil flow streaks in the wall shear stress direction measurement using digitized oil flow pictures

Chapter 3

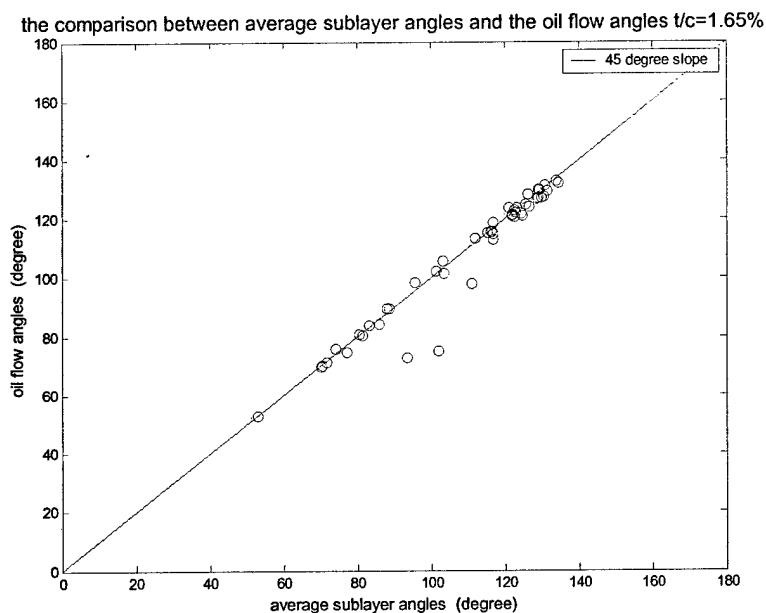


Figure 3.7 The comparison between the average sublayer flow angles and the wall shear stress angles relative to the x-axis in the bed coordinates $t/c=1.65\%$

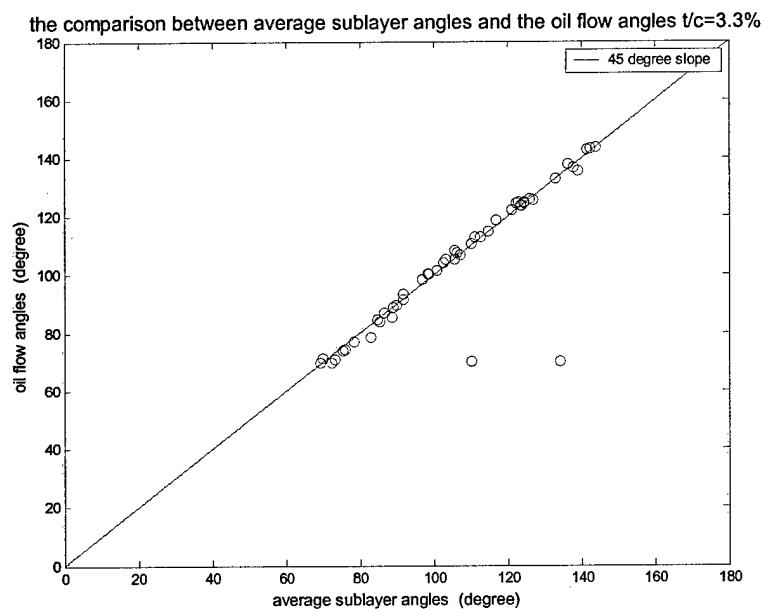


Figure 3.8 The comparison between the average sublayer flow angles and the wall shear stress angles relative to the x-axis in the bed coordinates $t/c=3.3\%$

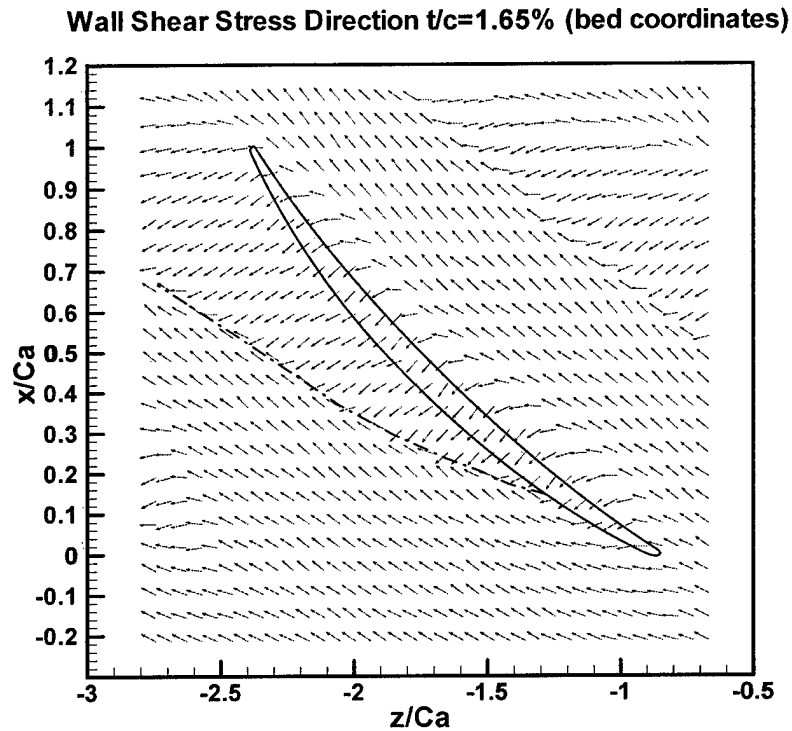


Figure 3.9 Wall shear stress direction $t/c=1.65\%$ (measured from the digitized oil flow pictures)

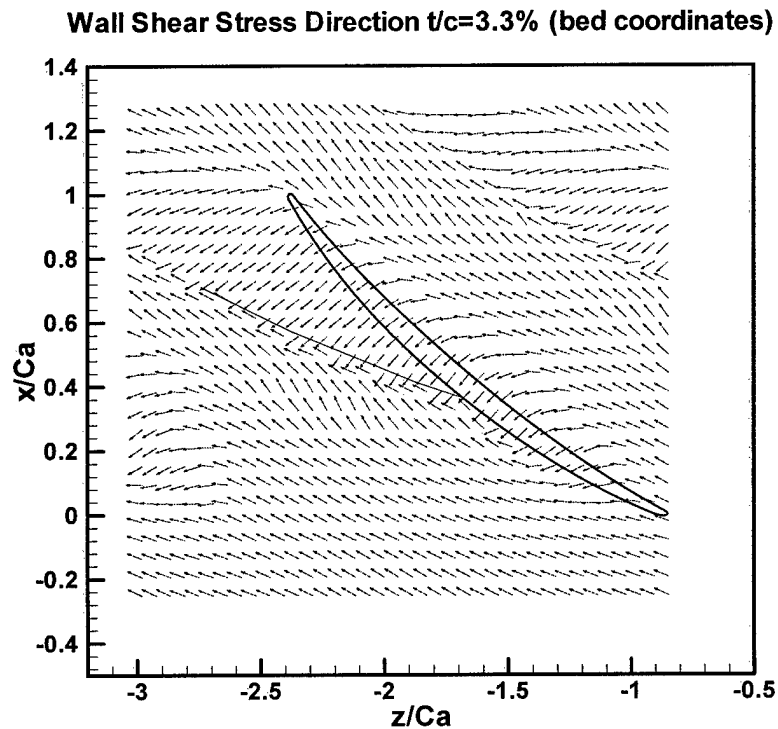


Figure 3.10 Wall shear stress direction $t/c=3.3\%$ (measured from the digitized oil flow pictures)

Chapter 3

flow angles (oil-flow and LDV) across the passage on the spanwise ($t/c=1.65\%$)

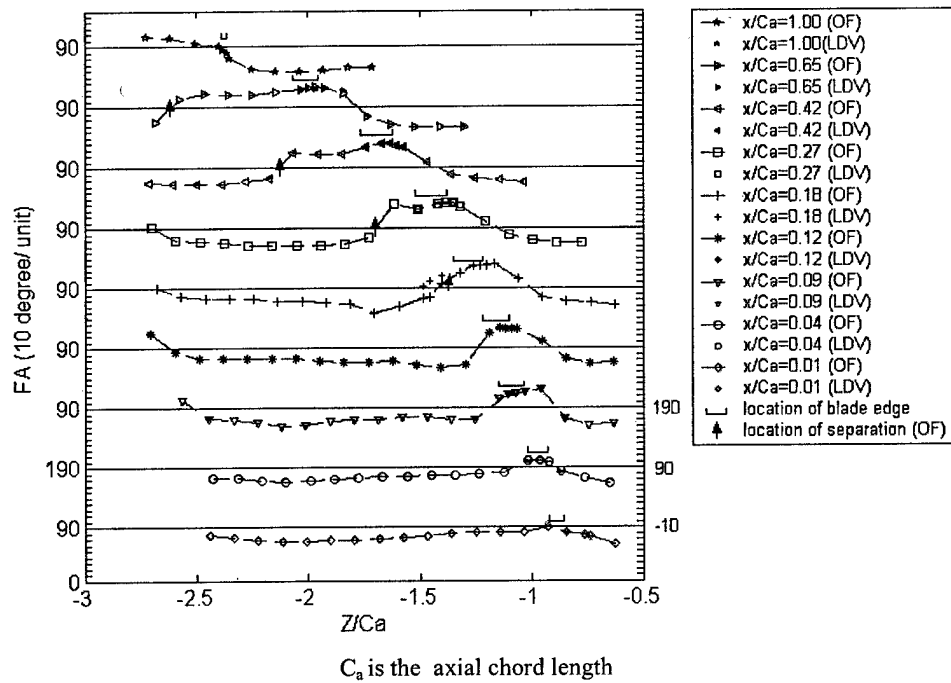


Figure 3.11 Wall shear stress angles relative to the x-axis in the bed coordinates changing along pitchwise $t/c=1.65\%$ (measured from the digitized oil flow pictures)

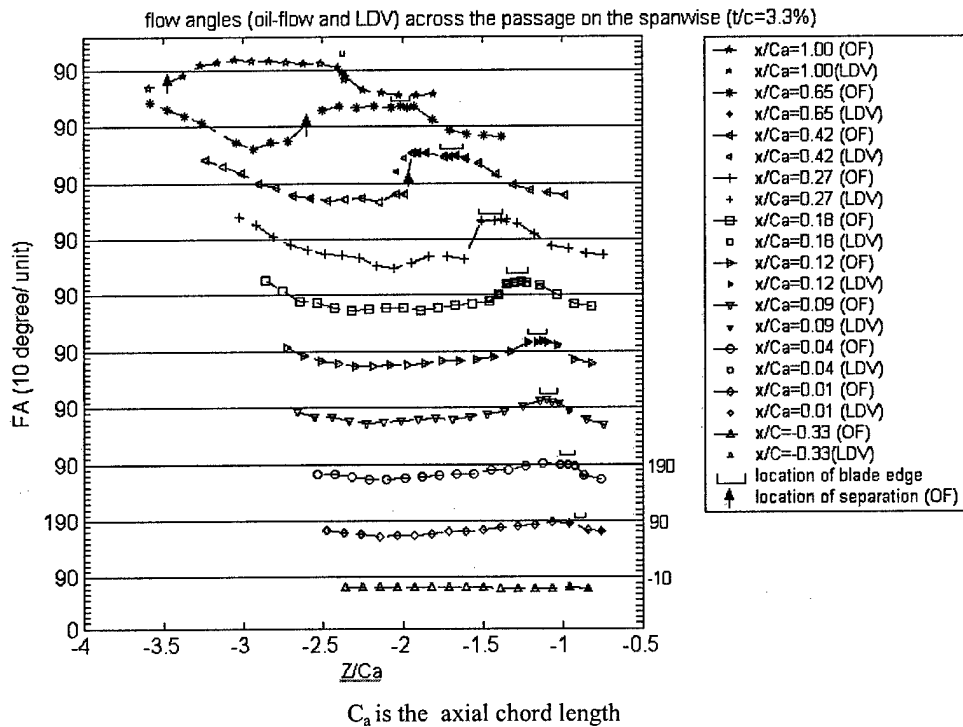


Figure 3.12 Wall shear stress angles relative to the x-axis in the bed coordinates changing along pitchwise $t/c=3.3\%$ (measured from the digitized oil flow pictures)

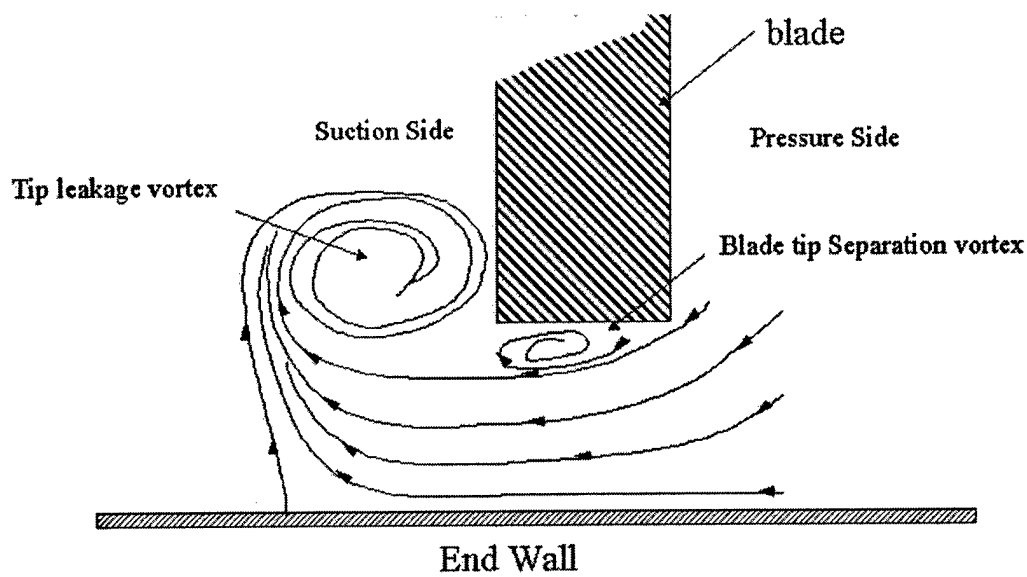


Figure 3.13 Flow structure in the Linear Cascade Tunnel based on the oil flow visualization and mean LDV velocity data

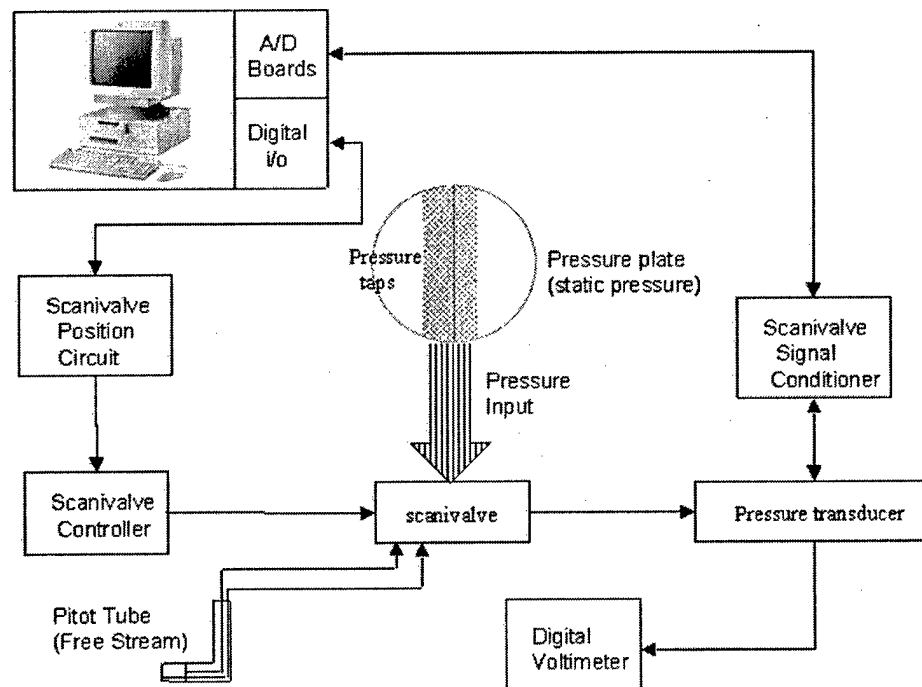


Figure 3.14 A schematic of ADAS (automated data acquisition system)

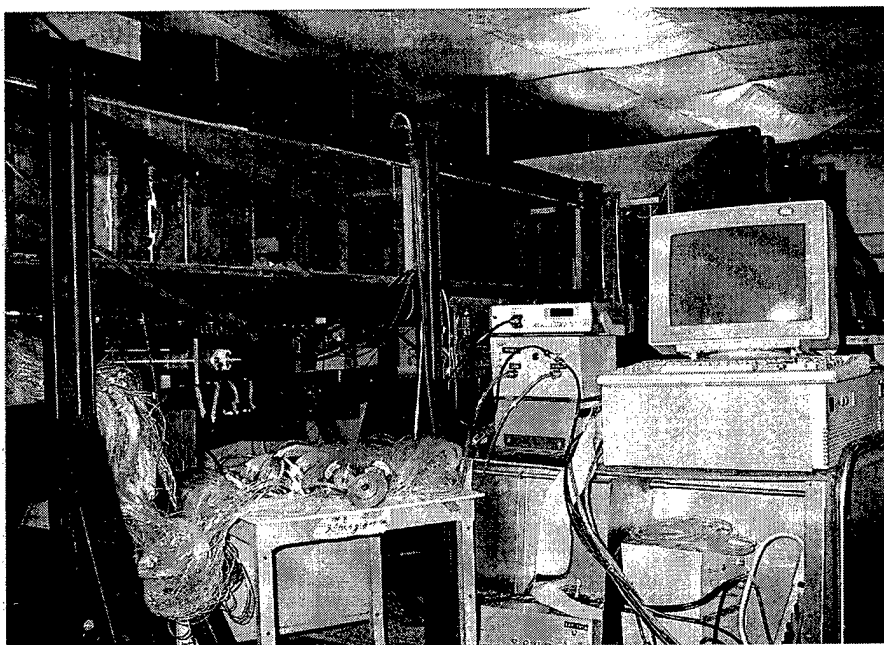


Figure 3.15 A picture of ADAS (automated data acquisition system)

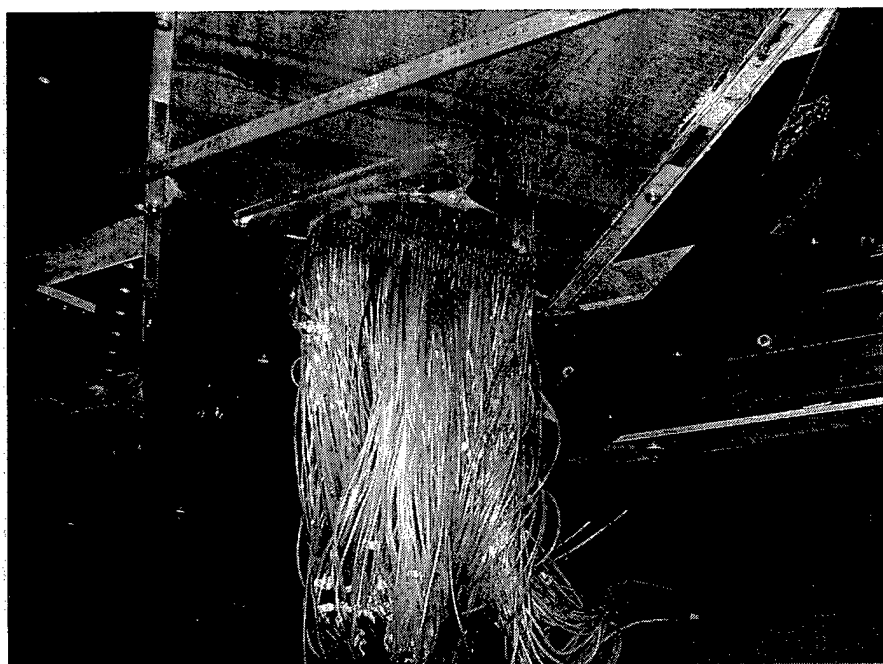


Figure 3.16 Pressure plate with pressure taps

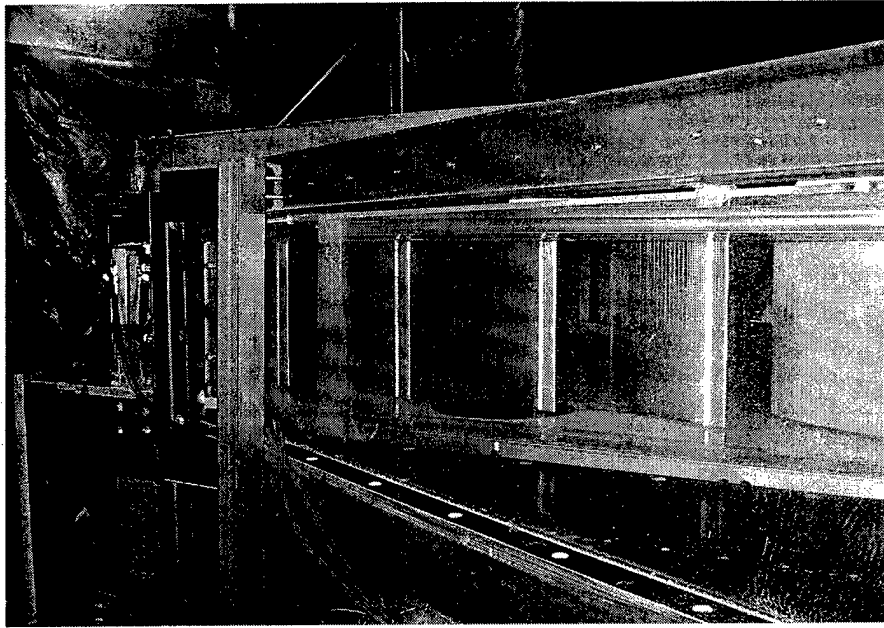


Figure 3.17 Pressure plate underneath the blades

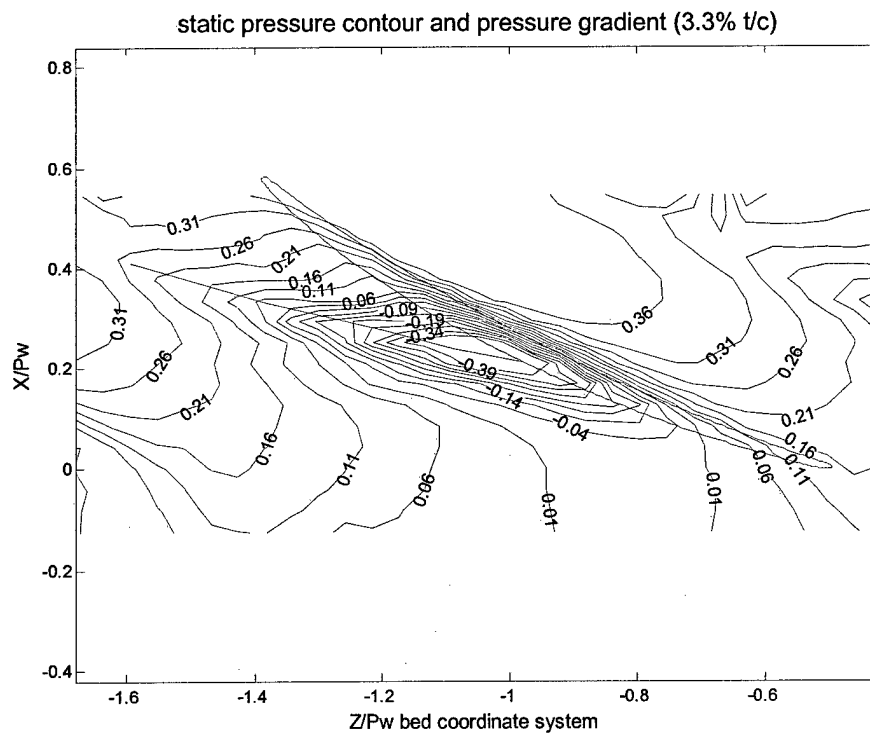


Figure 3.18 Contours of static pressure coefficient measured on the end-wall $t/c = 3.3\%$

The solid line is corrected separation line from the oil flow measurement

Chapter 3

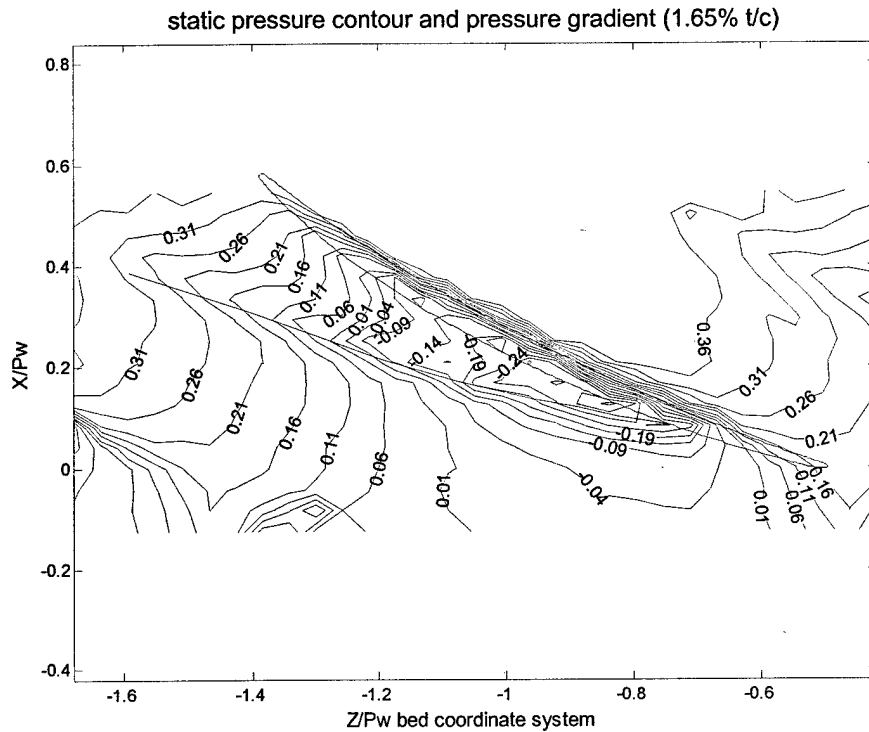


Figure 3.19 Contours of static pressure coefficient measured on the end-wall $t/c=1.65\%$

The solid line is corrected separation line from the oil flow measurement

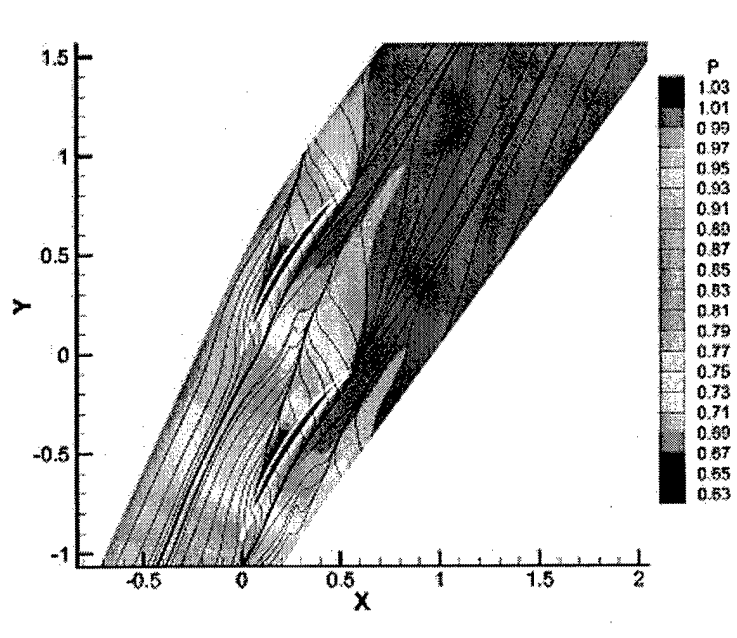


Figure 3.20 Contours of static pressure on the end-wall $t/c=1.65\%$ (from Sangmook Shin)

Chapter 3

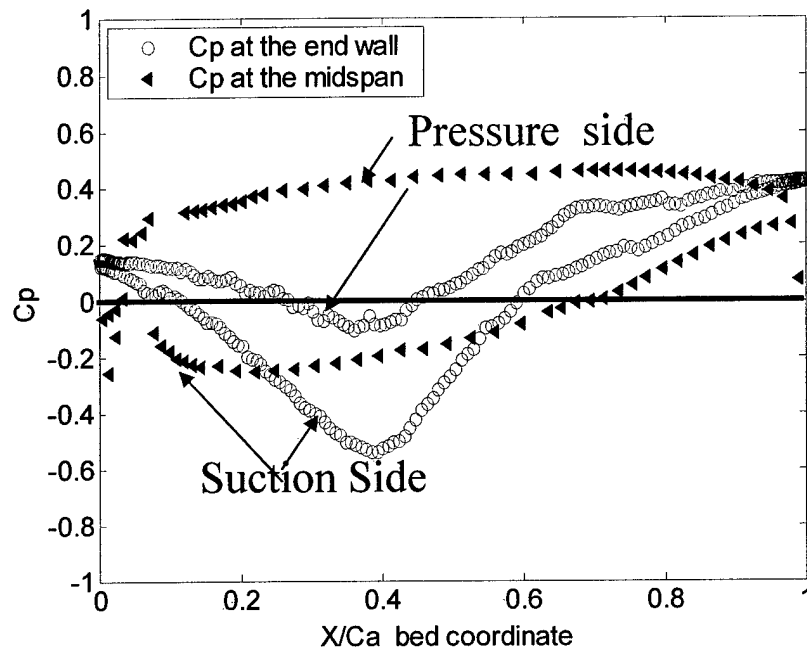


Figure 3.21 Static pressure comparison on the end-wall and on the mid span of the blade $t/c=3.3\%$ at blade contour locations

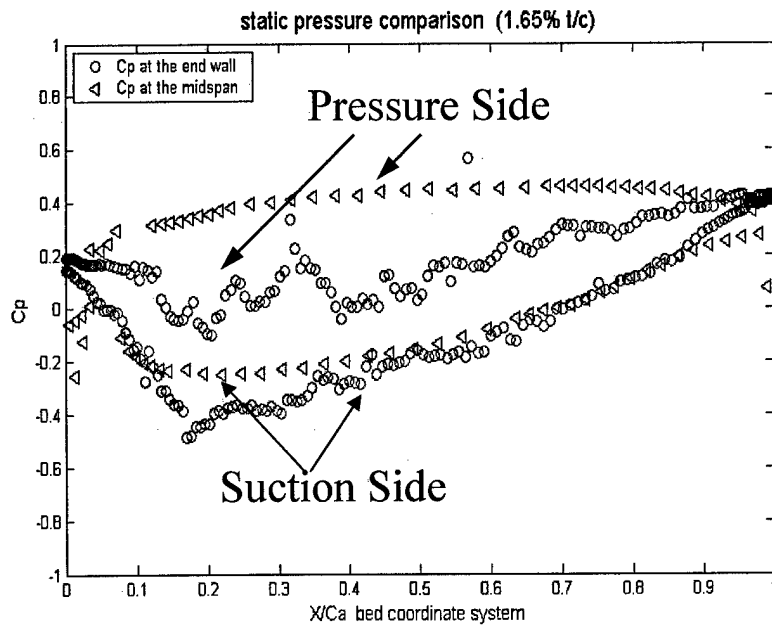


Figure 3.22 Static pressure comparison on the end-wall and on the mid span of the blade $t/c=1.65\%$ at blade contour locations

Chapter 3

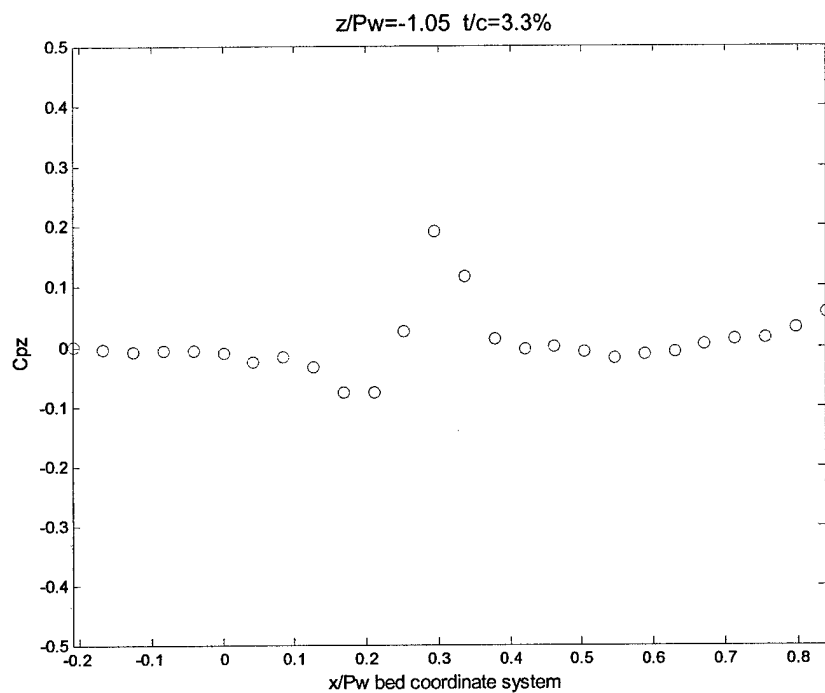


Figure 3.23 Pressure gradient C_{pz} plot at $z/P_w = -1.05 \quad t/c = 3.3\%$ in the bed coordinates

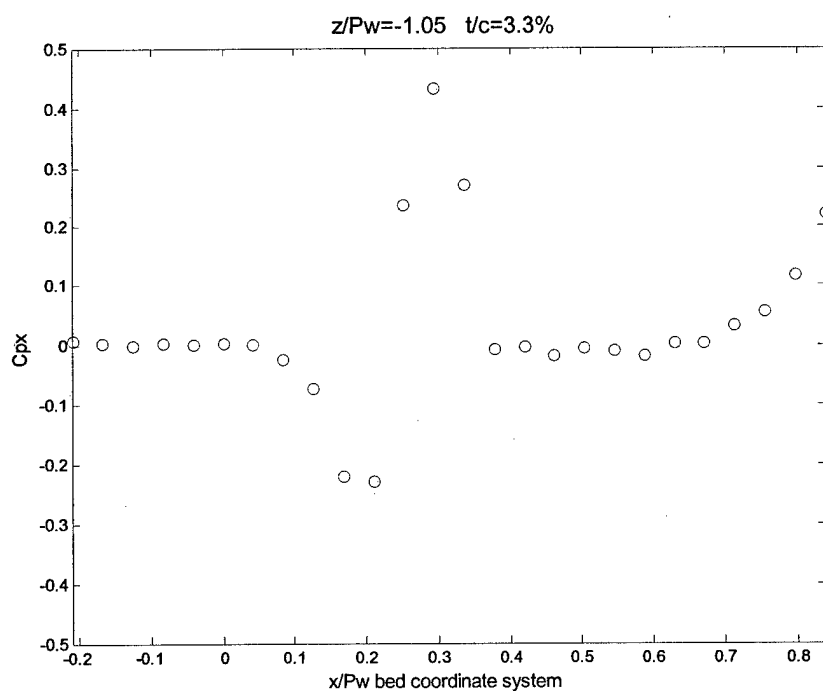


Figure 3.24 Pressure gradient C_{px} plot at $z/P_w = -1.05 \quad t/c = 3.3\%$ in the bed coordinates

Chapter 3

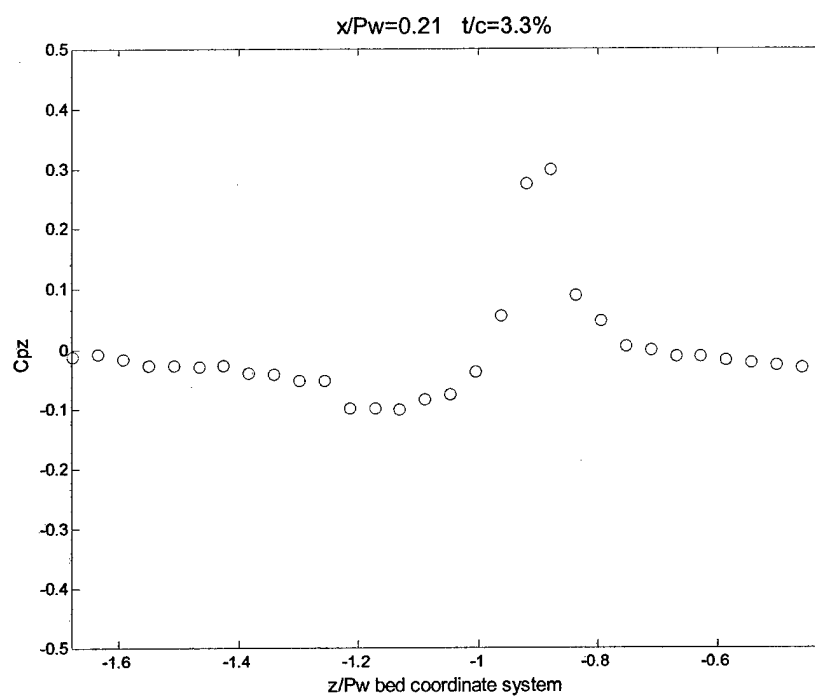


Figure 3.25 Pressure gradient C_{pz} plot at $x/P_w=0.21 \quad t/c=3.3\%$ in the bed coordinates

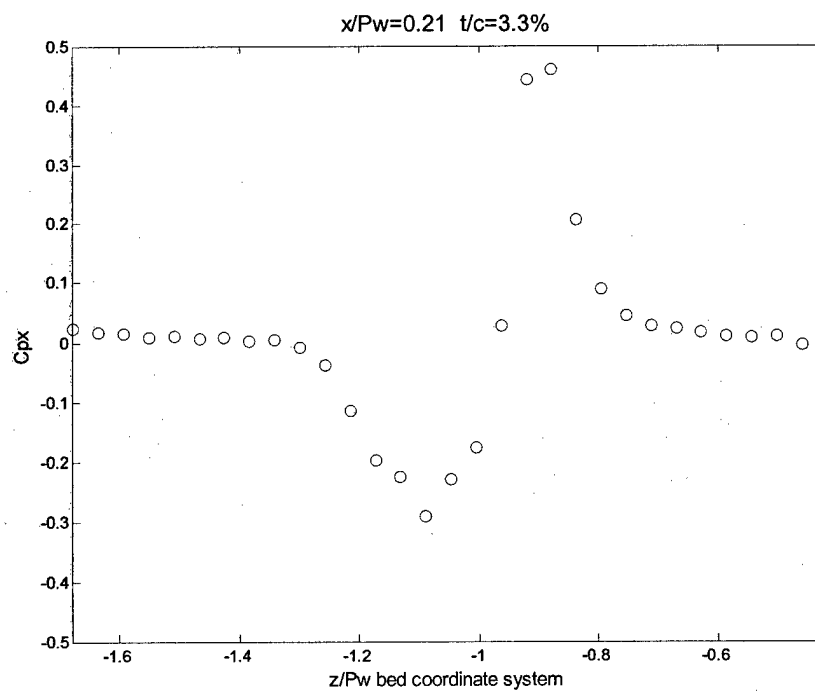


Figure 3.26 Pressure gradient C_{px} plot at $x/P_w=0.21 \quad t/c=3.3\%$ in the bed coordinates

Chapter 3

Friction Velocity Calculation With and Without Pressure Gradient ($t/c=1.65\%$)

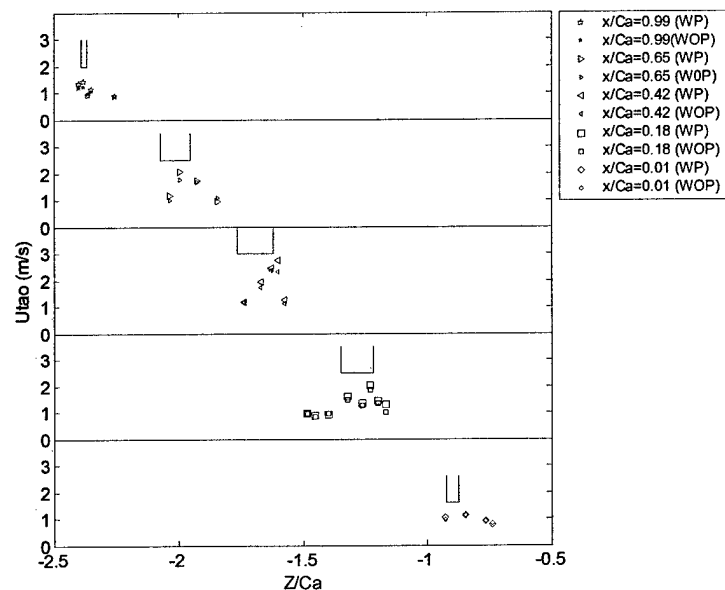


Figure 3.27 Skin friction velocity (in Table 4) comparison with and without pressure gradient $t/c=1.65\%$

Friction Velocity Calculation With and Without Pressure Gradient ($t/c=3.3\%$)

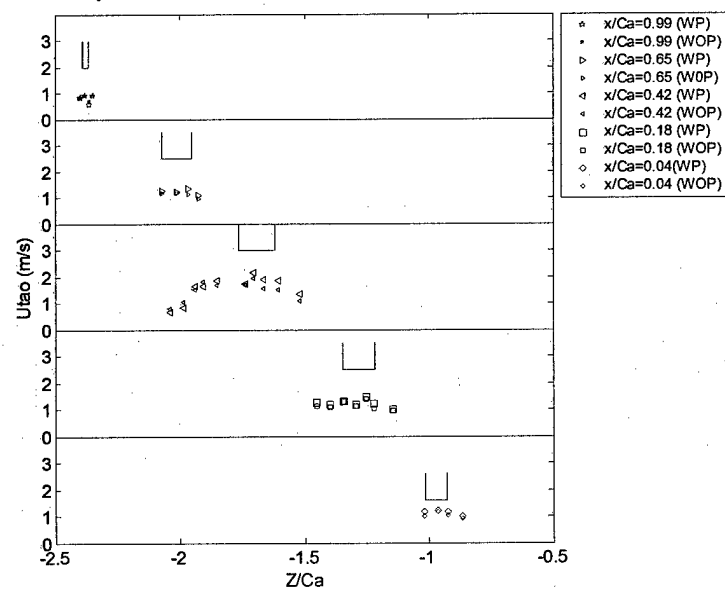


Figure 3.28 Skin friction velocities (in Table 5) comparison with and without pressure gradient $t/c=3.3\%$

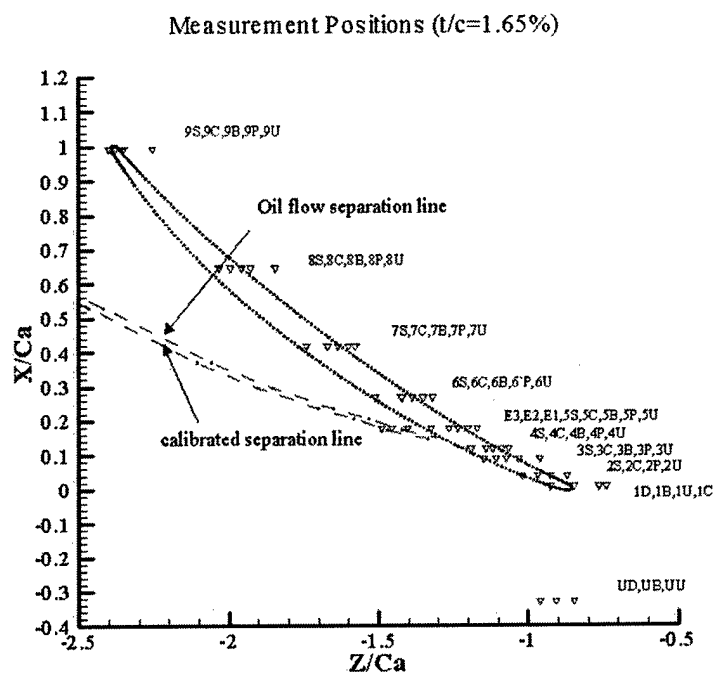


Figure 3.29 Measurement positions in the bed coordinate system $t/c=1.65\%$

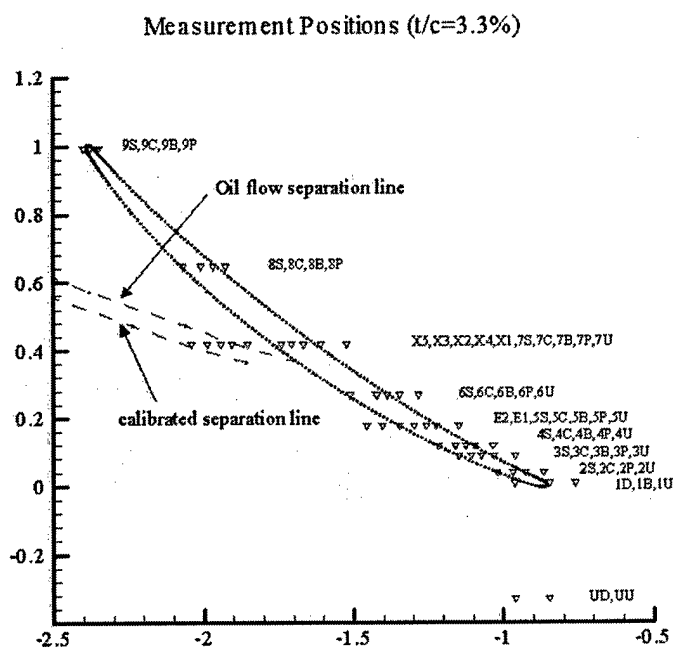


Figure 3.30 Measurement positions in the bed coordinate system $t/c=3.3\%$

4. OCTANT ANALYSIS

4.1 OBJECTIVE OF OCTANT ANALYSIS

With three-velocity-component laser Doppler velocimeter measurements, the instantaneous velocity can be measured and the statistical features of Reynolds stresses and triple products can be investigated from experiments. Here, a statistical technique named "octant analysis" is used to investigate the coherent structure of the turbulent boundary for the cascade flow. An octant analysis divides the instantaneous fluctuation velocities (u', v', w') into eight different events, which are based on the sign of the instantaneous fluctuation velocities, such as $u' > 0, v' < 0, w' > 0$ is associated with the sweep with positive w' in the turbulent boundary layer. From above classification, there are eight kinds of instantaneous motions in the turbulent boundary, based on the mean velocity. For each octant, the contribution to various quantities of a flow, such as the Reynolds stresses, and triple products can be computed. The contributions of octants to the total flow quantities are compared, and the dominant motions are determined. The intent of the octant analysis is to identify which octant plays an important role in the three-dimensional turbulent boundary layer, and which kind of coherent motion is more dominant. Since turbulence models which are developed in one particular flow should be

Chapter 4

only applied to the flow with the same coherent structure, and mean flow quantities can not give us enough information about this, octant analysis is one of the efficient statistical techniques by which much more information about coherent structures can be obtained. By comparing each octant's contribution, minor events can be eliminated and more dominant events can be discussed and considered in turbulence models. This may help simplify the turbulence modeling and develop more robust turbulence model.

In this chapter, first, in section 4.2, we are going to review of the development of the coherent structures, from the historical point of view. Section 4.3 gives the definition of the octants. Section 4.4 and 4.6 discuss the skewed mean flow. Section 4.5 includes the choice of coordinate systems. Flow and data quality in the upstream inflow to a blade are discussed in chapter 2 and compared with the two-dimensional turbulent boundary layer behavior. The section 4.7 talks about the conditional averaging. Then, in section 4.8, octant analysis is applied to the LDV data taken in the cascade tunnel with $t/c=3.3\%$ clearance with and without the moving wall, and octant contributions to the Reynolds stress and triple products under the blade tip are discussed. In section 4.9, the structural models will be constructed through a review of recent three-dimensional turbulent boundary layer structural experiments and the common elements of two-dimensional turbulent boundary layer structural experiments.

4.2 OVERVIEW OF COHERENT STRUCTURES AND MODELS FOR TURBULENT BOUNDARY LAYERS

Chapter 4

Coherent motion is a three-dimensional flow over which at least one fundamental flow variable (velocity component, density, temperature, etc.) exhibits significant correlation with itself or with another variable, over a range of space and/ or time that is significantly larger than the smallest local scales of the flow (Robinson, 1990). The term “coherent structure” is used interchangeably with turbulence structure. Coherent or eddy structure is the central dynamic element in the turbulent boundary and is directly associated with the production of the turbulent shear stress, dissipation of turbulent energy, and pressure fluctuations. In the past few decades, the study of turbulent structure was accumulated, but developed very slowly, due to the limitation of experimental technology and complicated turbulent motions. In the 1970s, the earliest experimental technology for studying turbulent structure, flow visualization (dye, smoke, and bubbles), was developed and provided much valuable information such as low speed streaks, ejections, sweeps, etc. However flow visualization can not give us quantitative results, and is limited only to low Reynolds number flow. In the 1970s and 1980s, the hot-wire anemometer played a major role in the study of turbulent coherent motion. Conditional-sampling methods were employed in the turbulent boundary layer studies, which provided the quantitative results, but the hot-wire anemometer has a poor performance in the viscous sublayer. The present work for this chapter used laser Doppler velocimeter data to investigate the coherent structure in the near-wall region.

Willmarth and Lu (1973) reported conditionally sampled measurements of the structure of the Reynolds stress at a single point very near a wall in the two-dimensional turbulent boundary layer. Willmarth and Lu first introduced a u', v' quadrant-splitting scheme, one of the statistical-analysis techniques. The results show that the ejection of

Chapter 4

low-momentum fluid ($u' < 0$ and $v' > 0$) from the wall is a dominant feature of the structure of the turbulent boundary, but sweeps ($u' > 0$ and $v' < 0$) did not show the same amount of contribution as ejections. Wallace et al.(1972) reported a larger contribution to turbulent shearing stress from the sweeps near the wall, in a channel flow. The reason for this discrepancy has not been determined.

Robinson (1990) described conceptual models for the structure of the two-dimensional zero pressure gradient turbulent boundary layer, which is a flat plate smooth wall boundary layer with a two-dimensional mean flow. A brief view of coherent motions is given here. Vortical structure in the flow field plays an important role in the coherent structure analysis. For low Reynolds-numbers, the near-wall (viscous sublayer layer and buffer layer) turbulence maintenance process is dominated by tilted quasi-streamwise vortices (QSV). The majority of the turbulence production in the entire boundary layer happens in the buffer region during intermittent violent outward ejections of low-speed fluid along one side of quasi-streamwise vortices and during sweeps of high-speed fluid at shallow angle toward the wall along the other side of quasi-streamwise vortices. This near-wall turbulence production process is considered to be an intermittent, quasi-cyclic sequence, usually referred to as a burst. In the outer region, three-dimensional bulges on the scale of the boundary layer thickness form in the turbulent/non-turbulent interface. Deep irrotational valleys occur on the edges of the bulges, through which free-stream fluid is entrained into the turbulent region. Arch-like vortices are found in the outer region, and the horseshoe shape is considered to be a useful model for the high log and wake region for the two-dimensional turbulent boundary layer case. Robinson and Kline (1990) grouped the various experimentally observed forms of coherent motions into eight

Chapter 4

classes. This unsorted classification is only one of several possibilities. It provides a useful framework for relating the various structural features; 1) low speed streaks in the viscous sublayer; 2) ejection of low speed fluid outward from the wall; 3) sweeps of high speed fluid inward toward the wall; 4) vortical structures of various forms (quasi-streamwise vortices and arch-like vortices); 5) sloping near-wall shear layers; 6) near-wall pocket; 7) large motions capped by three-dimensional bulges in the outer turbulent potential interface; 8) shear-layer "backs" of large scale out-region motions. The most causative coherent motion in the two-dimensional turbulent boundary layers may be characterised as either vortices or shear layers. According to Robinson (1990), the centers of QSVs can be found in the range $10 < y^+ < 250$ with the largest number of QSV centers found near $y^+ \sim 30$. For a two-dimensional turbulent boundary layer, the sublayer and buffer region are dominated by the bottoms of QSVs.

After some maturity in the study of the turbulent structure in two-dimensional turbulent boundary layer, there was some study of the turbulent structure for three-dimensional turbulent boundary layers. These studies assume that the structural detail of three-dimensional turbulent boundary layers does not differ significantly from that of two-dimensional turbulent boundary layers as reviewed by Robinson (1991). Anderson & Eaton (1989) suggest that spanwise flow reduces the strength of the quasi-streamwise vortices having the opposite sign of streamwise vortices to the mean spanwise flow, thus reduces the strong mixing that occurs between vortices of opposite signs. Littell & Eaton (1991) found that the crossflow inhibits strong sweeps from vortices having near-wall spanwise velocity in the same direction as the crossflow, while it inhibits strong ejections from vortices having spanwise velocity in the opposite direction.

Chapter 4

Sendstad and Moin (1991) performed the direct numerical simulation in a planar channel flow to investigate the effect of an impulsively started transverse pressure gradient on the turbulence structures. In agreement with experiments, the simulation shows a reduction in the Reynolds shear stress $u'v'$. It also shows a drop in the turbulent kinetic energy. These effects were found to be related to the break-up of the near-wall velocity streaks. The streamwise vortices are convected in the spanwise direction, breaking the original streak structures as they cross over them. It was also found that the vortices with the same sign as the developing mean streamwise vorticity were weakened. This physical explanation is consistent with those by the Simpson and Devenport (1990). Sendstad & Moin (1992) advanced four mechanisms by which the spanwise crossflow affects particle trajectories in the vortical structures, each important at different times, which serve to generate lower Reynolds stress and break up the near-wall streaks. They observed that QSV induced events do not penetrate as deeply into the wall layer. This discovery was corroborated by Flack and Johnston (1993). Flack and Johnston's (1993) flow visualization results further support the notion that the buffer layer is dominated by the bottoms of QSVs.

Fleming and Simpson (1994) found that the inner region flow of the three-dimensional turbulent boundary layers was more stable than that of the two-dimensional turbulent boundary layers; the three-dimensional turbulent boundary layers exhibited lower streak coalescence and division. They concluded that high speed sweeps do not penetrate as deeply into the near-wall region in three-dimensional turbulent boundary layers. Simpson and Devenport (1990) describe the physical model, upon which these interpretations were based; the mean flow obtains a third degree of spatial freedom and

Chapter 4

the displacement mechanism is no longer constrained to produce ejections with symmetric spanwise strength. The low-speed, near-wall fluid displaced in a sweep event develops a preference for spanwise motion under the influence of the spanwise pressure gradient. Thus, there is less fluid ejected upward, leading to lower Reynolds stresses.

Kang et al (1998) performed the experimental study on a shear driven 3-D turbulent boundary layers over a rotating disk in order to investigate the modification of the near-wall coherent structures in the three-dimensional turbulent layers. The result shows that asymmetries exist in the conditionally averaged velocity signals in the vicinity of strong ejections or sweeps. However, the quadrant analysis revealed that those asymmetries arose from the contribution of negative Reynolds-shear stress producing events which were not related to the Reynolds shear stress producing eddies. The near-wall vortical structures in the vicinity of strong ejection and sweep events were nearly symmetric in the spanwise direction.

Y.Nagano et al (1990) investigated the statistical characteristics of third-order moments (triple products) of velocity and scalar (Reynolds stresses) for the pipe flow from both experimental and theoretical points of view. On the basis of experiment data, they developed a structural turbulence model for triple products and Reynolds stresses. The results can be summarized as follows; 1) the triple products in the wall turbulence have a highly intermittent nature and are dominated almost completely by the coherent motions such as ejections and sweeps; 2) a very close similarity exists between the Reynolds shear stress \overline{uv} and a scalar flux $\overline{v\theta}$.

J.Jeong et al (1997) deduced the coherent structure near the wall in a numerically simulated turbulent channel flow using a conditional sampling scheme which extracts the

Chapter 4

entire extent of dominant vortical structure. The results shows that the vortical structure is correctly captured. The dominant near-wall educed coherent structure are highly elongated quasi-streamwise vortices; the coherent structures are inclined nine degrees in the vertical (x,y) plane and tilted 4 degrees in the horizontal (x,z) plane. There is no indication near the wall of hairpin vortices, not only in the educed data but also in the instantaneous fields.

The background for discussing the octant analysis has been established. The near-wall LDV measurements will be examined for clues about the dynamics of ejections, sweeps, and interactions.

4.3 OCTANT DEFINITIONS

Quadrant analysis is one of the statistical techniques chosen for two-dimensional turbulent boundary layers to capture the flow motion events. About thirty years ago, Lu and Willmarth (1973) applied quadrant analysis to the turbulent boundary layers in the u-v plane. Every instantaneous flow motion in the vertical (x, y) plane can be classified into one of the four quadrants in the u-v plane. Each quadrant is associated with one particular coherent motion, as follows;

Quadrant 1 ($u' > 0, v' > 0$) out-ward interaction

Quadrant 2 ($u' < 0, v' > 0$) out-ward ejection

Quadrant 3 ($u' < 0, v' < 0$) wall-ward interaction

Quadrant 4 ($u' > 0, v' < 0$) wall-ward sweep

Chapter 4

As mentioned above, "Octant Analysis" is an extension of the quadrant analysis to understand the coherent structure in the three-dimensional turbulent boundary layers. Each instantaneous flow motion can be classified into one of the eight octants in the u - v - w space, on the basis of the signs of the instantaneous velocity fluctuations. Each octant is associated with one particular coherent motion, as shown in table 4.1. Equations 4.2-4.16 demonstrate the results of breaking the Reynolds stress tensor and triple product into eight octants.

$$\overline{u'^2} = \sum_{i=1}^8 \beta_i (\overline{u'^2})_i \quad \overline{v'^2} = \sum_{i=1}^8 \beta_i (\overline{v'^2})_i \quad (4.2, 4.3)$$

$$\overline{w'^2} = \sum_{i=1}^8 \beta_i (\overline{w'^2})_i \quad \overline{u'v'} = \sum_{i=1}^8 \beta_i (\overline{u'v'})_i \quad (4.4, 4.5)$$

$$\overline{u'w'} = \sum_{i=1}^8 \beta_i (\overline{u'w'})_i \quad \overline{v'w'} = \sum_{i=1}^8 \beta_i (\overline{v'w'})_i \quad (4.6, 4.7)$$

$$\overline{u'^3} = \sum_{i=1}^8 \beta_i (\overline{u'^3})_i \quad \overline{v'^3} = \sum_{i=1}^8 \beta_i (\overline{v'^3})_i \quad (4.8, 4.9)$$

$$\overline{w'^3} = \sum_{i=1}^8 \beta_i (\overline{w'^3})_i \quad \overline{u'^2 v'} = \sum_{i=1}^8 \beta_i (\overline{u'^2 v'})_i \quad (4.10, 4.11)$$

$$\overline{u'^2 w'} = \sum_{i=1}^8 \beta_i (\overline{u'^2 w'})_i \quad \overline{v'^2 w'} = \sum_{i=1}^8 \beta_i (\overline{v'^2 w'})_i \quad (4.12, 4.13)$$

$$\overline{u'v'^2} = \sum_{i=1}^8 \beta_i (\overline{u'v'^2})_i \quad \overline{u'w'^2} = \sum_{i=1}^8 \beta_i (\overline{u'w'^2})_i \quad (4.14, 4.15)$$

$$\overline{v'w'^2} = \sum_{i=1}^8 \beta_i (\overline{v'w'^2})_i \quad \overline{u'v'w'} = \sum_{i=1}^8 \beta_i (\overline{u'v'w'})_i \quad (4.15, 4.16)$$

where

Reynolds normal stress corresponding to i th octant: $(\overline{u'^2})_i = \frac{\sum_{j=1}^N (u_j - U)^2}{N}$

Chapter 4

Reynolds shear stress corresponding to ith octant:
$$(\overline{u'v'})_i = \frac{\sum_{j=1}^N (u_j - U)(v_j - V)}{N}$$

Triple product corresponding to ith octant:
$$(\overline{u'^3})_i = \frac{\sum_{j=1}^N (u_j - U)^3}{N}$$

$$(\overline{u'^2v'})_i = \frac{\sum_{j=1}^N (u_j - U)(v_j - V)^2}{N}$$

i – the ith octant;

N- total number of valid samples in the corresponding octant;

u_j, v_j - instantaneous velocities of the jth valid sample in the corresponding octant;

U, V, W - the mean velocity based on the total samples.

The β_i is the weighted population percentage for the ith octant. The β_i would simply be defined as the number of events in "octant i" divided by the total number of events for all eight octants.

Table 4.1 presents the definition of each octant, which is the same definition as used by Madden (1997). The octants are also identified using names assigned by Madden as shown in figure 4.1. Figure 4.2 is a conceptual drawing of coherent motions, which represent the fluid motion for each octant. The first octant, where $u' > 0, v' > 0, w' > 0$, contains motions associated with interactions of high speed fluids away from the end wall with positive w' ; the second octant where $u' < 0, v' > 0, w' > 0$, contains outward ejection motions of low speed fluid with positive w' ; the third octant, where $u' < 0, v' < 0, w' > 0$, contains motions associated with wall-ward interactions of low speed fluids with positive w' ; the forth octant, where $u' > 0, v' < 0, w' > 0$, contains motions associated with wall-ward sweep of high speed fluids with positive w' ; The fifth octant, where $u' > 0, v' > 0, w' < 0$,

Chapter 4

contains motions associated with interactions of high speed fluids away from the wall with negative w' ; the sixth octant where $u' < 0, v' > 0, w' < 0$, contains outward ejection motions of low speed fluid with negative w' ; the seventh octant, where $u' < 0, v' < 0, w' < 0$, contains motions associated with wall-ward interactions of low speed fluids with negative w' ; and the eighth octant, where $u' > 0, v' < 0, w' < 0$, contains motions associated with wall-ward sweep of high speed fluids with negative w' . Bear in mind, that here out-ward and wall-ward motions are relative to the lower end-wall. In the cascade flow, the out-ward motion may be the wall-ward motion if it is related to the blade tip. Table 4.2 shows the sign of the octant events in any individual flow quantities, such as triple products and Reynolds stresses.

4.4 MEAN FLOW ANGLES

The flow angle (FA) indicates the degree of three-dimensionality of the mean flow (Ölçmen and Simpson, 1995). The flow angles relative to the x-axis were calculated in the bed coordinate system with positive values in the clockwise rotation about the y-axis. The flow angles in different coordinates have a constant angle difference, which is equal to the rotated angle from one coordinate system to the other coordinate system. Two kinds of flow angle plots are shown in here. One is the plot of the flow angles at each cross section in figures 4.3 (a), (b), (c), (d), (e), (f), figures 4.4 (a), (b), (e), (f), and figures 4.5 (a), (b), (c), (d), (e), (f), which show how the flow angles changes from the pressure side to the suction and in the tip gap. The other is the plot of the flow angles along the

Chapter 4

pressure side at the all cross sections and along the upstream of the pressure side in figures 4.4 (c), (d) and figures 4.6 (a), (b).

For the 3.3% tip gap to chord ratio, flow angles in the upstream profiles are at about -70 degrees, in bed coordinates and the maximum flow angle difference is less than five degrees away from the wall in figure 4.3 (a). Flow in this inflow is close to two-dimensional flow and is more collateral than those profiles in the downstream region. In the tip gap region as shown in figures 4.3 (a), (b), (c), (d), (e), (f), 4.4 (a), (b), (e), (f), and 4.5 (a), (b), (c), (d), (e), (f), from the leading edge to the trailing edge for these two different tip clearance ($t/c=1.65\%$ and 3.3%), the average flow angle in the near-wall region relative to the x-axis in the bed coordinate system at the cross section $X/C_a=0.09$ is about -100 degrees; at $X/C_a=0.18$, it is about -115 degrees; at $X/C_a=0.27$, it is about -125 degrees; at $X/C_a=0.42$, it is about -140 degrees; and at $X/C_a=0.64$, it is about -125 degrees. This means that in the near-wall region, from the leading edge to the trailing edge, flow turns toward the suction side, and after $X/C_a=0.5$, turns back to the pressure side. The pressure difference between the pressure side and suction side has a tremendously increase, has a peak at $X/C_a=0.5$ and then decreases. This span-wise pressure gradient forces the tip gap flow to turn toward a direction almost normal to the blade chord. The flow angles in the tip gap region and the suction side and the pressure side and upstream of the pressure side, show higher three-dimensionality than the upstream profiles. At $X/C_a=0.42$, the average flow angle in the near-wall region is about 140 degrees and the angle between chord and x-axis is about 56.2 degrees, which means that the flow angle at $X/C_a=0.42$ is approximately normal to the chord. Flow angles in the 1.65% tip gap case have the same trends as those in the 3.3% tip gap case, except that

Chapter 4

near-wall flow angle begins to turn back to the pressure side after $X/C_a=0.27$, because the maximum pressure difference occurs at $X/C_a=0.37$.

For 3.3% tip gap to chord ratio, away from the wall, the flow turns toward the downstream. The maximum flow angle change in the boundary layers for those profiles in the inflow in figures 4.3 (a) and 4.4 (e) is about five degrees. The maximum flow angle change for those profiles in upstream of the pressure side and tip leakage region in figures 4.3, 4.4, 4.5 and 4.6 is about 60 degrees in most of the cross section. The 1.65% tip gap has the same feature. The flow angle varies much from the wall to the mid gap region, which increases the difficulty in a choice of the coordinate system for the octant analysis. Octant plots for two different tip gap cases are done in three coordinate systems (wall collateral coordinate, mid tip gap coordinate and local flow direction coordinates). Those profiles (S, C, B, P, U) under the blade tip are discussed in above three coordinates. Thus, three coordinate systems are used in the octant analysis, and the relationships of wall collateral coordinate, and mid tip gap coordinate and are shown in table 4.3.

4.5 THE COORDINATE SYSTEMS

For the mean flow field, three coordinate systems are used. The bed coordinate system (X_{bed} , Z_{bed}) is aligned with the suction slot and the direction of travel of the belt. The chord coordinate system (X_{chord} , Z_{chord}) is aligned with the chord of the blades. The angle of x-axis between the bed coordinate and the chord coordinate is -56 degrees. The separation line coordinate system (X_{sep} , Z_{sep}) is aligned with the tangent directions of the separation lines at $X/C_a=0.42$ for $t/c=3.3\%$ and at $X/C_a=0.18$ for $t/c=1.65\%$ from the oil

Chapter 4

flow visualization, which changes with different tip gaps. The angle of the x-axis between the bed coordinate and the separation line coordinate for $t/c=3.3\%$ is about -73 degrees and the angle of the x-axis between the bed coordinate and the separation line coordinate for $t/c=1.65\%$ is about -77 degrees.

In two-dimensional turbulent boundary layers, because the near-wall and free-stream mean flow directions are the same, the coordinate system choice for the octant analysis is not an issue. Flow in the tip gap is three dimensional and is skewed different amounts from the wall. The near-wall and mid gap flow directions have big differences of approximately $60\sim 70$ degrees. Thus, the wall shear stress vector is no longer aligned with the mid tip gap flow velocity vector. Thus as discussed above, there are three kinds of coordinate systems discussed: one is in the near-wall region, one is in the mid tip gap height, and another is the local flow direction coordinate. Before examining the octant analysis data for flow structure, it is important to discuss the choice of coordinate system. The flow angle is not the only candidate in the choice of coordinate system reference. Flow angle (α_f), velocity gradient angle (α_g), Reynold shearing stress angle (α_τ), and intensity angle (α_i) are needed to be considered. As in the previous discussion for the flow angles, none of these angles is constant throughout the three-dimensional boundary layers.

In the previous coherent structure research (Robinson, 1990), QSV is the eddy structure in the two-dimensional turbulent boundary. In order to examine the near-wall flow structure, one coordinate should be aligned with the "preferred" direction of the QSVs. The "preferred" direction is defined as the direction from which the average angular deviation of the QSVs' axis is at a minimum. Unfortunately, the data in this

Chapter 4

experiment cannot be used to directly determine this direction. Here, a hypothesis is made, and it assumes that this direction does exist and that this direction is close to one of the flow property angles at some height in the viscous sublayer. Ideally, one of our candidates would be the wall shear-stress coordinate system. But, no direct measurements of the wall shear stress angle were made. It will be assumed that the α_f measurements near the wall are close in value to the wall shear-stress direction. The quasi-collateral nature of the flow provides the justification for this assumption. The "wall-collateral" coordinate system replaces the wall shear-stress coordinate system.

Madden (1997) found that the "gradient" coordinate system based on near-wall α_g and the wall-collateral coordinate system are nearly parallel and there is no need to treat the "gradient" coordinate system as a separate case. The lack of α_f 's reliability makes it a poor choice on which to base a coordinate system, therefore, it was not used in the analysis. The α_i and α_f almost coincide near the wall. An "intensity" coordinate system is nearly parallel to the wall collateral coordinate system, and there is no need to treat the intensity coordinate system as a separate case.

Thus, the list of coordinate choices was narrowed to flow angle coordinates. Here three coordinates are need to be considered, mid tip gap coordinates, wall collateral coordinates, and local flow direction coordinates. The mid tip gap coordinate system was chosen to capture the flow structure characteristics in the mid tip gap region. The wall-collateral coordinate system is the best coordinate system to describe the coherent structures in the near-wall region and provides a good contrast to the mid tip gap coordinate system.

Chapter 4

In the near-wall region (viscous sublayer and low buffer layer), the local mean flow angle coordinates are similar to the wall collateral coordinates; in the buffer layer and log layer, the local mean flow angle coordinates are similar to the mid tip gap coordinates. Thus, in the local mean flow angle coordinates, the octant events, which are dominant in the wall collateral coordinates and mid tip gap coordinates, are still dominant in the local mean flow angle coordinates. Based on above discussion, that coherent structure model based on the observation in the local mean flow angle coordinates in the tip gap region can still apply to wall collateral coordinates and mid tip gap coordinates. In previous research (Ha, 1993) on the coherent structure, the region of highest coherency is aligned with the mean flow direction. Thus, the local mean flow angle coordinate is the best coordinate to capture the coherent motions. Thus, in the later discussion, octant analysis results in the local flow angle coordinates are discussed and those plots in the wall collateral coordinates and the mid tip gap coordinates are in the Appendix B.

4.6 MEAN VELOCITY FIELD

In top parts of figures 4.7, 4.8 and 4.9 (Tang 2004), U , V , W are the dimensional velocities in the chord coordinates at $X/C_a = 0.42$ cross section for $t/c = 3.3\%$ tip gap to chord ratio. In the bottom parts of figures 4.7, 4.8 and 4.9, U , V , W are non-dimensional velocities normalized by the skin friction velocity with the pressure gradient in the chord coordinates at $x/ca = 0.42$ cross section. The disparities in the profile $x5$ and $x3$ are due to the smaller skin friction value in the vicinity of the separation. In figure 4.7 (Tang 2004), the end-wall boundary thickness ($U/U_e = 0.995$) is approximately at $y^+ = 700$, which is about $1/2$ of the tip gap thickness (8mm). In the figure 4.8 (Tang 2004), the larger

Chapter 4

negative values for those profiles in the tip gap region are due to the tip separation vortex and diving motion of the flow into the tip gap, and the larger non-zero values for those profiles in the tip leakage vortex region represent the motion of tip leakage vortex. In figure 4.9 (Tang 2004), in the near wall region ($y^+ < 100$), pitch-wise velocity is greater than the chord-wise velocity and the secondary flow, which is normal to the chord, is much stronger. The Reynolds number in the tip gap based on the tip gap thickness for $t/c=3.3\%$ case, Re_t , is about 14000. The boundary thickness in the tip gap for $t/c=3.3\%$ is about 0.25 inch ($\delta^+ \approx 700$) and Re_θ is about 1000.

The flow angle (FA) indicates the degree of three-dimensionality of the mean flow. In the figure 4.10 (Tang 2004), the flow angles relative to the x-axis were calculated in the chord coordinate system with positive values in the clockwise rotation about the y-axis. The flow angles in different coordinates have a constant angle difference, which is equal to the rotated angle from one coordinate to the other coordinate.). The above figure shows how the flow angles changes from the pressure side to the suction side. At $X/C_a=0.42$ for $t/c=3.3\%$ case, the average flow angle in the near wall region is about 90 degrees, which means that flow angle at $X/C_a=0.42$ is approximately normal to the chord. Away from the wall, the flow angle goes to zero and the flow turns toward to the chord direction. The flow angle difference while away from the wall is about 90 degrees, which means the tip gap flow is a highly three-dimensional flow.

Figure 4.11 (Tang 2004), is the non-dimensional turbulent kinetic energy normalized by the free-stream velocity. From the pressure side to the suction side of the blade, the turbulent kinetic energy increases. Near the blade tip, there is large turbulent kinetic energy production, introduced by the tip separation vortex. In the tip leakage

Chapter 4

vortex region, there is large turbulent kinetic energy production in the near-wall region and in the vicinity of the center of the tip leakage vortex.

One profile of moving end-wall data (Kuhl 2001) is at position 1F in the inflow. Looking at figures 4.12 and 4.13 (Kuhl 2001), the belt viscous layer tends to turn the flow to the belt movement direction. The vectors at the wall, and zero slip, are exactly in the belt direction. The vectors in the outer boundary layer are twisted into the upstream flow direction.

4.7 CONDITIONAL AVERAGING

The present work in three-dimensional turbulent boundary layer structures is focused on the near-wall flow. Turbulent eddies are the dynamic elements in the study of coherent structure. Quasi-streamwise vortices are just one type of eddy structure in the three-dimensional turbulent boundary layers. Since there are too many unknowns to build the relationship between a quasi-streamwise vortex and a particular octant, the results and analysis here are only focused on ejection, sweep, and interaction events without regard to the particular eddy structures.

Since not all the data points that fall within an octant are for in a particular coherent motion, one must distinguish those data points participating in a particular coherent motion from all the octant events. The threshold is defined as equation (4.17)

$$|uv|_i \geq HU * V \quad (4.17)$$

Chapter 4

i is the octant events with threshold H etc, 1,2,3,4,5,6,7,8

u_i, v_i is the instantaneous velocity in octant i

U, V is the r.m.s streamwise and normal velocity

Willmarth and Lu (1972) showed that the contribution of velocity data under $H = 0.5$ was 1% of the total $\overline{u'v'}$. Thus, these studies demonstrate that ejection events do dominate other quadrant data. Bogart and Tiederman (1986) compared the results of the quadrant analysis with flow visualization. Quadrant-2 data ($u' < 0, v' > 0$) that fell outside of a certain threshold had high probabilities of being associated with an ejection event. A similar study was not performed for sweeps.

$$|uv|_2 \geq HU * V \quad (4.18)$$

The same conditional sampling technology is used to check the coherent motion (ejection and sweep) contributions to the shear stress $\overline{u'v'}$. Here, three different thresholds are checked, namely $H=0, 0.5, 1$ for the profile in the upstream of the inflow. While $h=0$, no instantaneous velocity data is cut; choosing $H=0.5$ permits a comparison with Willmarth and Lu's results. The reason $H=1$ is chosen is that data points below $H=1$ have a random probability of belonging to an ejection event (Bogart and Tiederman, 1986). With the increase of the threshold from 0 to 1, more instantaneous data fall outside the threshold. In the viscous sublayer, the total population decreases from 1 to 0.9, but in the outer layer, there is a maximum 30 percent decrease in the population. The population plots in the figures 4.14 and 4.15 for different octants with different thresholds give us more details about where this decrease is coming from. With the increase of the threshold, the populations are almost unchanged in octants 1, 5, 2 and 6, but there is

Chapter 4

about 2 percent decrease in the viscous sublayer for every octant 3, 7, 4 and 8 between $H=0$ and $H=1$. In the outer layer, the average decrease is about 5 percent in every this octants. The drop of the population in the total population comes from the decrease of the population in octants 3, 7, 4 and 8.

Since the populations for different thresholds in octants 1, 5, 2 and 6, are almost unchanged, the shear stress $\overline{u'v'}$ for these octants should be identical, which is proved in figures 4.16 and 4.17. The 5 percent difference in the population in interaction octants 3 and 7 and sweep octants 4 and 8 contributes about 1% difference to the peak of the total shear stress ($y^+=100$). The difference is less than 1% in the sublayer and is more than 1% in the outer layer. Octants 4 and 8 have negative contributions and octants 3 and 7 have positive contributions to the total shear stress $\overline{u'v'}$. The changes of shear stress $\overline{u'v'}$ for interaction octants 3 and 7 and sweep octants 4 and 8 with different threshold cancel each other, and the total shear stress $\overline{u'v'}$ is almost the same for different thresholds. The contribution of points under $H = 1$ for the ejection events is less than 1% of total $\overline{u'v'}$, especially in the near-wall region, which is consistent with the discussion of the Willmarth and Lu. The contribution of data points under $H = 1$ for the sweep events is larger than that in the ejection events, but still less than 2 or 3% of $\overline{u'v'}$, especially in the near-wall region. Here we are interested in the contribution of octant events to a given flow quantity (Reynolds stress and triple product), and not population of octant events, therefore, no data will be excluded from the octant analysis for fear of losing important information or compromising comparisons between all octants. It will be assumed that contributions from structural events have a dominating influence over contributions from

Chapter 4

random events as demonstrated by Willmarth and Lu. Thus, the threshold technique developed by Willmarth and Lu (1972) will not be used in the octant analysis.

4.8 RESULTS AND DISCUSSION

Octant analysis is performed with the profiles in the cross section at $X/C_a = 0.42$, and $X/C_a = -0.33$ for $t/c = 3.3\%$, $X/C_a = 0.18$ and $X/C_a = -0.33$ for $t/c = 1.65\%$ for the stationary wall and at $X/C_a = -0.33$ with $t/c = 3.3\%$ for the moving wall case. At $X/C_a = -0.33$, the flow is almost two-dimensional and flow angle changes less than five degrees while away from the wall, and these octant results compare with the exactly two-dimensional octant results taken in the boundary layer tunnel at Virginia Tech. The reason for choosing cross sections at x $X/C_a = 0.42$ with $t/c = 3.3\%$ for stationary wall and $X/C_a = -0.33$ with $t/c = 3.3\%$ for moving wall case is that flow is highly three-dimensional in these region. Octant contributions to the Reynolds stresses for the 2D profile taken by Ölçmen in the boundary layer tunnel at Virginia Tech are shown in figure 4.18. Since the coherent structure study for the two-dimensional turbulent flow has been well developed in the last few decades (Robinson, 1990), the review of turbulent structure for the two-dimensional profile in the boundary layer tunnel based on octant analysis makes it possible to produce a turbulent model for the two-dimensional flow, which is the research foundation for the following coherent structure study for three-dimensional turbulent flow. For the two-dimensional turbulent boundary layers, our discussion refers to the two-dimensional profile in the boundary layer tunnel and the profiles at $X/C_a = -0.33$ for $t/c = 3.3\%$ with the stationary wall, upstream of the inflow.

Chapter 4

Figures 4.19 to 4.34 contain plots of the octant contributions to the Reynolds stresses and triple products, which are normalized by the free-stream velocity, for those profiles in cross section $X/C_a = 0.42$ with $t/c = 3.3\%$ clearance for the stationary wall, and one two-dimensional profile UU with $t/c = 3.3\%$ in the upstream of inflow of the cascade flow in the local mean flow angle coordinates. In every specified Reynolds stress, octant contributions are examined in the wall collateral coordinates, mid tip gap coordinates and local mean flow angle coordinates. Figure 4.35 to 4.37 contain plots of the octant contributions to the Reynolds stresses and triple products for one profile of the inflow at $X/C_a = -0.33$ with $t/c = 3.3\%$ for the moving wall case. Octant contribution plots for the Reynolds stress and triple product normalized by the free stream velocity in the wall collateral coordinate and the mid tip gap coordinates with $t/c = 3.3\%$ clearance are put in the Appendix B. In the Appendix C, there is a collection of octant contribution plots to Reynolds stresses, which are normalized by the square of the skin friction velocity, and triple products, which are normalized by the cube of the skin friction velocity for those two different tip tap chord ratios ($t/c = 3.3\%$ and 1.65%).

As mentioned in the conditional averaging, the population with threshold ($H=1$) in octants 3, 4, 7 and 8 has a 5% decrease, comparing with threshold ($H=0$), but their contributions to the shear stress $\overline{u'v'}$ are almost invariant. It means that the population cannot provide the information about the contribution of each octant to the Reynolds stress and triple product. Here, the population for each octant is not going to be discussed. The goal of this octant analysis is to find the dominant octant events to the Reynolds stress and triple products under the blade tip. The structural models will be constructed through a review of two-dimensional turbulent boundary layer structural experiments and

Chapter 4

an eduction of three-dimensional turbulent boundary layer structural experiments with the stationary wall and the moving wall.

The next several sections detail octant contributions to the six Reynolds stresses and ten triple products. Each section discusses: 1) the relative order of the octants by contributions between octants 4 and 8 and between octants 2 and 6; 2) the relative order of the octants by contributions between octants 4 and 6; 3) the relative order of the octants by contributions between octants 4 and 6 and octants 1 and 7; 4) the location of the contribution peak for each dominant octant (Reynolds stresses only). 5) the difference in contribution values between mid tip gap coordinates, wall-collateral coordinates, and local mean flow; 6) the average near-wall difference in contributions between ejections and sweeps associated with same-sign w' ($\overline{w'w'}$, $\overline{u'w'}$, and $\overline{v'w'}$ only); and 7) the comparison with the two-dimensional turbulence structure. The following discussion gives the detail octant contributions for the Reynolds stress and triple product. Since there are more than 500 octant contribution plots, in the following discussion, we are not going to refer to the plots one by one. Common features in the Reynolds stress and triple product in the different coordinates are extracted and discussed below. The casual reader may skip these sections and proceed to the discussion in section 4.9 for the dynamic model, which highlights the most important trends that are revealed in the analysis.

Octant contributions to $\overline{u'u'}$

Chapter 4

In the two-dimensional turbulent boundary layers, since mean U is positive and mean V is equal to zero, $+u'$ represents the high momentum coherent motions and $-u'$ represents the low momentum coherent motions. In the local mean flow angle coordinate, such as the profile UU shown in the figure 4.19, octant analysis reveals that octant events fall into two groups, based on the amount of the contributions. One group is octants 2, 4, 6 and 8. The other is octants 1, 3, 5 and 7. In the first group, ejections (octant 6), ejections (octant 2), sweeps (octant 4) and sweeps (octant 8) look similar and almost have the same amount of contribution to total stress $\overline{u'u'}$. The ejections and sweeps contribute more than interactions to the total stress $\overline{u'u'}$ in the turbulent boundary layer. Those interaction octants have the same contribution to the total stress, and the total contribution from interactions is less than the total contribution of ejection and sweep octants.

In the three-dimensional turbulent boundary layers of the tip gap flow, due to one additional dimension free, the spanwise pressure gradient generates a larger instantaneous fluctuation velocity along the spanwise direction than the induced instantaneous fluctuation velocity by the streamwise vortex in the two-dimensional case. As shown in the figure 4.19, the total $\overline{u'u'}$ for three-dimensional case is less than the one in the two-dimensional case and octants 2 and 8 contributions have a tremendous decrease and octants 4 and 6 contributions have a slight decrease. On the other hand, octants 1 and 7 contributions have a tremendous increase and interaction octants 3 and 5 contributions are almost unchanged, as compared with the two-dimensional case. Octant analysis also reveals that octant events fall into two groups, based on the amount of the contributions. One group is octants 1, 7, 4 and 6. The other is octants 2, 8, 3 and 5.

Chapter 4

The octant 6 (ejection events) and octant 4 (sweep events) contribute more than octant 1 (interaction events) and octant 7 (interaction events) to total stress $\overline{u'u'}$. The octant 1 (interaction events) and octant 7 (interaction events) contribute more than the octant 2 (ejection events) and octant 8 (sweep events). The octant 2 (ejection events), octant 8 (sweep events), octant 3 (interaction events) and octant 5 (interaction events) are alike, the smallest contributor and have the same contribution to total stress $\overline{u'u'}$.

In the three-dimensional turbulent boundary layers of the inflow for the moving wall case, as shown in figure 4.35, in the near-wall region, the $+w'$ octant 4 (sweep) has the largest contribution than the other octants to Reynolds stresses $\overline{u'u'}$ within $y^+ < 30$. The $+w'$ octant 1 and $-w'$ octant 7 (interaction) have the largest contribution than the other octants within $30 < y^+ < 200$. The thickness of these coherent motions dominant region is about $y^+ = 200$.

Octant contributions to $\overline{v'v'}$

In a two-dimensional turbulent boundary layer, the peak region of $\overline{v'v'}$ represents the region where the coherent motions are dominant. Kang *et al.* (1998) postulated that the peaks in figure 4.18 represent the signature of a pair of vortices that generate the strong Reynolds stress event. For the upstream profile UU in figure 4.20 in the cascade tunnel, the center of the peak is about $y^+ = 100$. In the wall collateral coordinate, the octant analysis also reveals that octant events fall into two groups as in $\overline{u'u'}$, based on the amount of the contributions. One group is octants 2, 8, 4 and 6, and the other is octants 1, 7, 3 and 5. Ejections (octant 6), ejections (octant 2), sweeps (octant 4) and sweeps (octant

Chapter 4

8) look similar and have the same amount of contribution to total stress $\overline{v'v'}$ outside of the viscous sublayer. The ejection and sweep contribute more than interactions to the total stress $\overline{v'v'}$ outside of the viscous sublayer. Those interaction octants have the same amount of contribution to the total stress.

For the three-dimensional turbulent boundary layers of the tip gap flow in local mean flow angle coordinates, as shown in figure 4.20, the octant analysis also reveals that octant events fall into two groups, based on the contribution to the total stress. One group is octants 1, 7, 4 and 6, and the other is octants 2, 8, 3 and 5. The group members are consistent with those in the Reynolds normal stress $\overline{u'u'}$. Due to tip leakage, the total $\overline{v'v'}$ is greater than two-dimensional case and octants 2 and 8 contributions have tremendous decrease and octants 4 and 6 contributions have a increase, on the other hand, octants 1 and 7 contributions have an increase and interaction octants 3 and 5 contributions almost unchanged, compared with the two-dimensional case. The octant 8 contribution has a tremendous decrease and it means that a sweep motion with negative w fluctuation toward the wall does not have enough kinetic energy to get as close to the wall as in the two-dimensional case. Octant 2 with positive w fluctuation has a tremendous decrease and it means that an ejection motion away from the wall does not have enough kinetic energy to get away from the wall as in two-dimensional case. This explains the decrease of the Reynolds shear stress uv . The center of the peak is about $y^+=200$, and is much further away from the wall compared with the two-dimensional case.

The octant 6 (ejection events) and octant 4 (sweep events) contribute more than octant 1 (interaction events) and octant 7 (interaction events) to total stress. The octant 1

Chapter 4

(interaction events) and octant 7 (interaction events) contribute more than the octant 2 (ejection events) and octant 8 (sweep events). The octant 2 (ejection events), octant 8 (sweep events), octant 3 (interaction events) and octant 5 (interaction events) are alike and have the same contribution to total stress $\overline{v'v'}$.

In the three-dimensional turbulent boundary layers of the inflow for the moving wall case, as shown in figure 4.35, in the near-wall region (viscous sublayer and low buffer layer), the $+w'$ octant 4 (sweep) has the largest contribution than the other octants to Reynolds stresses $\overline{v'v'}$ within $y^+ < 30$. The $+w'$ octant 1 and $-w'$ octant 7 (interaction) have the largest contribution than the other octants within $30 < y^+ < 200$. The thickness of these coherent motions dominant region is about $y^+ = 200$.

Octant contributions to $\overline{w'w'}$

In a two-dimensional turbulent boundary layer, w' is the induced fluctuation velocity by the streamwise vortex. For the upstream profile UU in figure 4.21, the contribution difference to the total $\overline{w'w'}$ among the sweeps, ejections and interactions is smaller than other stresses. In the wall collateral coordinate, octant analysis also reveals that stress $\overline{w'w'}$ contribution for each octant is relative same as compared to other stresses.

For the three-dimensional turbulent boundary layers of the tip gap flow in local mean flow angle coordinates, , as shown in figure 4.21, the occurrence of the large total Reynolds normal stress $\overline{w'w'}$ can be explained by the same mechanism as the $\overline{u'u'}$ in the two-dimensional case. Due to the spanwise velocity gradient, the instantaneous

Chapter 4

fluctuation velocity (the translational induced velocity and rotational induced velocity) along the spanwise is larger than the rotational induced instantaneous fluctuation velocity by the streamwise vortex in a two-dimensional case. Octants 4, 6, 1 and 7 contributions have a tremendous increase, and octants 2, 8, 3 and 5 contributions have a slight increase, as compared with the two-dimensional case. The total $\overline{w'w'}$ is larger than the two-dimensional case. Octant analysis also reveals that octant events fall into two groups, based on the amount of the contributions. One group is octants 1, 7, 4 and 6. The other is octants 2, 8, 3 and 5. The octant 6 (ejection events) and octant 4 (sweep events) contribute more than octant 1 (interaction events) and octant 7 (interaction events) to total stress $\overline{w'w'}$ outside of the viscous sublayer. The octant 1 (interaction events) and octant 7 (interaction events) contribute more than the octant 2 (ejection events) and octant 8 (sweep events). The octant 2 (ejection events), octant 8 (sweep events), octant 3 (interaction events) and octant 5 (interaction events) are alike and have the same contribution to total stress $\overline{w'w'}$.

In the three-dimensional turbulent boundary layers of the inflow for the moving wall case, as shown in figure 4.35, in the near-wall region, the $+w'$ octant 4 (sweep) has the largest contribution than the other octants to Reynolds stresses $\overline{w'w'}$ within $y^+ < 30$. The $+w'$ octant 1 and $-w'$ octant 7 (interaction) have the largest contribution than the other octants within $30 < y^+ < 200$. The thickness of these coherent motions dominant region is about $y^+ = 200$.

Octant contributions to $\overline{u'v'}$

Chapter 4

In a two-dimensional turbulent boundary layer, ejection and sweep have a negative contribution to the total stress $\overline{u'v'}$ and the interaction has a positive contribution to the total stress. In the wall collateral coordinate, as the upstream profile UU in figure 4.22, octant analysis reveals that octant events form two groups, based on the amount of the contributions. One group is even octants having negative values and the other group is odd octants having positive values for these two different tip gap cases. The ejection and sweep events contribute more than interactions to the total stress $\overline{u'v'}$ outside of the viscous sublayer, and the total $\overline{u'v'}$ is negative. Those interaction octants have the same contribution to the total stress $\overline{u'v'}$, and all the even octants are similar and contribute the same amount to the total stress $\overline{u'v'}$. In the two-dimensional turbulent boundary layers, the wall ward motion of high momentum streaks and the out ward motion of the low momentum streaks generated the most part of the Reynolds shear stress $\overline{u'v'}$.

For the three-dimensional turbulent boundary layers of the tip gap flow in local mean flow angle coordinates, , as shown in figure 4.22, the total shear stress $\overline{u'v'}$ is less than that in the two-dimensional case and octants 2 and 8 contributions have a tremendous decrease, on the other hand, octants 4 and 6 contributions have a slightly increase, octants 1 and 7 and interaction octants 3 and 5 contributions are unchanged, compared to the two-dimensional case. From the previous discussion of normal stress $\overline{u'u'}$ and $\overline{v'v'}$, octants 2 and 8 contributions are much lower compared with those in the two-dimensional case. Thus for the shear stress $\overline{u'v'}$, the contributions from octants 2 and 8 are approximately close to zero. Octants 4 and 6 have an increase contribution to the total stress $\overline{v'v'}$, and have a slightly decrease to the total $\overline{u'u'}$, as compared with those in

Chapter 4

two-dimensional case. Thus octants 4 and 6 are the octant pairs with the largest contribution to the total $\overline{u'v'}$. The interaction pair of octants 1 and 7 have a tremendous increase contribution to the normal stress $\overline{u'u'}$ and $\overline{v'v'}$, compared with the two-dimensional case, and octants 1 and 7 is ranked as the second contributors to the total shear stress $\overline{u'v'}$. The octant 6 (ejection) and octant 4 (sweep) contribute more than octant 1 (interaction) and octant 7 (interaction) to total stress $\overline{u'v'}$. The octant 1 (interaction) and octant 7 (interaction) contribute more than the octant 2 (ejection) and octant 8 (sweep). The octant 2 (ejection), octant 8 (sweep), octant 3 (interaction) and octant 5 (interaction) are alike and have the same contribution to total stress $\overline{u'v'}$.

For those profiles under the blade tip, low speed streaks are dominant in the vicinity of the solid boundary, end-wall and blade tip. For those profiles in the passage on the pressure side and suction side of the blade, not including those profiles in the tip leakage vortex, low speed streaks happen near the end-wall and while away from the wall, and in the cross region of the passage flow and cross flow. High-speed streaks occur frequently away from the solid boundary, between those two low-velocity regions. The production of the turbulence is due to the intermittent ejection and sweep motion between the high momentum and low momentum streaks. The definition for the ejection is the outward motion of low speed fluid from the low velocity regions to the high-speed region, and the definition for the sweep is the wallward motion of high-speed fluid from the high velocity regions to the low speed region. Due to the formation of the additional low speed streaks above the end-wall and around the blade tip, compared with the two-dimensional case, the interaction 1 is much more like the sweep motion, the tip-ward motion of the high

Chapter 4

speed streaks and interaction 7 is much more like the ejection motion, the outward motion of low speed streaks. Again, the nature of the turbulence production is due to the intermittent ejection and sweep motion between the high momentum and low momentum streaks.

In the three-dimensional turbulent boundary layers of the inflow for the moving wall case, as shown in figure 4.35, in the near-wall region, the $+w'$ octant 4 (sweep) has the largest contribution than the other octants to Reynolds stresses $\overline{u'v'}$ within $y^+ < 30$. The $+w'$ octant 1 and $-w'$ octant 7 (interaction) have the largest contribution than the other octants within $30 < y^+ < 200$. The thickness of these coherent motions dominant region is about $y^+ = 200$.

Octant contributions to $\overline{u'w'}$

In a two-dimensional turbulent boundary layer, as the upstream profile UU in figure 4.23, in the wall collateral coordinate, octant analysis reveals that octant events form two groups, based on the amount of the contributions. One group is octants 2, 4, 6, 8 and the other group is octants 1, 3, 5, 7 for these two different tip gap cases. Ejection and sweep events contribute more than interactions to the total stress $\overline{u'w'}$ outside of the viscous sublayer. Octants 4 and 6 looks similar, having positive value and octants 2 and 8 are alike, having negative value, also octants 4, 6 and octants 2, 8 are symmetry about zero line. Thus the total of all event octant is close to zero. Octants 3 and 7 are symmetry about zero line, also octants 5 and 1 are symmetry about zero line, thus the total of event

Chapter 4

octant is close to zero and total stress uw is close to zero. In an ideal two-dimensional turbulent boundary layer, $\overline{u'w'}$ is exactly zero.

For the three-dimensional turbulent boundary layers of the tip gap flow in local flow direction coordinates, as shown in figure 4.23, the total shear stress $\overline{u'w'}$ is greater than the two-dimensional case and greater than zero and octants 2 and 8 contributions have a tremendous decrease, and close to the same contribution as interaction octants 3 and 5, on the other hand, octants 1 and 7 and octants 4 and 6 have an increase contribution to the total stress, compared with the two-dimensional case. The octant 6 (ejection) and octant 4 (sweep) contribute more than octant 1 (interaction) and octant 7 (interaction) to total stress $\overline{u'w'}$. The octant 1 (interaction) and octant 7 (interaction) contribute more than the octant 2 (ejection) and octant 8 (sweep). The octant 2 (ejection), octant 8 (sweep), octant 3 (interaction) and octant 5 (interaction) are alike and have the same contributions to total stress $\overline{u'w'}$.

From the previous discussion of normal stress $\overline{u'u'}$ and $\overline{w'w'}$, octants 2 and 8 contributions are much lower compared to those in two-dimensional case in the normal stress $\overline{u'u'}$, and octants 2 and 8 have slightly increase compared with those in 2d case in the normal stress $\overline{w'w'}$. Thus for the shear stress $\overline{u'w'}$, the octants 2 and 8 contributions are approximately close to zero. Octants 4 and 6 have an increase contribution to the total stress $\overline{u'w'}$, and octants 4 and 6 has a slightly decrease to the total $\overline{u'u'}$, as compared with those in two-dimensional case. Thus octants 4 and 6 are the octant pairs with the largest contribution to the total $\overline{u'w'}$. Interaction pair of octant 1 and 7 have a tremendous increase contribution to the normal stress $\overline{u'u'}$ and $\overline{w'w'}$, as compared with the two-

Chapter 4

dimensional case, and octants 1 and 7 is ranked the second for the contribution to the total shear stress $\overline{u'w'}$. The increase contribution in octants 1 and 7 and octants 4 and 6 to $\overline{u'w'}$ mainly comes from the increase contribution in $\overline{w'w'}$. Thus all of these increase are due to the additional dimension free.

In the three-dimensional turbulent boundary layers of the inflow for the moving wall case, as shown in figure 4.35, in the near-wall region, the $+w'$ octant 4 (sweep) has the largest contribution than the other octants to Reynolds stresses $\overline{u'w'}$ within $y^+ < 30$. The $+w'$ octant 1 and $-w'$ octant 7 (interaction) have the largest contribution than the other octants within $30 < y^+ < 200$. The thickness of these coherent motions dominant region is about $y^+ = 200$.

Octant contributions to $\overline{v'w'}$

In a two-dimensional turbulent boundary layer, as the upstream profile UU in figure 4.24, in the wall collateral coordinate, octant analysis to $\overline{v'w'}$ reveals that octant events form two groups, based on the amount of the contributions. One group is octants 2, 4, 6, 8 and the other group is octants 1, 3, 5, 7. Octants 4, 6, 3, 5 have negative contribution to the total stress $\overline{v'w'}$ and octants 1, 2, 8, 7 have positive contribution to the total stress $\overline{v'w'}$ for these two different tip gap cases. Ejection and sweep contribute more than interactions to the total stress $\overline{v'w'}$ outside of the viscous sublayer. Octants 4 and 6 looks similar, having negative values and octants 2 and 8 are alike, having positive values, also octants 4, 6 and octants 2, 8 are symmetry about zero line. Thus the total stress $\overline{v'w'}$ of

Chapter 4

event octants is close to zero. Octants 3 and 7 are symmetry about zero line, also octants 5 and 1 are symmetry about zero line, thus the total stress $\overline{v'w'}$ of odd octants is close to zero. It explains that the total stress $\overline{v'w'}$ is close to zero.

For the three-dimensional turbulent boundary layers of the tip gap flow in local flow direction coordinates, as shown in figure 4.24, the total shear stress $\overline{v'w'}$ is less than two-dimensional case and less than zero and octants 2 and 8 have a tremendous decrease, on the other hand, octants 1 and 7, octants 4 and 6 and interaction octants 3 and 5 have an increase contribution to the total stress, compared with the two-dimensional case. The octant 6 (ejection) and octant 4 (sweep) contribute more than octant 1 (interaction) and octant 7 (interaction) to total stress $\overline{v'w'}$. The octant 1 (interaction) and octant 7 (interaction) contribute more than the octant 2 (ejection) and octant 8 (sweep). The octant 2 (ejection), octant 8 (sweep), octant 3 (interaction) and octant 5 (interaction) are alike and have the same contribution to total stress $\overline{v'w'}$.

From the previous discussion of normal stress $\overline{v'v'}$ and $\overline{w'w'}$, octant 2 and 8 contributions have tremendous decrease compared with those in two-dimensional case in normal stress $\overline{v'v'}$, and octants 2 and 8 contributions have slightly increase compared with those in two-dimensional case in normal stress $\overline{w'w'}$. Thus for the shear stress $\overline{v'w'}$, the octants 2 and 8 are approximately close to zero. Octants 4 and 6 have an increase contribution to the total stress $\overline{v'w'}$, and octants 4 and 6 has an increase contribution to the total $\overline{v'v'}$, as compared with those in two-dimensional case. Thus octant 4 and 6 are the octant pairs with the largest contribution to the total $\overline{v'w'}$. Interaction pair of octants 1

Chapter 4

and 7 has a tremendous increase contribution to the normal stress $\overline{v'v'}$ and $\overline{w'w'}$, as compared with the two-dimensional case, and octants 1 and 7 is ranked the second for the contribution to the total shear stress. The increase contribution in octants 1 and 7 and octants 4 and 6 to $\overline{v'w'}$ mainly comes from the increase contribution in $\overline{w'w'}$. Again all of these increase are due to the additional dimension free.

In the three-dimensional turbulent boundary layers of the inflow for the moving wall case, as shown in figure 4.35, in the near-wall region, the $+w'$ octant 4 (sweep) has the largest contribution than the other octants to Reynolds stresses $\overline{v'w'}$ within $y^+ < 30$. The $+w'$ octant 1 and $-w'$ octant 7 (interaction) have the largest contribution than the other octants within $30 < y^+ < 200$. The thickness of these coherent motions dominant region is about $y^+ = 200$.

Octant Contributions To Triple Products

First, as in the previous discussion, the previously developed statistical method is applied to understand the further details of statistical characteristics of the triple products. Next based on the octant distribution, the dynamical model of flow structures, which is developed in the Reynolds stresses, is rechecked, from an entirely new point of view on the basis of the triple products. Consistently, the statistical characteristics of triple products are essentially dominated by the dynamical model of flow structures, which is based on the Reynolds stresses.

Chapter 4

The triple products ($\overline{u'u'v'}$, $\overline{u'u'w'}$, $\overline{v'v'w'}$, $\overline{u'v'v'}$, $\overline{u'w'w'}$, $\overline{v'w'w'}$, $\overline{u'v'w'}$, $\overline{u'u'u'}$, $\overline{v'v'v'}$, $\overline{w'w'w'}$) in the local mean flow angle coordinates are shown in the figures 4.25-4.34. For the two-dimensional turbulent boundary layers, as the upstream profile UU in figure figures 4.25-4.34, in the wall collateral coordinate, octant analysis reveals that the disparities in the triple products between the octants becomes larger than those in the Reynolds stress. As with contribution to the Reynolds stresses, event octants (ejection and sweep events) are larger contributors than the interaction events. For the three-dimensional turbulent boundary layers of the tip gap flow, in the figures 4.25-4.34, in the near-wall region, as in the two-dimensional turbulent boundary layers, the disparity in the triple products between the octants becomes larger than that for the Reynolds stresses. The octant 6 (ejection) and octant 4 (sweep) contribute more than octant 1 (interaction) and octant 7 (interaction) to the total triple products. The octant 1 (interaction) and octant 7 (interaction) contribute more than the octant 2 (ejection) and octant 8 (sweep). The octant 2 (ejection), octant 8 (sweep), octant 3 (interaction) and octant 5 (interaction) are alike and have the same contribution to total triple products. In the previous discussion, octants 1 and 7 are actually ejection and sweep like motion related to the blade tip. Thus the triple products have a highly intermittent nature and are dominated by coherent motions. It is obvious that the similarity of the disparity between the Reynolds stress and triple products exists. The large amplitude fluctuations of triple products for the three-dimensional turbulent boundary layers in the tip gap are associated only with the fluid motions categorized as the octants 4, 6, 1 and 7 events. Just as the octants 4, 6, 1 and 7 events contribute greatly to the production of turbulence, so they are regarded as the main contributors to the production process of the triple products.

Chapter 4

Hence the total triple products are determined by the disparity in contributions among octants 4, 6, 1 and 7 events. The fluid motions classified as octants 2, 8, 3 and 5 events, contribute very little to the total triple products because both contributions are quite small in absolute value, comparing with others. The experimental facts need to be utilized for modeling the triple products. The third order moments in the wall turbulence have a highly intermittent nature and are dominant and almost completely by the coherent motions such as ejections and sweeps.

In the three-dimensional turbulent boundary layers of the inflow for the moving wall case, as shown in figures 4.36 and 37, in the near-wall region, the $+w'$ octant 4 (sweep) has the largest contribution than the other octants to triple products within $y^+ < 30$. The $+w'$ octant 1 and $-w'$ octant 7 (interaction) have the largest contribution than the other octants within $30 < y^+ < 200$ to triple products. The thickness of these coherent motions dominant region is about $y^+ = 200$.

4.9 OCTANT ANALYSIS CONCLUSIONS

By comparing each octant's contribution, minor events can be eliminated and dominant events can be discussed and considered in turbulence models. This will help simplify the turbulence modeling and develop more robust turbulence model. The structural model will be constructed through a review of the three-dimensional turbulent boundary layer structural experiments and the common elements with the two-dimensional turbulent boundary layer structural experiments.

In order to have consistency in the following discussion, all the results discussed here are in the local mean flow coordinates. In these coordinates, the x axis is aligned

Chapter 4

with the local mean flow direction, y axis is normal to the end-wall and z is normal to the x-y plane, determined by the right hand rule. In the local mean flow angle coordinates, the mean U is positive and mean W is always equal to zero, which helps us to determine the high speed streaks and low speed streaks. In the two-dimensional flow, such as the far upstream profile UU in the figure 4.19 and in the figure 4.21, the peak of the total normal stress $\overline{u'u'}$ is about 0.014, and is 3 times the peak of the total normal stress $\overline{w'w'}$ which is about 0.0045. Thus in the two-dimensional turbulent boundary layers, $u' > 0$ represents the high speed structures and $u' < 0$ represents low speed structures. In the three-dimensional flow, such as the profiles 7U, 7P, 7B, 7C, and 7S in the figure 4.19 and in the figure 4.21, the peaks of total normal stress $\overline{u'u'}$ and $\overline{w'w'}$ are of the order of 0.01, which means the high speed and low speed streaks are determined by the fluctuation of the u component and w component. Here $u' > 0$ and $w' > 0$ represent the highest speed structures and $u' < 0$ and $w' < 0$ represents the low speed structures, compared to $u' > 0$ and $w' > 0$.

For the two-dimensional turbulent boundary layers, as upstream profile UU shown in the Reynolds stresses and triple products plots (figures 4.19 to 4.28) in local mean flow coordinates, when this octant classification is applied, the following trends are obtained:

- 1) The $+w'$ octant 2 (ejection) have the same amount of contribution as the $-w'$ octant 6 (ejection) for all Reynolds stresses and triple products outside of the sublayer.
- 2) The $-w'$ octant 8 (sweep) have the same amount contribution as the $+w'$ octant 4 (sweep) for all Reynolds stresses and triple products outside of the viscous sublayer.
- 3) The octant 2 and octant 6 (ejections) have the same contribution as the octant 4 and 8 (sweeps) for all Reynolds stresses and triple products outside of the viscous sublayer.

Chapter 4

4) The thickness of this coherent motion dominant region is about $y^+ = 1000$, and boundary thickness in the inflow is 0.67 inch ($\delta^+ \approx 1000$).

5) Sweeps and ejections contribute about 60% to 90% to the Reynolds stresses and triple products outside of the viscous sublayer.

6) The contribution difference to $\overline{w'w'}$ between sweeps, ejections and interaction is smaller than other stresses.

7) The total $\overline{v'w'}$ and $\overline{u'w'}$ are very close to zero.

Based on the above observations, octants 2, 4, 6 and 8 are the dominant octant events as shown in the figure 4.38. For octants 4 and 8, u' is positive, which represents the high speed streaks, and v' is negative, which is consistent to the wall-ward motion of the high speed streaks. Octants 4 and 8 are classified as sweep motions. For octants 2 and 6, u' is negative, which represents the low speed streaks, v' is positive, which means the low speed streaks move away from the end-wall. Octants 2 and 6 are classified as ejection motions. The ejections of the low speed streaks outward from the wall and the sweeps of high speed streaks inward toward the wall are shown in the figure 4.41. The likeness and symmetry of the octant events in the shear stress $\overline{v'w'}$ and $\overline{u'w'}$ gives the physical evidence that these positive and negative stream-wise vortices happen evenly in the average of time and space domains to produce zero for a time mean two-dimensional turbulent boundary layer. In two-dimensional turbulent boundary layers, sweeps and ejections are frequently associated with quasi-stream-wise vortices, the quasi-streamwise vortices convect downstream, and leave near-wall low-speed streaks trailing from the upward-rotation side of the vortex and high-speed fluid on the opposite side (Robinson,

Chapter 4

1991). The rotational motion of the QSV induces its own moderate w' , and in two-dimensional turbulent boundary layers, the QSVs of opposing signs appear in equal strength and equal numbers (Sendstad and Moin, 1992). For the normal stress $\overline{w'w'}$, the contributions for all octant events are very close, and total $\overline{v'w'}$ and $\overline{u'w'}$ are close to zero.

For a three-dimensional turbulent boundary layer, an octant analysis is performed to those profiles under the blade tip in the mid tip gap coordinates, wall-collateral coordinates and the local flow angle coordinates. A number of octant trends are common in these three sets of coordinates. Here, the dynamic model for the three-dimensional turbulent boundary layers is proposed, based on the results in the local mean flow angle coordinates. In the viscous sublayer, it is very hard to tell which coherent motion has the dominant contribution, and the difference in the different octants is very little for all six Reynolds stresses. When the octant analysis for the three-dimensional turbulent boundary layers is applied to Reynolds stress and triple product, the following trends are obtained, as shown in the figures 4.19 to 4.34:

1) The $-w'$ octant 6 (ejection) has the larger contribution than the $+w'$ octant 2 (ejection) for all Reynolds stresses and triple products.

2) The $+w'$ octant 4 (sweep) has the larger contribution than the $-w'$ octant 8 (sweep) for all Reynolds stresses and triple products.

3) The $-w'$ octant 6 (ejection), $+w'$ octant 4 (sweep), $+w'$ octant 1 (interaction) and $-w'$ octant 7 (interaction) contribute about 60%~80% to the Reynolds stresses and triple products. The $-w'$ octant 6 (ejection) and $+w'$ octant 4 (sweep) contribute more than $+w'$ octant 1 (interaction) and $-w'$ octant 7 (interaction) for all Reynolds stresses and triple

Chapter 4

products. The $+w'$ octant 1 (interaction) and $-w'$ octant 7 (interaction) contribute more than the $+w'$ octant 2 (ejection) and $-w'$ octant 8 (sweep), for all Reynolds stresses and triple products. The $+w'$ octant 2 (ejection), $-w'$ octant 8 (sweep), $+w'$ octant 3 (interaction) and $-w'$ octant 5 (interaction) are alike and approximately have the same contribution for all Reynolds stresses and triple products.

4) The thickness of this coherent motion dominant region of the end wall is about $y^+ < 700$ and boundary thickness of the end-wall in the tip gap is about 0.165 inch ($\delta^+ \approx 700$).

The cross flow under the blade tip is highly three-dimensional, and the appearance of another solid boundary (blade tip) above the end-wall affects the near-wall behavior of the coherent motions. As in the previous discussion about the high speed and low speed flow in the three-dimensional turbulent boundary layers, high speed and low speed streak are determined by the fluctuation of the u component and w component, here $u' > 0$ and $w' > 0$ represent the highest speed streaks and $u' < 0$ and $w' < 0$ represents the low speed streaks, compared to the highest speed streaks. Based on above octant results for the three-dimensional turbulent boundary layers, octants 1, 4, 6 and 7 are the dominant octants events as shown in the figure 4.39. For octant 4, u' and w' are positive, which represents the high speed streaks, and v' is negative, which means the high speed streaks move toward the end-wall. For octant 1, u' and w' are positive, which represents the high speed streaks, and v' is positive, which means the high speed streaks move away from the end-wall, but toward the blade tip and if related to the blade tip, actually it is sweep like motion. Octants 1 and 4 are classified as sweep like motion. For octant 6, u' and w' are

Chapter 4

negative, which represents the low speed streaks, v' is positive, which means the low speed streaks move away from the end-wall. For octant 7, u' and w' are negative, which represents the low speed streaks, v' is negative, which means the low speed streaks move toward to the end-wall, but away from the blade tip and if related to the blade tip, actually it is ejection-like motion. Octants 6 and 7 are classified as ejection motion. The ejections of the low speed streaks outward from the solid wall (blade tip and end-wall) and the sweeps of high speed streaks inward toward the wall (blade tip and end-wall) are the dominant motions as shown in the figure 4.42. These ejections and sweeps in the Reynolds stresses and triple products shows the high correlation of the instantaneous velocities of dominant coherent motions. The production of the turbulence is due to the intermittent ejection and sweep motion between the high momentum and low momentum streaks.

In the three-dimensional turbulent boundary layers, with the occurrence of the spanwise velocity gradient, the disparities in octant contributions for $\overline{w'w'}$ are among the widest by percentage, which is smaller in the two-dimensional turbulent boundary layers. The explanation about the production of the spanwise fluctuation velocity can be made, based on the ejection/sweep process of two-dimensional turbulent boundary layers. In the two-dimensional turbulent boundary layers, the stream-wise velocity gradient in the turbulent boundary introduces the span-wise vortex, and while going downstream, due to the instability, the span-wise vortex breaks into the stream-wise vortex, which is associated with the ejection/sweep motions, moves fluid vertically, and produces translationally u' fluctuations because through a stream-wise velocity gradient in the turbulent boundary. In the three-dimensional turbulent boundary layers, a spanwise

Chapter 4

velocity evolves with its own gradient. The spanwise velocity gradient must play an important role in the dynamics of this three-dimensional turbulent boundary layers. Thus, the mechanism of w' should bring to our attention to explain the occurrence of non-zero $\overline{u'w'}$ and $\overline{v'w'}$ and the tremendous drop of $\overline{u'v'}$.

Octant analysis is performed to one profile for $t/c=3.3\%$ case in the inflow for the moving wall case in the local flow angle coordinates. The moving wall mean flow angles and mean velocity magnitude are as shown in the figure 4.12 and 4.13. Here, the three-dimensional turbulent boundary layer dynamic model for the moving wall case with $t/c=3.3\%$ is made, based on the octant contribution results (figures 4.35 to 4.37) in the local flow angle coordinates. The following observations are obtained, in the near-wall region:

- 1) The $+w'$ octant 4 has the largest contribution than the other octants to all Reynolds stresses and triple products within $y^+ < 30$.
- 2) The $+w'$ octant 1 and $-w'$ octant 7 have the largest contribution than the other octants to all Reynolds stresses and triple products within $30 < y^+ < 200$.
- 3) The thickness of this coherent motion dominant region is about $y^+ = 200$.
- 4) Above $y^+ = 200$, there is no dominant octant.

For the moving wall case, the near-wall flow is a shear flow driven by the moving belt, while away from the wall, the flow is pressure driven. Since the flow is highly three-dimensional and also in the local mean flow angle coordinates, the definitions for the high speed and low speed fluid are same as those in the cross in the tip gap flow. As shown in above observations, octants 4, 1 and 7 are the dominant octants events as shown in the figure 4.40. For octant 4, u' and w' are positive, which represents the high speed streaks, and v' is negative, which means the high speed streaks move toward the moving

Chapter 4

end-wall in the region $y^+ < 30$. Octant 4 is classified as a sweep motion, as shown in the figure 4.43. The shear flow reinforces the sweep motion. Because the moving belt introduces the higher momentum to the near-wall fluid, less low speed streaks are generated, and also ejection events are little. For octant 1, u' and w' are positive, which represents the high speed streaks, and v' is positive, which means the high speed streaks move away from the end-wall in the region $30 < y^+ < 200$. For octant 7, u' and w' are negative, which represents the low speed streaks, v' is negative, which means the low speed streaks move toward to the end-wall in the region $30 < y^+ < 200$. The region $30 < y^+ < 200$ is actually the interaction region of the high speed streaks and the low speed streaks between the shear flow and the pressure driving flow as shown in the figure 4.43. The production of the turbulence is due to the intermittent ejection and sweep motion between the high momentum and low momentum streaks.

Table 4.1 Octant definition

Octant Definitions				
octant #	Sign of			event
	u'	v'	w'	
1	+	+	+	Interaction
2	-	+	+	Ejection
3	-	-	+	Interaction
4	+	-	+	Sweep
5	+	+	-	Interaction
6	-	+	-	Ejection
7	-	-	-	Interaction
8	+	-	-	Sweep

Table 4.2 The sign of each octant in individual flow quantities

Octant #	uuv	vww	vvv	uuw	vvw	www	uvv	uww	uuu	uvw	uv	uw	vw
1	+	+	+	+	+	+	+	+	+	+	+	+	+
2	+	+	+	+	+	+	-	-	-	-	-	-	+
3	-	-	-	+	+	+	-	-	-	+	+	-	-
4	-	-	-	+	+	+	+	+	+	-	-	+	-
5	+	+	+	-	-	-	+	+	+	-	+	-	-
6	+	+	+	-	-	-	-	-	-	+	-	+	-
7	-	-	-	-	-	-	-	-	-	-	+	+	+
8	-	-	-	-	-	-	+	+	+	+	-	-	+

Table 4.3 The relationship between the different coordinate systems in the different tip gaps

theta1 is the angle difference between Wall Collateral Coordinates and bed coordinates

theta2 is the angle difference between Half Tip Gap Coordinate and bed coordinates

Profile Name	3.3% t/c case					1.65% t/c case				
	7S	7C	7B	7P	7U	5S	5C	5B	5P	5U
theta1	-139	-137	-137	-132	-127	-115	-125	-127	-132	-131
theta2	-113	-111	-108	-103	-95	-108	-109	-106	-102	-95

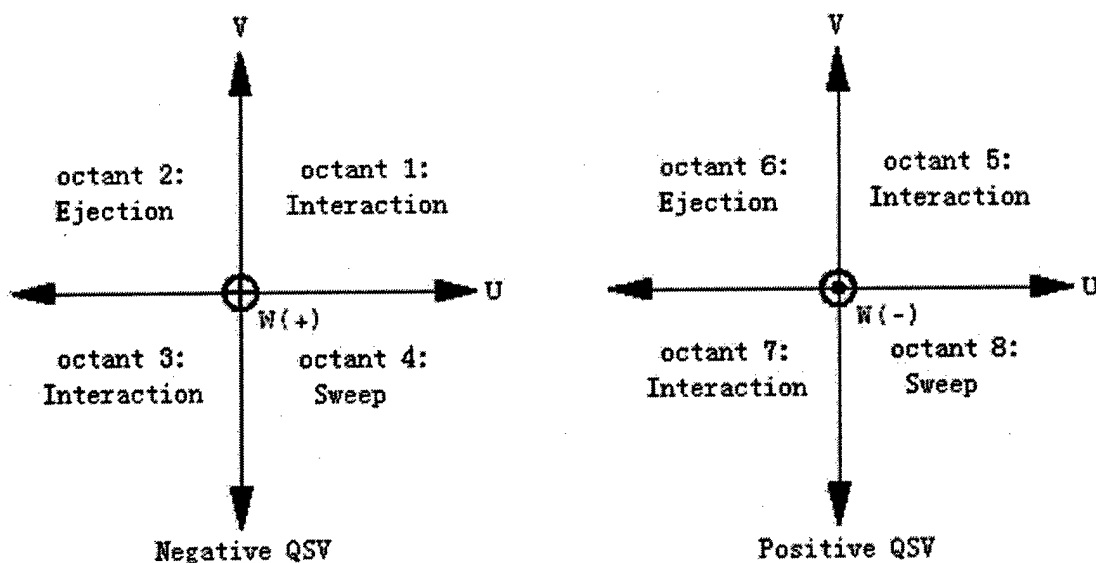


Figure 4.1 Octant names

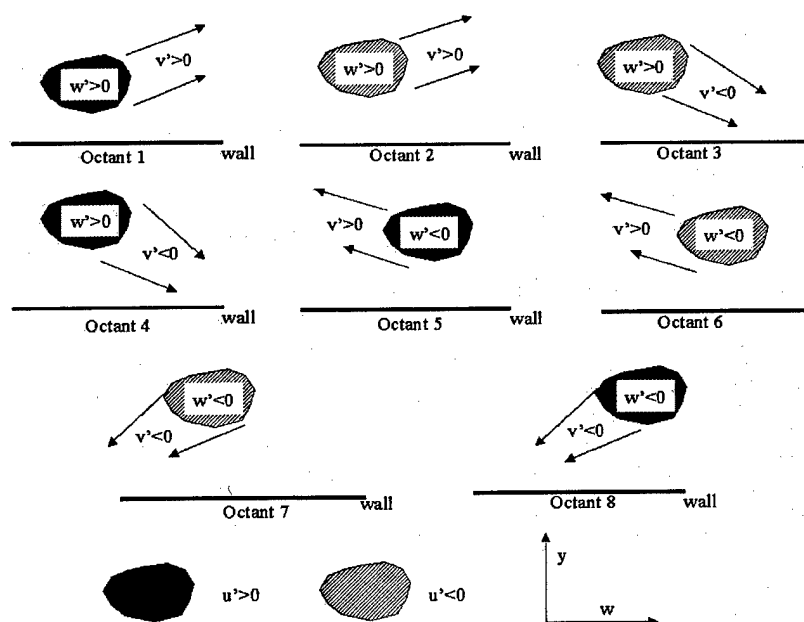


Figure 4.2 Conceptual drawing of eddies in each octant

Chapter 4

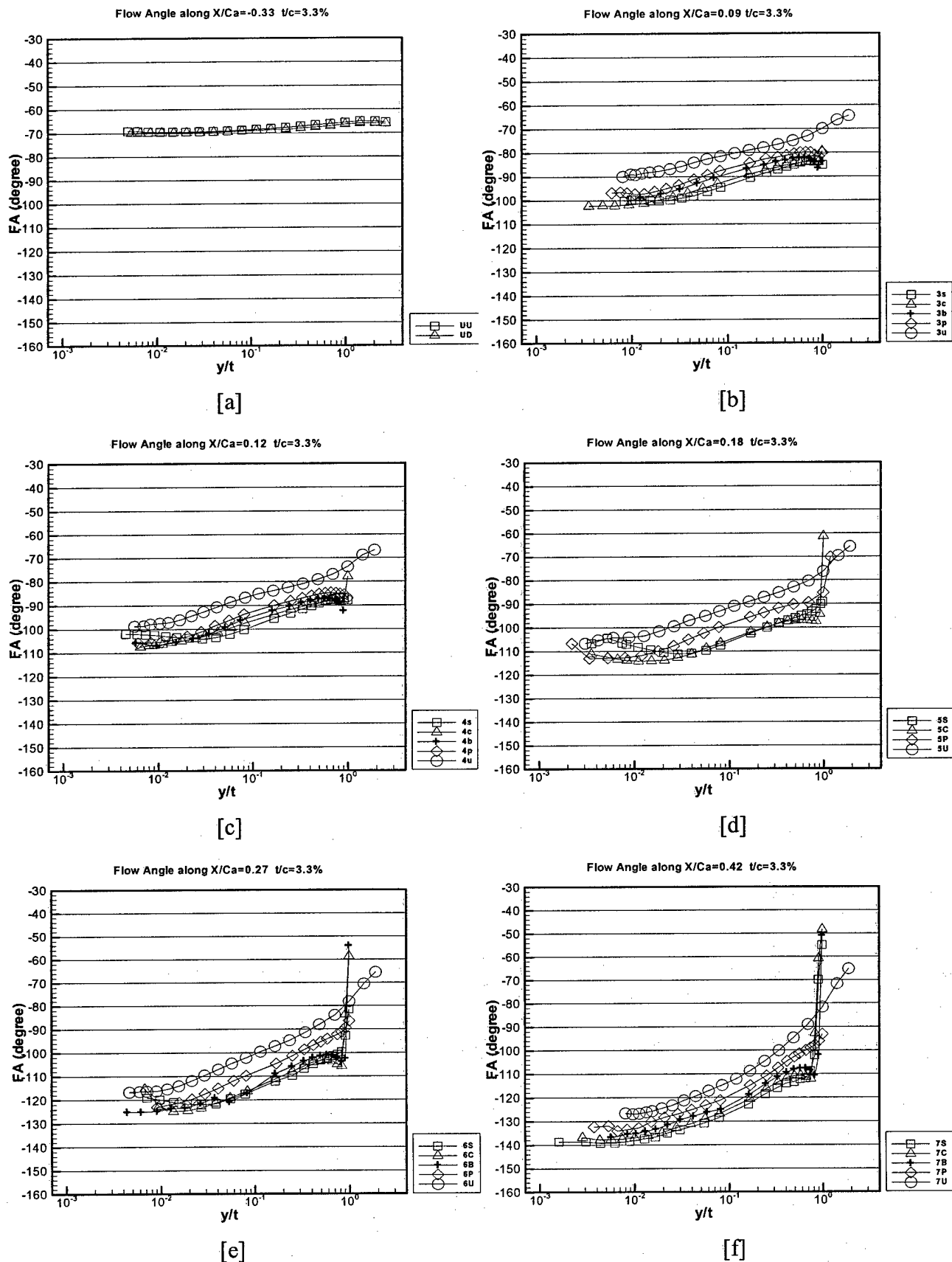


Figure 4.3 Flow Angle in the Bed Coordinates

Chapter 4

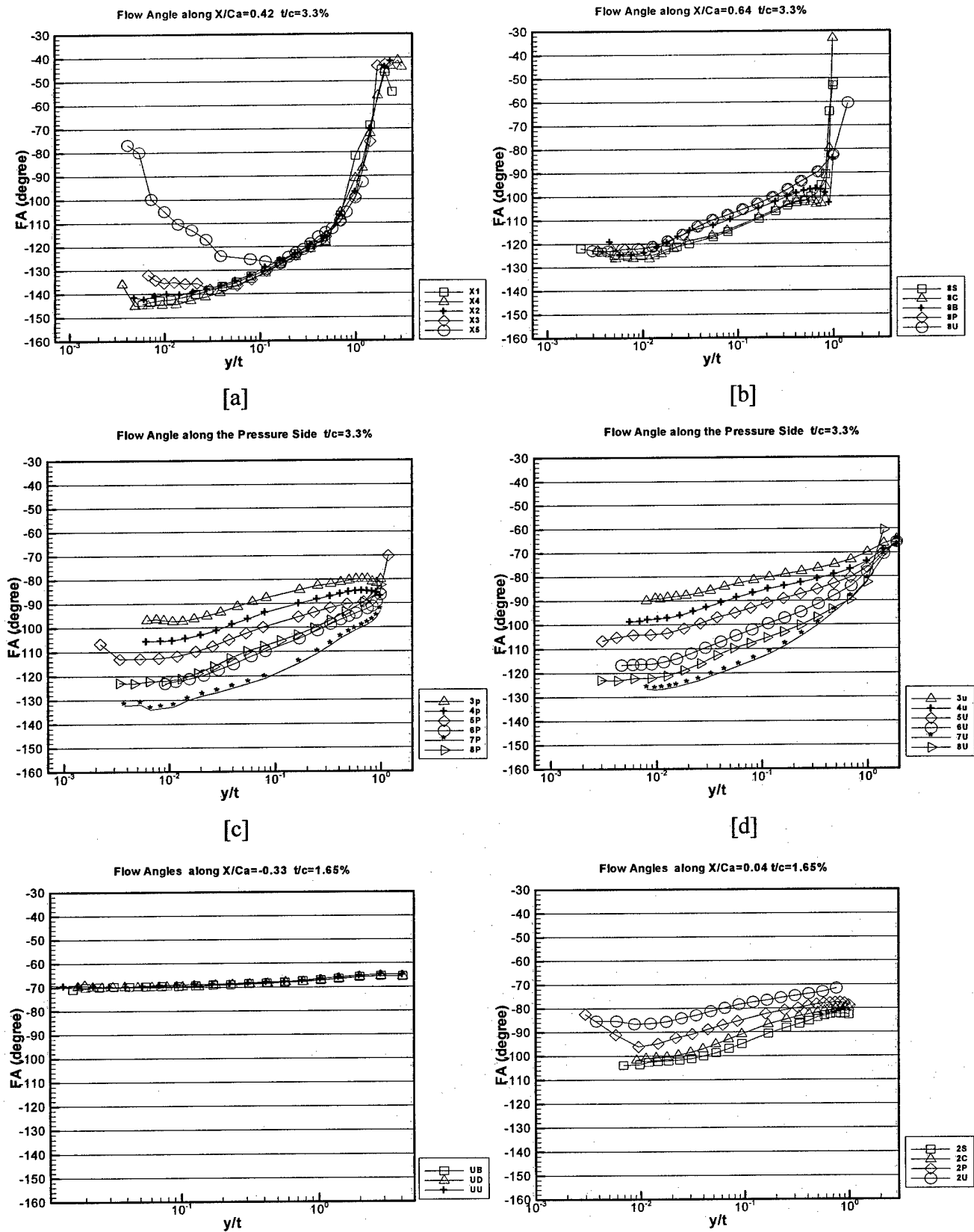


Figure 4.4 Flow Angle in the Bed Coordinates FA: Flow Angles

Chapter 4

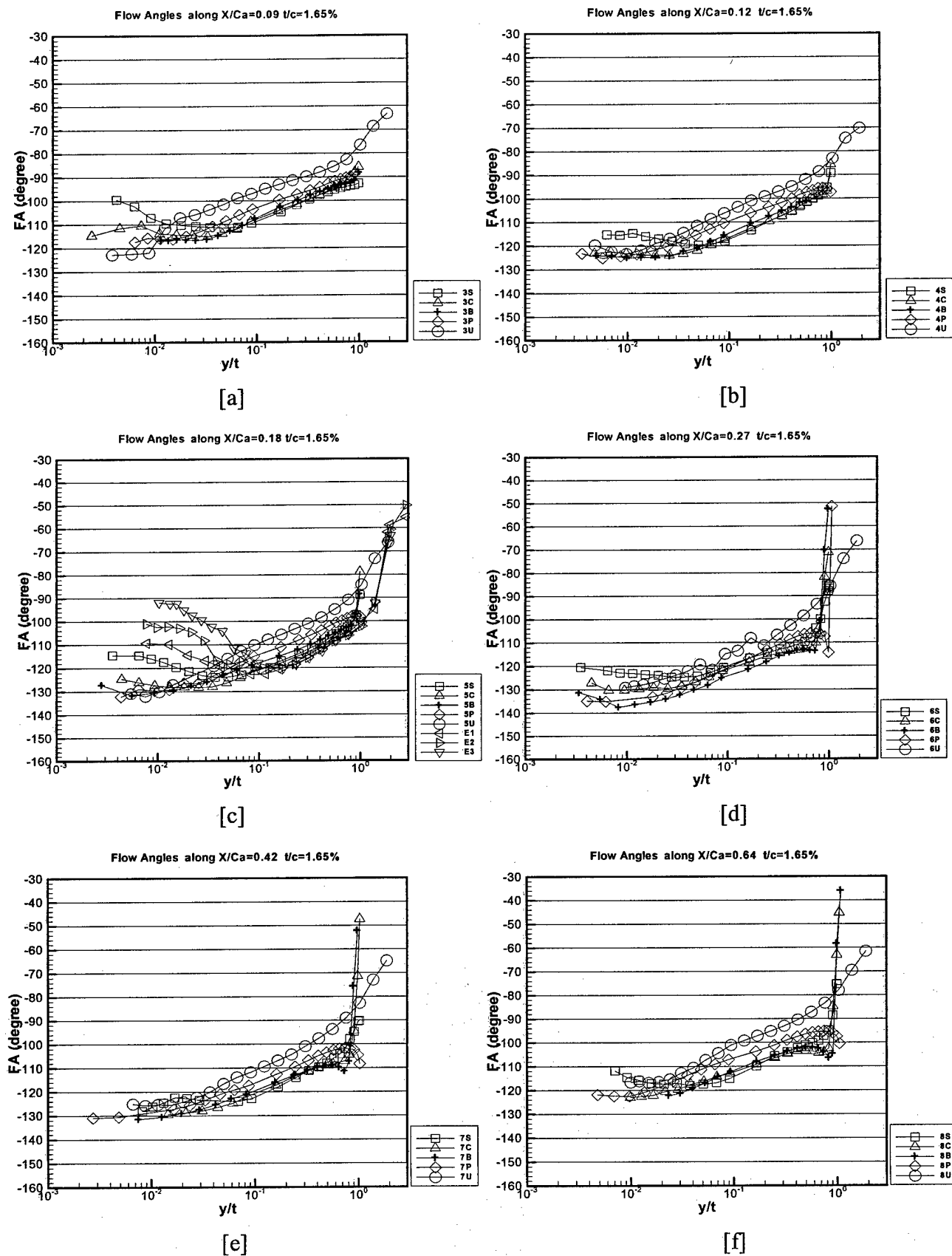


Figure 4.5 Flow Angle in the Bed Coordinates FA: Flow Angles

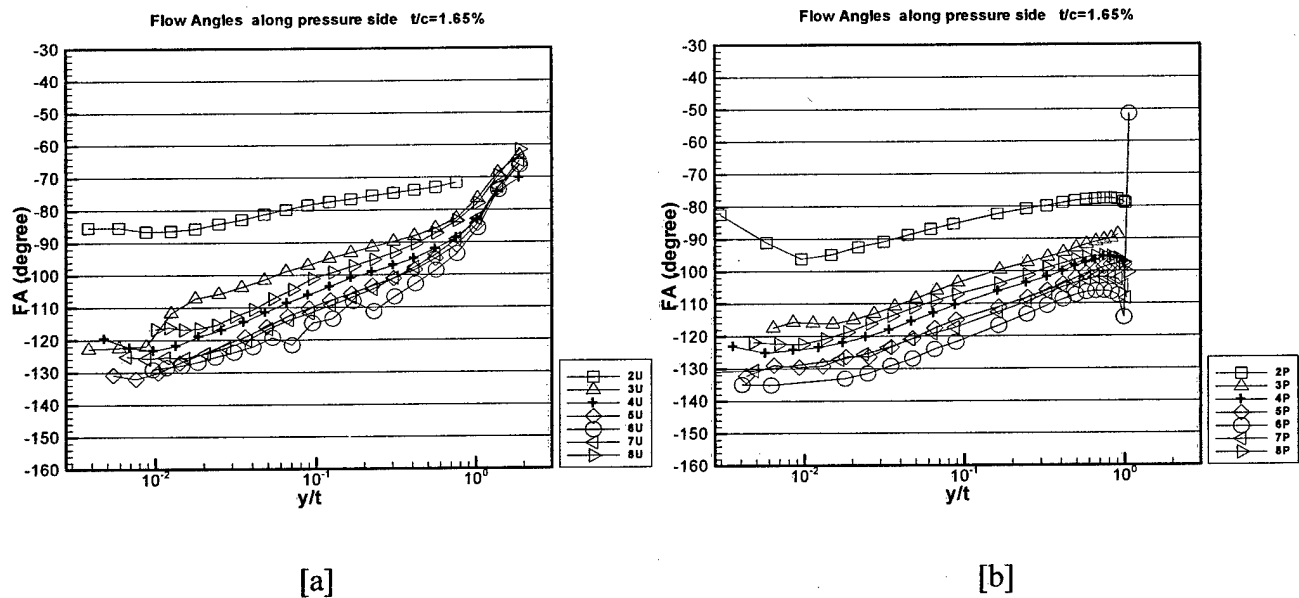


Figure 4.6 Flow Angle in the Bed Coordinates FA: Flow Angles

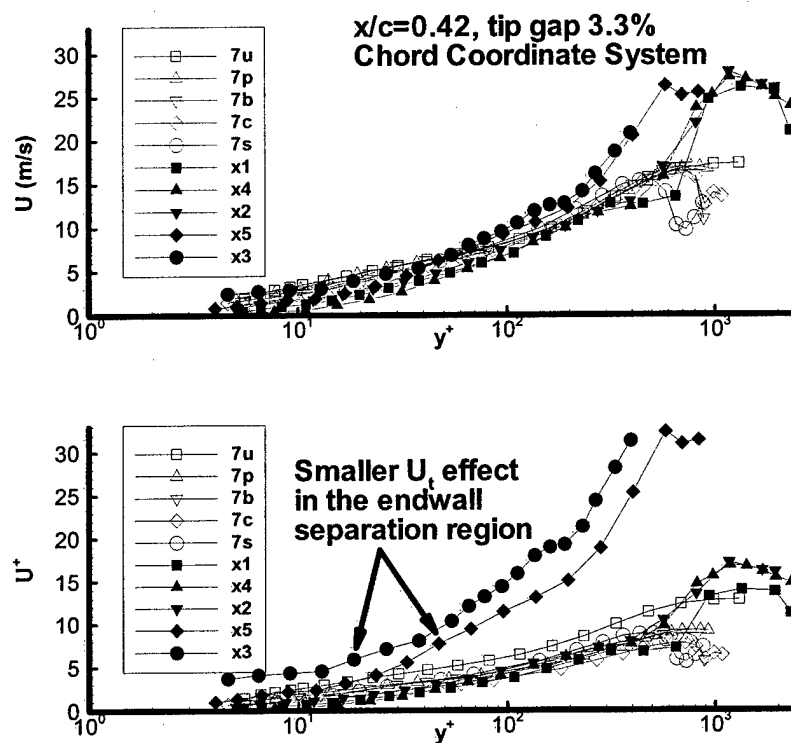


Figure 4.7 Mean U at $X/C_a=0.42$ cross section in the chord coordinate (Tang 2004)

U^+ is normalized velocity by skin friction velocity (U_t)

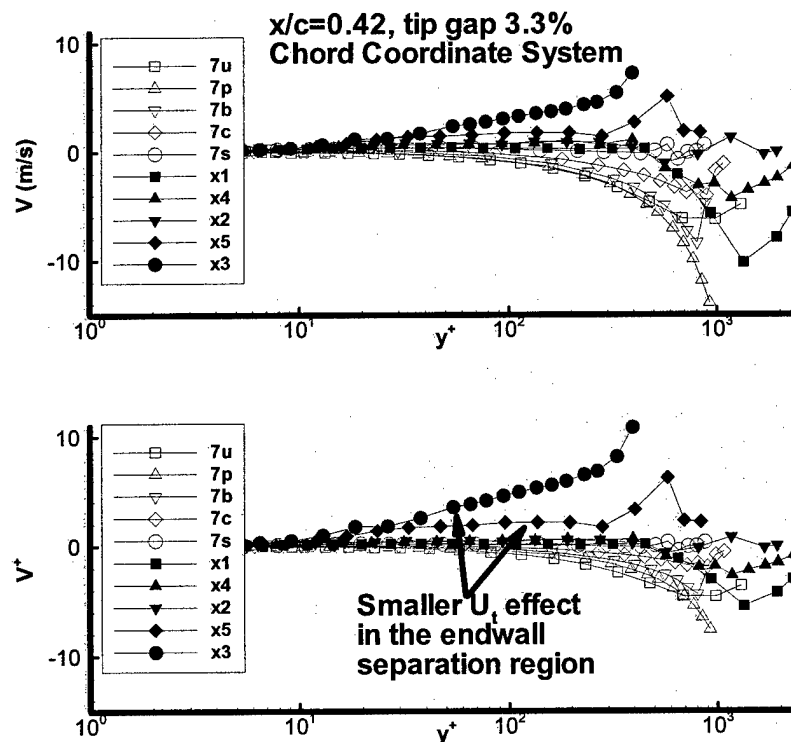


Figure 4.8 Mean V at $X/C_a=0.42$ cross section in the chord coordinate (Tang 2004)

V^+ is normalized velocity by skin friction velocity (U_t)

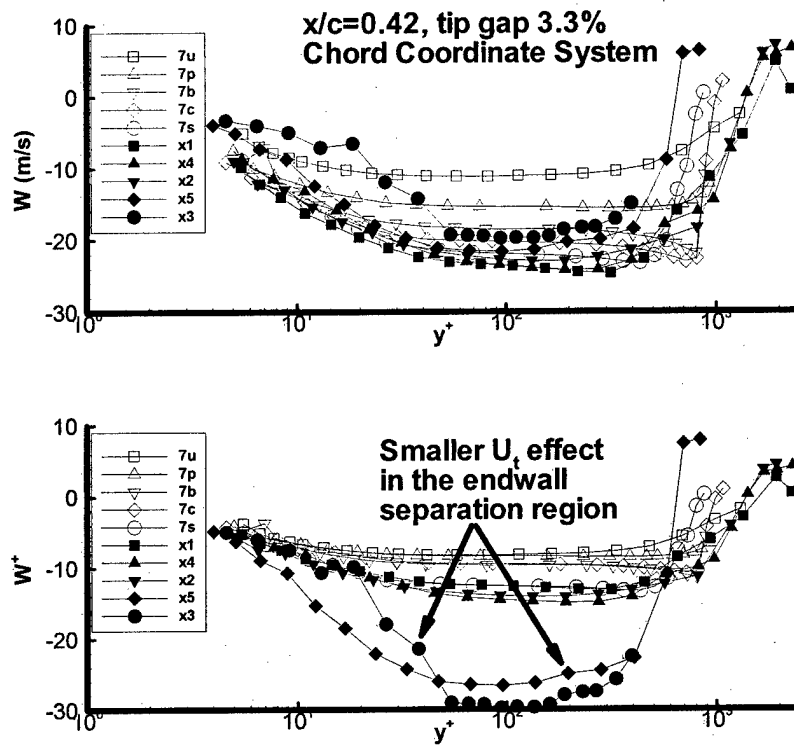


Figure 4.9 Mean W at $X/C_a=0.42$ cross section in the chord coordinate (Tang 2004)

W^+ is normalized velocity by skin friction velocity (U_t)

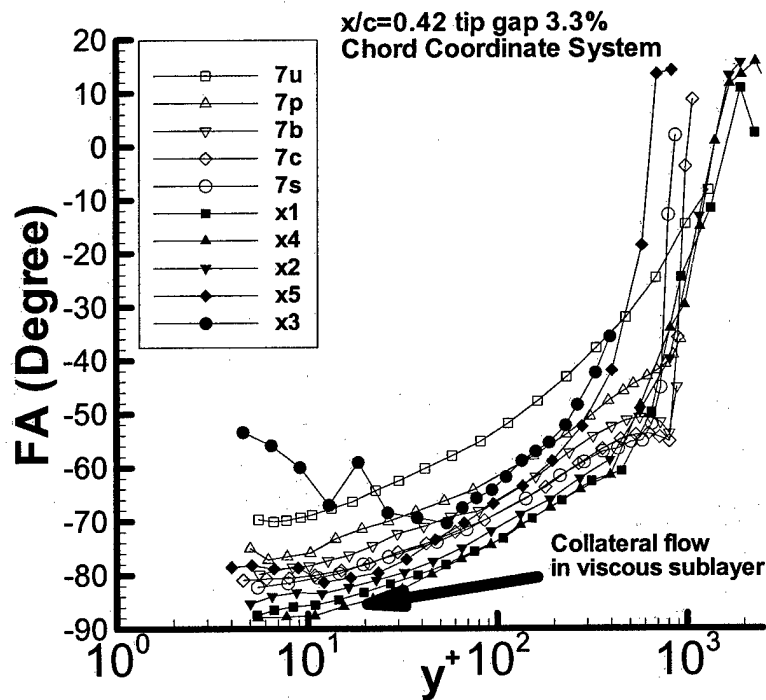


Figure 4.10 Mean flow angles at $X/C_a=0.42$ cross section in the chord coordinate (Tang 2004)

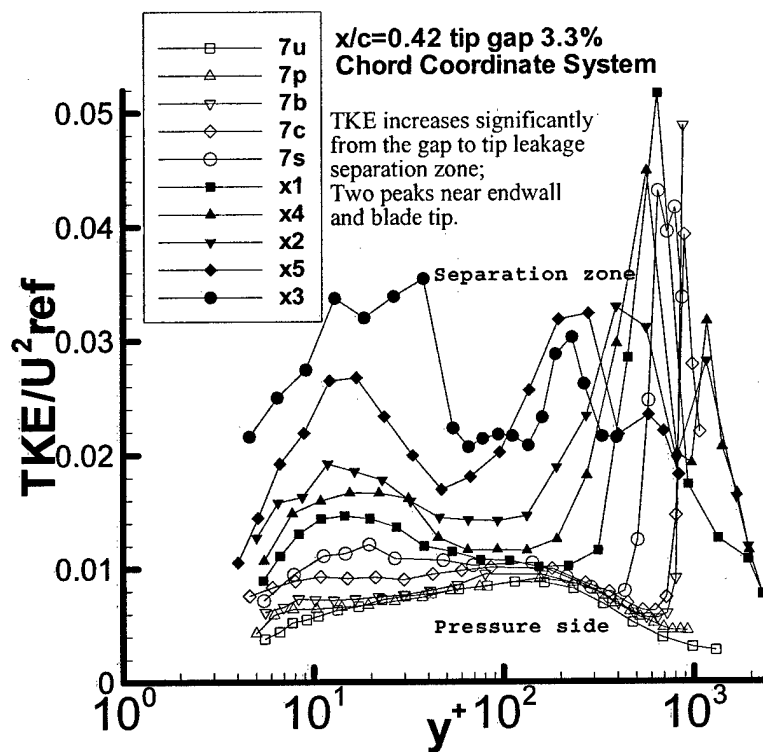
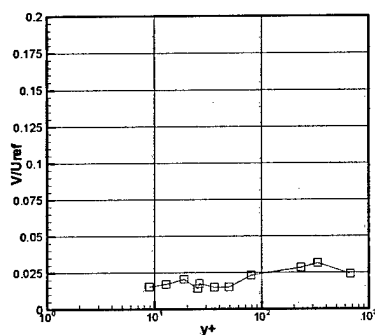
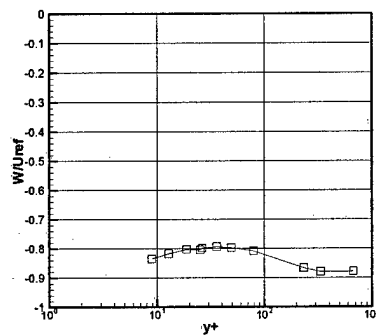


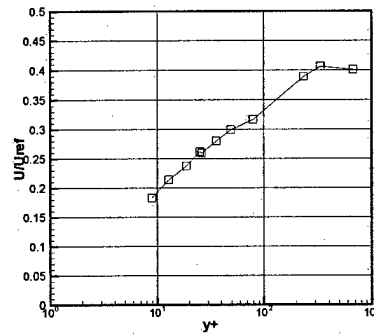
Figure 4.11 TKE results at $X/C_a=0.42$ cross section in the chord coordinate (Tang 2004)



[a]



[b]



[c]

Figure 4.12 Moving wall flow mean velocities, in bed coordinate system (Kuhl 2001)

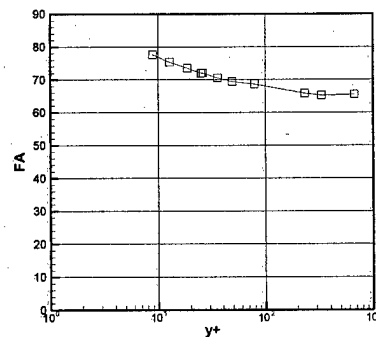


Figure 4.13 Moving Wall Flow Angle (Kuhl 2001)

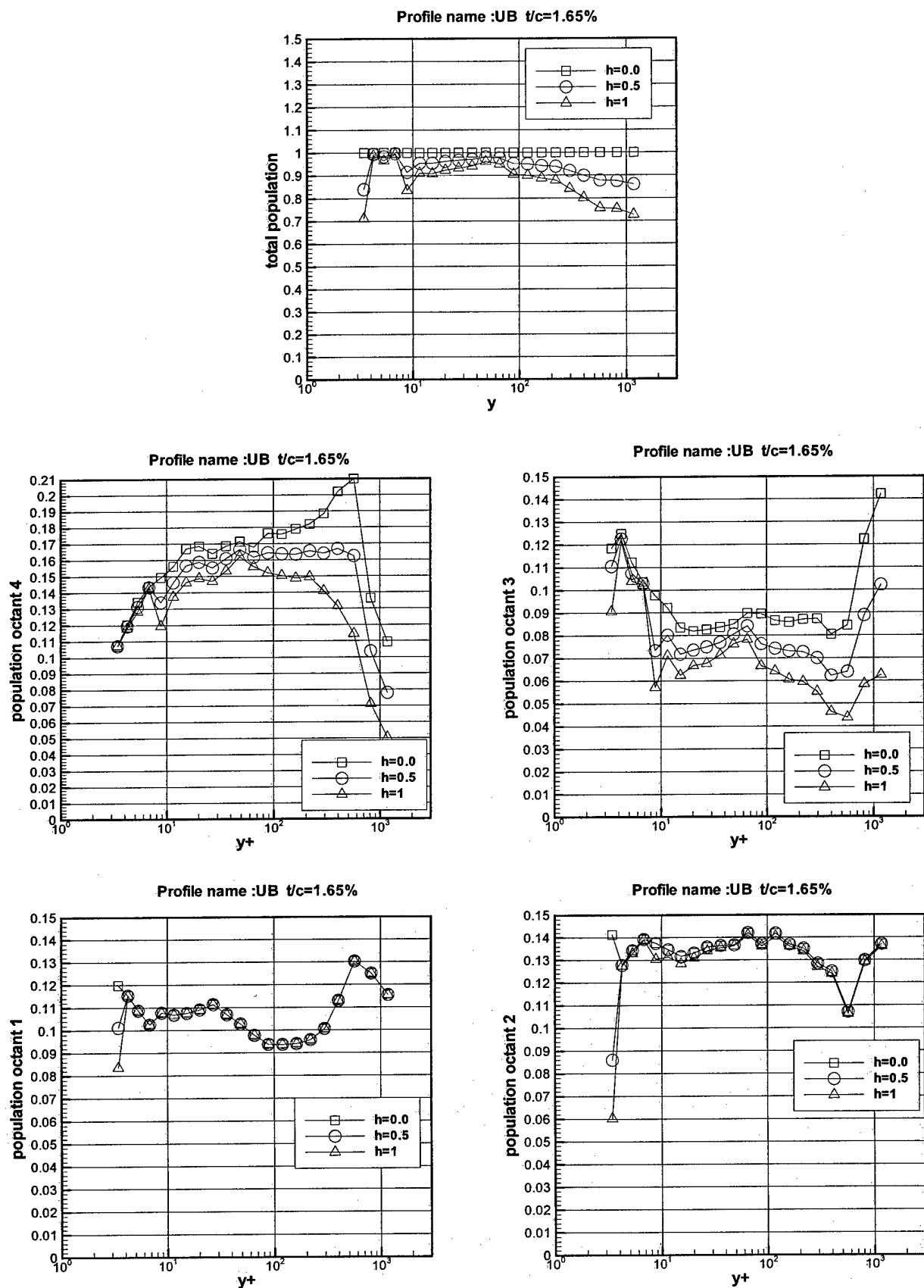


Figure 4.14 The population variation in the condition sampling

Chapter 4

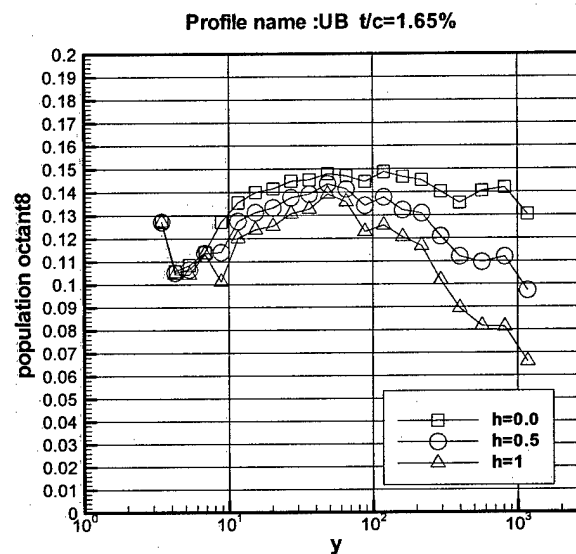
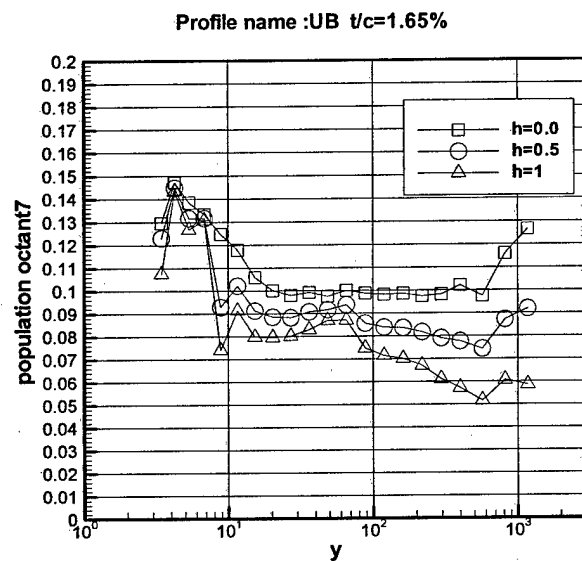
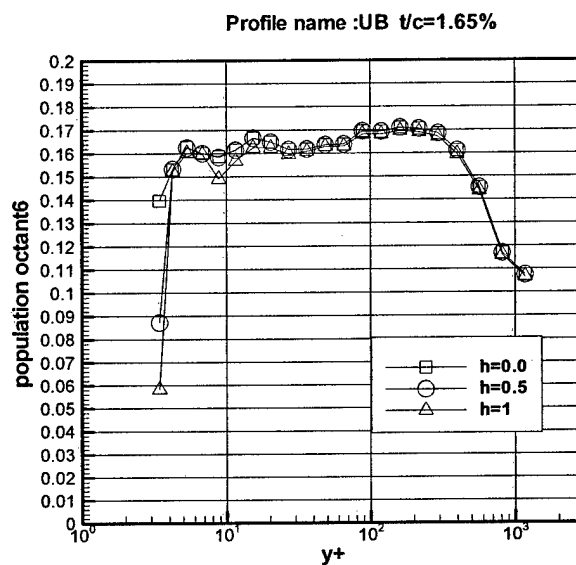
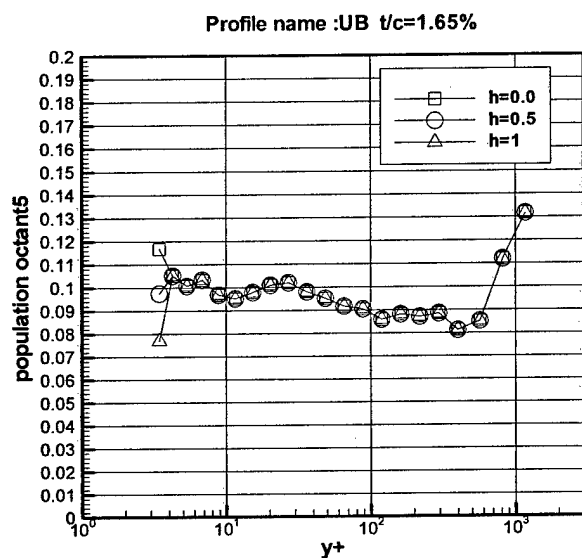


Figure 4.15 The population variation in the condition sampling

Chapter 4

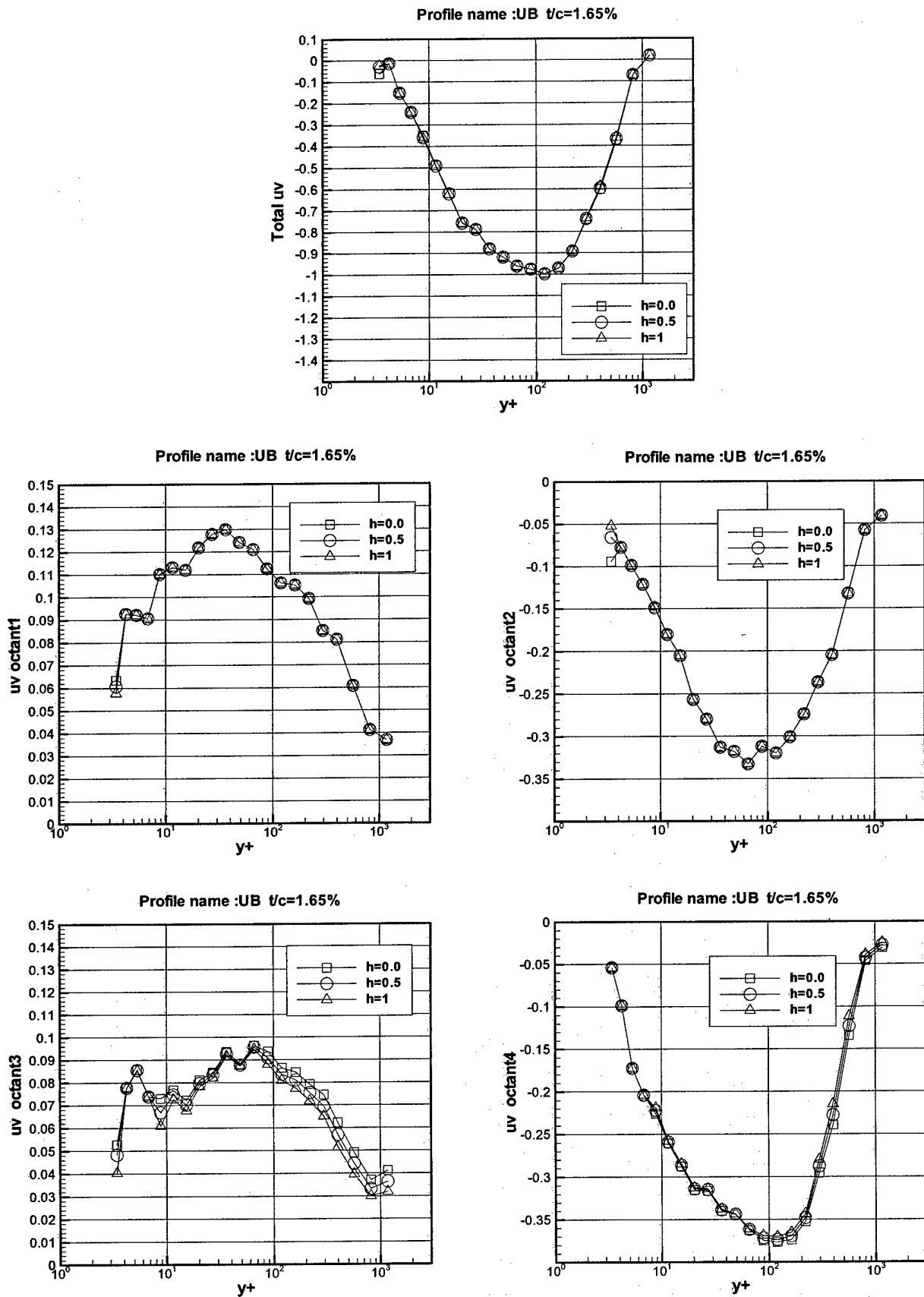


Figure 4.16 The Reynolds stress uv variation in the condition sampling

Chapter 4

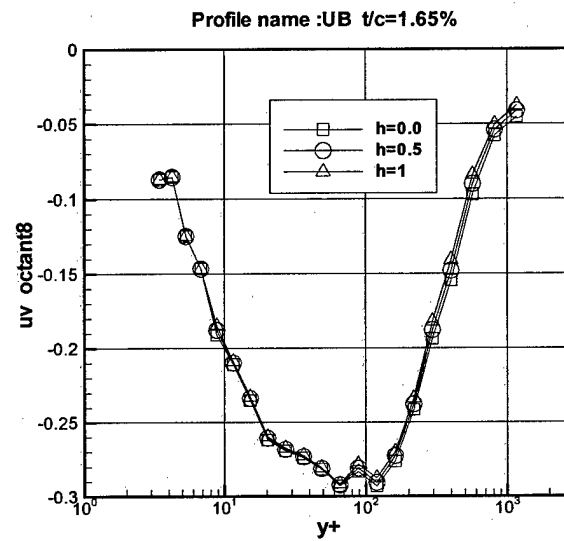
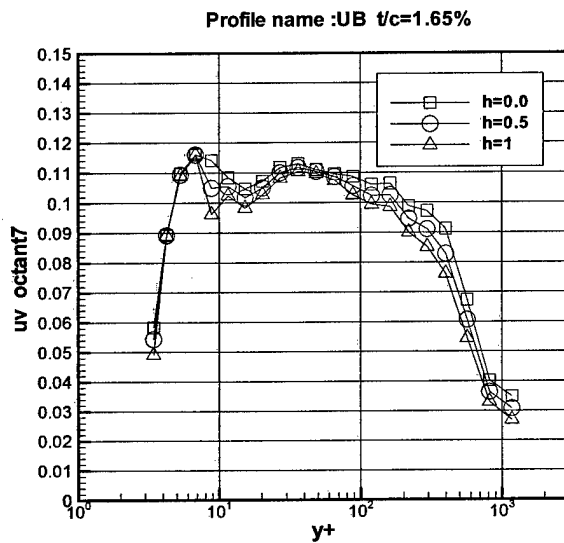
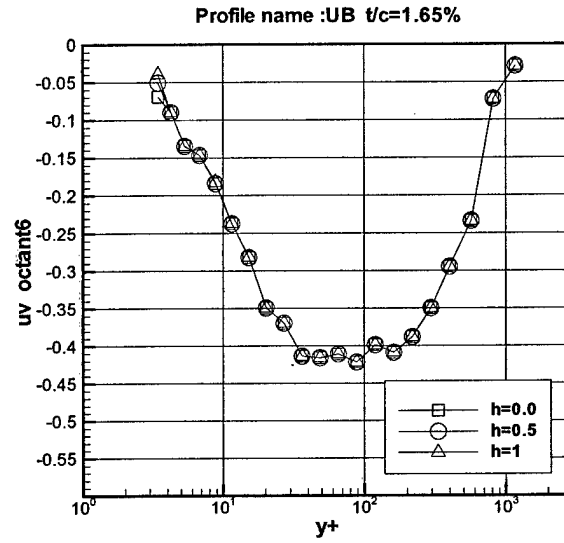
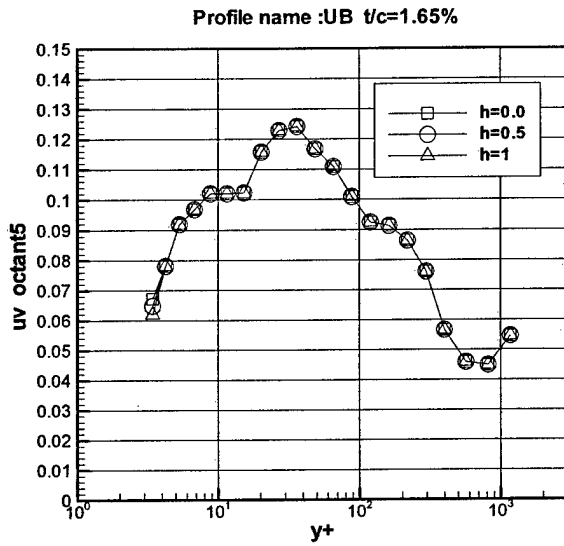


Figure 4.17 The Reynolds stress uv variation in the condition sampling

Chapter 4

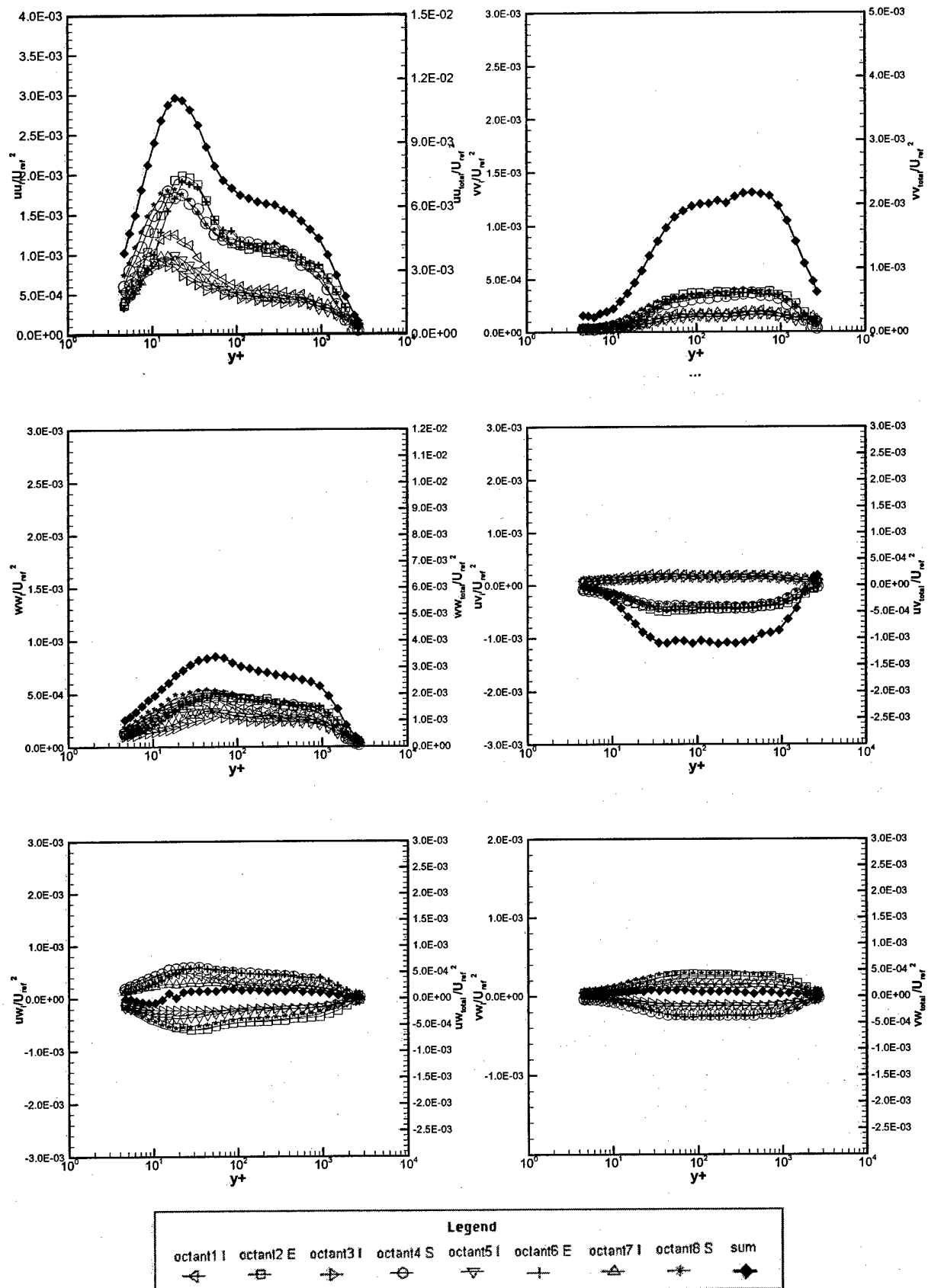


Figure 4.18 Octant contributions to Reynolds stress, wall collateral coordinates

U_{ref} is the free-stream velocity Profile name: [2D]

Chapter 4

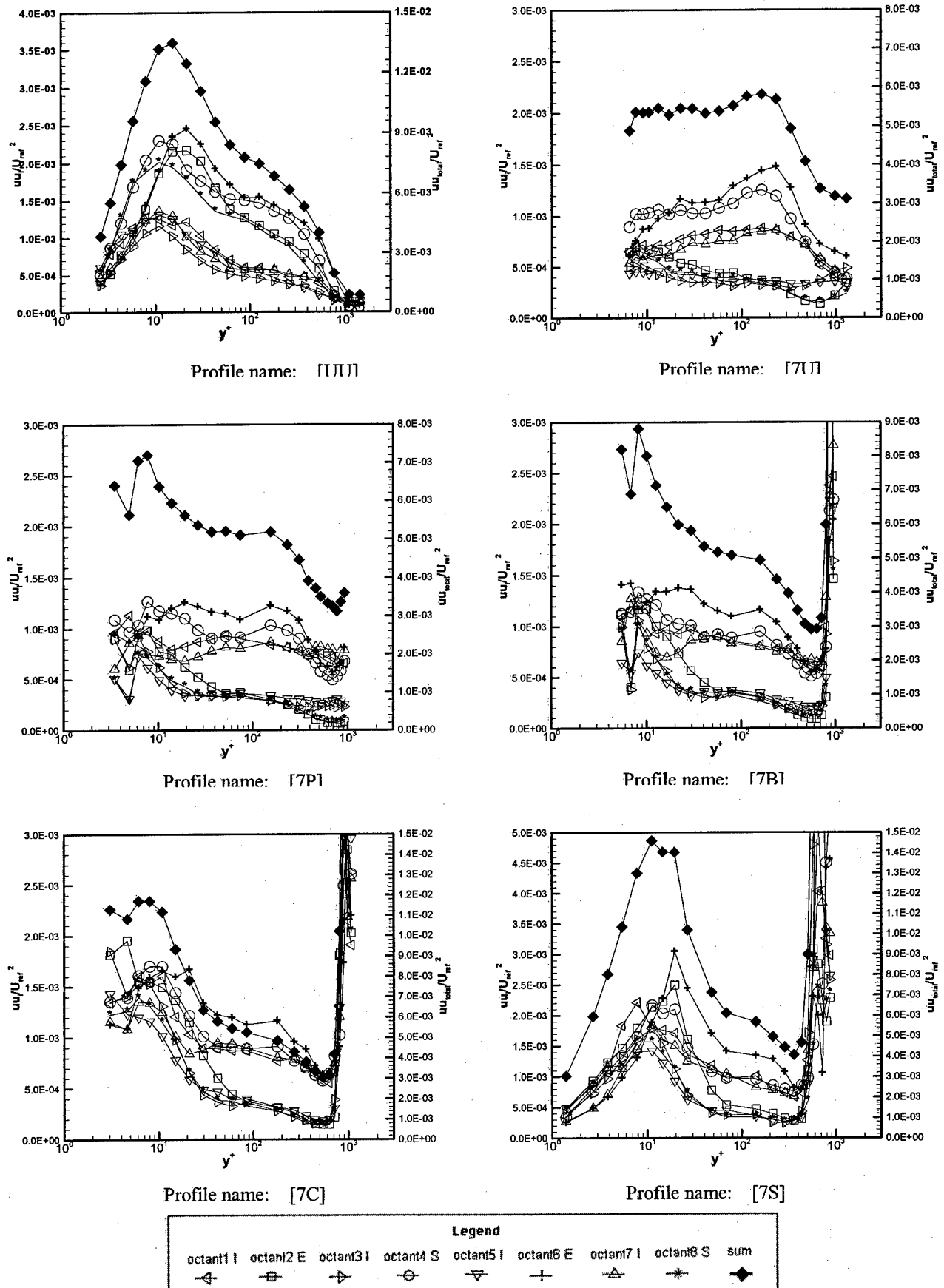


Figure 4.19 Octant contributions to Reynolds stress uu (U_{ref} is the free-stream velocity, local mean flow angle coordinates)

Chapter 4

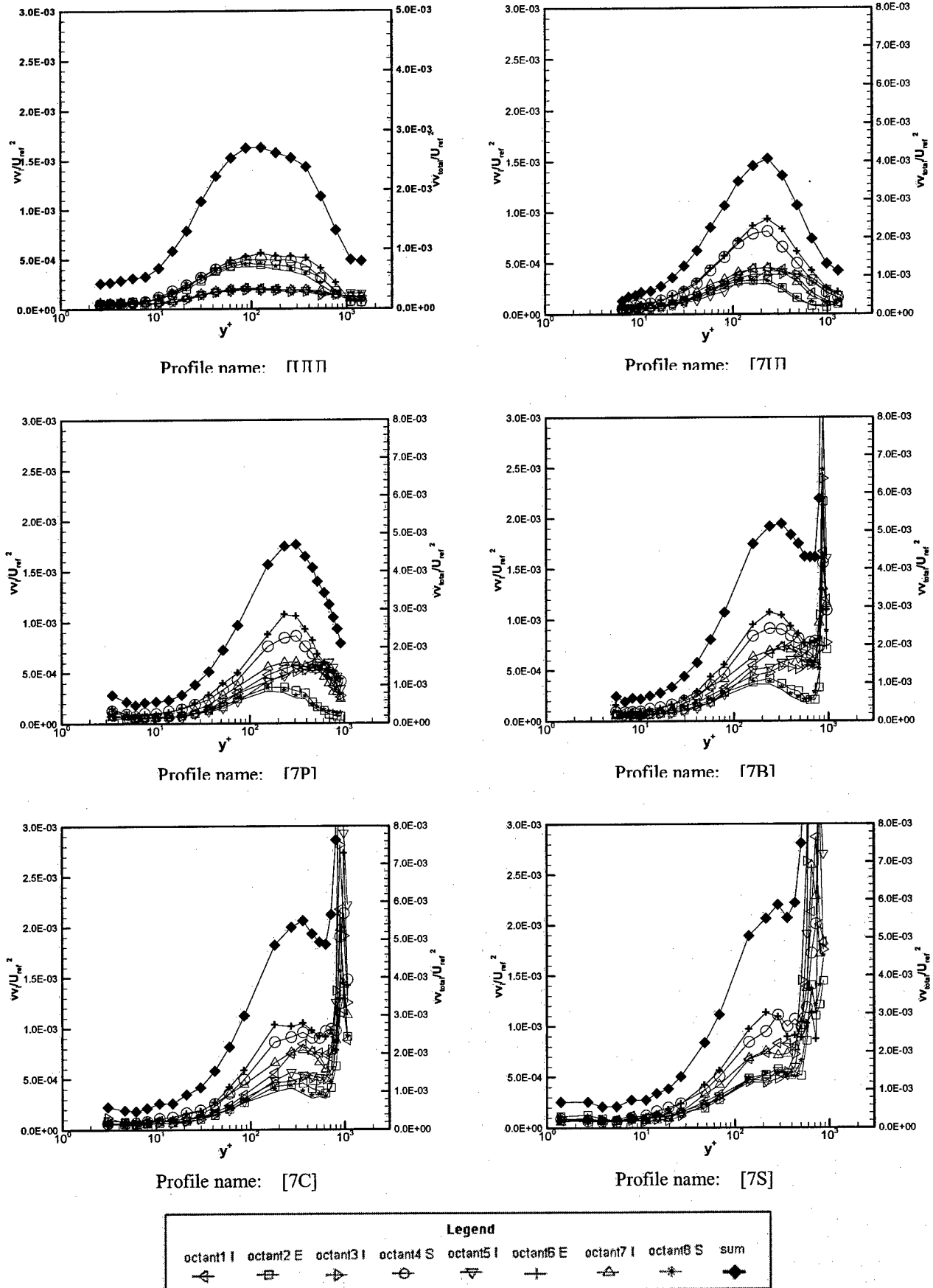
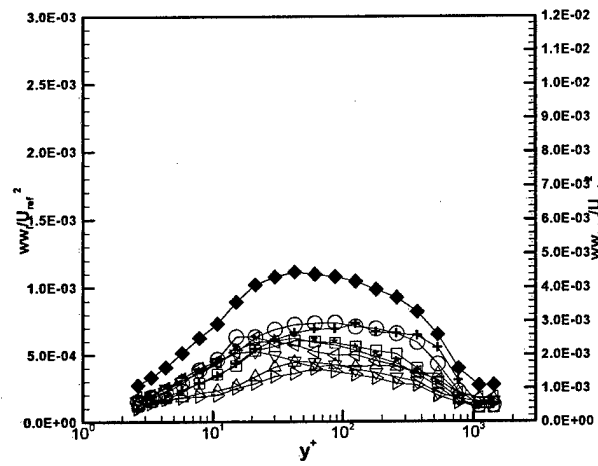
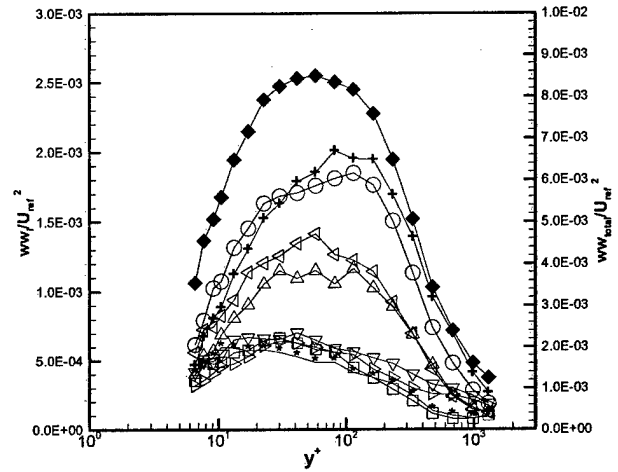


Figure 4.20 Octant contributions to Reynolds stress vv (U_{ref} is the free-stream velocity, local mean flow angle coordinates)

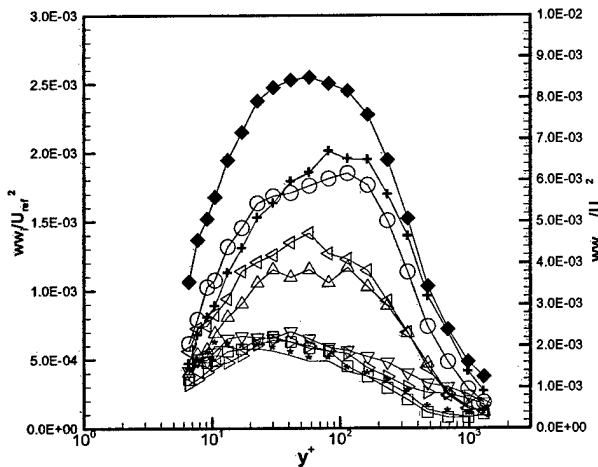
Chapter 4



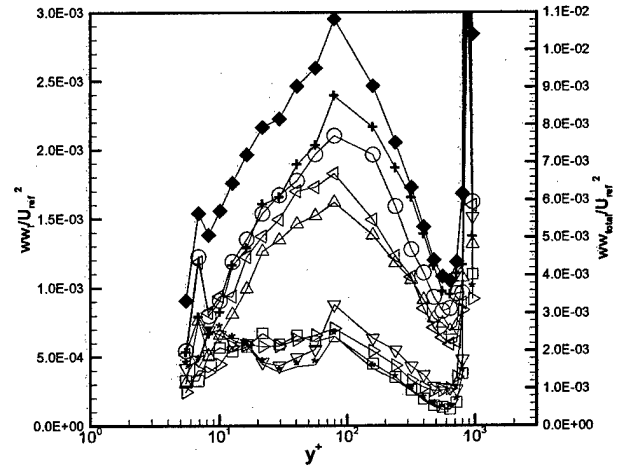
Profile name: [ΠΠΠ]



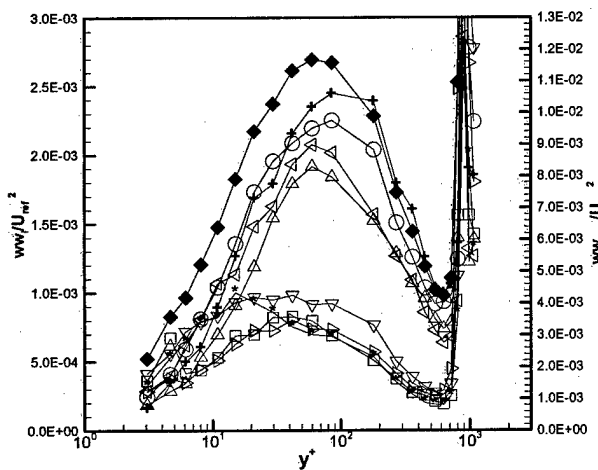
Profile name: [7U]



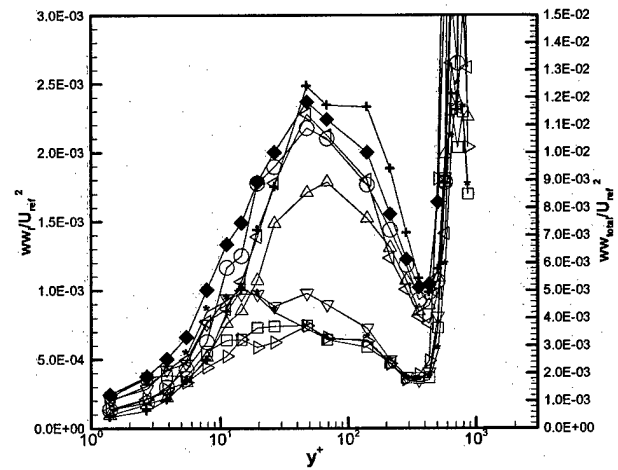
Profile name: [7P]



Profile name: [7B]



Profile name: [7C]



Profile name: [7S]

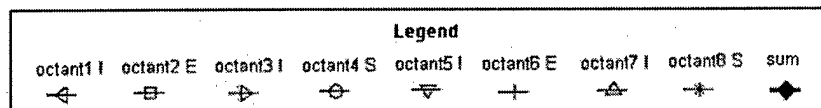
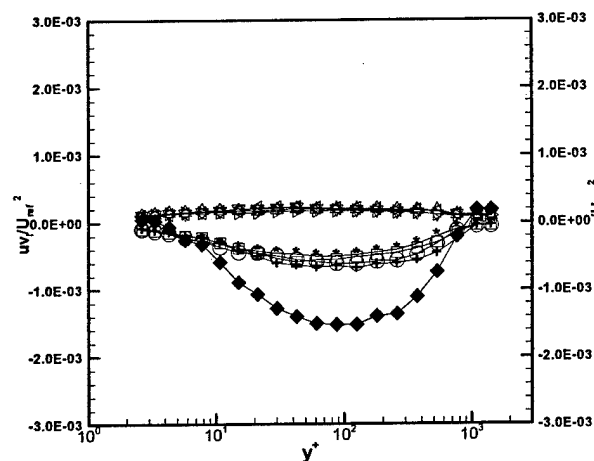
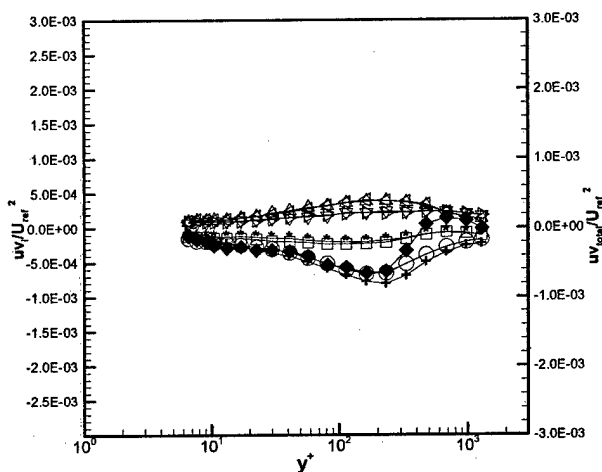


Figure 4.21 Octant contributions to Reynolds stress ww (U_{ref} is the free-stream velocity, local mean flow angle coordinates)

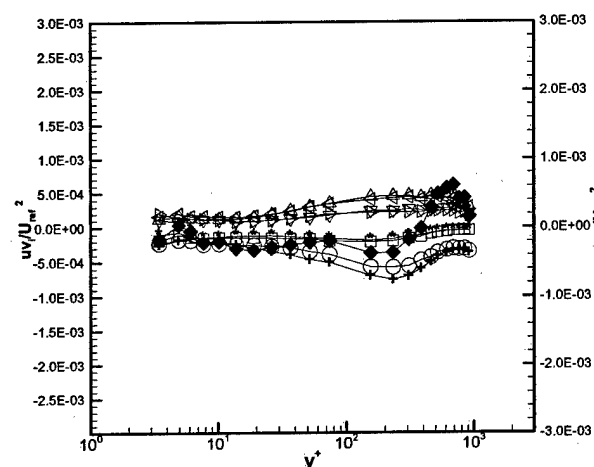
Chapter 4



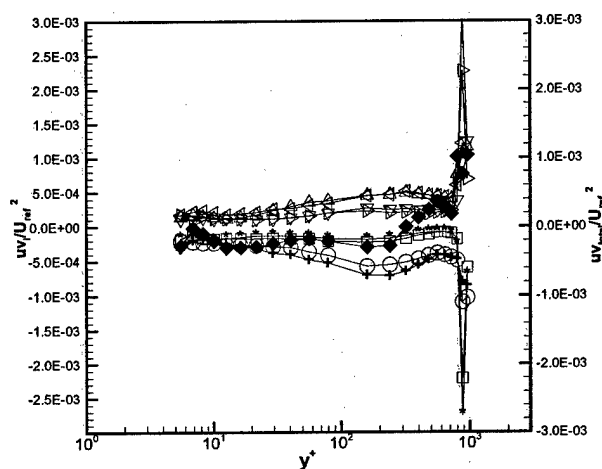
Profile name: [ΠΠ]



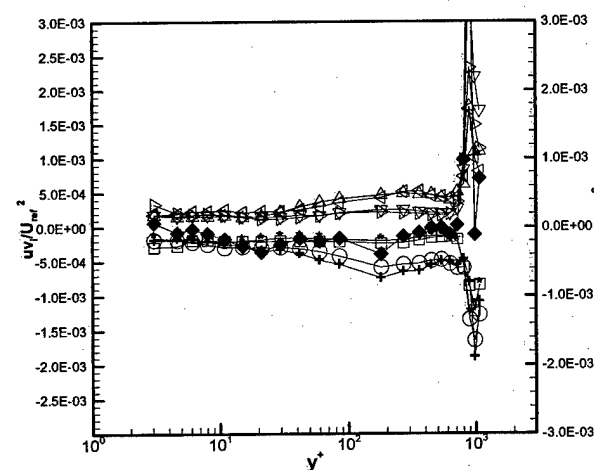
Profile name: [7Π]



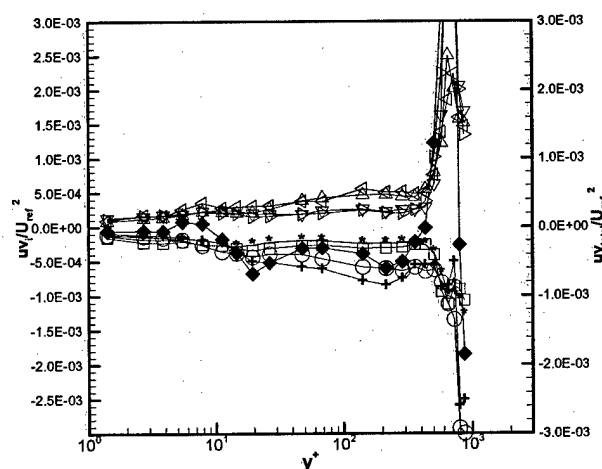
Profile name: [7P]



Profile name: [7B]



Profile name: [7C]



Profile name: [7S]

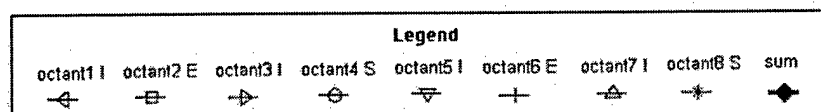


Figure 4.22 Octant contributions to Reynolds stress uv (U_{ref} is the free-stream velocity, local mean flow angle coordinates)

Chapter 4

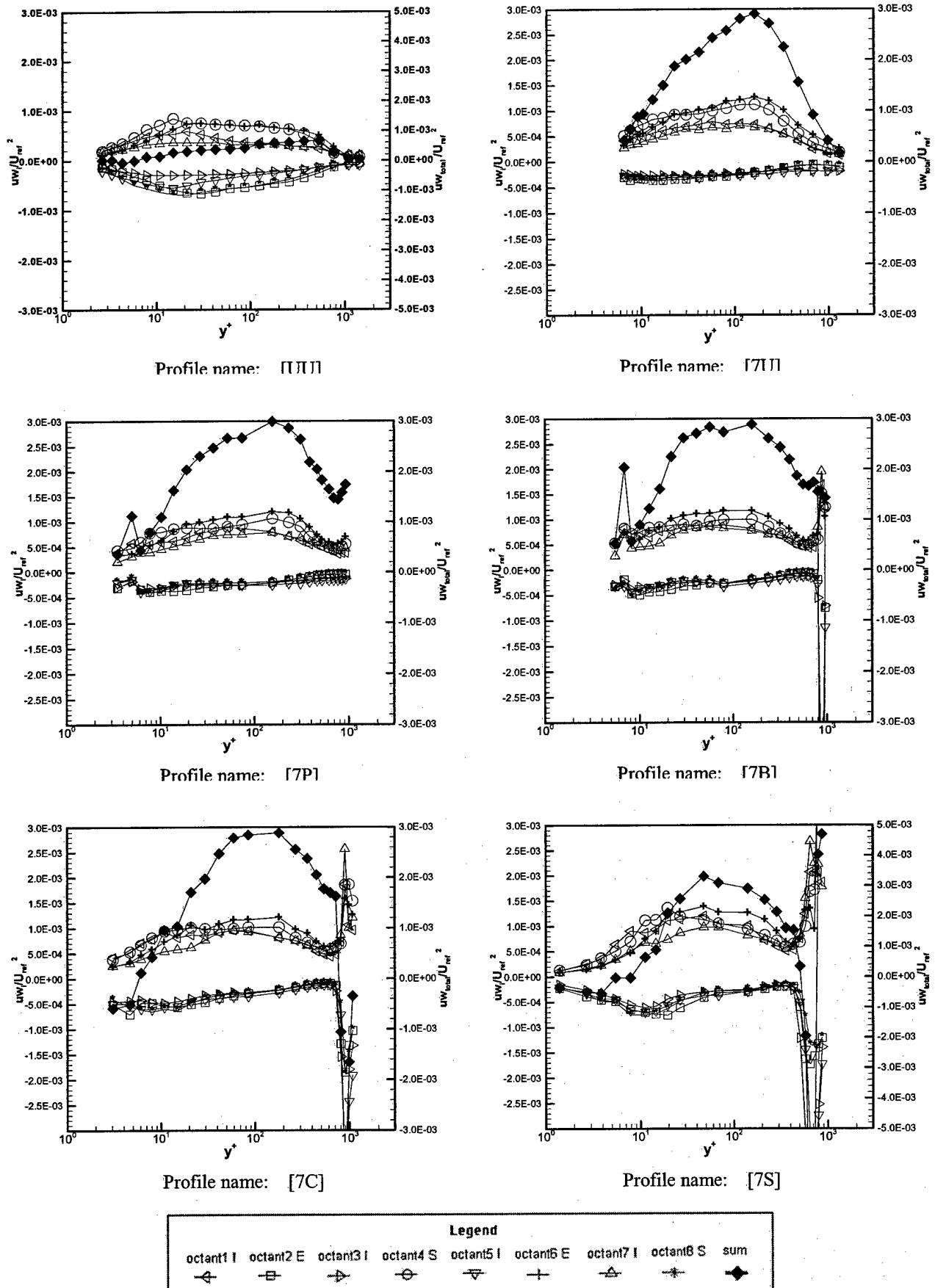
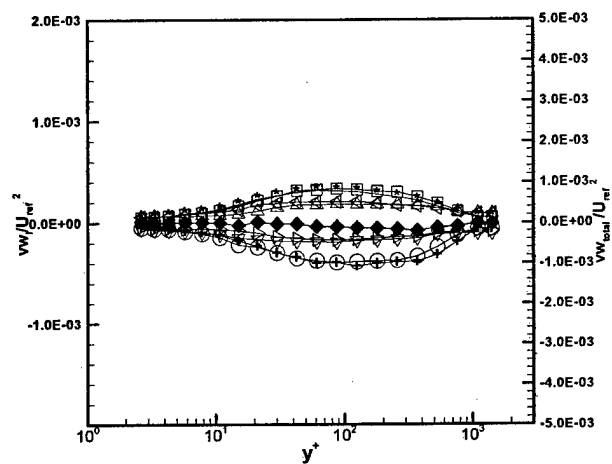
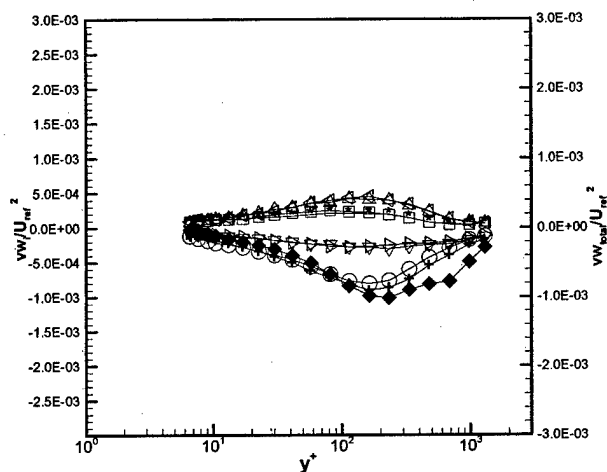


Figure 4.23 Octant contributions to Reynolds stress uw (U_{ref} is the free-stream velocity, local mean flow angle coordinates)

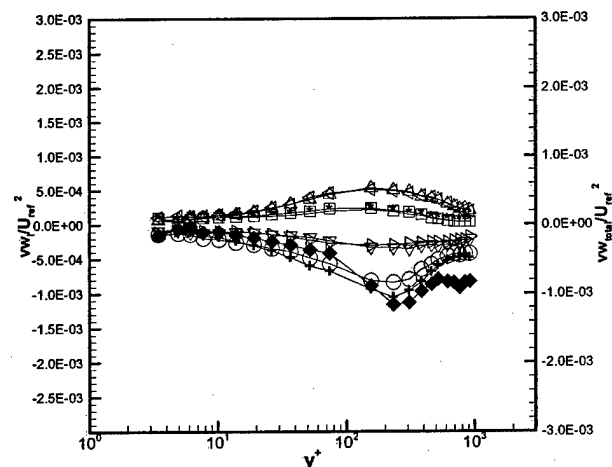
Chapter 4



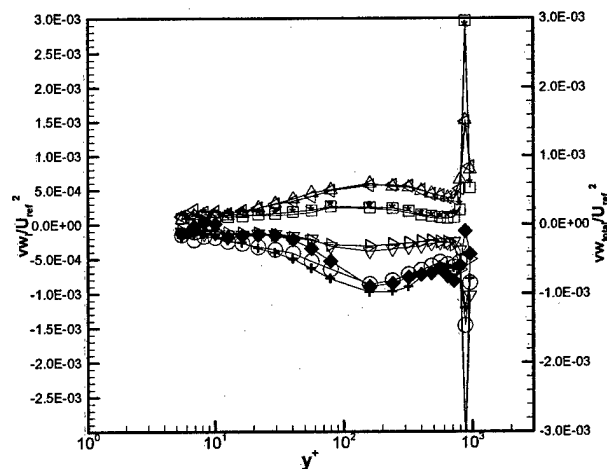
Profile name: [UU]



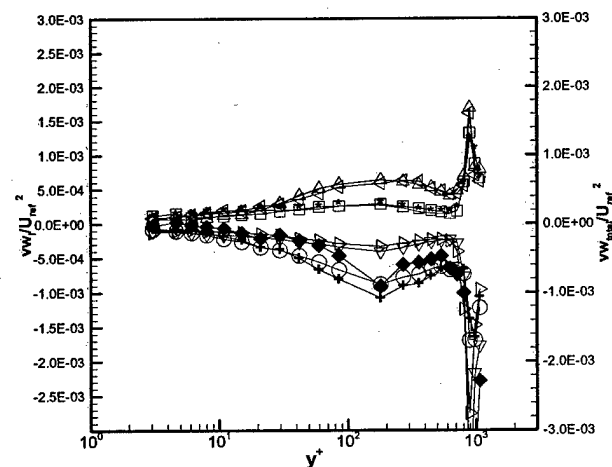
Profile name: [7U]



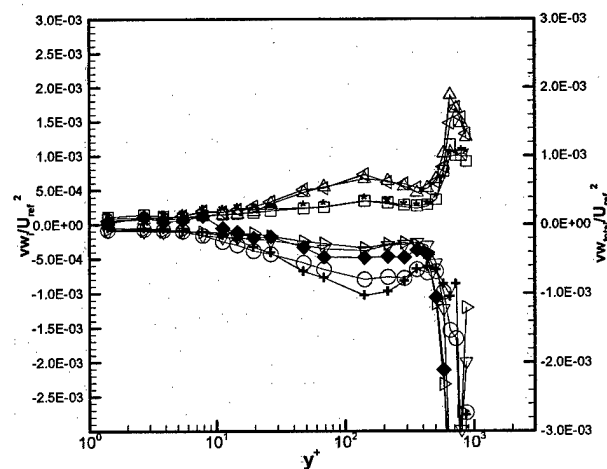
Profile name: [7P]



Profile name: [7B]



Profile name: [7C]



Profile name: [7S]

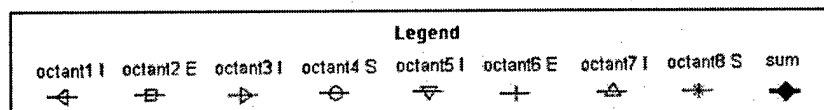


Figure 4.24 Octant contributions to Reynolds stress vw (U_{ref} is the free-stream velocity, local mean flow angle coordinates)

Chapter 4

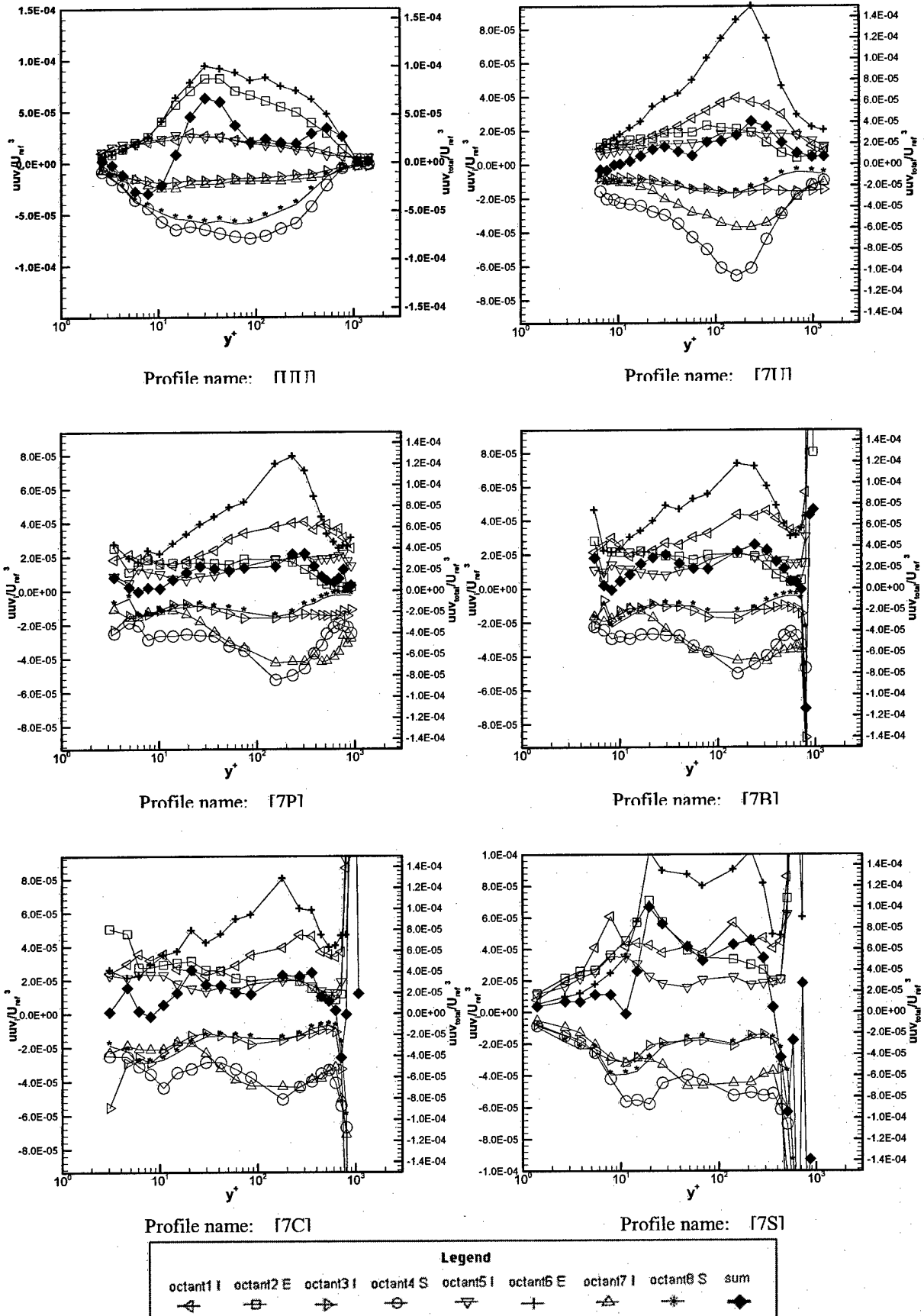


Figure 4.25 Octant contributions to uuv (U_{ref} is the free-stream velocity, local mean flow angle coordinates)

Chapter 4

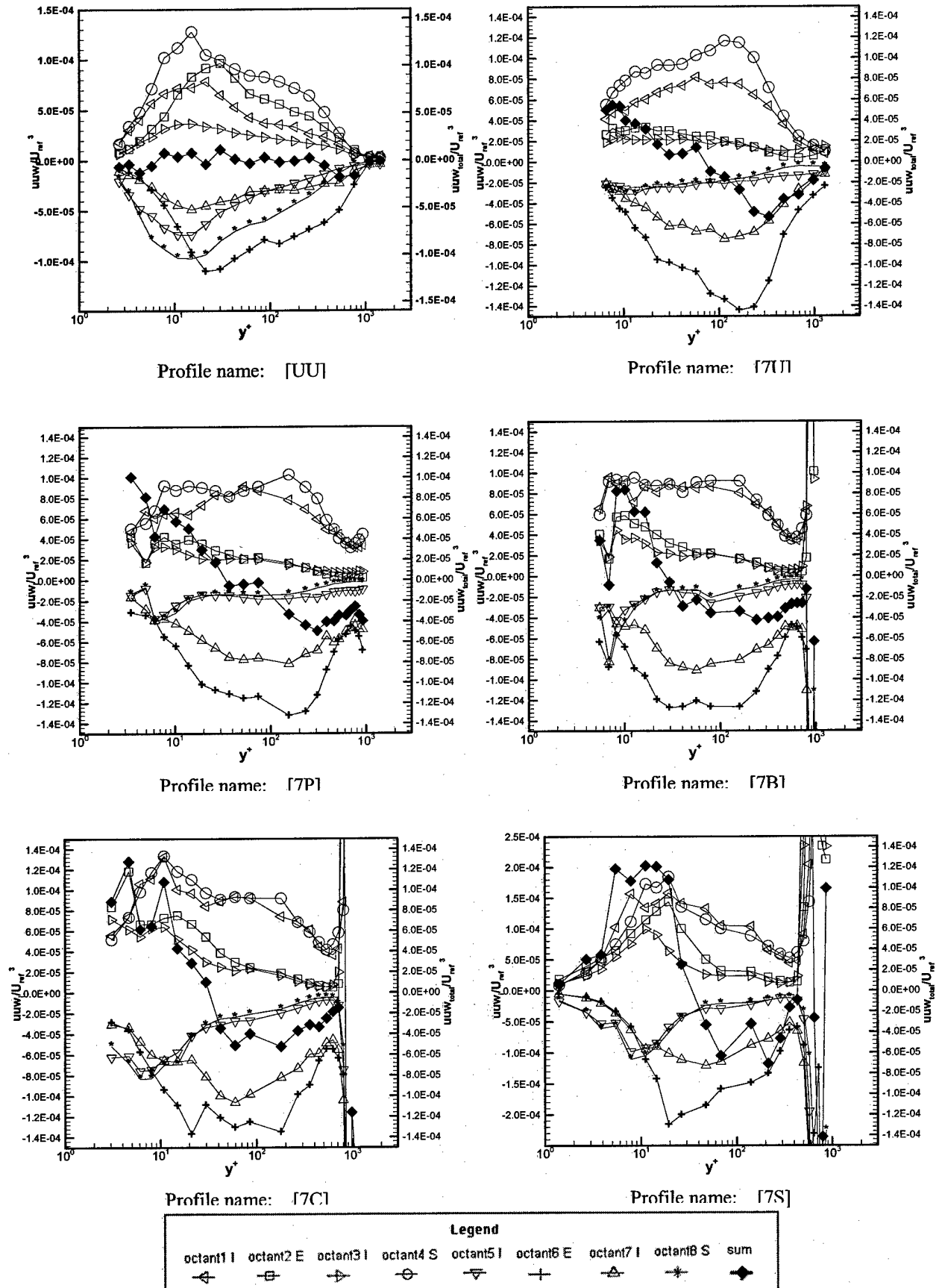


Figure 4.26 Octant contributions to $u w$ (U_{ref} is the free-stream velocity, local mean flow angle coordinates)

Chapter 4

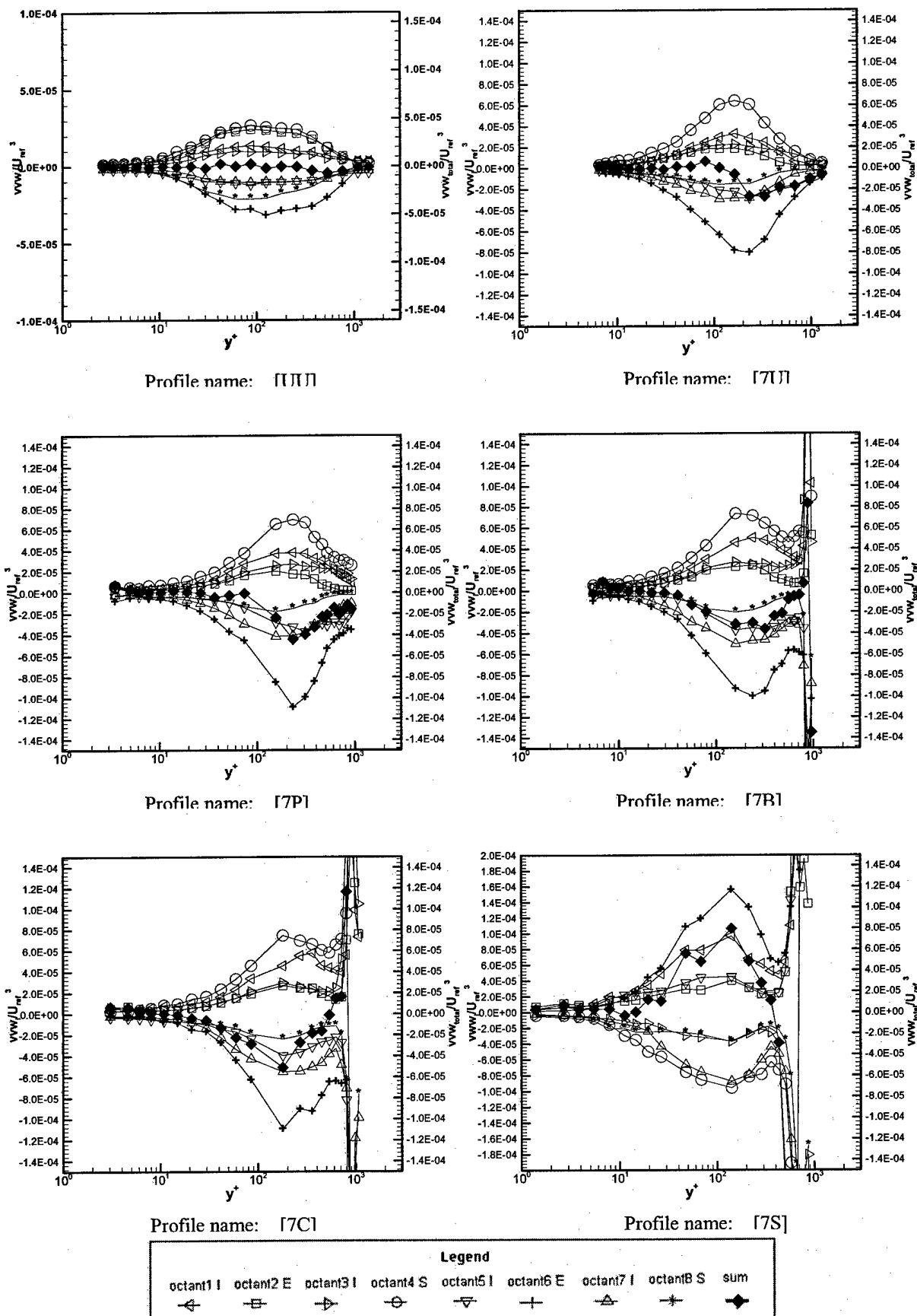


Figure 4.27 Octant contributions to vw (U_{ref} is the free-stream velocity, local mean flow angle coordinates)

Chapter 4

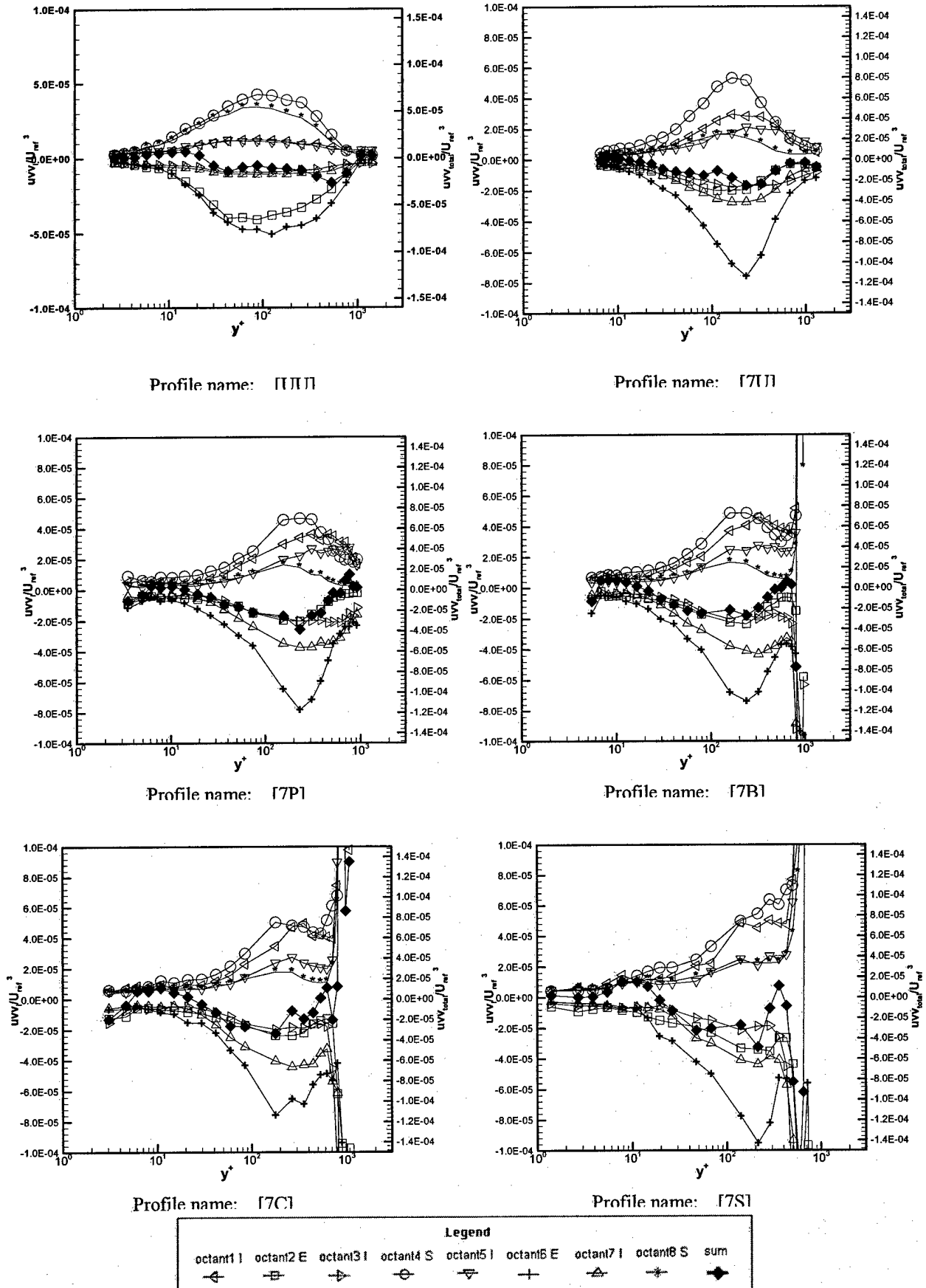


Figure 4.28 Octant contributions to uvv (U_{ref} is the free-stream velocity, local mean flow angle coordinates)

Chapter 4

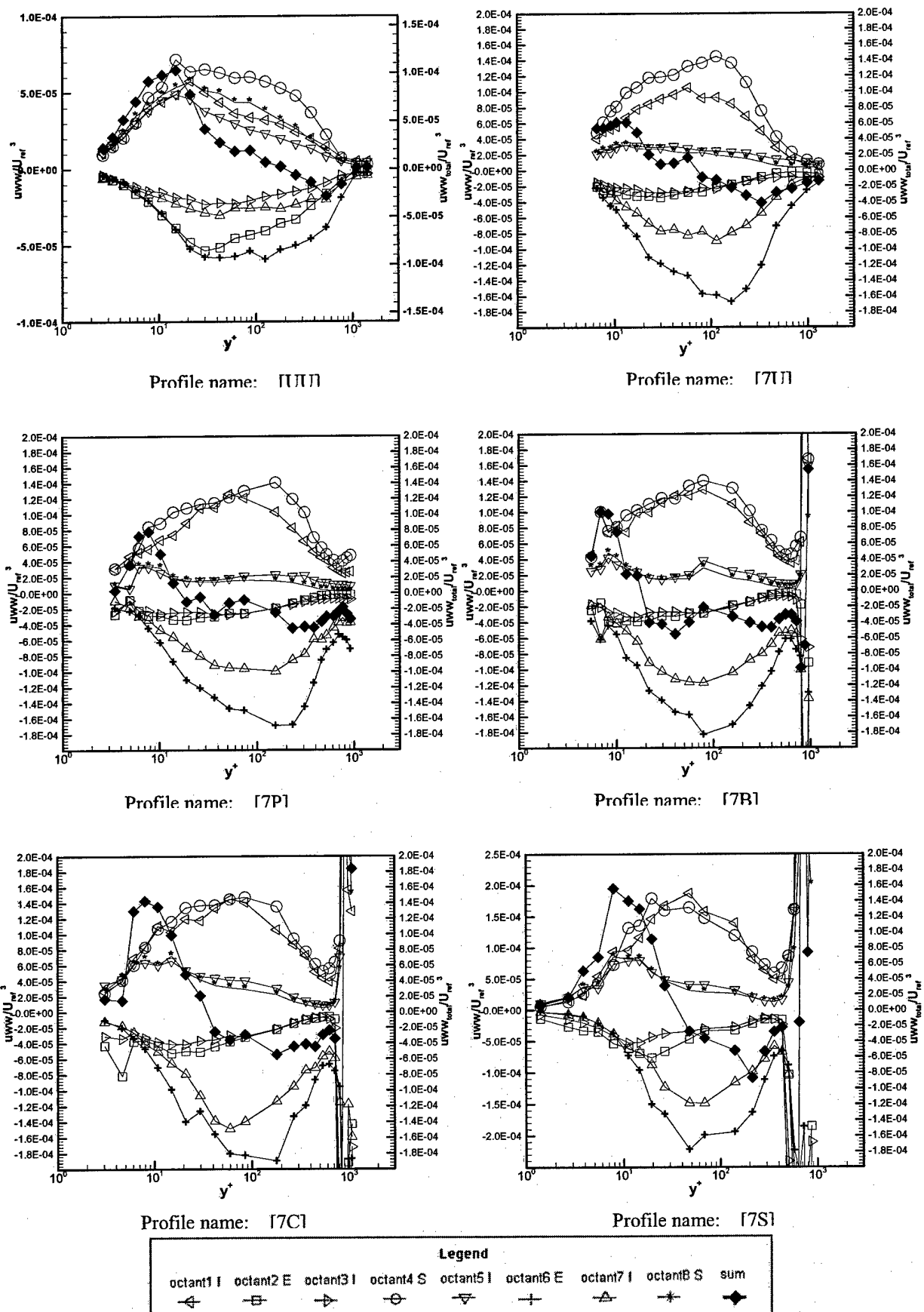


Figure 4.29 Octant contributions to uww (U_{ref} is the free-stream velocity, local mean flow angle coordinates)

Chapter 4

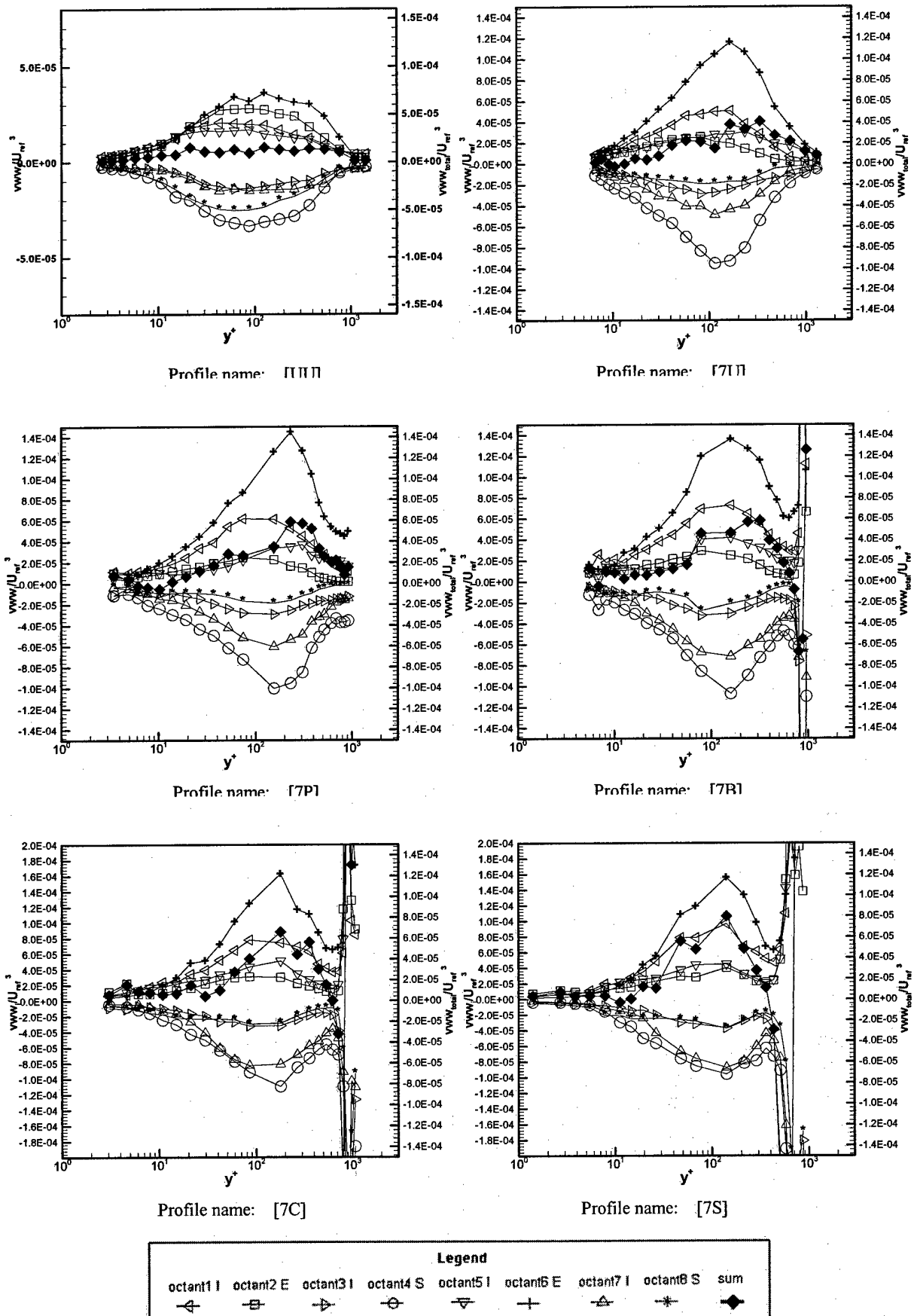


Figure 4.30 Octant contributions to v_{ww} (U_{ref} is the free-stream velocity, local mean flow angle coordinates)

Chapter 4

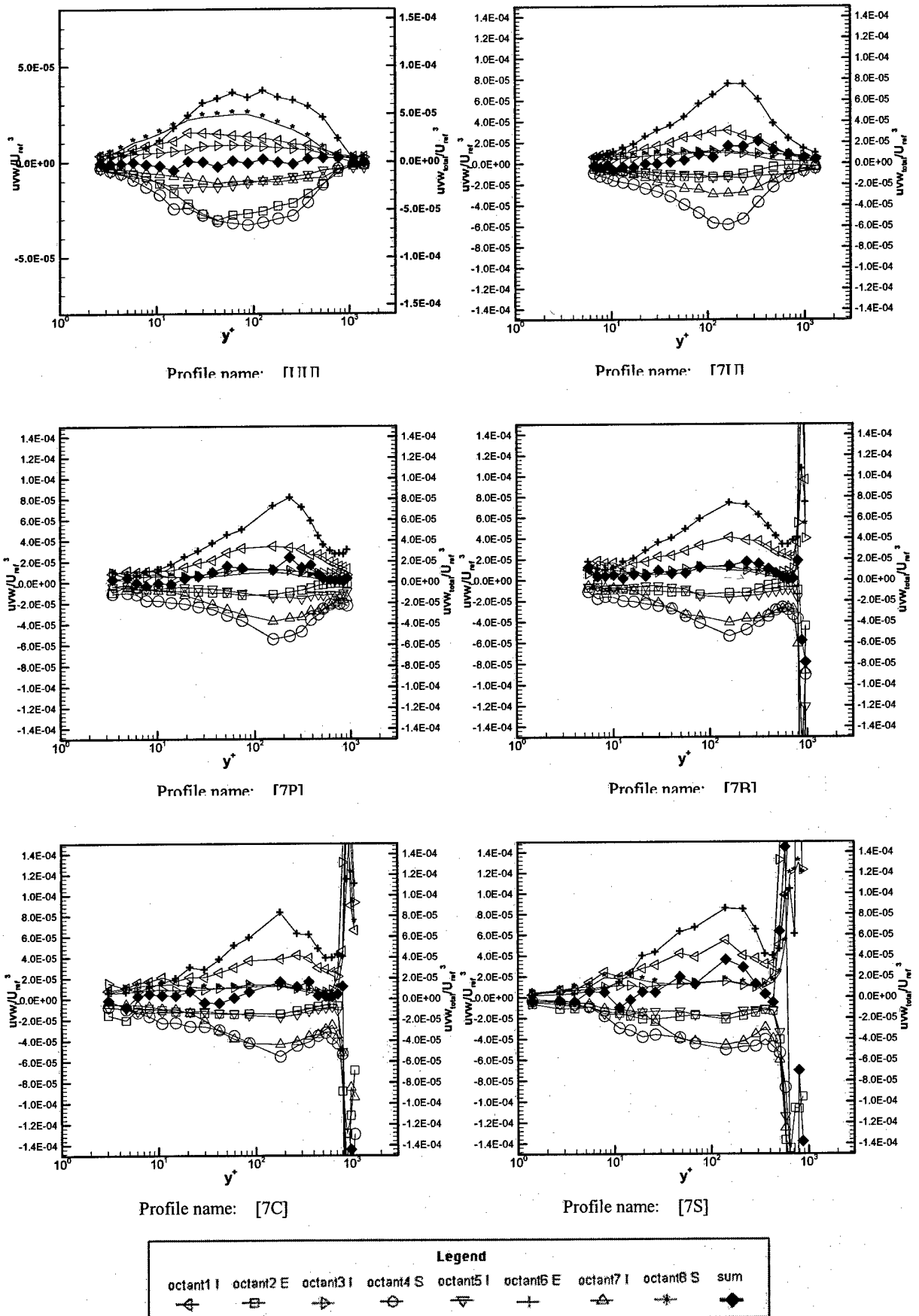


Figure 4.31 Octant contributions to uvw (U_{ref} is the free-stream velocity, local mean flow angle coordinates)

Chapter 4

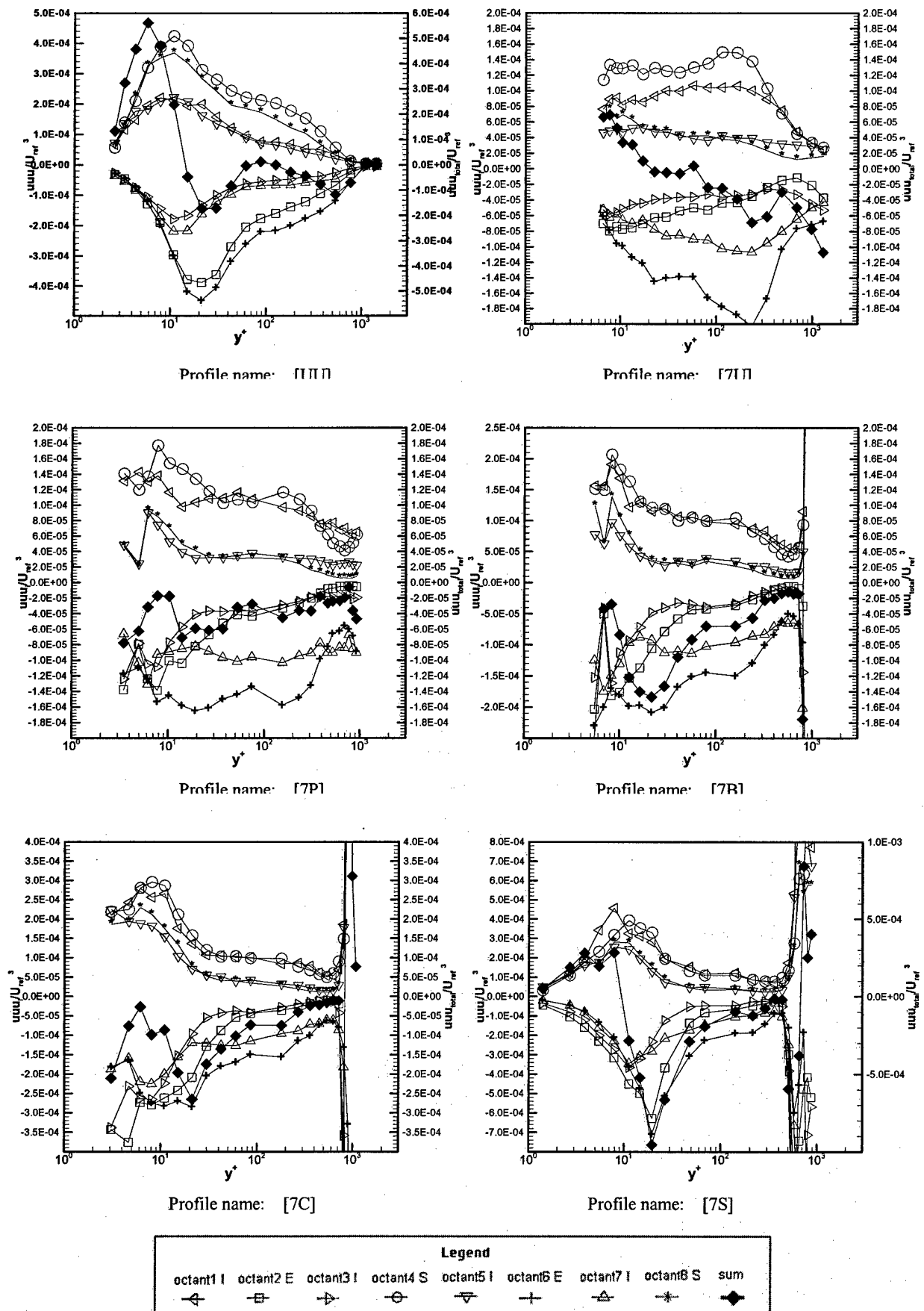


Figure 4.32 Octant contributions to uuu (U_{ref} is the free-stream velocity, local mean flow angle coordinates)

Chapter 4

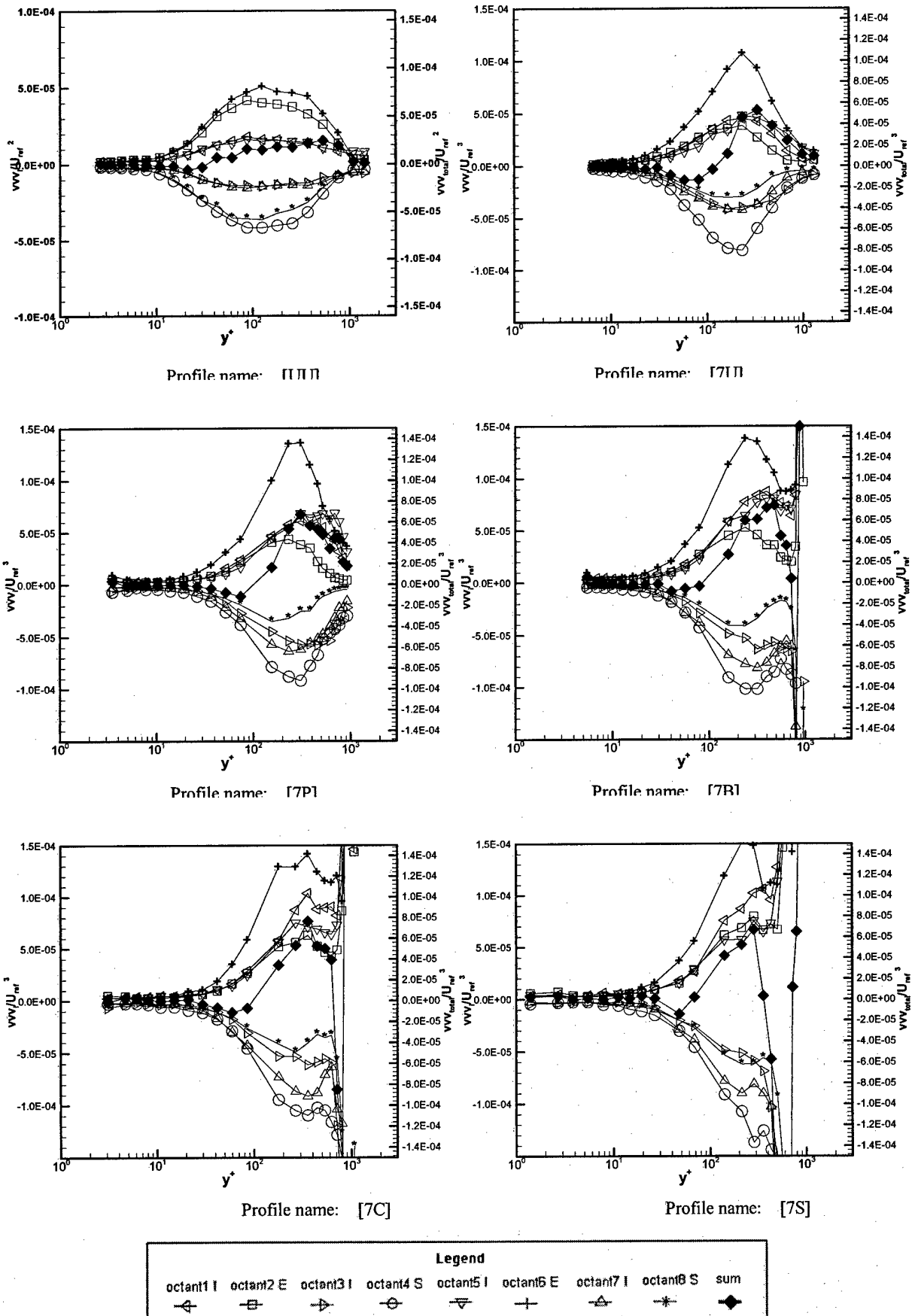


Figure 4.33 Octant contributions to vvv (U_{ref} is the free-stream velocity, local mean flow angle coordinates)

Chapter 4

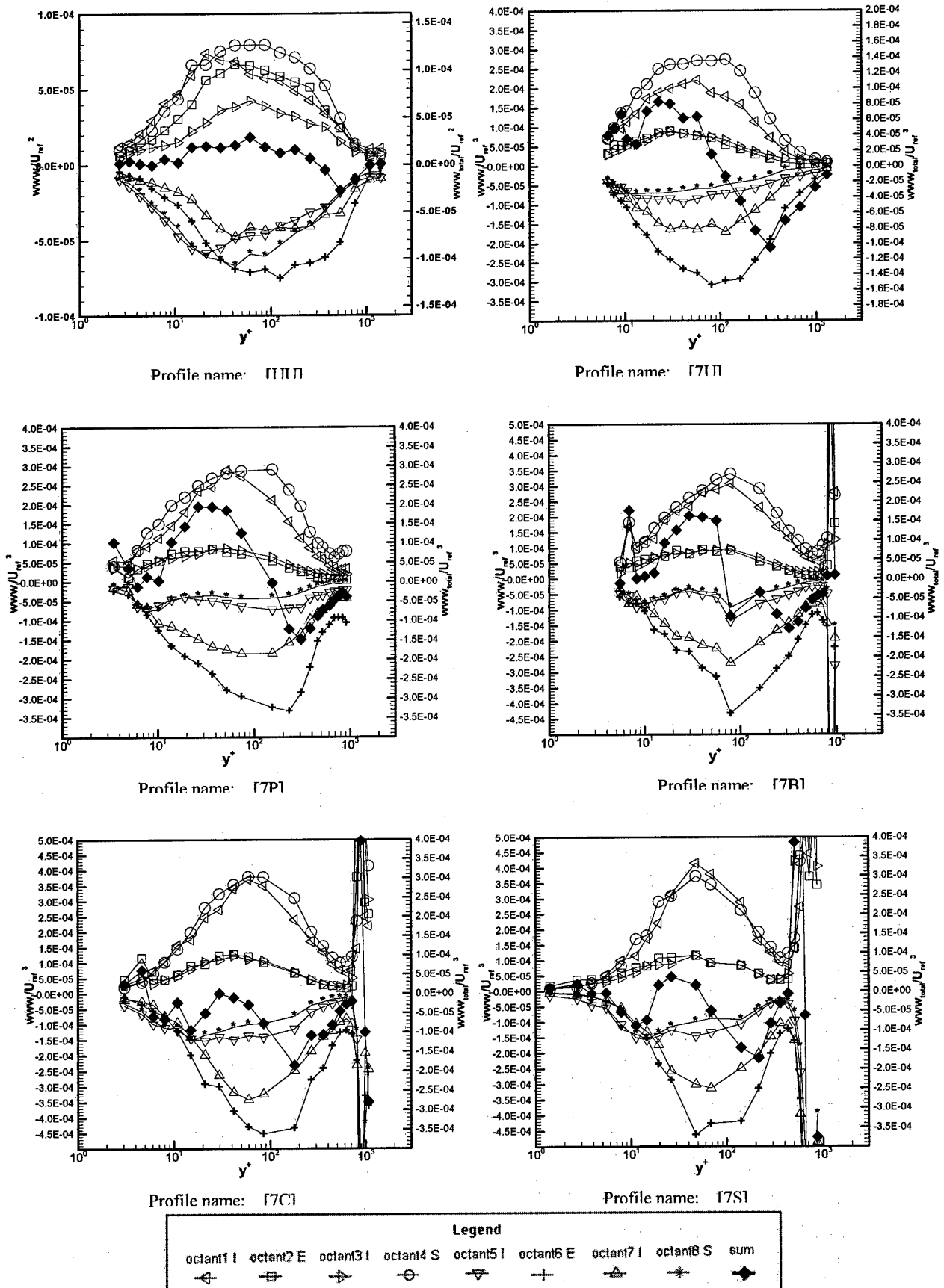


Figure 4.34 Octant contributions to w/w (U_{ref} is the free-stream velocity, local mean flow angle coordinates)

Chapter 4

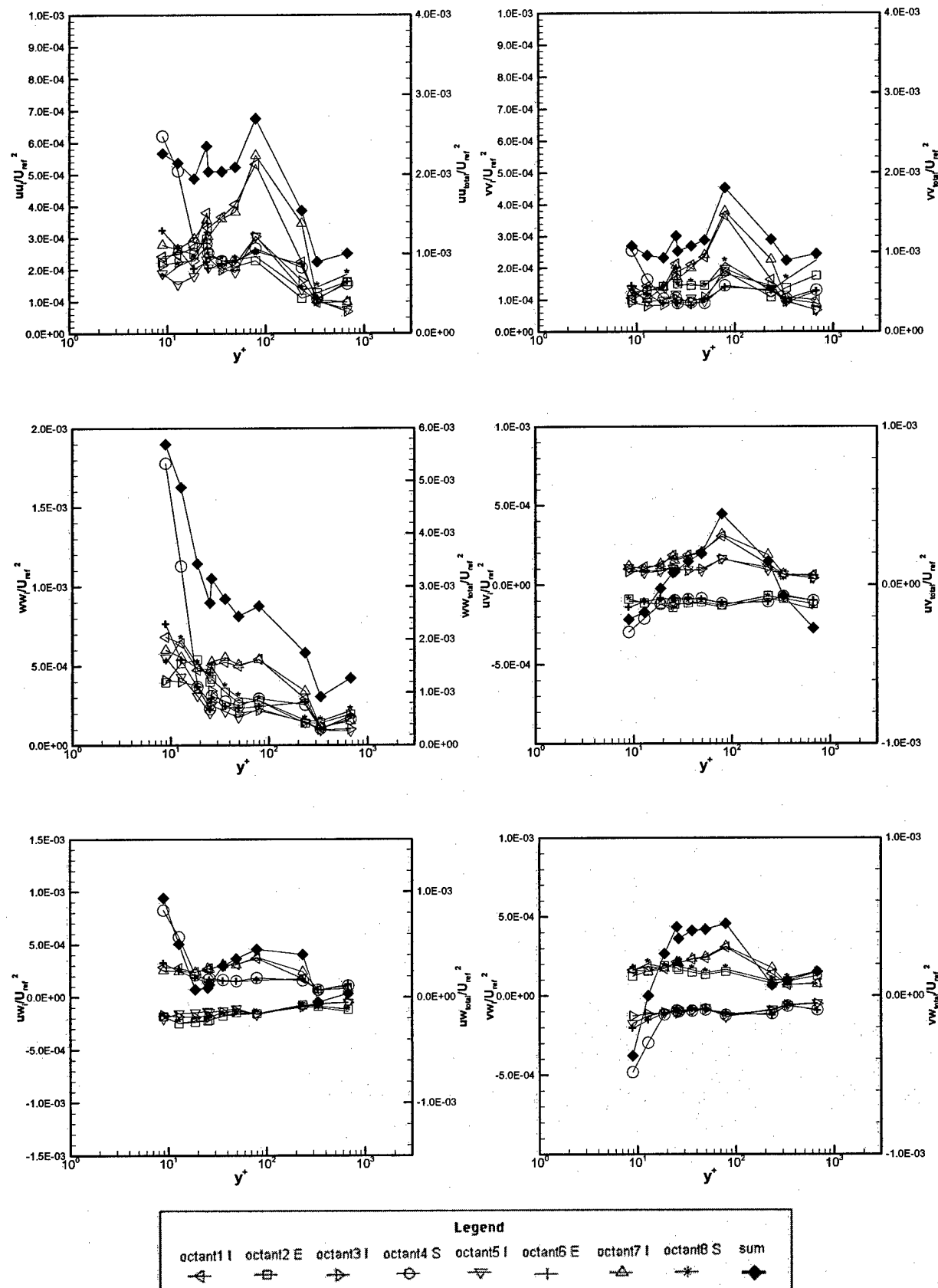


Figure 4.35 Octant contributions to Reynolds stress, local mean flow coordinates

U_{ref} is the free-stream velocity Profile name: Moving wall flow

Chapter 4

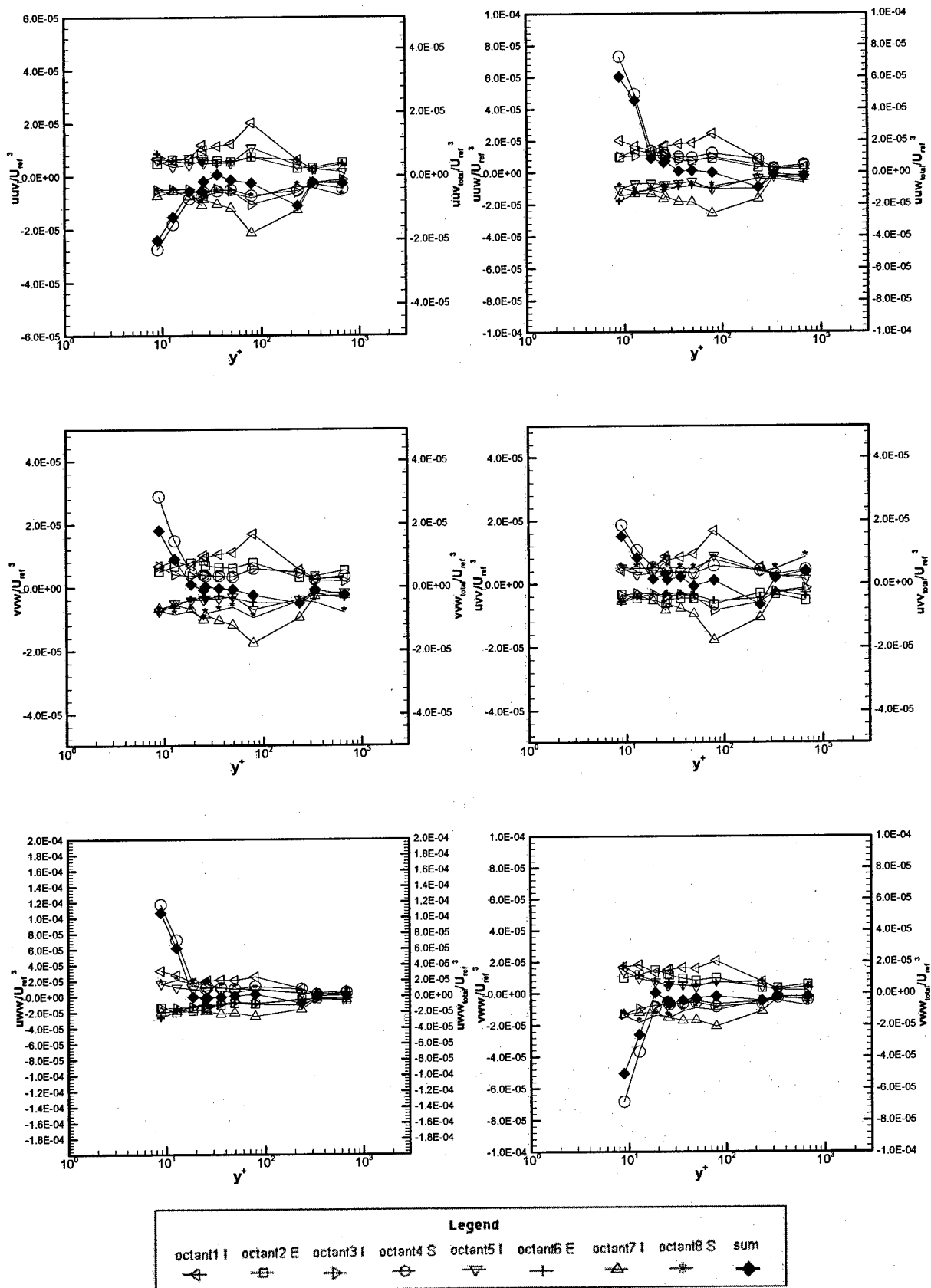


Figure 4.36 Octant contributions to triple product, local mean flow coordinates

U_{ref} is the free-stream velocity Profile name: Moving wall flow

Chapter 4

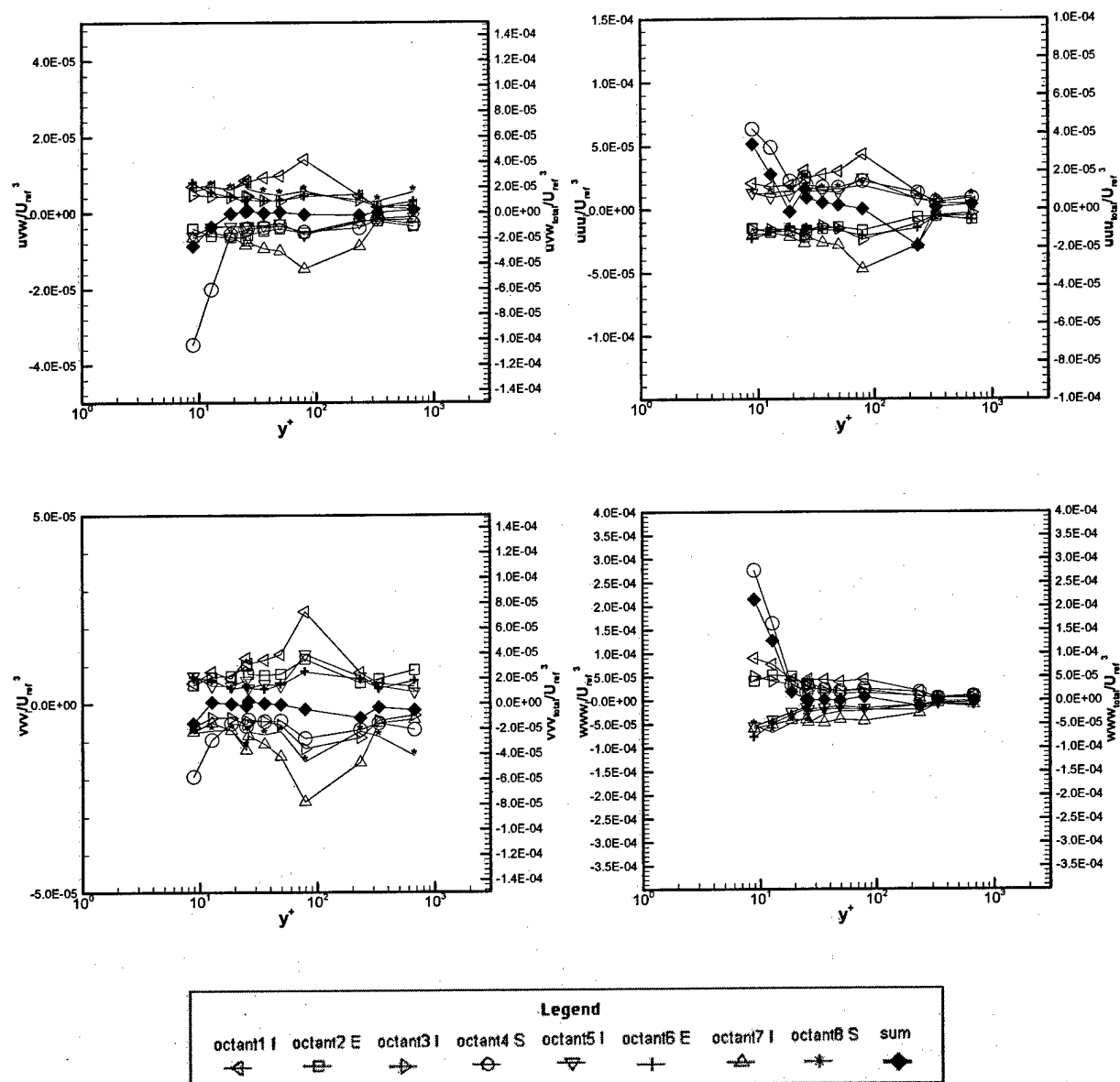
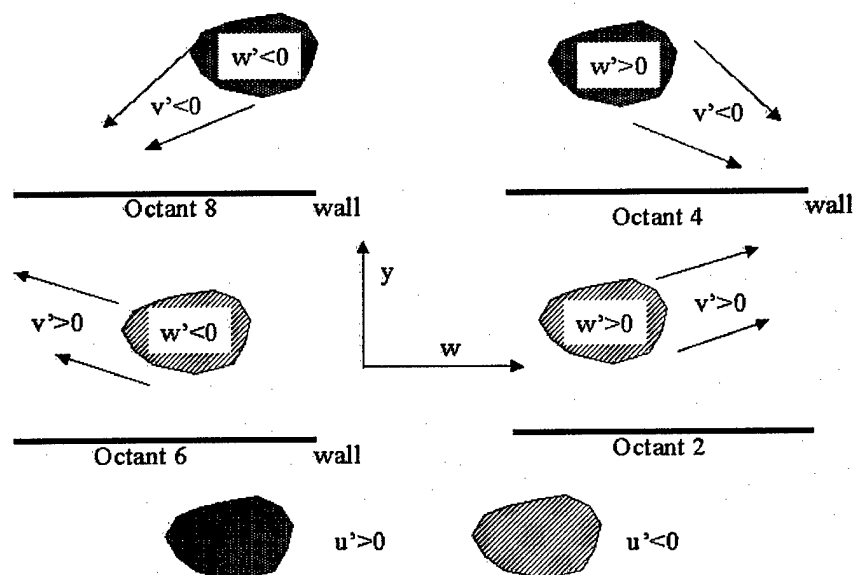


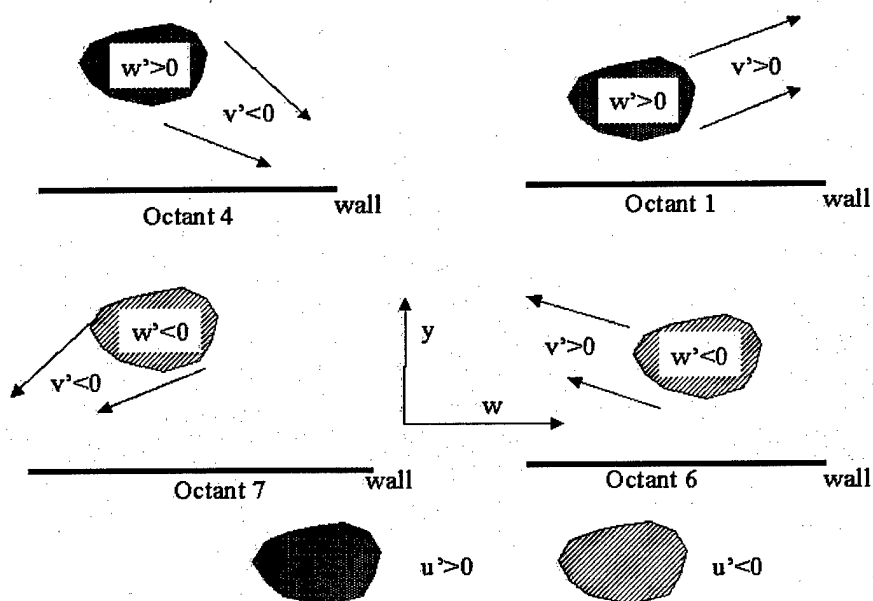
Figure 4.37 Octant contributions to triple product, local mean flow coordinates

U_{ref} is the free-stream velocity Profile name: Moving wall flow



High speed streaks: $u' > 0$; Low speed streaks: $u' < 0$ $y^+ < 1000$

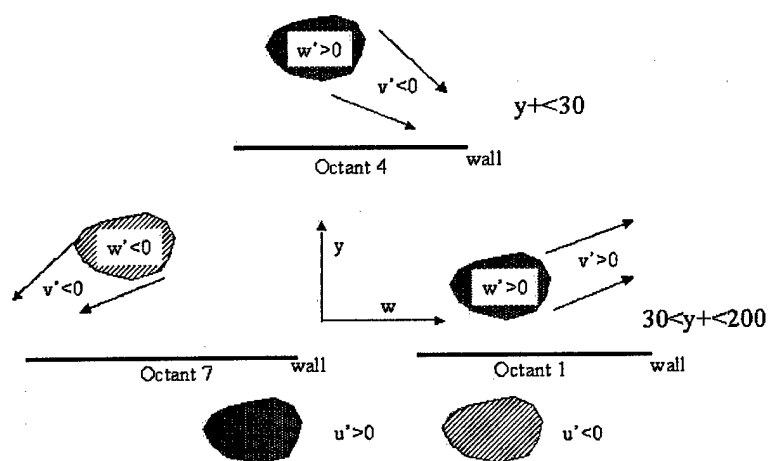
Figure 4.38 Dominant Octant Events in the 2D TBL



High speed streaks: $u' > 0$, $w' > 0$; Low speed streaks: $u' < 0$, $w' < 0$ $y^+ < 1000$

Figure 4.39 Dominant Octant Events in the 3D TBL

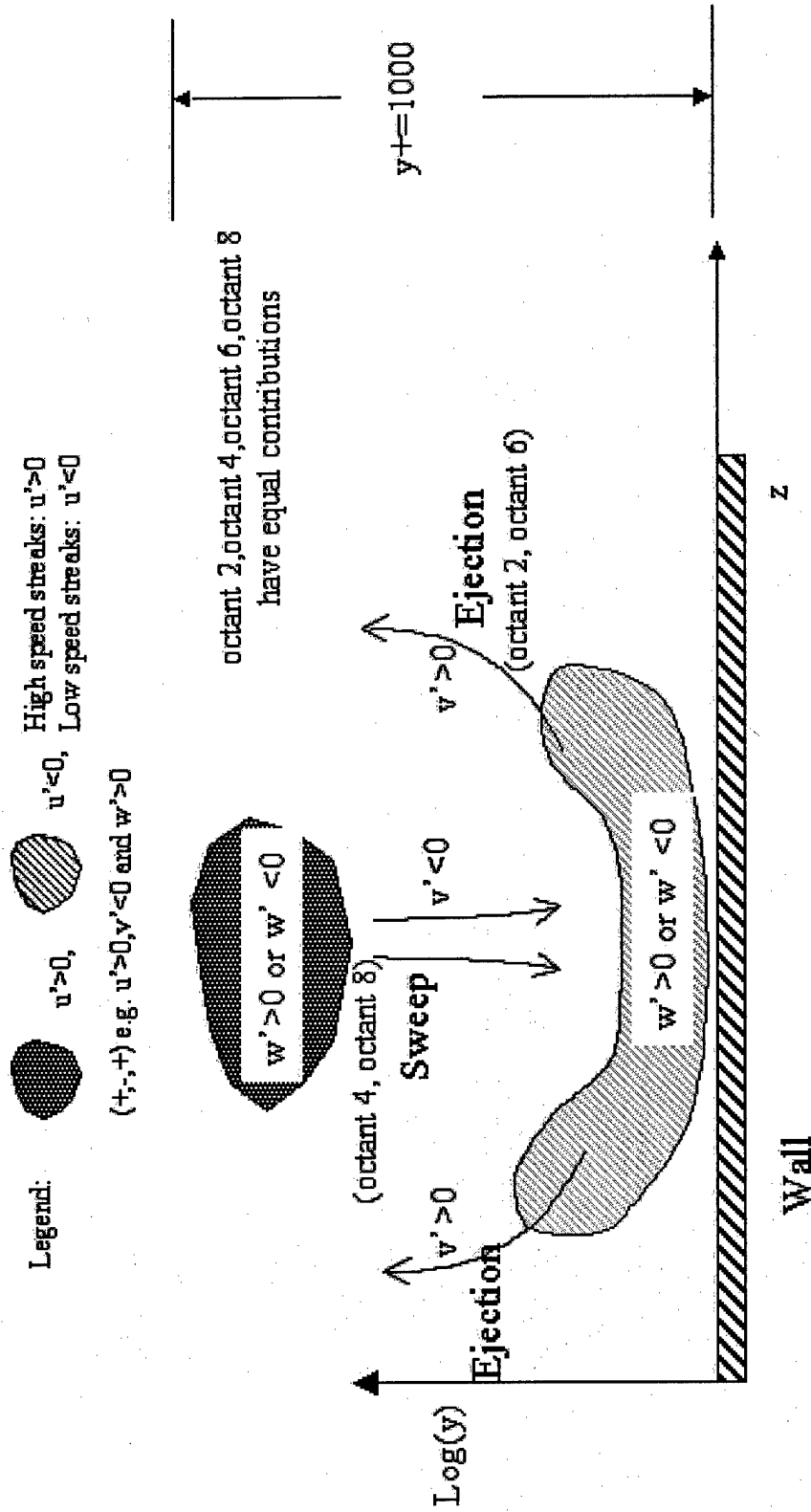
Chapter 4



High speed streaks: $u' > 0, w' > 0$; Low speed streaks: $u' < 0, w' < 0$ $y^+ < 1000$

Figure 4.40 Dominant Octant Events in the moving wall flow

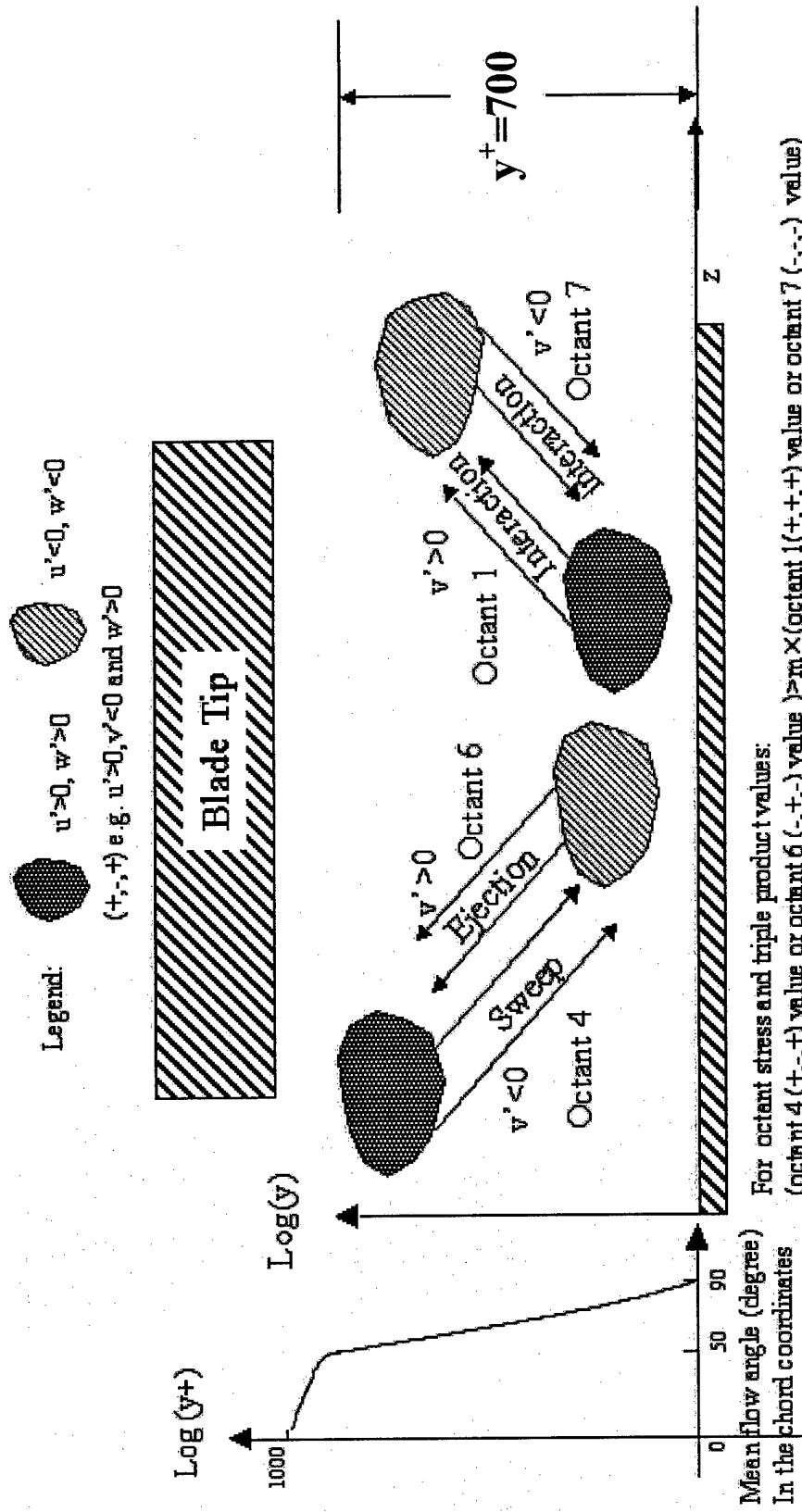
Spanwise Elevation View



Note: Mean $U > 0$, mean $W = 0$, Octant 2 ($-, -, +$), octant 4 ($+, -, +$), octant 6 ($-, +, -$), and octant 8 ($+, -, -$) contribute 60% - 90% to Reynolds stresses and triple products. Coherent motions are in the stream-wise direction

Figure 4.41 Out side sublayer near-wall sweep-ejection motion for 2D TBL

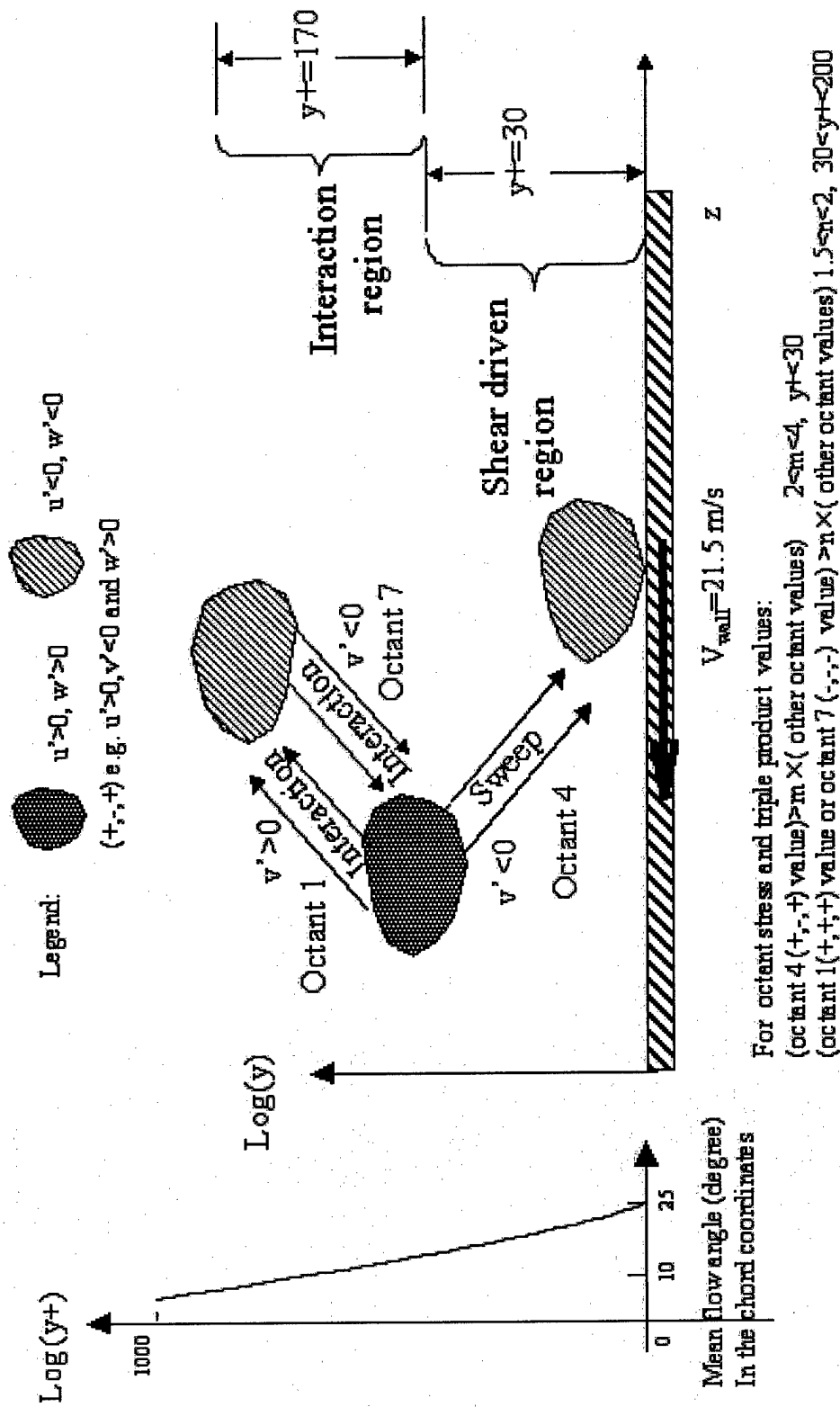
Spanwise Elevation View



Note: Mean $U > 0$, mean $W = 0$ in local mean flow coordinates, octant 4 $(+, -, +)$, octant 6 $(-, +, -)$, octant 1 $(+, +, +)$, and octant 7 $(-, -, -)$ contribute 60% - 80% to Reynolds stresses and triple products. Coherent motions are in the local mean flow direction.

Figure 4.42 The near wall sweep-ejection motion for 3D TBL in the blade tip gap

Spanwise Elevation View



Note: $U > 0, W = 0$, octant 4 (+,+,+) in $y^+ < 30$, and octant 1 (+,+,+) and octant 7 (-,-,-) in $30 < y^+ < 200$ contribute large values to Reynolds stresses and triple products. Coherent motions are in the local mean flow direction

Figure 4.43 The near wall seep-ejection motion for 3D TBL above Moving Wall

5. CONCLUSIONS

Experimental measurements (oil flow visualization, pressure measurements, and LDV measurements) were conducted in the Department of Aerospace and Ocean Engineering Low Speed linear Cascade Wind Tunnel of Virginia Tech. Surface oil flow visualizations for two different tip gaps ($t/c=1.65\%$ and 3.3%) were done on the lower end-wall with tip gap clearance. From the details of the flow pattern on the oil flow visualization, the features of flows (passage flow, cross flow and the tip leakage vortex) in this cascade inner flow are captured. The oil flow visualization on the blade surface used the same experimental procedure as the end-wall flow visualization. Oil flow visualization on the blade surface reveals the reattachment of the tip leakage vortex on the blade surface. For the 3.3% tip gap to chord ratio, the reattachments with and without the moving wall have the same shape, but the reattachment moves toward the leading edge of the blade.

Measurements of the static pressure on the end-wall were done using an automated data acquisition system (ADAS) with a pressure tap plate with 426 pressure ports, one pressure transducer and scanivalve system. The pressure data show that a huge pressure gradient exists between the pressure side and the suction side. The static pressure increases from the upstream to the downstream. From the pressure side to the suction side,

Chapter 5

the static pressure decreases and then increases. The trajectory of the tip leakage vortex coincides with a trough in pressure contour plots measured on the end-wall. The distributions are remarkably similar for both tip gaps. The origin of the trough matches with the local minimum pressure location on the end-wall, which is located under the blade tip. The local minimum pressure location is the origin of the tip leakage vortex. The CFD calculation with the Navier-Stokes code using K-epsilon model from Shin (2001) has a similar trough. The position of minimum pressure on the end-wall moves progressively downstream of the leading edge as the tip clearance is increased. Using the quadratic surface curve fit to the pressure data, the pressure gradient data were obtained.

The three-dimensional turbulent flow in the blade tip gap and tip leakage vortex was measured with a simultaneous three-orthogonal velocity component fiber optic laser Doppler anemometer (LDA) with and without a moving end wall. A post-processing data reduction procedure uses the momentum equation and pressure gradient in the direction of the wall shear stress in a least square fit of sublayer data to extract two unknowns, the skin friction (C_f) and wall position refinement (Δy). Resultant trends of the skin friction velocities match with the observation in the oil flow visualization. The investigation introduced a dynamic model that explains the octant results.

In the two-dimensional turbulent boundary layers, ejections of the low speed streaks outward from the wall and the sweeps of high speed streaks inward toward the wall are generated in with nearly equal contributions to Reynolds stresses. The likeness and symmetry of the octant events in the shear stresses $\overline{u'w'}$ and $\overline{v'w'}$ gives the physical evidence that these positive and negative stream-wise vortices happen evenly in the average of time and space domains. In the two-dimensional turbulent boundary layers, for

Chapter 5

the normal stress $\overline{w'w'}$, the contributions for all octants events are near equal, and $\overline{u'w'}$ and $\overline{v'w'}$ are close to zero.

For the three-dimensional turbulent boundary layers, the cross flow under the blade tip, is highly three-dimensional, and the appearance of another solid boundary (blade tip) above the end-wall affects the near-wall behavior of the coherent motions. The ejections of the low speed streaks outward from the solid wall (blade tip and end-wall) and the sweeps of high speed streaks inward toward the wall (blade tip and end-wall) are the dominant motions. These ejections and sweeps (octants 4 and 6) and interactions (octants 1 and 7) dominations in the Reynolds stresses and triple products show the high correlation of the instantaneous velocities of dominant coherent motions. The production of the turbulence is due to the intermittent motion between the high momentum and low momentum streaks. The spanwise velocity gradient plays an important role in the dynamics of this three-dimensional turbulent boundary layers. Thus, the mechanism of w' should bring to our attention to explain the occurrence of non-zero $\overline{u'w'}$ and $\overline{v'w'}$ and the tremendous drop of $\overline{u'v'}$.

For the moving wall case, the near-wall flow is a shear flow, driven by the moving belt, while away from the wall, the flow is pressure driven. The shear flow reinforces the sweep motion. Because the moving belt introduces the higher momentum to the near-wall fluid ($y^+ < 30$), less low speed streaks are generated, and also ejection events are little. The region $30 < y^+ < 200$ is actually the interaction region of the high speed streaks and the low speed streaks between the shear flow and the pressure driving flow. The production of the

Chapter 5

turbulence is due to the intermittent ejection and sweep motion between the high momentum and low momentum streaks.

6. REFERENCE

AGARD, Advisory Group for Aerospace Research and Development, 1996, "Turbulent Boundary Layers in Subsonic and Supersonic Flow," AGARD-AG-335, North Atlantic Treaty Organization, pp. 25-28.

Anderson, S.D., and J.K. Eaton, Aug. 1987, "Experimental Study of a Pressure-Driven, Three-Dimensional, Turbulent Boundary Layer," AIAA J., Vol. 25, No. 8pp. 1086-1092.

Chesnakas, C. J. and Simpson, R. L., 1994, "Three-Dimensional Turbulence Structure in the Vicinity of a 3-D Separation.", Forum on Turbulence in Complex Flows, Chicago.

Chiang, C. and Eaton, J. K., June 1993, "An Experimental Investigation of Corotating Disks and Single Disk Flow Structures", Thermosciences Division, Stanford University, Report MD-62.

Durst, F., Martinuzzi, R., Sender, J., and Thevenin, D., 1992, "LDA-Measurements of Mean Velocity, RMS-Values and Higher Order Moments of Turbulence Intensity Fluctuations in Flow Fields with Strong Velocity Gradients", Proceedings of the 6th International Symposium on Applications of Laser Techniques to Fluid Mechanics, Lisbon, Portugal, paper 5.1.1. Durst, F., Melling, A., and Whitelaw, J.H., 1981 Principles and Practice of Laser-Doppler Anemometry, Second ed., Acad. Press, pp. 32.

Durst, F., Jovanovic, J. and Sender, J., 1995, "LDA measurements in the near-wall region of a turbulent pipe flow", Journal of Fluid Mechanics, Vol. 295, pp. 305-335.

Durst, F., Kikura, H., Lekakis, I., Jovanovic, J. and Ye, Q., 1996. "Wall shear stress determination from near-wall mean velocity data in turbulent pipe and channel flows", Experiments in Fluids, 20, pp. 417-428.

Eaton, J. K., June 1994, "The Effects of Mean Flow Three Dimensionality on the Turbulent Boundary Layer Structure", 25th AIAA Fluid Dynamics Conference, Colorado, AIAA-94-2225.

Flack, K. A., and Johnston, J. P., July 1993, "Near-Wall Investigation of Three-Dimensional Turbulent Boundary Layers", Thermosciences Division, Stanford University, Report MD-63.

Chapter 6

Fleming, J. and Simpson, R., January 1994, "Experimental Investigationn of the Near-wall Flow Structure of a Low Reynolds Number 3-D Turbulent Boundary Layer", 32nd Aerospace Sciences Meeting & Exhibit, Reno, AIAA-94-0649.

Fleming, J. L., Simpson, R. L. and Shinpaugh, K. A., January 1995, "Further Investigation of the Near-wall Flow Structure of a Low Reynolds Number 3-D Turbulent Boundary Layer", 33rd Aerospace Sciences Meeting & Exhibit, Reno, AIAA-95-0788.

Jeong, J. F., Hussain, W. S., and Kim, J., 1997, "Coherent Structures Near the Wall of Turbulent Channel Flow," *Journal of Fluid Mechanics*, 332, pp.185-214.

Kang, H. S., Choi, H., and Yoo, J. Y., 1998, "On the Modification of the Near-Wall Coherent Structure in a Three-Dimensional Turbulent Boundary Layer on a Free Rotating Disk" *Physics of Fluids* 10, 9, pp. 2315-2322.

Kang S and Kirsh C, 1993a, "Experimental study of the three-dimensional flow within a compressor cascade with tip clearance: Part 1 - Velocity and pressure fields", *Journal of Turbomachinery*, vol. 115, July, pp 435-443.

Kang S and Kirsh C, 1993b, "Experimental study of the three-dimensional flow within a compressor cascade with tip clearance: Part 2- The tip-leakage vortex", *Journal of Turbomachinery*, vol. 115, July, pp 444-452.

Kang S and Hirsh C, 1994, "Tip leakage flow in a linear compressor cascade", *Journal of Turbomachinery*, vol. 116, pp. 657-664.

Kim, J., Moin, P. and Moser, R. 1987 "Turbulence statistics in fully developed channel flow at low Reynolds number", *Journal of Fluid Mechanics* Vol. 177, pp. 133-166.

Kuhl D D, 2001, "Near-wall investigation of three-dimensional turbulence boundary layer", M.S. thesis, Aerospace and Ocean Engineering Dept., Virginia Polytechnic Institute and State University.

Kuhl D D and Simpson R L, 2000, "Near-wall investigation of embedded streamwise vortex pairs", Tenth International Symposium on Applications of Laser Techniques to Fluid Mechanics, Lisbon, Portugal.

Lakshminarayna, B., 1970, "Method of Predicting the Tip Clearance Effects in Axial Flow Turnbomachinery", *ASME Journal of Basic Engineering*, Vol.92, pp.467-480.

Littell, H.S., and J.K. Eaton, 1991, "The Unsteady Flowfield Behind a Vortex Generator Rapidly Pitched to Angle of Attack," *AIAA J.*, Vol. 29, No. 4pp. 577-584.

Chapter 6

Ma, R., 2003, "Unsteady Turbulence Interaction in a Tip Leakage Flow Downstream of a Simulated Axial Compressor Rotor", Ph.D dissertation, Aerospace and Ocean Engineering Dept., Virginia Polytechnic Institute and State University.

Madden, M.M., and Simpson, R.L. 1997 "Octant Analysis of the Reynolds Stresses in the Three-Dimensional Turbulent Boundary Layer of a Prolate Spheroid", Aerospace and Ocean Engineering Dept, VPI&SU, Report Number VPIAOE- 252.

Macrodyne 1992 "Laser Doppler Velocimetry (LDV) Electronics Frequency Domain Processor Model 3100 Users Manual ", Rev. 060192A, Macrodyne Inc., 4 Chelsea Place, PO box 376, Clifton Park, NY 12065.

Moore, J., and Tilton, J. S., 1988, "Tip leakage flow in a linear Turbine cascade", ASME Journal of Turbomachinery, Vol. 100, pp. 18-26.

Muthanna C, 1998, "Flowfield downstream of a compressor cascade with tip leakage", M.S. thesis, Aerospace and Ocean Engineering Dept., Virginia Polytechnic Institute and State University.

Muthanna C, 2002, "The effects of free stream turbulence on the flow field through a compressor cascade", Ph.D. dissertation, Aerospace and Ocean Engineering Dept., Virginia Polytechnic Institute and State University.

Nagano, Y. and Tagawa, M., June 1990, "A structural turbulence model for triple products of velocity and scalar", J. Fluid Mech. (UK) 215 pp.639-57.

Ölçmen, S.M. and Simpson, R.L., 1995 "A five-velocity -component laser-Doppler velocimeter for measurements of a three-dimensional turbulent boundary layer", Measurement Science and Technology, Vol. 6, pp. 702-716.

Prasad, C.P.K., 1977, "Tip Clearance Effect in Axial Flow Turbines", Indian Institute of Science, Report No. ME-TURBO-1-77.

Tian, Qing, Simpson, R. L., and Tang, Genglin, 2004, "Surface Oil Flow Visualization in the Linear Compressor Cascade with Tip Leakage", Under consideration for publication in Journal of Flow Visualization.

Robinson, S. K., Kline, S. J., and Sparlart, P. R., May 1989, "A Review of Quasi-Coherent Structures in a Numerically Simulated Turbulent Boundary Layer", Moffet Field, NASA-TM-102191.

Robinson, S. K., June 1990, "A Perspective on Coherent Structures and Conceptual Models for Turbulent Boundary Layer Physics", AIAA 21st Fluid Dynamics, Plasma Dynamics and Lasers Conference, Seattle, AIAA-90-1638,.

Chapter 6

Robinson, S. K., 1991, "Coherent Motions in the Turbulent Boundary Layer", *Annu. Rev. Fluid Mech.*, Vol. 23, pp. 601-639.

Sendstad, O. and Moin, P., December 1992, "On the Mechanics of 3-D Turbulent Boundary Layers", Thermosciences Division, Stanford University, Report No. TF-57.

Sendstad, O. and Moin, P., 1999, "The Near-wall Mechanics of Three-Dimensional Turbulent Boundary Layers", Eighth Symposium on Turbulent Shear Flows, Munich, pg. 5.4.1 - 5.4.5.

Shin, S., Ragab, S. A. and Devenport, W. J., 1999, "Numerical Simulation of Highly Staggered Cascade Flow Using an Un-structured Grid", AIAA 99-3713.

Shin, S., Ragab, S. A. and Devenport, W. J., 2001, "PANS Computation of Tip Clearance Flow in a Compressor Cascade Using an Unstructured Grid", AIAA 2001-2999.

Simpson, R. L. and Devenport, W. J., 1990, "A Conceptual Model for the Near-wall Region of Three- Dimensional Turbulent Boundary Layers", Boundary-Layer Structure Workshop, Langley Research Center, Hampton, Virginia.

Spalart, P.R., 1988, "Direct simulation of a turbulent boundary layer up to $R=1410$ ", *Journal of Fluid Mechanics*, Vol.187, pp. 61-98.

Tang, Genglin, Simpson, R. L., and Tian, Qing, 2004, "Measurement of the tip-gap turbulence structure for a stationary end-wall in a low-speed compressor cascade", Under consideration for publication in AIAA journal.

Tiederman, W. G. and Luchik, T. S., 1987, "Timescale and Structure of Ejections and Bursts in Turbulent Channel Flows", *Journal of Fluid Mechanics*, Vol. 174, pp. 529-552.

Volino, RJ and Simon, TW, 1994, "An Application of Octant Analysis to Turbulent and Transitional Flow Data", *ASME J. Turbomachinery*, Vol. 116, pp. 752-758.

Willmarth, W. W. and Lu, S. S., 1972, "Structure of the Reynolds Stress Near the Wall", *Journal of Fluid Mechanics*, Vol. 55, pp. 65-92.

Wang, Y., Muthanna, C., and Devenport, W. J., 1999, "The Design and Operation of a Moving End-wall System for a Compressor Cascade Wind Tunne", 37th Aerospace Sciences Meeting and Exhibit, Reno, NV, AIAA paper 99-0741, January 11-14.

Wang, Y, 2000, "Tip leakage flow downstream a compressor cascade with moving end wall", MS Thesis, Aerospace and Ocean Engineering Dept., Virginia Polytechnic Institute and State University.

Chapter 6

Wetzel, T. G., Simpson, R. L., and Chesnakas, C. J., 1998, "Measurement of Three-Dimensional Crossflow Separation", AIAA Journal, Vol. 36, No. 4, pp. 557-564.

You, D., Mittal, R., Wang, M., and Moin, P., 2002, "Large-Eddy Simulation of a Rotor Tip-Clearance Flow", AIAA 2002-0981.

Appendix A

A.1 Uncertainty analysis for the measurement location of the pressure measurement

The positions of the pressure ports in the cascade tunnel are measured as following process; firstly, the relative positions of the pressure ports to the center of the pressure plate are measure by using the vernier caliper, and the minima scale is 1/50 inch (0.00051m) and the uncertainty is ± 0.00025 m; secondly, let the blue line align in figure 1 with the x axis in the bed coordinates, which is normal to the tunnel edge, and the position of the center of the pressure plate in the bed coordinates need to measured by a ruler with ± 0.0005 m uncertainty, thus initial positions of the pressure ports in the cascade tunnel without pressure plate rotation are obtained through the coordinates transform; finally, the angle of the rotation of the pressure plate (about 45 degree once) relative to the initial position is measured by half-circle protractor, with the ± 0.25 degree uncertainty. Based on the measurement process of the pressure port position in the cascade tunnel, the uncertainties of the measurement location are coming from the above three uncertainties. The maximum displacement uncertainty from the angle rotation as shown in equation (A1) is proportional to the distance relative to the center of the pressure plate, and the maximum displacement uncertainty is ± 0.00044 m.

$$\delta_2 = \frac{\delta_1}{180} \times 3.14 \times R \quad (A1.1)$$

where

Appendix A

δ_1 is the angle uncertainty of the rotation

δ_2 is the displacement uncertainty of the rotation

R is the radius of the pressure plate is 0.1016 m.

The total uncertainty is given by the equation A2, and equal to the square root of the summation of the square of the each uncertainties.

$$\delta_5 = \sqrt{\delta_2^2 + \delta_3^2 + \delta_4^2} \quad (A1.2)$$

Where, $\delta_2 = 0.00044$ m, $\delta_3 = 0.0005$ m $\delta_4 = 0.00025$ m

Thus the total maximum uncertainty of the positions of the pressure ports in the cascade tunnel is ± 0.00071 m, and for those ports, which are closer to the center of the plate, the uncertainty for the pressure ports position should be less than 0.00071 m, and in the center of the plate, there is no angle rotation uncertainty and δ_2 is equal to zero.

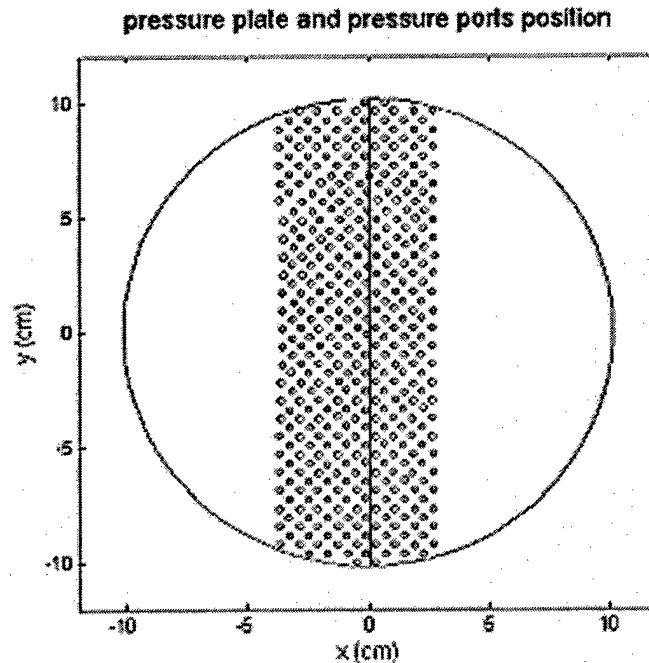


Figure a.1 The dimension of the pressure plate and the relative positions of the pressure tap

Appendix A

A.2 Uncertainty analysis of the pressure measurement

As the discussion in the A1, the existence of uncertainties of the positions of the pressure ports in the cascade tunnel can introduce the uncertainty of the pressure while interpolating the random distributed original pressure data, (quadratic surface fit A3 is used here). The static pressure data $C_p = f(x, z)$ on the end-wall is a function of x and z . Using the first order Taylor expansion of the equation, the uncertainties for pressure distribution function can be calculated. Using Equation A4 below.

$$C_p = a_1x^2 + a_2z^2 + a_3zx + a_4x + a_5z + a_6 \quad (\text{A2.1})$$

$$\delta_{C_p} = \sqrt{\frac{\partial C_p^2}{\partial z} \times \delta_z^2 + \frac{\partial C_p^2}{\partial x} \times \delta_x^2} \quad (\text{A2.2})$$

Where δ_z, δ_x are the position uncertainties of the pressure ports, here total maximum uncertainty of the positions of the pressure ports is chosen as the δ_z, δ_x . There are pressure gradient terms, which are associated and varied with different positions, in the equation A4. The average uncertainty of C_p in those positions having LDV profiles, are calculated for both tip gap case. δ_{C_p} for $t/c=3.3\%$ case is ± 0.011 and δ_{C_p} for $t/c=1.65\%$ case is about ± 0.017 . The reason that uncertainty in $t/c=3.3\%$ case is lower than the one in $t/c=1.65\%$ case is that the pressure gradient in $t/c=1.65\%$ case is higher than the one in the same point in $t/c=3.3\%$ case. Again, this uncertainty is the average uncertainty, which is associated with the pressure gradient, and the uncertainty of the measurement position.

Appendix A

A.3 Uncertainty analysis of wall shear stress direction measurement with the digitalized oil flow images

In chapter 3, the technology of the flow angle measurement with the digitalized oil flow images is discussed. With these digitized oil pictures having various details of the cascade flow, AutoCAD, one of engineering design software, was used to measure the wall shear stress angles where we are interested. The streaks in the oil flow pictures correspond to the wall shear stress direction, which can be measured and compared with the average flow angles in the viscous sublayer from LDV measurement. In the measurement process, we need to draw a line passing through the measurement point and tangent to the streaks and the tangent line is drawn, based on the visual judgement. The resolution of this software (Autocad) for the angle measurement is 0.0001 degree, and the uncertainty of the flow angles in the LDV measurement is approximately ± 0.5 degree, (Kuhl, 2001). Thus, the main uncertainty is due to the visual judgement of drawing the tangent line. Based on the several angle measurements on the same measurement point, the angle uncertainty from the visual judgement is about $\pm 1^\circ$ and the same order as the uncertainty for the flow angle from the LDV measurements. The root mean square of these flow angles difference between the LDV and the oil flow measurement is $\pm 1.65^\circ$. This gives us confidence in these wall shear stress angles from the oil flow measurement, and it is also a simple way to measure wall shear stress angles for those positions where we do not have LDV data.

Appendix A

A.4 The least square fit of a quadratic surface

The quadratic surface can be fit to the static pressure data $C_p = f(x, z)$ on the end-wall, ie,

$$C_p = a_1 x^2 + a_2 z^2 + a_3 xz + a_4 x + a_5 z + a_6 \quad (\text{A4.1})$$

The least square fit require,

$$S = \sum_{i=1}^n [C_{pi} - (a_1 x_i^2 + a_2 z_i^2 + a_3 z_i x_i + a_4 x_i + a_5 z_i + a_6)]^2 \quad (\text{A4.2})$$

In order to be minimized, by setting following derivative equal to zero.

$$\frac{\partial S}{\partial a_1} = 0 \quad (\text{A4.3})$$

$$a_1 \sum x_i^4 + a_2 \sum z_i^2 x_i^2 + a_3 \sum z_i x_i^3 + a_4 \sum x_i^3 + a_5 \sum z_i x_i^2 + a_6 \sum x_i^2 = \sum C_{pi} x_i^2$$

$$\frac{\partial S}{\partial a_2} = 0 \quad (\text{A4.4})$$

$$a_1 \sum z_i^2 x_i^2 + a_2 \sum z_i^4 + a_3 \sum z_i^3 x_i + a_4 \sum xz_i^2 + a_5 \sum z_i^3 + a_6 \sum z_i^2 = \sum C_{pi} z_i^2$$

$$\frac{\partial S}{\partial a_3} = 0 \quad (\text{A4.5})$$

$$a_1 \sum z_i x_i^3 + a_2 \sum z_i^3 x_i + a_3 \sum z_i^2 x_i^2 + a_4 \sum z_i x_i^2 + a_5 \sum x_i z_i^2 + a_6 \sum x_i z_i = \sum C_{pi} x_i z_i$$

$$\frac{\partial S}{\partial a_4} = 0 \quad (\text{A4.6})$$

$$a_1 \sum x_i^3 + a_2 \sum z_i^2 x_i + a_3 \sum z_i x_i^2 + a_4 \sum x_i^2 + a_5 \sum x_i z_i + a_6 \sum x_i = \sum C_{pi} x_i$$

$$\frac{\partial S}{\partial a_5} = 0 \quad (\text{A4.7})$$

$$a_1 \sum z_i x_i^2 + a_2 \sum z_i^3 + a_3 \sum z_i^2 x_i + a_4 \sum z_i x_i + a_5 \sum z_i^2 + a_6 \sum z_i = \sum C_{pi} z_i$$

$$\frac{\partial S}{\partial a_6} = 0 \quad (\text{A4.8})$$

$$a_1 \sum x_i^2 + a_2 \sum z_i^2 + a_3 \sum z_i x_i + a_4 \sum x_i + a_5 \sum z_i + a_6 n = \sum C_{pi}$$

Appendix A

Reorganizing above equations in the matrix form (A3.9),

$$\begin{bmatrix} \sum x_i^4 & \sum z_i^2 x_i^2 & \sum z_i x_i^3 & \sum x_i^3 & \sum z_i x_i^2 & \sum x_i^2 \\ \sum z_i^2 x_i^2 & \sum z_i^4 & \sum z_i^3 x_i & \sum z_i^2 x_i & \sum z_i^3 & \sum z_i^2 \\ \sum z_i x_i^3 & \sum z_i^3 x_i & \sum z_i^2 x_i^2 & \sum z_i x_i^2 & \sum z_i^2 x_i & \sum z_i x_i \\ \sum x_i^3 & \sum z_i^2 x_i & \sum z_i x_i^2 & \sum x_i^2 & \sum z_i x_i & \sum x_i \\ \sum z_i x_i^2 & \sum z_i^3 & \sum z_i^2 x_i & \sum z_i x_i & \sum z_i^2 & \sum z_i \\ \sum x_i^2 & \sum z_i^2 & \sum z_i x_i & \sum x_i & \sum z_i & n \end{bmatrix} \begin{bmatrix} a_1 \\ a_2 \\ a_3 \\ a_4 \\ a_5 \\ a_6 \end{bmatrix} = \begin{bmatrix} \sum C_{pi} x_i^2 \\ \sum C_{pi} z_i^2 \\ \sum C_{pi} x_i z_i \\ \sum C_{pi} x_i \\ \sum C_{pi} z_i \\ \sum C_{pi} \end{bmatrix} \quad (A4.9)$$

Here, n is 10, we choose the closest ten pressure data points to interpolate the point which is interested. Ten data points contain the local pressure information. Since x , z and C_p are known, a_1, a_2, a_3, a_4, a_5 and a_6 can be solved from above equation.

Appendix A

A.5 skin friction coefficient derivation with the pressure gradient term

Through out the near-wall region certain terms of the governing momentum equations can be discarded as being negligibly small compared to those remaining. For sufficiently small values of y , all derivatives with respect to x are negligible; at $y=0$ all x and z derivatives are exactly zero. Since the wall is impermeable, $v=0$ at $y=0$, and the continuity equation requires that $v=0$ as long as $\frac{\partial u}{\partial x} = \frac{\partial w}{\partial z} = 0$. Thus the momentum equation in the direction of the wall shear stress reduces to

$$-\frac{1}{\rho} \frac{\partial p}{\partial s} + \frac{\partial}{\partial y} (-\overline{uv} + \nu \frac{\partial U}{\partial y}) = 0 \quad (\text{A5.1})$$

Integration with respect to y , where $\frac{\partial p}{\partial s}$ is the component of the surface pressure gradient in the wall shearing stress direction:

$$-\overline{uv} + \nu \frac{\partial U}{\partial y} = \frac{\tau}{\rho} = \frac{\tau_w}{\rho} + \frac{y}{\rho} \frac{dp_\infty}{ds} \quad (\text{A5.2})$$

$$\frac{\partial u}{\partial x} + \frac{\partial v}{\partial y} + \frac{\partial w}{\partial z} = 0 \quad (\text{A5.3})$$

Considering the above fluctuation continuity equation, just away from the wall, the u and w are proportional to y and mean v is proportion to y^2 . Thus $-\overline{uv}$ is proportional to y^3 . It is reasonable that we assume $-\overline{uv} = C_3 y^3$, substitute this into the momentum equation (3.9), and integrate with respect to y to produce

$$Q = C_1 y + C_2 y^2 + C_4 y^4 \quad (3.13)$$

$$\text{Where } C_1 = \frac{\tau_w}{\mu}, C_2 = \frac{U_\infty^2}{4\nu} \frac{dC_p}{ds} \quad u_\tau = \sqrt{\frac{\tau_w}{\rho}}$$

Once the pressure gradient along the surface skin friction line is calculated, C_2 is known. In order to get C_1 and C_4 , a curve fit needs to be done with the viscous sublayer ($y^+ < 9$) velocity data. Once C_1 is known, through the relationship between friction velocity and

Appendix A

wall shear stress, the friction velocity which is the characteristic velocity scale in the wall region can be obtained.

Appendix A

A.6 Uncertainty Analysis for the Skin-friction Velocity Calculation

The uncertainty of the skin-friction velocity should be examined in two levels. The first part corresponds to the uncertainty in the individual experimental measurement at same circumferential locations in same flow conditions. The second one is uncertainty in the skin-friction velocity calculation with a least square fit to the equation 3.13. The y-shifts calculated from the fit of equation 3.13 present the uncertainty of the finding the wall, which is in $\pm 55\mu\text{m}$. Since the correlation coefficient in the least square fit is more than 0.99, the uncertainty of the skin friction velocity from the curve fit should be less than 2%. In the following discussion, the uncertainty from the experimental measurement will be visited.

The modified momentum equation in the viscous sublayer is shown as equation 3.13. In this equation, once the pressure gradient along the surface skin friction line is calculated, C_2 is known. In order to get C_1 and C_4 , a curve fit need to be done with the viscous sublayer ($y^+ < 9$) velocity data. Once C_1 is known, through the relationship between friction velocity and wall shear stress, the skin friction velocity, which is the characteristic velocity scale in the wall region, can be obtained.

$$Q = C_1 y + C_2 y^2 + C_4 y^4 \quad (3.13)$$

$$\text{Where } C_1 = \frac{\tau_w}{\mu}, C_2 = \frac{U_\infty^2}{4\nu} \frac{dC_p}{ds} \quad u_\tau = \sqrt{\frac{\tau_w}{\rho}}$$

Appendix A

Equation A.6.1 is the skin friction velocity presented by the velocity, y position, viscosity and density. Here u_τ is a function of y , C_2 and curve fit velocity Q . While in the least square fit, there are more than 5 data points used in the viscous sublayer. Plugging those data points with their uncertainties used in the curve fitting into equation A6.2, uncertainties for skin friction results can be obtained. The uncertainties are calculated using 21 to 1 odds and uncertainties are calculated as $\pm 2\sigma$. The skin friction velocity for profiles 2U and 4S are 1.00 and 1.07. The uncertainties based on A6.2 for profiles 2U and 4S are 0.04 and 0.06 respectively. The average uncertainty of skin friction velocity in this measurement should be less than 5%.

$$u_\tau = \sqrt{\frac{C_1 \times \mu}{\rho}} = \sqrt{\frac{(Q - C_2 y^2 - C_3 y^4) \times \mu}{\rho \times y}} \quad (\text{A6.1})$$

$$\delta u_\tau = \sqrt{\sum_{i=1}^5 \left(\frac{\partial u_\tau}{\partial Q_i} \right)^2 (\Delta Q_i)^2 + \sum_{i=1}^5 \left(\frac{\partial u_\tau}{\partial y_i} \right)^2 (\Delta y_i)^2 + \left(\frac{\partial u_\tau}{\partial C_2} \right)^2 (\Delta C_2)^2} \quad (\text{A6.2})$$

Appendix A

Table a 7.1 Pressure Gradients Results for both Two Tip Gaps

profile	t/c=1.65%			10 points			profile	t/c=3.3%			10 points		
	Z/Ca	X/Ca	Cp _x	Cp _z	Cp _x	Cp _z		Z/Ca	X/Ca	Cp _x	Cp _z	Cp _x	Cp _z
1C	-0.74	0.01		-0.02154	0.01702		1D	-0.96	0.01	0.033		0.041	
1D	-0.93	0.01		0.0717	0.07331		1B	-0.85	0.01	0.018		0.026	
1B	-0.85	0.01		0.0264	0.0199		1U	-0.76	0.01	-0.010		0.004	
1U	-0.76	0.01		-0.01436	0.01754		2S	-1.02	0.04	0.055		0.055	
2S	-1.02	0.04		0.11562	0.08486		2C	-0.97	0.04	0.032		0.048	
2C	-0.97	0.04		0.05967	0.09551		2P	-0.92	0.04	0.020		0.039	
2P	-0.92	0.04		0.03926	0.06717		2U	-0.87	0.04	0.023		0.022	
2U	-0.87	0.04		0.04819	0.01988		3S	-1.15	0.09	0.042		0.066	
3S	-1.15	0.09		0.15653	0.05205		3C	-1.1	0.09	0.074		0.086	
3C	-1.1	0.09		0.14727	0.17652		3B	-1.07	0.09	0.059		0.090	
3B	-1.07	0.09		0.10138	0.17089		3P	-1.03	0.09	0.048		0.074	
3P	-1.03	0.09		0.0951	0.14154		3U	-0.96	0.09	0.019		0.052	
3U	-0.96	0.09		0.02311	0.07749		4S	-1.22	0.12	0.053		0.022	
4S	-1.19	0.12		0.17218	0.04704		4C	-1.16	0.12	0.079		0.062	
4C	-1.14	0.12		0.29231	0.11137		4B	-1.12	0.12	0.069		0.094	
4B	-1.12	0.12		0.22334	0.22531		4P	-1.1	0.12	0.081		0.119	
4P	-1.09	0.12		0.15365	0.19446		4U	-1.03	0.12	0.033		0.075	
4U	-1.06	0.12		0.09791	0.15977		5S	-1.35	0.18	0.060		-0.038	
5S	-1.32	0.18		0.2164	0.21308		5C	-1.3	0.18	0.112		0.084	
5C	-1.26	0.18		0.25102	0.32352		5B	-1.26	0.18	0.137		0.135	
5B	-1.23	0.18		0.31388	0.40942		5P	-1.22	0.18	0.138		0.191	
5P	-1.2	0.18		0.15008	0.40319		5U	-1.15	0.18	0.057		0.153	

Appendix A

5U	-1.17	0.18	0.19688	0.45093	E1	-1.4	0.18	-0.005	-0.087
E1	-1.4	0.18	-0.04988	-0.11915	E2	-1.45	0.18	-0.029	-0.144
E2	-1.45	0.18	-0.04492	-0.1558	6S	-1.51	0.27	0.052	-0.089
E3	-1.49	0.18	-0.05568	-0.17493	6C	-1.42	0.27	0.231	0.273
6S	-1.51	0.27	0.08533	0.09735	6B	-1.39	0.27	0.241	0.292
6C	-1.42	0.27	0.21216	0.43269	6P	-1.35	0.27	0.193	0.262
6B	-1.39	0.27	0.32815	0.4891	6U	-1.28	0.27	0.069	0.142
6P	-1.35	0.27	0.29395	0.42037	7S	-1.74	0.42	0.065	0.267
6U	-1.32	0.27	0.17901	0.28079	7C	-1.71	0.42	0.176	0.372
7S	-1.74	0.42	0.14895	-0.00646	7B	-1.67	0.42	0.342	0.544
7C	-1.67	0.42	0.15948	0.48825	7P	-1.61	0.42	0.264	0.501
7B	-1.63	0.42	0.33942	0.51714	7U	-1.52	0.42	0.119	0.222
7P	-1.6	0.42	0.36616	0.53241	X1	-1.85	0.42	-0.036	0.074
7U	-1.58	0.42	0.24137	0.40668	X4	-1.91	0.42	-0.061	-0.005
8S	-2.03	0.65	0.09267	0.22625	X2	-1.94	0.42	-0.056	-0.044
8C	-2	0.65	0.34251	0.5635	X3	-1.99	0.42	-0.056	-0.097
8B	-1.96	0.65	0.3679	0.488	X5	-2.04	0.42	-0.101	-0.196
8P	-1.93	0.65	0.21023	0.13168	8S	-2.07	0.65	0.054	0.125
8U	-1.84	0.65	0.00014	0.02756	8C	-2.01	0.65	0.089	0.243
9S	-2.4	0.99	0.02121	0.05465	8B	-1.97	0.65	0.115	0.309
9C	-2.38	0.99	0.03894	0.05455	8P	-1.93	0.65	0.111	0.250
9B	-2.36	0.99	0.03492	0.05109	9S	-2.4	0.99	0.011	0.039
9P	-2.35	0.99	0.04419	0.04658	9C	-2.38	0.99	0.010	0.034
9U	-2.25	0.99	0.01326	-0.01733	9B	-2.36	0.99	0.009	0.028
					9P	-2.35	0.99	0.008	0.024

Appendix B

Octant contribution plots for the Reynolds stress in the wall collateral coordinates and the mid tip gap coordinates with $t/c=3.3\%$ clearance, normalized by the square of the free-stream velocity.

Appendix B

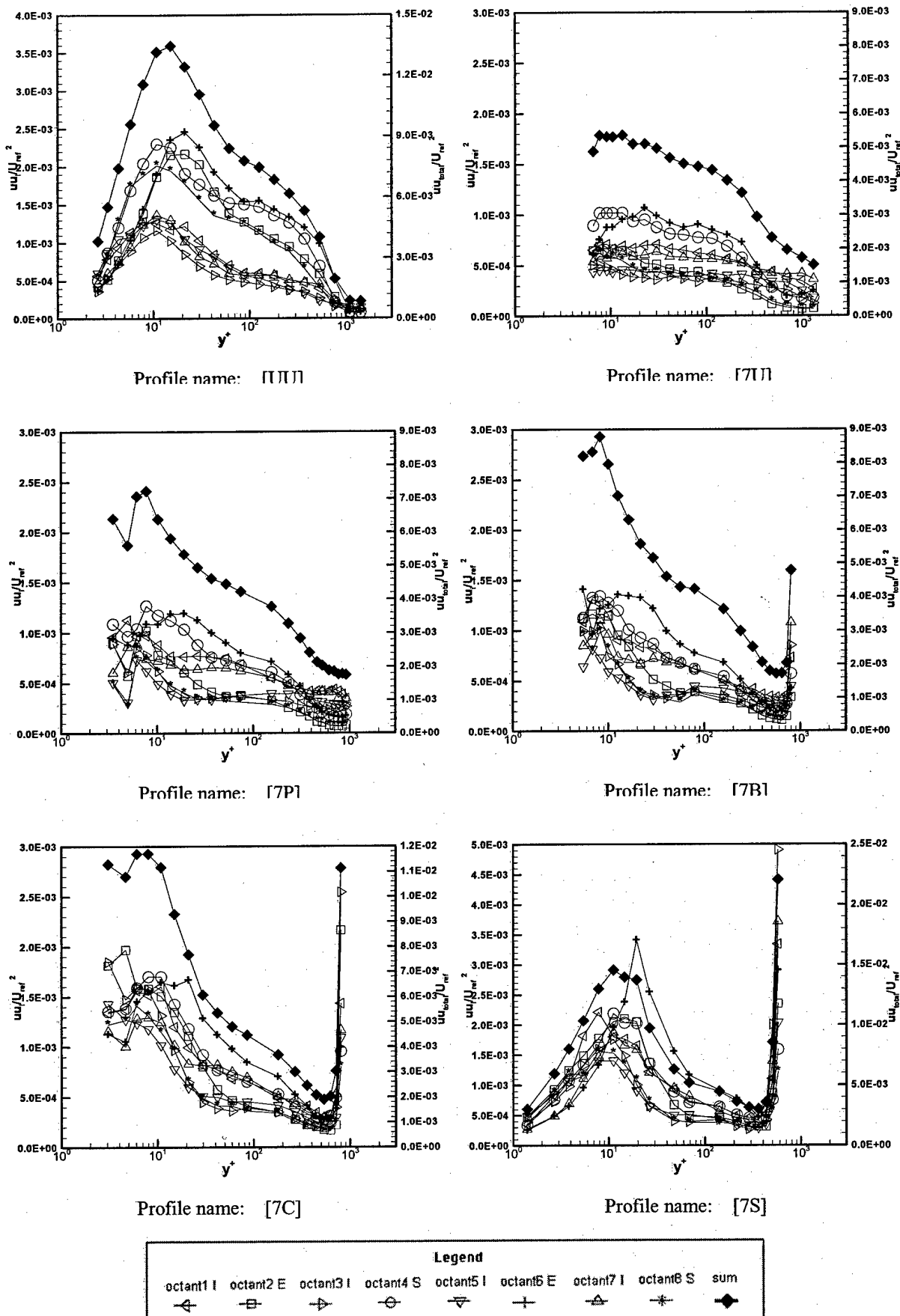
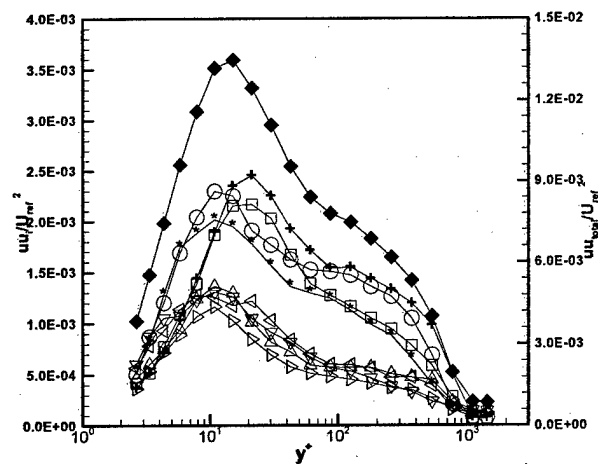
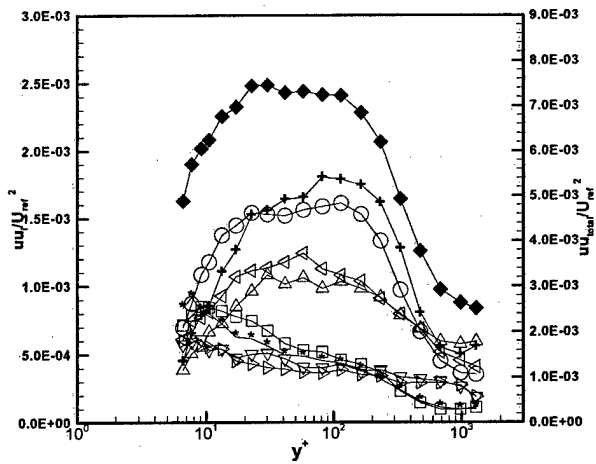


Figure b.1 Octant contributions to Reynolds stress uu (U_{ref} is the free-stream velocity, wall collateral coordinates)

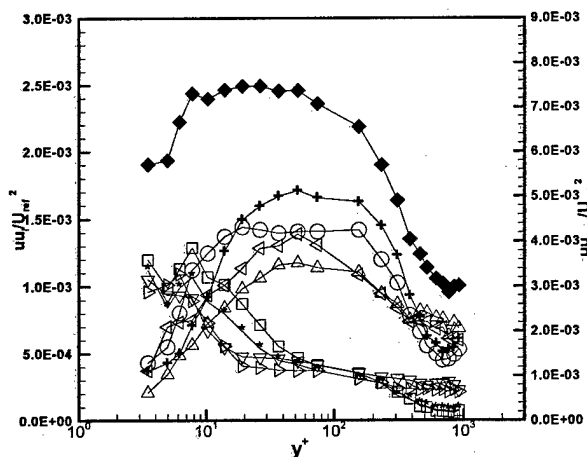
Appendix B



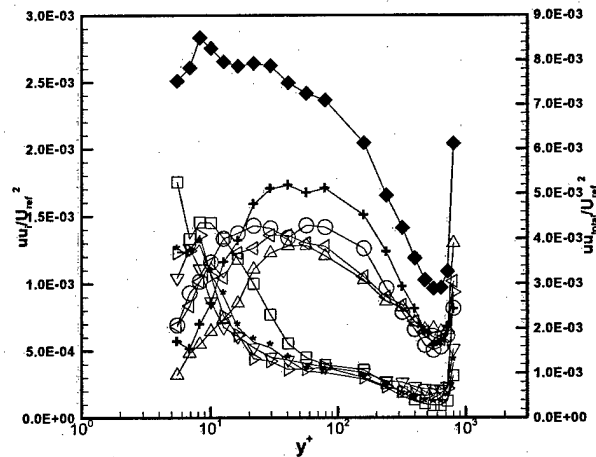
Profile name: [PII]



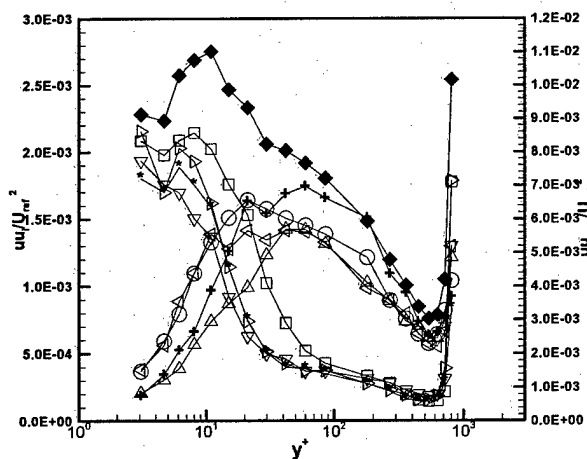
Profile name: [7II]



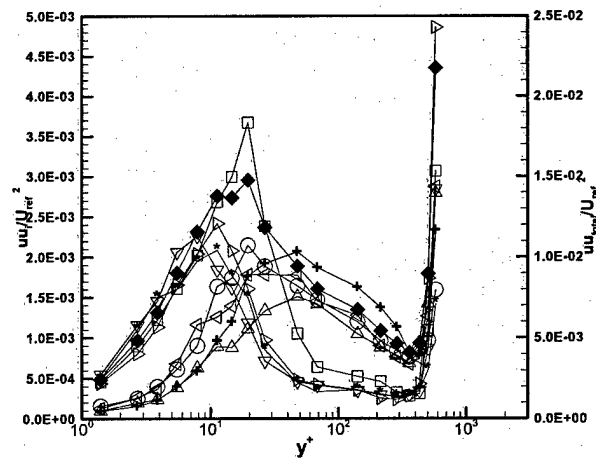
Profile name: [7P]



Profile name: [7B]



Profile name: [7C]



Profile name: [7S]

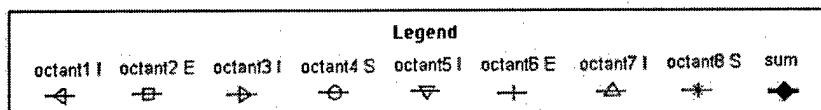


Figure b.2 Octant contributions to Reynolds stress uu (U_{ref} is the free-stream velocity, mid tip gap coordinates)

Appendix B

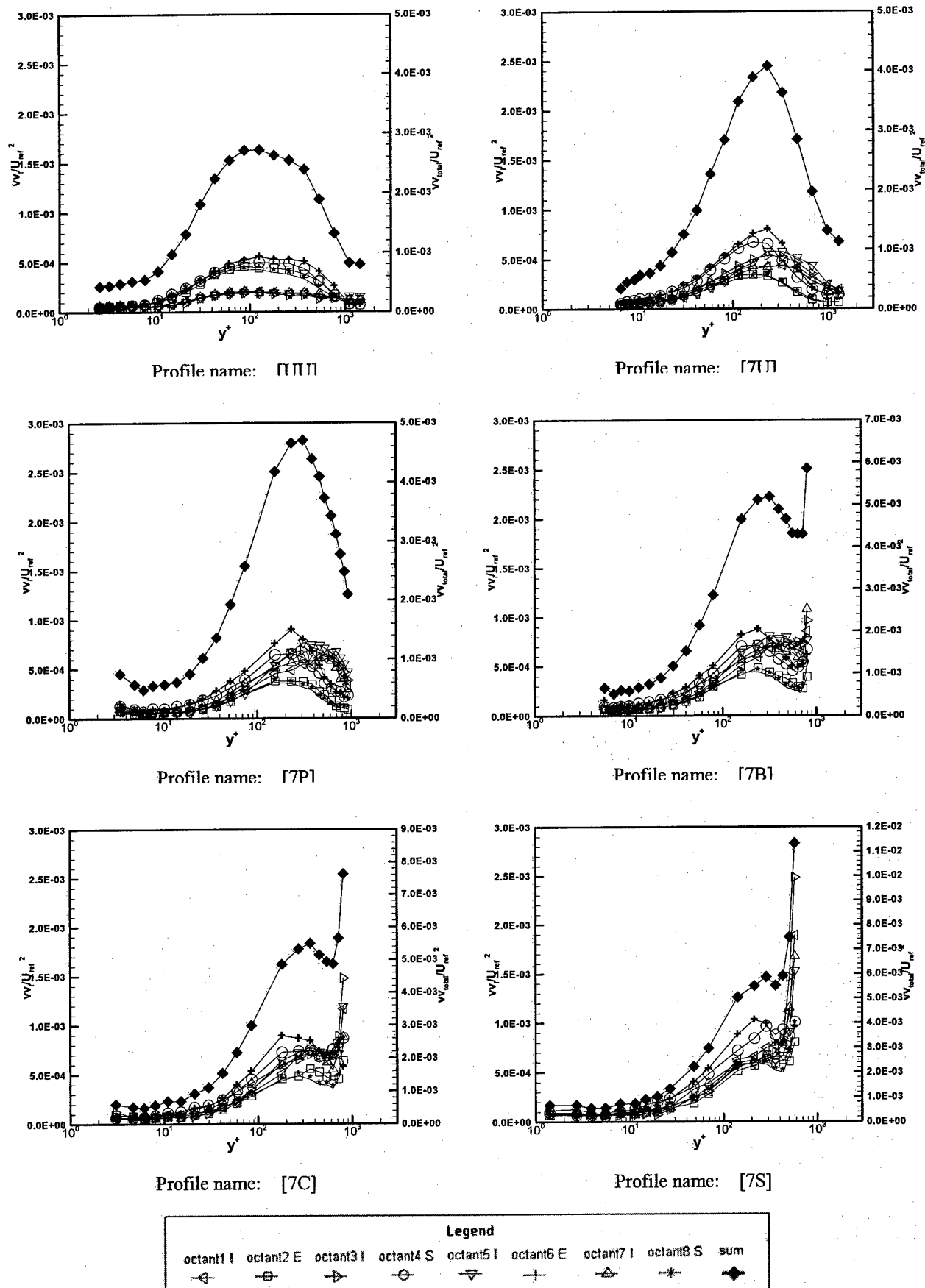
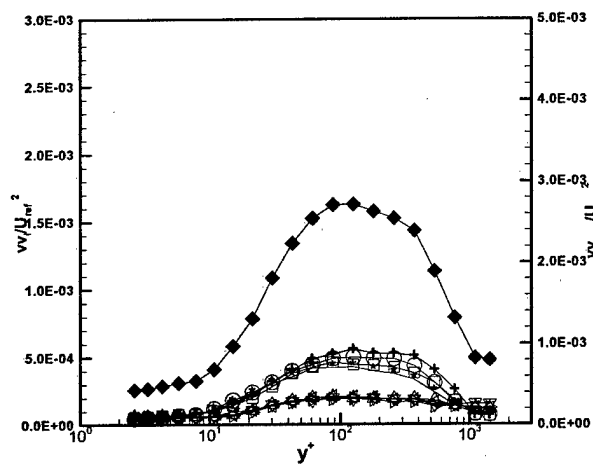
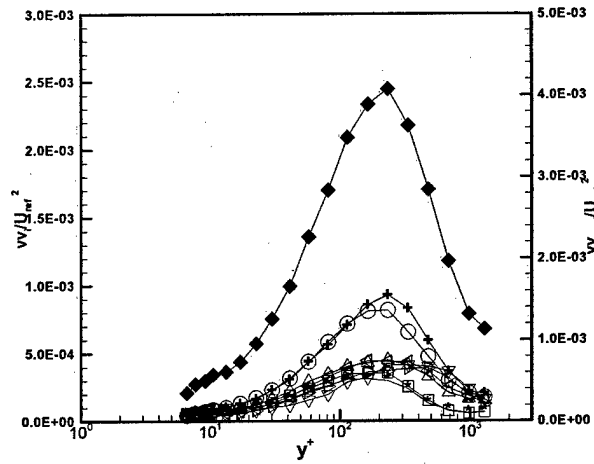


Figure b.3 Octant contributions to Reynolds stress vv (U_{ref} is the free-stream velocity, wall collateral coordinates)

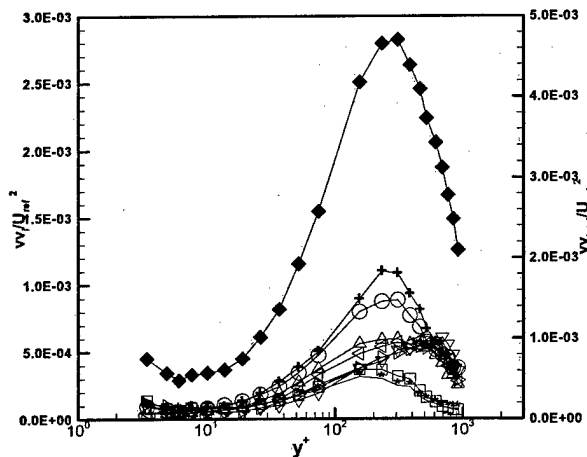
Appendix B



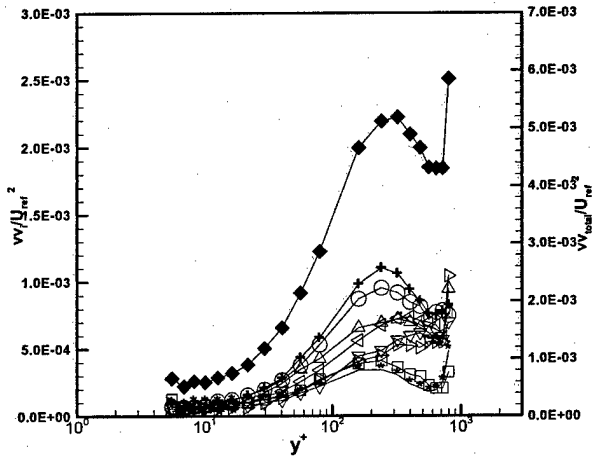
Profile name: [UU]



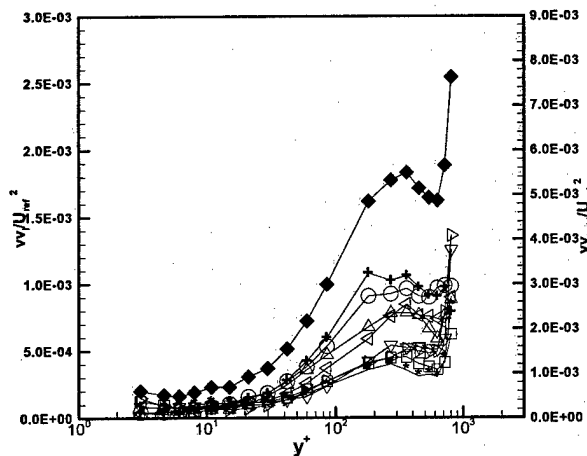
Profile name: [7U]



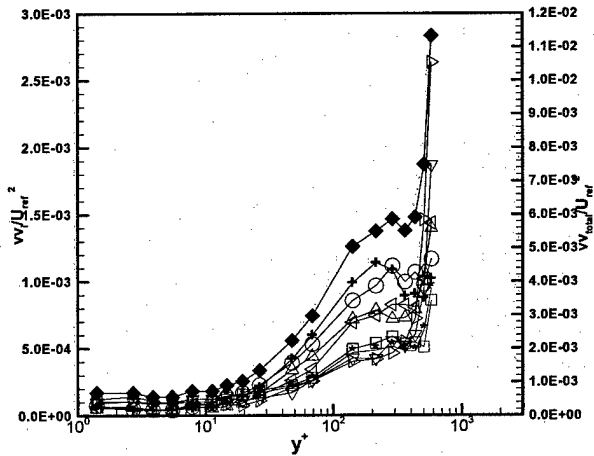
Profile name: [7P]



Profile name: [7B]



Profile name: [7C]



Profile name: [7S]

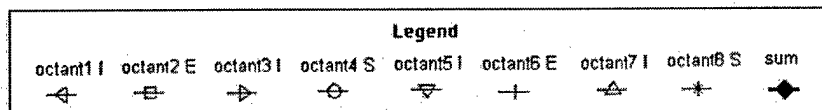


Figure b.4 Octant contributions to Reynolds stress vv (U_{ref} is the free-stream velocity, mid tip gap coordinates)

Appendix B

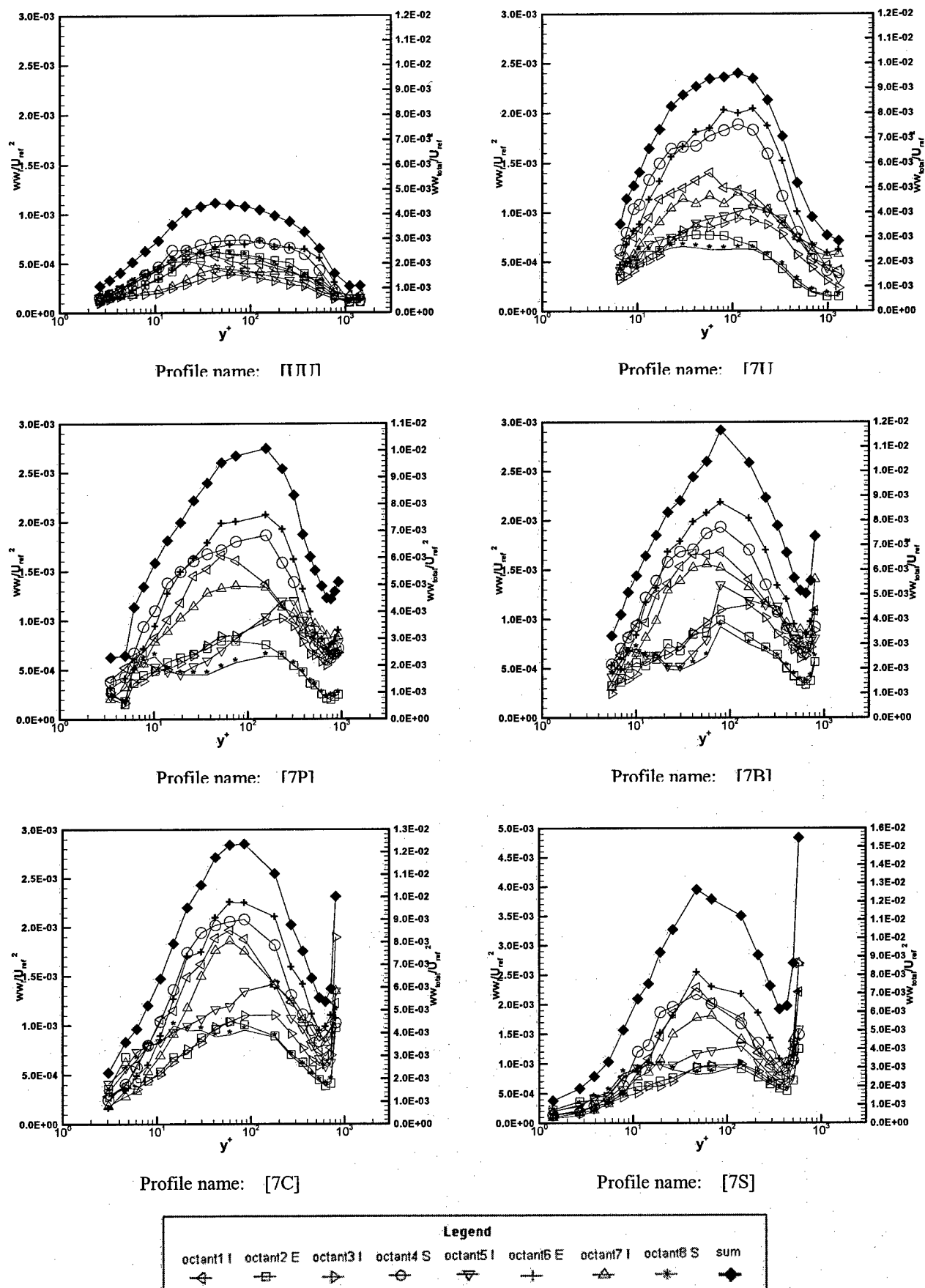


Figure b.5 Octant contributions to Reynolds stress ww (U_{ref} is the free-stream velocity, wall collateral coordinates)

Appendix B

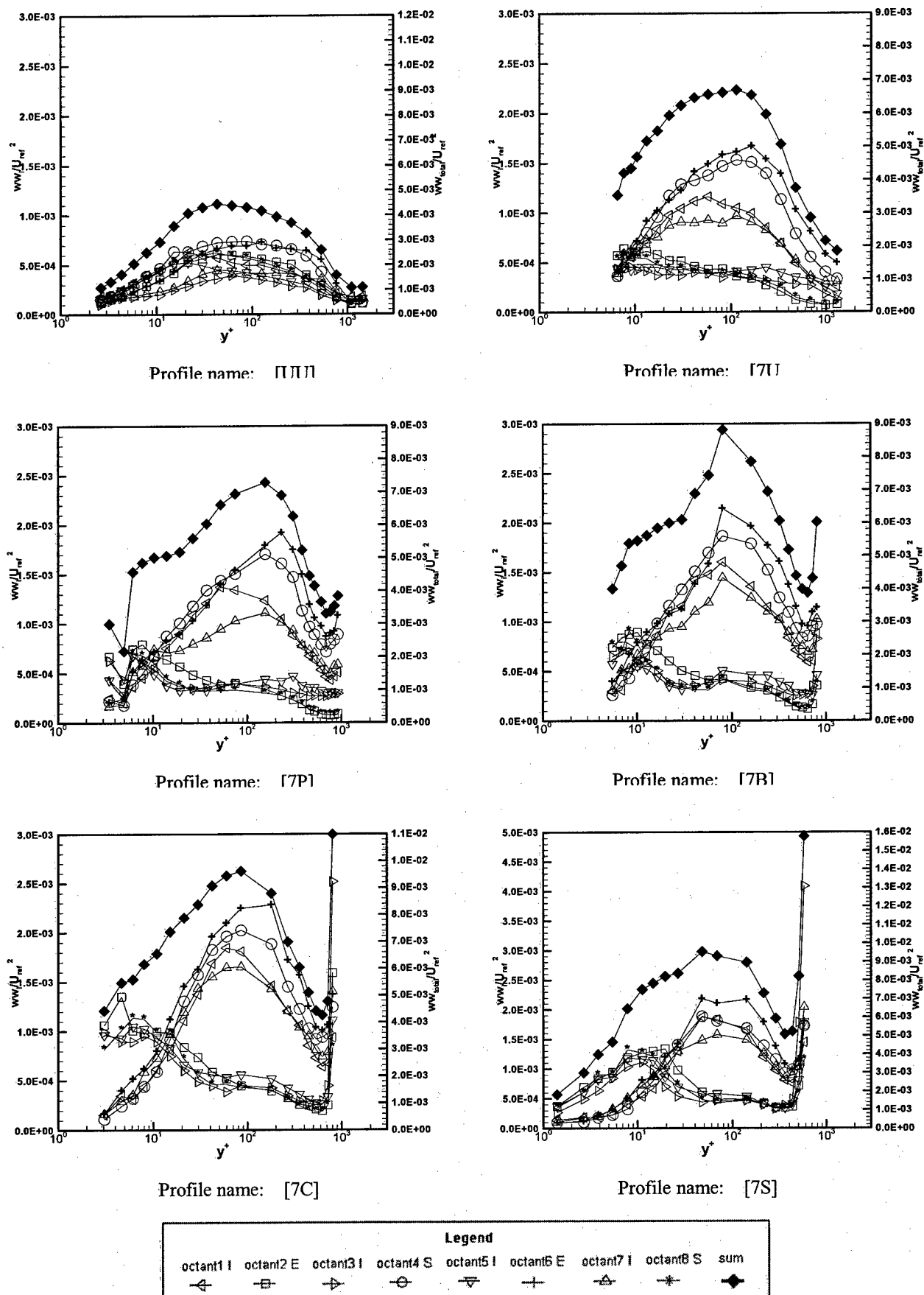


Figure b.6 Octant contributions to Reynolds stress ww (U_{ref} is the free-stream velocity, mid tip gap coordinates)

Appendix B

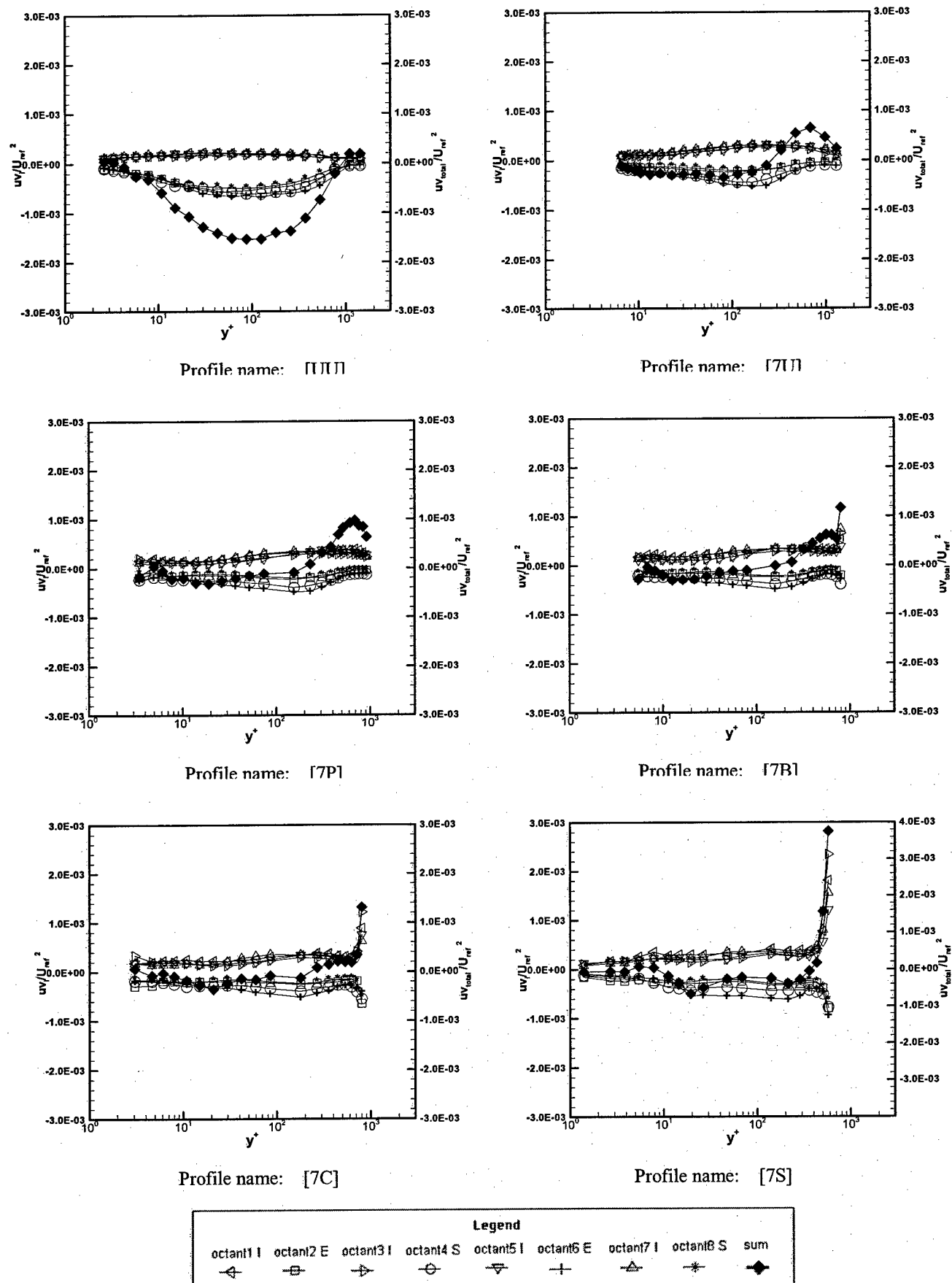


Figure b.7 Octant contributions to Reynolds stress uv (U_{ref} is the free-stream velocity, wall collateral coordinates)

Appendix B

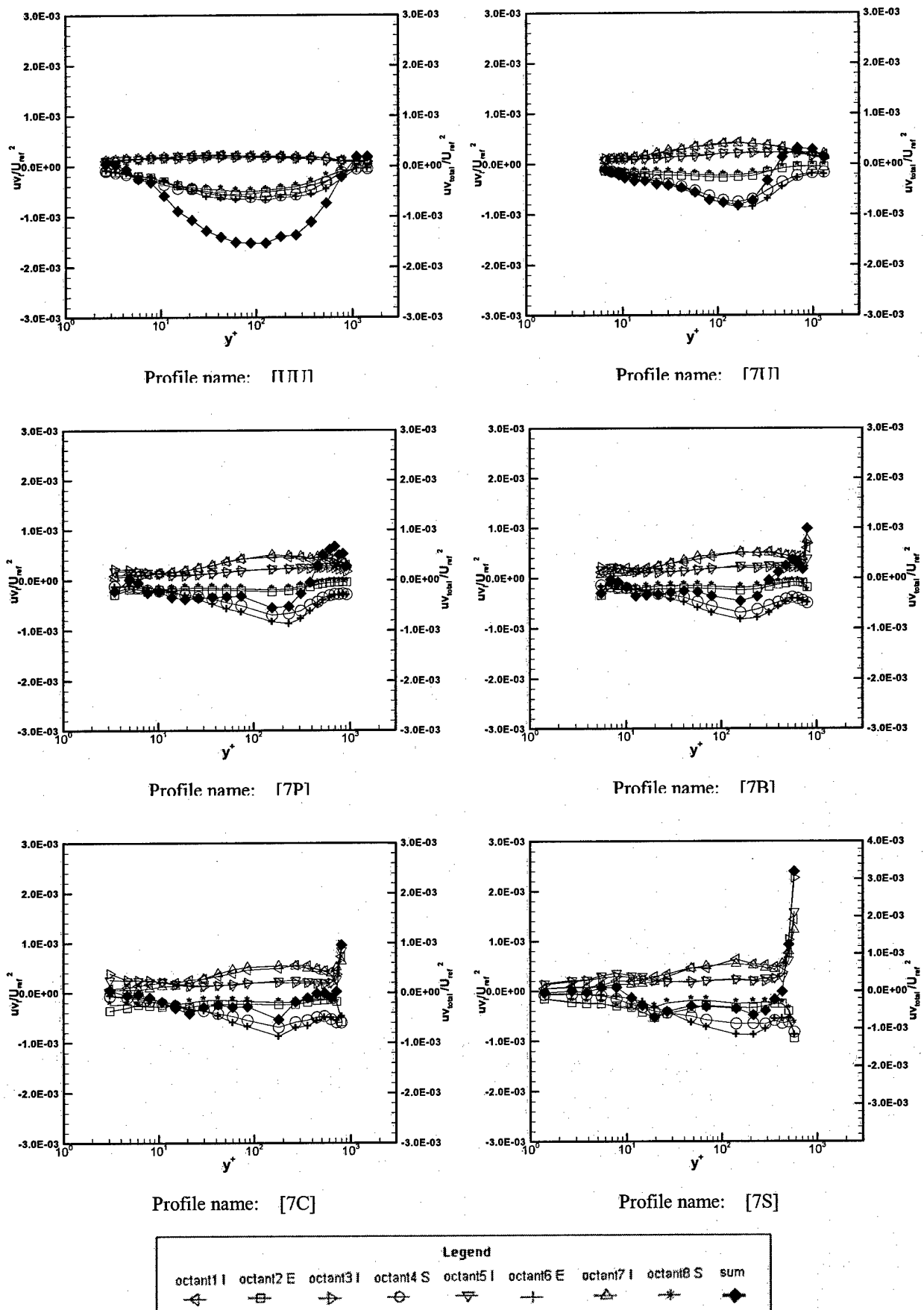
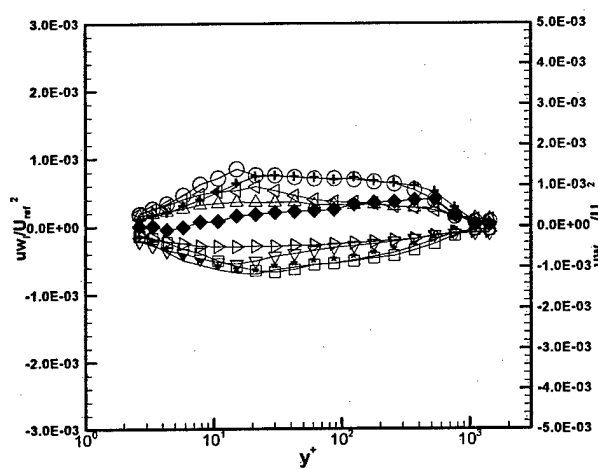
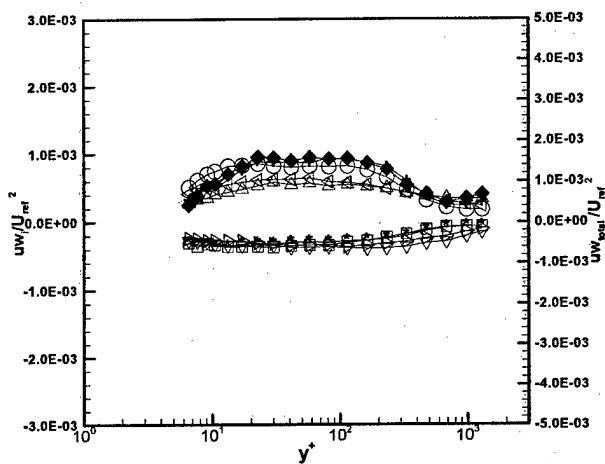


Figure b.8 Octant contributions to Reynolds stress uv (U_{ref} is the free-stream velocity, mid tip gap coordinates)

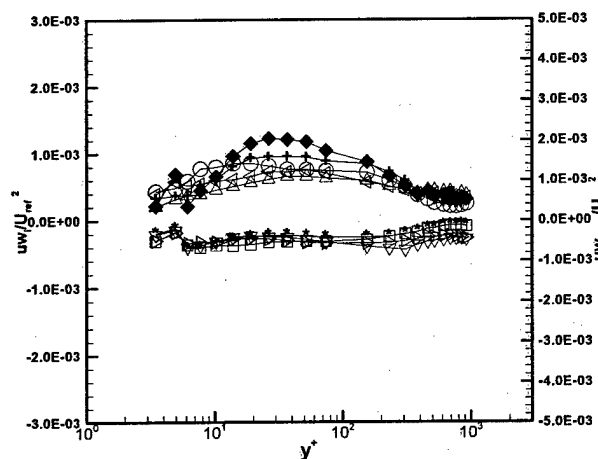
Appendix B



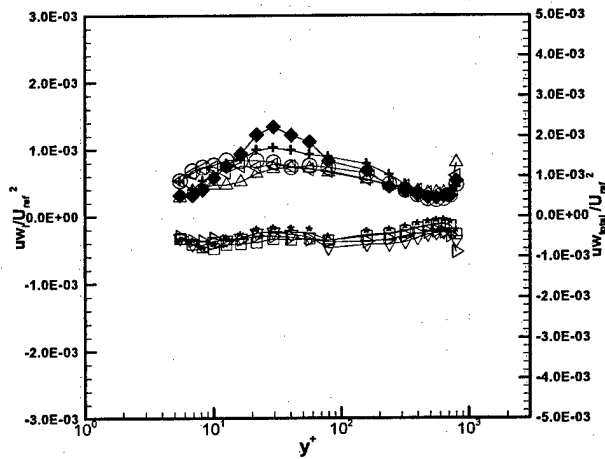
Profile name: [UU]



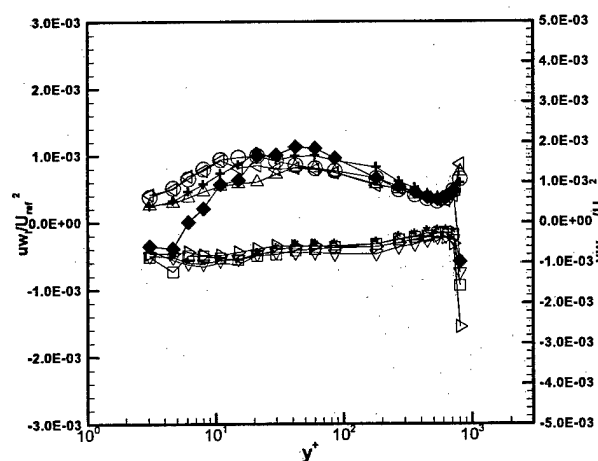
Profile name: [7U]



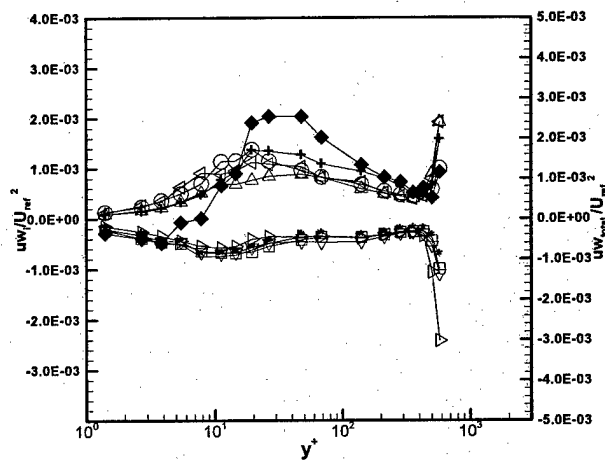
Profile name: [7P]



Profile name: [7B]



Profile name: [7C]



Profile name: [7S]

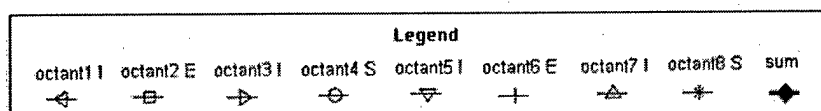


Figure b.9 Octant contributions to Reynolds stress uw (U_{ref} is the free-stream velocity, wall collateral gap coordinates)

Appendix B

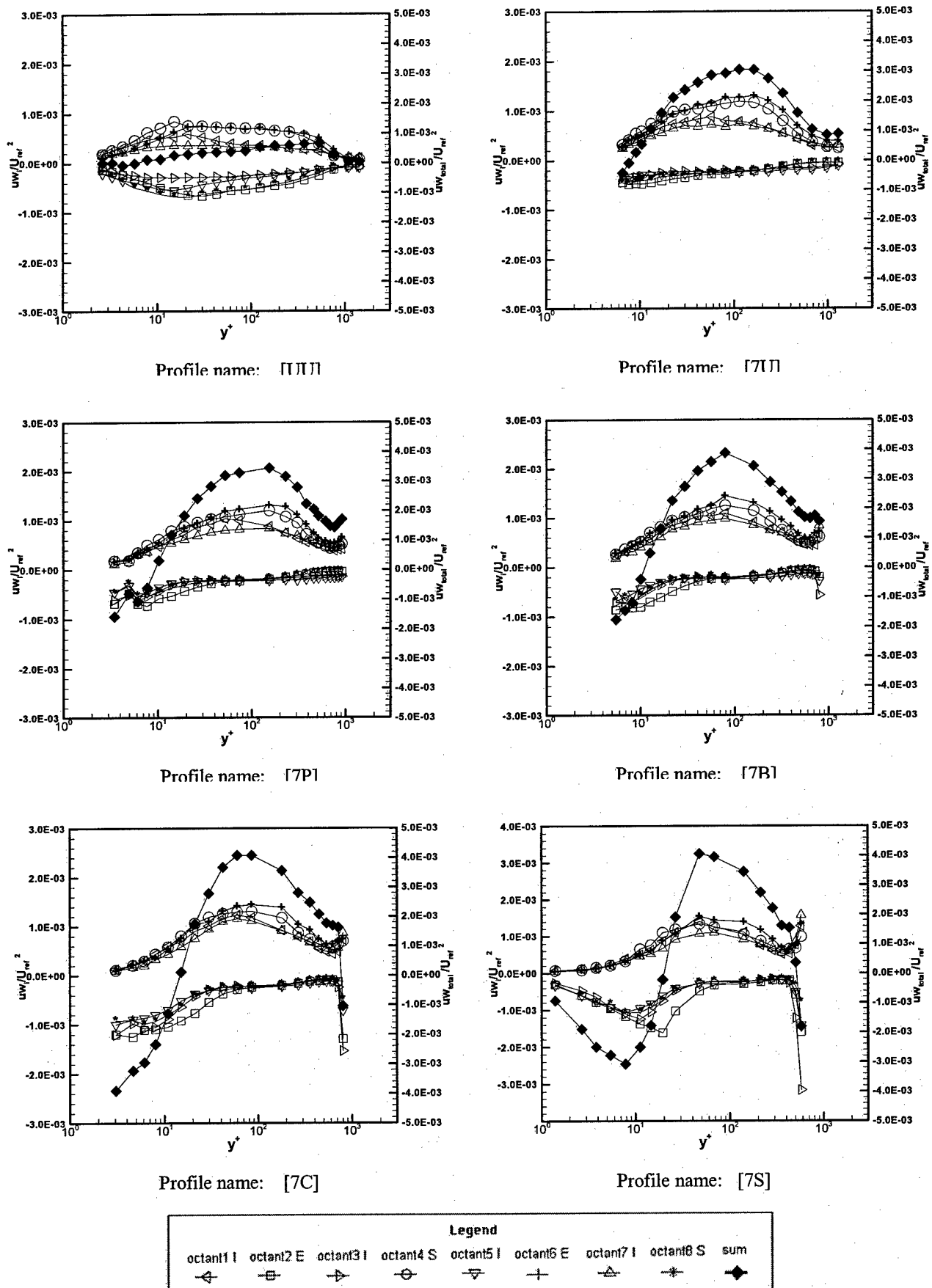
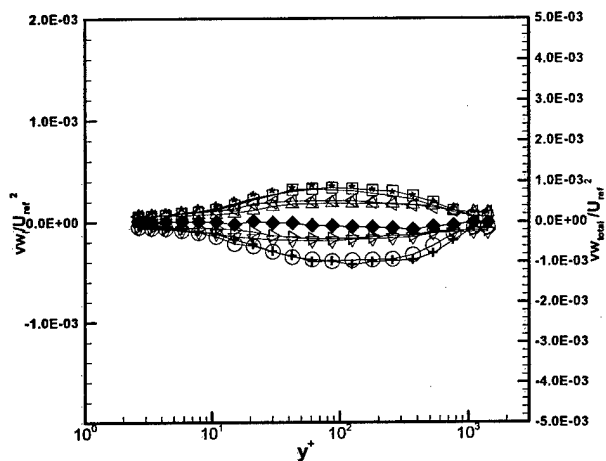
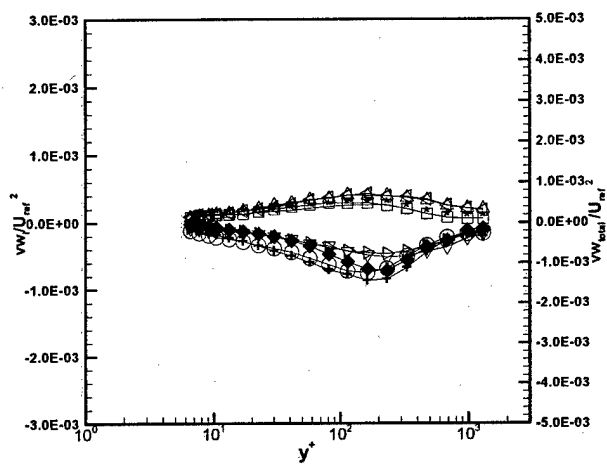


Figure b.10 Octant contributions to Reynolds stress uw (U_{ref} is the free-stream velocity, mid tip gap coordinates)

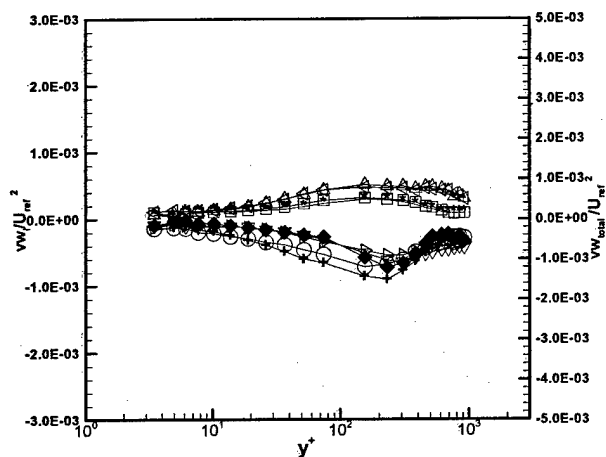
Appendix B



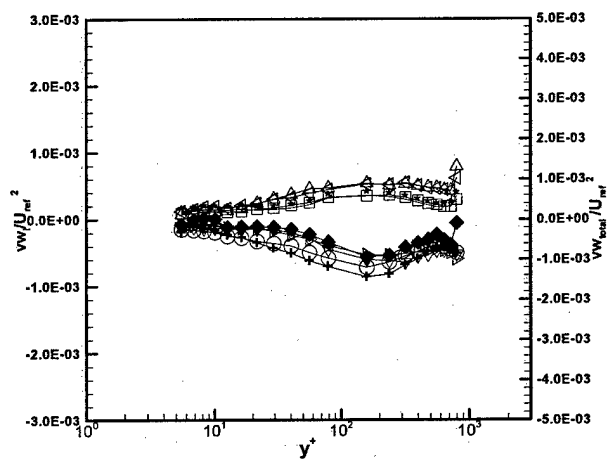
Profile name: [ΠΠΠ]



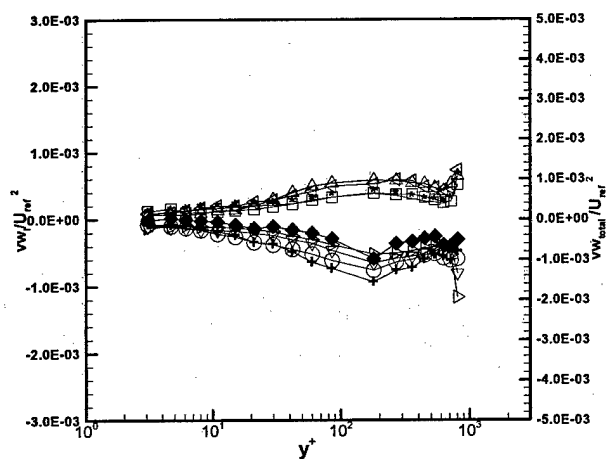
Profile name: [7ΠΠ]



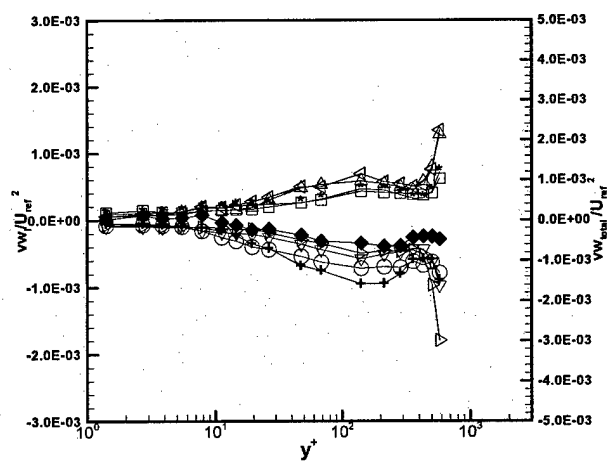
Profile name: [7Π]



Profile name: [7B]



Profile name: [7C]



Profile name: [7S]

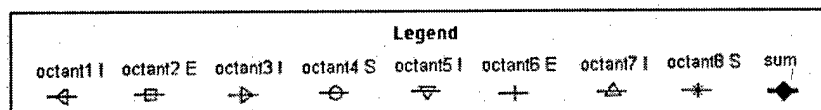
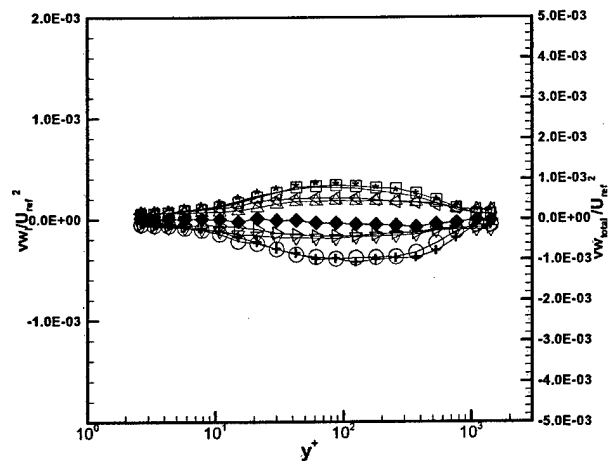
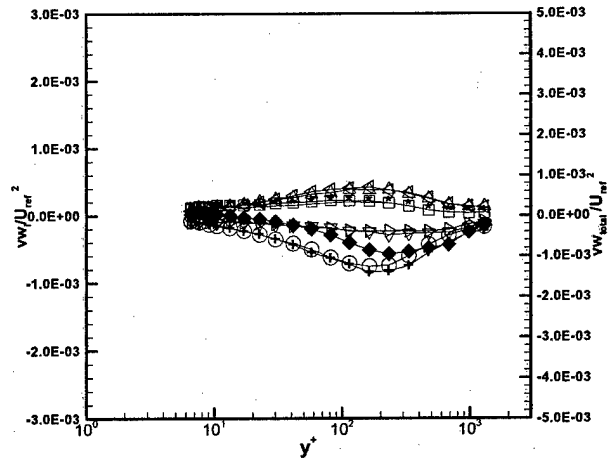


Figure b.11 Octant contributions to Reynolds stress vw (U_{ref} is the free-stream velocity, wall collateral gap coordinates)

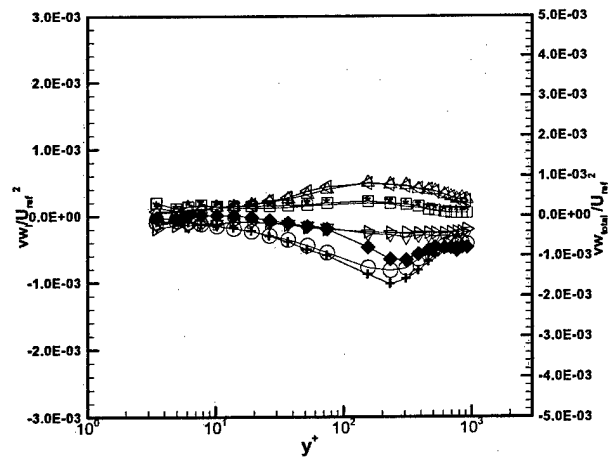
Appendix B



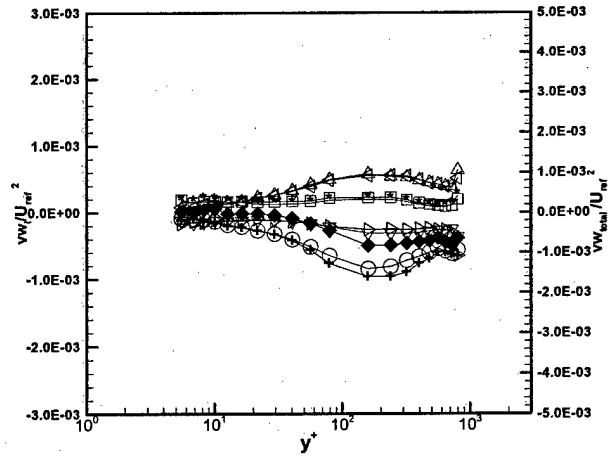
Profile name: [ΠΠΠ]



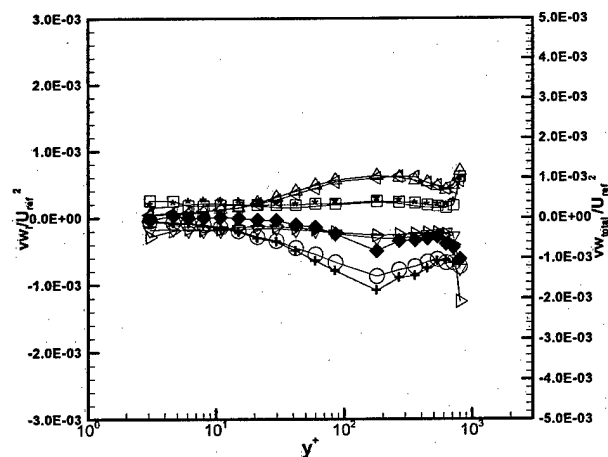
Profile name: [7ΠΠ]



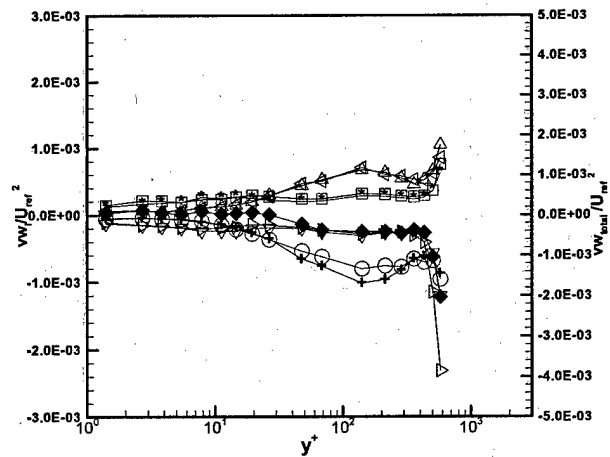
Profile name: [7P1]



Profile name: [7B1]



Profile name: [7C]



Profile name: [7S]

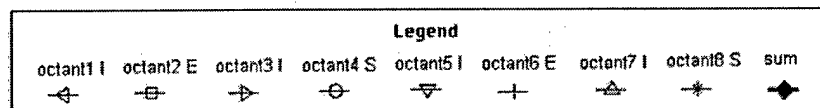


Figure b.12 Octant contributions to Reynolds stress vw (U_{ref} is the free-stream velocity, mid tip gap coordinates)